1-1-2011

The Effect of Static Pressure on the Inertial Cavitation Threshold and Collapse Strength

Kenneth Bryan Bader
University of Mississippi

THE EFFECT OF STATIC PRESSURE ON THE INERTIAL CAVITATION THRESHOLD AND BUBBLE COLLAPSE STRENGTH

A Dissertation Submitted as Part of the Requirements for a Doctor of Philosophy

The Department of Physics and Astronomy

The University of Mississippi

Kenneth Bryan Bader

May, 2011

ABSTRACT

The amplitude of the acoustic pressure required to nucleate a gas and/or vapor bubble in a fluid, and to have that bubble undergo an inertial collapse, is termed the inertial cavitation threshold. The hydrostatic dependence of the inertial cavitation threshold was measured up to 30 MPa in ultrapure water using a high quality factor spherical resonator. The threshold increased linearly with the hydrostatic pressure and was found to be temperature dependent. The strength of the bubble collapse at the threshold was measured in terms of shock waves and light emissions. The shock amplitudes increased linearly with the hydrostatic pressure, while the number of photons increased quadratically. The increase of the collapse strength was attributed to the increased threshold, and therefore to the amount of available acoustic energy.

DEDICATION

This work is dedicated to my parents, Keith and Karen Bader, and sister, Lauren Bader, whose support, advice, and (on occasion) technical expertise have made all the difference.

LIST OF ABBREVITATIONS

ABS	Acrylonitrile butadiene styrene
ASTM	American Society for Testing and Materials
FWHM	Full width at half max
GPIB	General Purpose Interface Bus
HDPE	High-density polyethylene
HiP	High Pressure Equipment Company, Erie, PA
HPLC	High performance liquid chromatography
ID	Inner diameter
IDI	Impulse Devices, Inc., Grass Valley, CA
ISO	International Organization for Standards
MOSFET	Metal-oxide Semiconductor Field Effect Transistor
NDF	Neutral density filter
OD	Outer diameter
PCD	Passive cavitation detector
PR	Pulser/receiver
PRF	Pulse repetition frequency
PTFE	Polytetrafluoroethylene
QE	Quantum efficiency of PMT
SBSL	Single bubble sonoluminescence
SL	Sonoluminescence
SS	Stainless Steel
Swage	Swagelok Company, Solon, OH
TTL	Transistor-transistor Logic

LIST OF SYMBOLS

a	Inner radius of spherical shell; also radius of crevice mount
b	Outer radius of spherical shell
f	Frequency
k_B	Boltzmann's Constant
P_A	Acoustic Pressure
P_G	Partial Pressure of Gas
P_H	Hydrostatic Pressure
P_V	Vapor Pressure
R	Time dependent bubble radius
$\dot{R} = \frac{dR}{dt}$	Time dependent bubble wall velocity
$\ddot{R} = \frac{d^2R}{dt^2}$	Time dependent bubble wall acceleration
R_0	Initial bubble radius
T	Temperature
α	Contact angle
α_A	Advancing contact angle
α_R	Receding contact angle
β	Half angle of apex of conical crevice
γ	Ratio of specific heats; also used to denote gas transfer in crevice model
μ	Fluid viscosity
ρ	Fluid density
σ	Surface tension
$\omega = 2\pi f$	Angular frequency

ACKNOWLEDGEMENTS

If John Donnes' quote "no man is an island" is an allegory for an individual's dependence on others, my landmass be akin to the super continent Pangea. I would like to thank:

Dr. Charles C. Church, my advisor, for his support, guidance, and advice over the years,

The ultrasound research group at the National Center for Physical Acoustics, in particular Dr. Joel Mobley whose advice and suggestions were pivotal to shaping this research, and Mr. Jason Raymond, who was key to helping develop the early stages of this project,

The technical and administrative staffs at NCPA and the physics department, in particular Mr. Paul Dakin, Mr. Ronnie Oswalt, and Mr. Gary Daugherty for their assistance with the construction of various aspects of the experimental set-up,

Dr. Lucien Cremaldi and Dr. Peter Sonnek for their help in calibration of the photomultiplier tubes,

Dr. Glynn Holt and Dr. Robert Hiller, for providing insightful suggests for improvement of the experiment,

The technical staff at Impulse Devices, Inc., in particular Mr. Joe Wellhoff, Mr. Brant Callahan, Mrs. Jennifer Potter, and Dr. Felipe Gaitan, for their expertise and guidance, and for the financial support of Impulse Devices, Inc.

TABLE OF CONTENTS

LIST OF TABLES

LIST of FIGURES

1. INTRODUCTION

1.1. Statement of the Problem

The energy concentration of sonoluminescence (SL) has been known for some years (Frenzel and Schultes 1934), and the large pressures and temperatures reached within the bubble have led some to speculate on whether thermonuclear conditions were attainable (Flynn 1982). The claims of Taleyarkhan (2002) of achieving such success have been criticized, due in part to the irreproducibility of his results (Shapira and Saltmarsh 2002). Nevertheless, the inertially confined plasma electron density within sonoluminescence has been shown to be comparable to that generated by the Nova laser at Lawrence Livermore National Lab in inertial confinement fusion experiments (Flannigan and Suslick 2010).

The recent work by Gaitan et al. (2010) concerns mechanisms for driving the collapse of bubbles. By increasing the static pressure of the fluid (up to 300 bar/30 MPa), Gaitan et al. found that the amplitude of emitted shock waves and SL flashes from transient cavitation events increased 1000 fold over those measured for single bubble sonoluminescence (SBSL) (Gaitan et al. 1992). These observations suggest elevated static pressures have the potential for creating the conditions for thermonuclear fusion.

The transient events observed by Gaitan et al. (2010) occur after a threshold tension has been pulled in the liquid. The cavitation threshold for water under varying conditions is well documented, but the static pressure dependence above 100 bar (10 MPa) is a parameter space that has not been explored. Such data would be useful for explaining the observations of Gaitan et al., but it would also provide new information about the bubble nucleation process itself. This, in turn, could potentially explain the discrepancy of the theoretical predictions of the threshold and the experimentally measured values.

The remainder of this introduction is divided into four subsections. First, there is a review of the literature on cavitation thresholds and cavitation at elevated static pressures. This is followed by a discussion of the dynamics of cavitation in regards to nucleation processes and the inertial collapse of bubbles. Finally, the calculation of eigenmodes of spherical resonators like the one used for these experiments is outlined.

1.2. Literature Review

1.2.1. Cavitation Threshold Measurements

References to the creation of bubbles in liquids date back to the mid 19th century (Gernez 1867, Tomlinson 1867, Blake 1949). Many of these reports were concerned with effervescent materials in liquids. François Donny is first credited with systematically investigating the liquids under tension (Leighton 1994, Trevena 1987). He found that sulfuric acid in one arm of a U-tube could support its weight when the other arm was evacuated. He attributed this to the cohesion between the fluid molecules and the adhesion of the fluid to the glass. Donny was also able to show that dissolved gases within fluids lowered the sustainable tensile stress. In 1850, Berthelot used water encased in a glass capillary tube to measure the tensile strength of water (Trevena 1987, Blake 1949). The tubes were heated so that any remaining gas bubbles were

dissolved into solution. The tubes were then cooled until the liquid fractured, as marked by a loud, audible click. The volume change of the tubes was calculated from the differential thermal expansion and the measured temperature change. The tension in the liquid was then computed assuming the liquid "expansibility" was equal to the compressibility measured under positive pressures. These so-called Berthelot tubes inspired the mineral inclusion method (Herbert et al. 2006, Davitt et al. 2010, Caupin and Herbert 2006). Mineral inclusion entraps water in small fissures (~10-100 μm) in quartz crystals. The fissures are sealed with an autoclaving process, which also determines the final density of the water. The crystals are then cooled and the tensile strength of water is determined in the same manner as the Berthelot tubes. The maximum liquid tension measured was 1400 bar (140 MPa), although this was only in one sample, and there appeared to be large scatter in the data (Davitt et al. 2010).

Both the Berthelot tubes and mineral inclusion methods require extrapolating the equation of state of water from positive pressures to negative pressures, which is not warranted (Caupin and Herbert 2006). Briggs (1950) is often cited as having measured the largest tensions within water (Mørch 2007, Finch 1964, Leighton 1994, Apfel 1984). Briggs employed a centrifugal method by spinning a z-shaped glass capillary tube open at both ends, such that the tube's center intersected the projected spin axis (i.e. the tube spun horizontally about the z-plane). The pressure in the fluid column in the central channel varied as

$$P = P_0 - \frac{1}{2}\rho\omega^2\left(r - \frac{L}{2}\right)^2 \qquad (1)$$

where L is the length of the fluid column, ρ is the fluid density, ω is the angular frequency of the column rotation, and r is the distance from the center of the fluid column. From Equation (1), the tension within the liquid increased as ω^2 and was largest at the center of the fluid column. Briggs

increased ω until the water column broke, as detected by a marked change in the refraction of the tube. The maximum tensile strength of water was 277 bar at 10 ºC. Below 10 ºC, the tensile strength decreased with a slope of -48 bar/ºC. Above 10 ºC, the tensile strength decreased with a slope of -2 bar/ºC. Mørch (2007) postulated that the rapid decrease in the tensile strength of Briggs' measurements below 10 ºC was attributed to a build-up in solid-like layers of water molecules next to the glass surface. This sets up considerable tensile stress on the inner-most layer (i.e. the layer in contact with the glass), facilitating detachment from the surface.

Acoustic methods have been used extensively for testing the tensile strength of liquids (Apfel 1970a, Crum 1979, Davitt et al. 2010, Finch 1964, Fowlkes and Crum 1988, Galloway 1964, Herbert et al. 2006, Holland and Apfel 1990, Lieberman 1959, Messino et al. 1963, Messino et al. 1967, Roy et al. 1985, Sette and Wanderlingh 1962, Strasberg 1959, Greenspan and Tscheigg 1967, Barger 1964). A summary of experiments done before 1949 is summarized in Blake (1949). The acoustic methods typically rely on either standing waves or traveling waves. The standing wave method relies on concentrating acoustic energy using a resonant mode of the vessel-fluid system. This method has the advantage of creating large acoustic pressures with minimal applied power. Also, the normal modes of the resonant device can be chosen such that the resonator walls are pressure nodes, thereby minimizing nucleating on the walls of the cavitation vessel. Spherical geometries are typically employed (Roy et al. 1985, Finch 1964, Strasberg 1959, Galloway 1964, Lieberman 1959, Barger 1964), although other geometries, such as cylinders, have also been used (Crum 1979, Greenspan and Tscheigg 1967). These resonant cavities are typically excited in the low kilohertz region (20-60 kHz), where the cavitation threshold is independent of frequency (Crum 1979). Traveling wave set-ups use focused transducers (Willard 1953, Messino et al. 1963, Herbert et al. 2006, Sette and Wanderlingh 1962,

Davitt et al. 2010, Fowlkes and Crum 1988, Holland and Apfel 1990), which allow careful control over the spatial location in which cavitation can occur (e.g. in the bulk of the fluid away from vessel walls) due to the small focal region. In addition, these transducers are typically operated on a very short duty cycle and will only be excited for a few acoustic cycles (the frequency is typically in the low MHz), as opposed to standing wave set-ups which require continuous wave excitation.

A third, seldom used acoustic technique was introduced by Apfel (1970a) whereby a droplet of the test fluid was acoustically levitated in a host fluid with a much larger tensile strength than the test fluid. The volume of the droplet was chosen to be small enough such that few, if any, impurities would be present. Also, any nucleation sites due to container effects are negated by levitating the sample in the bulk of the host fluid. The acoustic field used to levitate the test fluid is increased until the test fluid spontaneously turns to vapor. Apfel found the threshold for superheated ether submerged in glycerin corresponded well with homogenous nucleation theory (discussed in section 1.3.1 below).

The parameter spaces explored with these acoustic studies varied markedly. Barger (1964) used several resonant modes of a spherical resonator to explore the frequency dependence of the cavitation threshold. At low gas concentrations (~1% saturation), the threshold had a local minimum of 5 bar at 200 kHz, while at the lower (~20 kHz) and higher frequency (1 MHz) ranges the threshold maximized out at 50 bar. As the gas content increased, the threshold transitioned from having a local minimum to being linear with frequency. Many of the studies varied the amount of dissolved gases in the liquid. Galloway (1964) found a strong dependence on the threshold with dissolved gas concentration above 1% saturation. Crum (1979) and Strasberg (1959) found similar dependencies on the gas content. In contrast, Greenspan's

measurements (1967) were not as strongly dependent on the dissolved gas concentration. Apfel (1970) was able to reconcile these conflicting data by showing the threshold is largely independent of gas concentration when nuclei are smaller than a critical size. Since Greenspan used a filter with a pore size of 0.2 μm, Apfel reasoned that only nuclei which are smaller than the critical size were present. Roy et al. (1985) was able to show that the threshold was inversely proportional to the nuclei sizes by varying the pore size of the filters used in a closed loop system. Several authors have also explored the temperature dependence on the cavitation threshold. Davitt et al. (2010) and Herbert et al. (2006) used a focused transducer over the range 0-200 ºC and found a linear relationship between the threshold and temperature. Using a standing wave set-up, Crum (1979) found a weak dependence on the temperature when the dissolved gas concentration was small (4% saturation), but a larger dependence as the gas concentration increased to 35%. Strasberg (1959) also found a decrease in the threshold as the dissolved gas concentration increased. Crum (1982) made aqueous solutions of surfactant agents to vary the surface tension of the fluid, and found that an increase in the surface tension decreased the threshold. Roy et al. (1985) varied dissolved KI salt to vary the ionic concentration from 0.01 mmol/l to 10 mmol/l. The threshold had a local maximum at 1 mmol/l, and had a similar dependence for higher concentrations to that reported by Akulichev (1966). However, Sirotyuk (1970) found little variation of the threshold after reducing the fluid conductivity two orders of magnitude. Finally, several authors found irradiating fluid with high energy particles lowered the threshold (Finch 1964, Greenspan and Tscheigg 1967, Lieberman 1959, Sette and Wanderlingh 1962). This will be further discussed in section 1.3.4.

1.2.2. Experimental Detection of Inertial Cavitation

In a laboratory setting, the threshold is defined in terms of the macroscopically observable effects of cavitation. Early authors relied on visual detection of cavitation (Strasberg 1959, Messino et al. 1963, Messino et al. 1967, Finch 1964, Sette and Wanderlingh 1962) or audible "pops or cracks" (Crum 1979, Galloway 1964) as indication of inertial cavitation. As detection techniques improved, light emissions (Roy et al. 1985, Fowlkes and Crum 1988) or scattering of the driving acoustic pressure cavitation (Holland and Apfel 1990, Herbert et al. 2006) could be used for passive indication of inertial cavitation. Greenspan (1967) would monitor a rectified and differentiated signal of a sensor in contact with his fluid. A sudden drop in the conditioned signal indicated cavitation. Roy et al. developed a technique for actively detecting bubbles, although the technique has been shown to aid in nucleation (Roy et al. 1990).

1.2.3. Experimental Definition of Inertial Cavitation Threshold

Many early authors would define the inertial threshold as the acoustic pressure at which cavitation was detected after a predetermined time interval. Finch (1964) would increase the acoustic pressure incrementally until one event was nucleated after a five second wait time. Leiberman (1959) and Strasberg (1959) would increase the pressure in +1 dB steps until one event was nucleated after the 15 second wait-time. Greenspan (1967) would increase the pressure until one event occurred at the end of a 30 second wait time. Several authors would linearly ramp the acoustic pressure until the onset of inertial cavitation (Fowlkes and Crum 1988, Roy et al. 1985, Holland and Apfel 1990). The ramp was typically repeated 20 times, and the threshold was defined as the mean. Hodnett (2008) defined the threshold as the point at which high frequency emissions (> 1 MHz) in the liquid were 10% above the monitoring sensor's intrinsic noise level.

Some authors using focused transducers would measure the probability that cavitation would occur at a certain driving level (Herbert et al. 2006, Sette and Wanderlingh 1962, Messino et al. 1963). The data at several driving levels would then be fit to a thresholding type function (i.e. sigmoid curve), and the threshold would be defined as a parameter on the thresholding function.

1.2.4. Fluid Quality

As Apfel states (1981), the variation in liquid quality and preparation, history of the liquid, and methodology result in variation of the reported threshold, which makes direct comparison of these studies difficult. However, none of the measurements discussed (sans the mineral inclusion and Apfel's droplet methods) are near the theoretically predicted threshold for homogenous nucleation (to be discussed in section 1.3.1).

The fluid cleanliness is a point of concern for these threshold experiments, and most authors used the most up-to-date techniques of their day to purify their water [excluding Strasberg (1959) who inexplicably used tap water]. Distillation was used early on (Crum 1979, Finch 1964, Holland and Apfel 1990, Messino et al. 1963, Sette and Wanderlingh 1962) before deionization techniques were adopted (Davitt et al. 2010, Roy et al. 1985, Herbert et al. 2006). The advances in the semiconductor industry required purer sources of water (in particular, higher resistivity), which prompted standards to be set for water purity. The ASTM D1193-6 is the most common standard, and its specifications are shown in Table 1.

Measurement (Unit)	Type I	Type II	Type III
Resistivity (MΩ-cm) at 25 ºC	>18	>10	4
Total Organic Content (ppb)	< 0	< 50	< 00
Sodium (ppb)	< 1	< 5	< 10
Chloride (ppb)	< 1	< 5	< 10
Total Silica (ppb)	< 3	< 3	< 500

Table 1: ASTM D1193-6 standard for classifying water purity.

Resistivity is a measure of the number of dissolved ions in the fluid. At present, the techniques for refining the resistivity of the water have reached their theoretical limit of 18.24 MΩ-cm at 25 ºC. This value is based on the dissociation of water itself (Ohmi 1993). The total organic carbon (TOC) is the number of organic compounds in the fluid. There are several techniques the purify water up to the desired standard. Table 2 lists several of these techniques and their effectiveness in removing certain types of contaminates.

	Distillation	Reverse Osmosis	Deionization	Filtration	Ultrafiltration	Adsorption	Ultraviolet Oxidation
Inorganic Ions							
Dissolved Gases							
Organics							
Particles							
Bacteria							
Pyrogens							
Nucleases							

Table 2: Potential water contaminates and effectiveness of purifying techniques. Rectangles shaded green denote excellent removal of contaminate, blue denote moderate removal of contaminate, and the hatched cells denote poor removal of contaminate. Reproduced from the Thermo Scientific Waterbook (2009).

1.2.5. Cavitation at elevated static pressures

Literature on the effect of static pressure on the cavitation threshold is limited. Harvey et al. (1944) suggested that pre-pressurization of water to 1000 bar for 30 minutes would crush pre-existing nuclei in the fluid, thereby increasing the cavitation threshold (Trevena 1987). Evans (1979) was able to show that a similar increase in the cavitation threshold can be achieved with a more modest initial pressurization of the fluid to 20 bar.

Several investigators have studied the influence of overpressure on the intensity of SL, as summarized in Walton (1984). Walton assumed that the origin of light emissions was thermal in nature, and was able to show that the final temperature within the bubble was given by

$$T_{MAX} = \frac{T_0}{R_0^3}\left(P_H + \frac{2\sigma}{R_0}\right)^{-1}(\gamma - 1)(P_A + P_H)\left(\frac{4}{3\omega}\right)^3 (P_A - P_H)^3 \left(\frac{2}{\rho P_A}\right)^{3/2}\left[1 + \frac{2}{3P_H}(P_A - P_0)\right] \quad (2)$$

and therefore dependent on the static pressure, P_H. However, as the static pressure increases, the range of available nuclei present that will be able to collapse inertially decreases. Harvey (1939) visually monitored the intensity of light emissions at constant acoustic pressure while hydraulically increasing the static pressure. He found that the light intensity increased until 2.3 bars, beyond which the light emissions ceased. Finch (1964) found similar results by increasing the static pressure both hydraulically and by increasing the gas pressure above his test fluid (light emissions were most intense at 1.5-1.7 bar). Walton argues that the initial increase in light emissions is due to the effect of the overpressure driving the inertia of the fluid to collapse. However, as the overpressure increases, the initial radius (and therefore maximum radius) of the microbubble decreases, resulting in a shorter collapse time and therefore mitigating the intensity of light emissions. The maximum of the light emissions occur when these two effects counterbalance each other. Chendke and Fogler (Walton and Reynolds 1984) measured the spectrum of light emissions in nitrogen saturated water (driving frequency 20 kHz) in 1 bar increments, up to 15 bar. The temperature calculated from blackbody curves of the spectrum is essentially independent of static pressure, although the intensity had a maximum at 6 bar. These results are in contradiction with recent findings by Brujan et al. (2005) and Wolfrum et al.

(2001), who used a laser to create dielectric breakdown in pressurized water. They found that both the pulse width and the number of photons increased up to 10 bar. In addition, the measured blackbody temperature increased by 20% between 1-10 bar.

Barger (1964) investigated the effect of under pressure over the range of 0.01- 1 bar on water by evacuating the gas above his fluid. He found that the threshold was approximately constant from twice the static pressure to 1 bar. The threshold decreased quickly below twice the static pressure, and decreased with increasing dissolved gas content. Strasberg (1959) used normal modes of a spherical resonator (~25 kHz) to investigate the effect of overpressure on the inertial cavitation threshold over the range of 1-20 bar. He found that the threshold increased linearly with increasing static pressure, varying between 3-13 bar. However, the slope would decrease if the pressure were decreased from an initial overpressure, producing a hysteresis effect. Herbert et al. (2006) used a focused transducer and also found a linear increase in the threshold up to 80 bar, whose slope depended on the fluid temperature. Herbert et al. found that the tension required to create cavitation varied with temperature, but was independent of the static pressure. For instance, at 4 ºC, the fluid required 260 bar tension in order to create cavitation, regardless of the static pressure.

1.3. Nucleation Mechanisms

Apfel (1981) relates in his three golden rules of any cavitation experiment that it is necessary to "know thy liquid," including its solid impurities. It is thought that these impurities are the limiting factor of the tensile strength of liquids, and their presence would account for the large discrepancy between theory and experiment (Roy et al. 1985, Herbert et al. 2006, Crum 1982, Caupin and Herbert 2006). The exact mechanism by which these particulates aid in bubble nucleation is now known (Apfel 1981, Crum 1982), but, as Roy et al. (1985) states, they are

considered to be present in the fluid. This section will outline possible nucleation methods for cavitation.

1.3.1. Homogenous Nucleation

Homogenous nucleation can be described in terms of a phase transformation, whereby a portion of the liquid under tension spontaneously transforms to a vapor bubble. The formalism as developed in Herbertz (1988) will be used to discuss homogenous nucleation. This formulism differs slightly from the traditional formulation (Fisher 1948, Fisher 1948a, Pettersen and Balibar 1994); however, the two have been shown to be essentially equivalent (Church 2002). The total energy, W_n, to create a vapor bubble of radius r can be written

$$W_n = \frac{4}{3}\pi r^3 (P_H + P_A - P_V) + 4\pi\sigma r^2 \qquad (3)$$

A critical bubble radius, r_C, represents the minimum size a nucleus can be if it is to spontaneously grow. r_C can be calculated by setting the differential of Equation (3) with respect to r to zero and solving for r:

$$r_C = -\frac{2\sigma}{3(P_H + P_A - P_V)} \qquad (4)$$

The critical energy barrier, $W_{C,max}$, associated with the creation of a critically sized nucleus can be calculated by substituting Equation (4) into Equation (3)

$$W_{n,max} = \frac{16\pi\sigma^3}{3(P_H + P_A - P_V)} \qquad (5)$$

The Maxwell-Boltzmann distribution of molecular energies can be used to calculate the probability density of a given energy state, w, in reference to the normalized energy level, $u = W_n/k_BT$, where k_B is Boltzmann's constant and T is the temperature of the liquid (Tolman 1979):

$$w = 2\sqrt{\frac{u}{\pi}}e^{-u} \tag{6}$$

The integral of Equation (6) over the energies needed to create a critical or larger sized nucleus (i.e. from $W_{n,max}$ to infinity) is the probability of homogenously nucleating a bubble:

$$P = \frac{2}{\sqrt{\pi}}\int_{u_c}^{\infty}\sqrt{u}\,e^{-u}\,du = 1 + 2\sqrt{\frac{u_c}{\pi}}\,e^{u_c} - \operatorname{erf}(\sqrt{u_c}) \tag{7}$$

where $u_c = W_{n,max}/k_BT$. In order to calculate the number n of independent nucleation events a spatial temporal correlation volume, C, must be calculated such that within the critically sized volume, $V_C = 4\pi r^3_C/3$, only one independent nucleus may be formed during time t_C:

$$C = \int_0^{t_C} V_C dt = \int_0^{r_C}\frac{4\pi}{3c}r^3 dr = \frac{\pi}{3}\frac{r_C^4}{c} \tag{8}$$

where c is the sound speed in the liquid. The nucleation rate can be defined as

$$n = \frac{P}{C} \tag{9}$$

where n is the number of independent nucleating events per unit time per unit volume.

1.3.2. Crevice model

Tap water typically contains between 50,000- 100,000 solid particles per milliliter (Apfel 1981). The majority of these particulates can typically be removed via filtration. However, when

the particle size becomes smaller than 0.5 μm, Brownian motion dominates the motion of the particle (Flynn 1964). Flynn (1964) suggests that this Brownian motion limit may be ascribed to the upper size of particulates entrapped in the liquid. Crum (1979) was able to show that the surface of larger particulates (~10μm) are quite irregular. Mørch (2007) notes, however, that small particles (sub micron sized) are quite smooth. In either case, the surfaces of these particulates are also likely hydrophobic (Mørch 2007). In the case of a surface with irregularities, the hydrophobic nature of the particulate would cause imperfect wetting of the crevice, which may harbor gas and therefore serve as a nucleation site.

This so-called crevice model of nucleation was introduced by Harvey et al. (1944) and later investigated by (among others) Strasberg (1959), Crum (1979), and Borkent et al. (2009). The problem is typically treated as a conical crevice with a contact line along the base of the crevice, as shown in Figure 1. The fluid interface bows to the apex of the crevice, and, in this case, surface tension acts to promote the growth of the gas. In this way, the gas pocket is stabilized against dissolving into the fluid.

The position and shape of the contact line depends on the history of the liquid. Initially, the contact line remains stationary and the contact angle, denoted by α in Figure 1, changes with respect to changes in the expanding or collapsing forces. For instance, if the contracting forces (positive pressure in the liquid) were increased for the scenario in Figure 1, as would be the case for an increase of the hydrostatic pressure, the contact line would remain fixed while the contact angle increased. For continually increasing contracting forces, α would eventually reach the so-called advancing contact angle, α_A, at which point the contact angle would remain fixed at α =

α_A. If the contracting forces continued to increase, the contact line would regress toward the apex of the crevice.

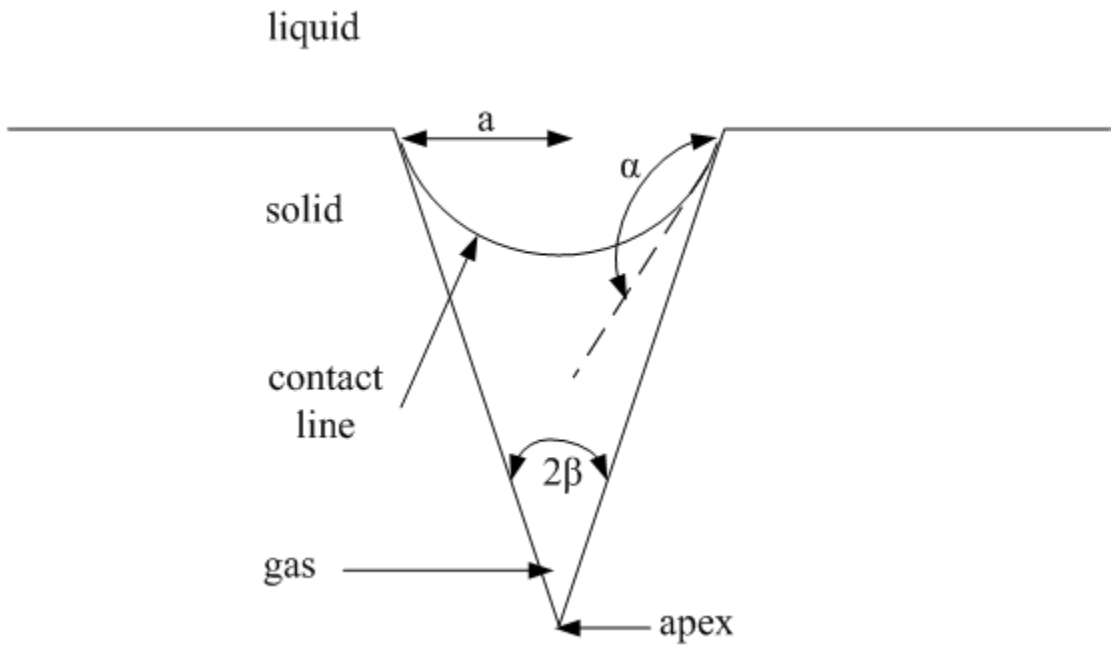

Figure 1: Diagram of parameters for crevice nucleation, after Apfel (1970).

Alternatively, as the collapsing forces decrease (negative pressure in the liquid), the contact line remains stationary while the contact angle decreases until it reaches the so-called receding contact angle, α_R. A further reduction in the collapsing forces in the liquid will result in the contact line ascending the crevice with the contact angle fixed at α_R. Apfel (1970) defines the quasi static pressure at which the receding contact angle is reached as the threshold for nucleation, which occurs at acoustic pressures of

$$P^A{}_A \geq P_H\text{-}\gamma P_G\text{-}P_V\text{+}(P_H\text{-}P_G\text{-}P_V)\left|\frac{\cos(\alpha_R\text{-}\beta)}{\cos(\alpha_A\text{-}\beta)}\right| \qquad (10)$$

where γ is a constant associated with the transfer of gas into and out of the nucleus. Crum (1979) was able to re-write Equation (10) in terms of experimentally measured quantities of typical crevice geometries and incorporate the effects of surface tension:

$$P_A^A = P_H\text{-}P_V\text{-}\gamma P_G + \frac{P_H\text{-}P_V\text{-}P_G}{\delta}\left[\cos(\phi)\left(\frac{C}{\sigma}+1\right)+\sin(\phi)\left[1-\left(\frac{C}{\sigma}-1\right)^2\right]^{\frac{1}{2}}\right] \qquad (11)$$

where *C* is a parameter that depends on the surface properties of the solid. For non-polar substances such as paraffin and beeswax, $C \sim 50$ mN/m. δ and φ are fitting parameters that depend upon the crevice geometry.

Atchley and Prosperetti (1989) argued that the receeding contact angle is not necessarily a necessary and sufficient condition for nucleation. As the Laplace pressure (i.e. the pressure associated with surface tension) falls with increasing nucleus radius (at this point, the interface is concave to the crevice apex and therefore the Laplace pressure is a collapsing pressure), so does the internal gas pressure. Only when the expanding forces decrease slower than the collapsing forces will the interface become mechanically unstable and the nucleus will expand to the surface of the cavity. This can be formally expressed as the condition that

$$\frac{d}{dR}(P_V + P_G) < \frac{d}{dR}\left(P_L + \frac{2\sigma}{R}\right) \qquad (12)$$

This condition is met when the acoustic pressure reaches

$$P_A^B = P_L + P_V - \frac{4\sigma}{3a_0}\left(\frac{2\sigma}{3a_0 P_G}\frac{(cot(\beta)+\eta_R)|cos(\alpha_R-\beta)|^3}{cot(\beta)-\eta_R}\right)^{1/2} \qquad (13)$$

where a, as defined in Figure 1, is the radius of the crevice at the depth of the contact point, and can be calculated as

$$a = \frac{2\sigma}{P_H - P_G - P_V} |cos(\alpha - \beta)| \quad (14)$$

The subscript 0 in Equation (13) denotes the initial conditions of the crevice, before pressure P_A^B is applied and η is a factor that depends on the crevice geometry:

$$\eta = \frac{2 - sin\,(\alpha - \beta)[2 + cos^2(\alpha - \beta)]}{|\,cos^2(\alpha - \beta)|} \quad (15)$$

The larger of Equations (10) and (13) are what Atchely terms the first cavitation threshold, or the threshold at which the contact line will be drawn to the surface of the crevice. In order for a bubble to actually be nucleated, the gas must be drawn from along the surface of the particulate, out of the crevice, and into the liquid. This is deemed the second cavitation threshold. As before, the threshold requires the condition of minimum contact angle between the gas and surface of the particulate, α_R, and mechanical instability of the contact line. The first condition is met when the amplitude of the acoustic pressure is

$$P_A^C = P_L + P_V - \frac{2\sigma}{a_m} + \frac{cot(\beta) - \eta_0}{2 + cot(\beta)} \frac{a_0^3}{a_m^3} P_G \quad (16)$$

where a_m is the radius of the mouth of the crevice. The condition of mechanical instability is met when the amplitude of the acoustic pressure is

$$P_A^D = P_L + P_V - \frac{4\sigma}{3a_0} \left(\frac{2\sigma}{3a_0 P_G} \frac{2 + cos(\alpha_R)\,(2 + sin^2(\alpha_R))}{cot(\beta) - \eta_0} \right)^{1/2} \quad (17)$$

As for the first cavitation threshold, the larger of Equations (16) and (17) is defined as the second cavitation threshold. When the volume of the crevice is much larger than the spherical cap on the surface of the particulates (as is frequently the case), the interface is unstable at P_A^C, as defined in Equation (16). The threshold for nucleation of a bubble will be determined by the maximum of Equations (10), (13), (16), and (17).

Other authors have extended Atchely and Prosperetti's formulism to more complicated geometries (Chappell and Payne 2007), and, under known crevice geometries, the model is in agreement with experimental data (Borkent et al. 2009). However, the relative amplitudes of Equations (10), (13), (16), and (17) are dependent on the contact angle, crevice geometry, intial conditions, etc., which are neither *a priori* known nor uniformly distributed for naturally occuring nucleation sites within the liquid. That is, depending on the conditions, any one of Equations (10), (13), (16), and (17) may determine the threshold. This makes Atchley and Prosperetti's formulism difficult to use as a predictive measure except under the most controlled of experimental conditions.

The analysis of Apfel, and Atchley and Prosperetti neglects gas diffusion into or out of the interface. Hence, the conclusions of these models are most applicable at higher acoustic frequencies (> 100 kHz) where gas diffusion is expected to be less effective. However, Crum (1979) was able to get good experimental agreement with Equation (10) over a wide range of values for the surface tension, gas pressure, and temperature.

1.3.3. Variable permeable skin model

Water samples generally contain some orgainic impurities in the form of fatty acids. It is thought that these impurities can accumulate on the surface of a gas bubble, effectively forming a stabilizing skin. The hydrophilic heads of such amphiphilic molecules stabilize the bubble against dissolution by neutralizing the dangling bonds of the water molecules (Mørch 2007), effectively reducing surface tension. This concept was first introduced by Fox and Herzfeld (1954), who proposed a rigid skin of organic molecules. Herzfeld withdrew the model after Strasberg (1959) found a linear dependence of the cavitation threshold on static pressure. Herzfeld reasoned that the threshold would deviate from being linear at a sufficiently high static pressure when the nuclei were crushed (Crum 1982). Others proposed a layer of polar molecules along the surface of the bubble to achieve stabilization (Leighton 1994, Mørch 2007). However, the experimental findings of the ion dependance on the cavitation threshold are contradictory (Sirotuk 1970, Akulichev 1966, Atchley et al. 1984, Roy et al. 1985).

Yount (1979, 1997) proposed an elastic organic skin, which would still stabilize the bubble against dissolution, and the elasticity could account for Strasberg's results. This model was consistent with the observations of Johnson and Cooke (1981), who noted that bubbles injected into seawater eventually ceased to dissolve. Yount (1984) found similar results for bubbles injected in water and gelatine mixtures. It has been shown that these stabilized bubbles would collapse inertially at similar radii to bubbles without organic skins (Mørch 2007).

Mørch (2007) combined Yount's organic skin with the crevice model (Apfel 1970, Atchley and Prosperetti 1989) to propose a hybrid model for bubble nucleation. Organic molecules which are attached to a particulate may stray from the contours of the surface when confronted with an

irregularly shaped crevice. This essentially creates a stabilized gas pocket in the crevice similar to that shown in Figure 1, except the surfactant molecules now stabilize the nucleus, regurdless of its geometry (concave or convex).

1.3.4. Radiation induced cavitation

Nucleation can come in the form of thermal spikes caused by the atomic recoil of high energy particles. Neutrons are generally the radiation source of choice (Finch 1964, Greenspan and Tscheigg 1967, Lieberman 1959, Sette and Wanderlingh 1962), although α disintegration and fission sources have also been used (Greenspan and Tscheigg 1967). β sources were also tested, although no cavitation was detected (Lieberman 1959). Sette (1962) proposed that recoil by heavier atomic nuclei produce supersaturated regions in the fluid. These regions are stabilized on short time scales by gas freed from the solution. Recoil by protons was ruled out based on calculations of proton/neutron scattering cross section and the experimentally measured time for nucleation to occur (Lieberman 1959, Sette and Wanderlingh 1962).

Greenspan (1967) used different neutron sources to vary the energy of the emitted neutrons and found D-T reactions (~14 MeV) lowered the cavitation threshold nearly an order of magnitude from D-D reactions (~2.5 MeV). Sette (1962) continually added layers of paraffin to the outer porition of his test chamber to mitigate the strength of his 10 MeV neutron source. When the paraffin was more than 10 mm thick, which coincides with the mean free path of 1-10 MeV neutron, the cavitation threshold was increased to its nominal value. Sette thus concluded that neutrons greater than 10 MeV are required to aid in nucleation.

Neutrons from cosmic-rays are a potential source of cavitation nuclei. Greenspan (1967) asserted that the preliminary measured flux of cosmic neutrons at sea level is 65 n/cm^2/hr,

although only 7 percent of this flux had energies greater than 10 MeV. Tajima (1967) found that the flux for neutrons in the range 2-10 MeV has an altitude dependence proportional to $\exp(-0.0063x)$, where x is the atmospheric depth in g/cm^3. In all, Greenspan found that the cosmic-neutron background was equivalent to the in house neutron source (1.47×10^7 n/s at an 80 meter radius), and only a small fraction of the measured neutrons were larger than 2 MeV.

1.4. Inertial Cavitation

Flynn (1964) classifies bubble phenomenology with three limiting models:

1. Linear cavitation: A bubble that oscillates linearly about its equilibrium radius.
2. Stable cavitation: A bubble that oscillates non-linearly about its equilibrium radius.
3. Transient cavitation: A bubble that grows explosively over a few acoustic cycles. As the bubble contracts from some maximum radius R_M, its initial collapse will approximate a Rayleigh cavity (to be discussed in Rayleigh Collapse below), until the internal pressure of the bubble builds up and arrests the collapse.

These descriptions were accurate according to the observations of the day. However, more recently discovered phenomena such as single bubble sonoluminescence (Gaitan et al. 1992) could encompass the latter two categories. Subsequent work suggests that Flynn's second category be changed to "inertial cavitation" (Church 2007). The term "inertial" is descriptive as to dynamics of the bubble, whereas "transient" only describes the lifetime of the bubble.

The role of fluid inertia on the bubble collapse is discussed in this section. The Rayleigh collapse is also discussed, followed by Flynn's analysis of the role of the fluid inertia in bubble collapse. Finally, the threshold of inertial cavitation is discussed.

1.4.1. Rayleigh Collapse

Rayleigh is credited with first treating the collapse of bubbles (Leighton 1994). He modeled the bubble as a spherically empty void of radius R_M. The external pressure of the liquid would collapse the bubble until its size was infinitesimal (i.e. $R = 0$). Rayleigh equated the potential energy lost by the liquid as the bubble collapsed to the liquid's gain in kinetic energy to derive an expression relating the bubble's instantaneous size, R, to wall velocity, $\dot{R}$:

$$\dot{R}^2 = \frac{2P_\infty}{3\rho}\left(\frac{R_M^3}{R^3} - 1\right) \tag{18}$$

where $P_\infty = P_H - P_A\sin(\omega t)$. The time required for the bubble to collapse can be calculated by integrating $\dot{R}$ calculated in Equation (18) over the initial and final bubble radii [R_M and 0, respectively]:

$$\tau_{\mathrm{Ray}} = \int_{R_M}^{0} \frac{dR}{\dot{R}} \approx 0.915 R_M \sqrt{\frac{\rho}{P_\infty}} \tag{19}$$

For example, a Rayleigh cavity with an initial radius of 10 μm subject to 1 bar of static pressure would collapse in approximately 92 μs.

1.4.2. The role of internal gas pressure on inertial collapses

The Rayleigh collapse is valid as the internal pressure of the bubble goes to zero. A physical bubble, however, has internal pressures that will ultimately prevent the bubble from becoming a singularity. These pressure forces (e.g. gas and vapor) are latent until the very final stages for Rayleigh-like collapses. However, they ultimately must overcome the inertia of the converging

liquid. Flynn (1964) examined the relative strengths of the inertial and pressure forces during bubble collapse.

The Rayleigh-Plesset equation (Prosperetti and Lezzi 1986) describes the volumetric oscillations of a bubble subject to a time varying pressure, $P_A\sin(\omega t) = P_H + P_\infty$

$$R\ddot{R} + \frac{3}{2}\dot{R}^2 = \frac{1}{\rho}\left[\left(P_H + \frac{2\sigma}{R_0} - P_V\right)\left(\frac{R_0}{R}\right)^{3\gamma} - \frac{2\sigma}{R} - \frac{4\mu\dot{R}}{R} - P_\infty + P_V\right] \quad (20)$$

Equation (20) can be solved for the bubble wall acceleration:

$$\ddot{R} = -\frac{3}{2}\frac{\dot{R}^2}{R} + \frac{1}{R\rho}\left[\left(P_H + \frac{2\sigma}{R_0} - P_V\right)\left(\frac{R_0}{R}\right)^{3\gamma} - \frac{2\sigma}{R} - \frac{4\mu\dot{R}}{R} - P_\infty + P_V\right] \quad (21)$$

The first term on the right side of Equation (21) represents the acceleration due to spherical convergence of the liquid and is termed the inertial function (IF). The second term represents the acceleration due to the summed pressure forces within the bubble, and is termed the pressure function (PF). The inertial function is always negative, except when the bubble wall velocity is zero (e.g. minimum and maximum bubble radius), and has a minimum value at the maximum bubble speed, just before the interior pressure halts the collapse. The pressure function is initially negative and slowly decreases to a minimum before increasing as the pressures within the bubble overtake the converging liquid. The pressure function is slowly changing at its minimum such that if

$$\text{IF} \leq \text{PF}_{\text{MIN}} \quad (22)$$

the inertial function will dominate the collapse (i.e. the bubble will collapse inertially).

The pressure function, inertial function, and bubble wall acceleration are plotted for different initial expansion ratios in Figure 2-Figure 4. In Figure 2 the initial expansion ratio is R_{max}/R_0 = 1.5, and the bubble collapses under the static pressure of the liquid. During collapse, the bubble wall acceleration only varies from the pressure function as the wall velocity approaches its maximum (i.e. IF is at its minimum). Shortly thereafter, PF increases rapidly and the bubble wall decelerates until the collapse is complete. A similar plot is shown for a bubble with an initial expansion ratio of R_{max}/R_0 = 2.3 (Figure 3 and Figure 4). The onset of the inertial collapse is characterized by a shifting of the minimum of IF (maximum bubble wall velocity) to later stages of the collapse. For instance, in Figure 2 IF reaches its minimum after approximately 90% of the collapse has occurred, whereas in the inertial collapse (Figure 4) IF reaches its minimum after 99% of the collapse has occurred (the collapse is considered to be 100% complete when the bubble reaches its minimum radius). Since PF is essentially zero until after the maximum bubble wall velocity, the later in the collapse IF reaches its minimum, the more the collapse resembles a Rayleigh cavity.

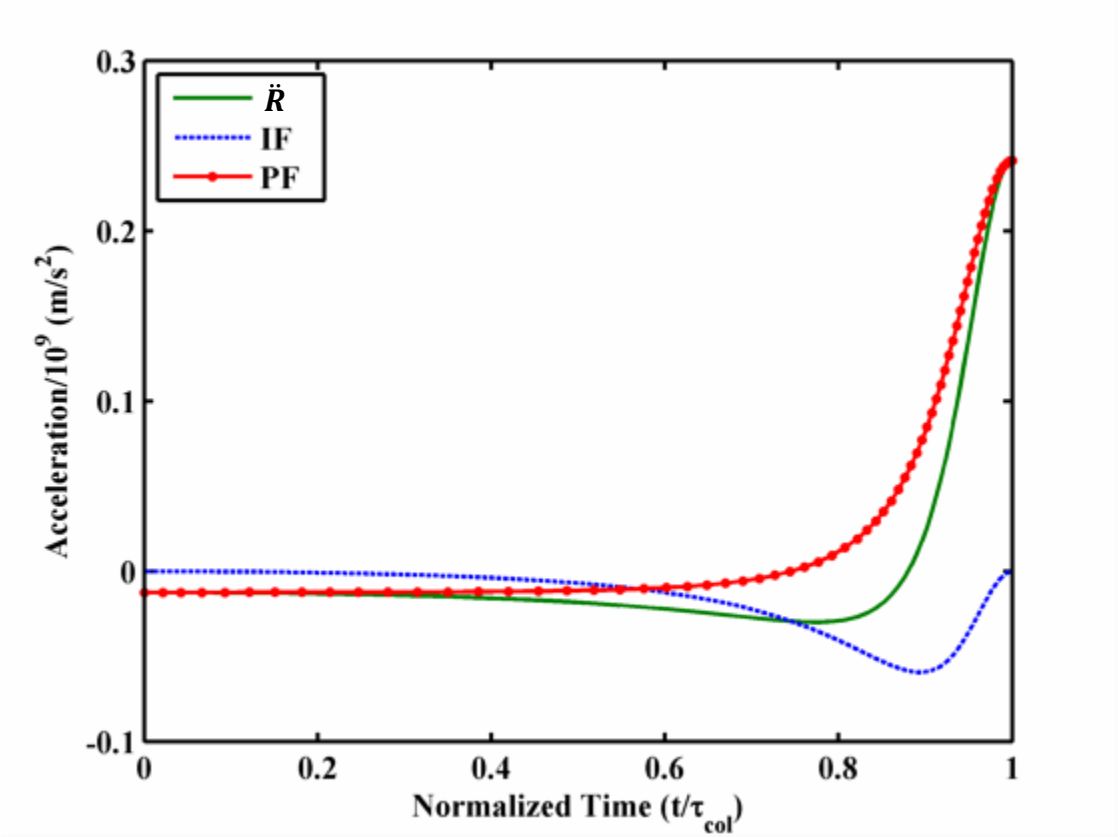

Figure 2: IF, PF, and bubble wall acceleration for a bubble with initial expansion ratio of R_{max}/R_0 = 1.5. The bubble reaches its minimum size at τ_{col} = 0.76 μs. After Leighton (1994).

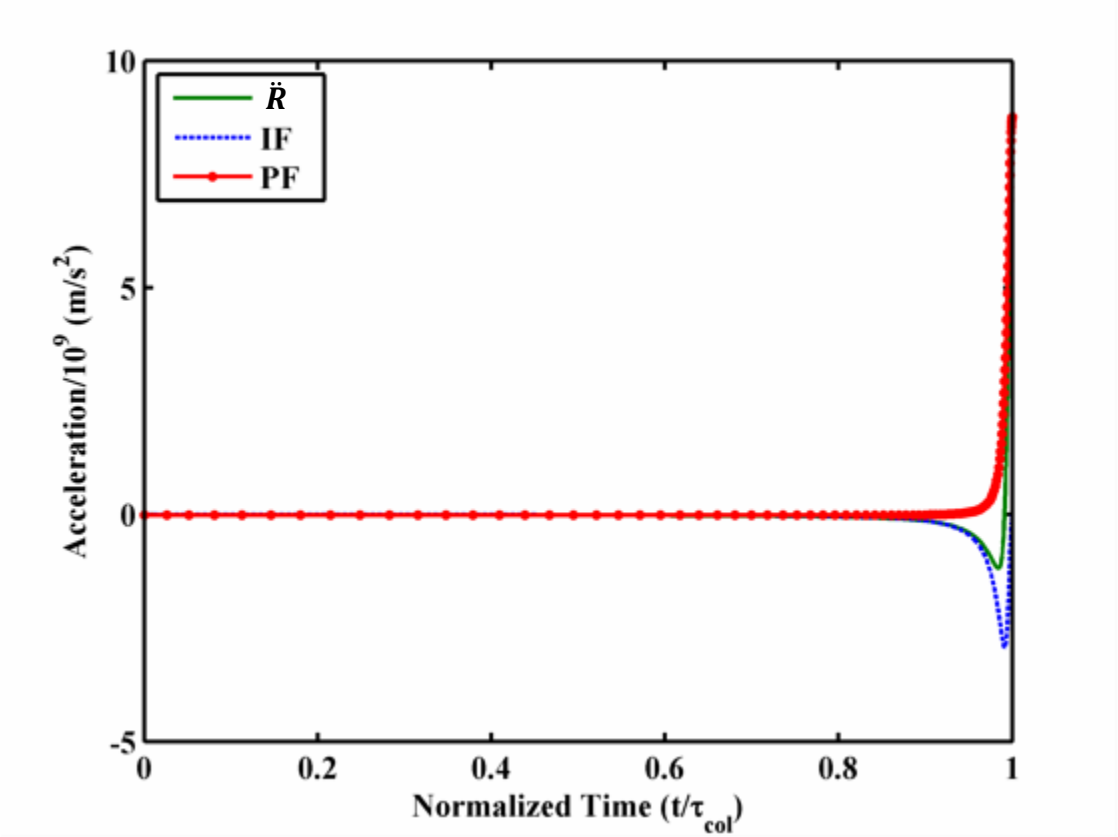

Figure 3: IF, PF, and bubble wall acceleration for a bubble with initial expansion ratio of R_{max}/R_0 = 2.3. The bubble reaches its minimum size at τ_{col} = 1.04 μs. After Leighton (1994).

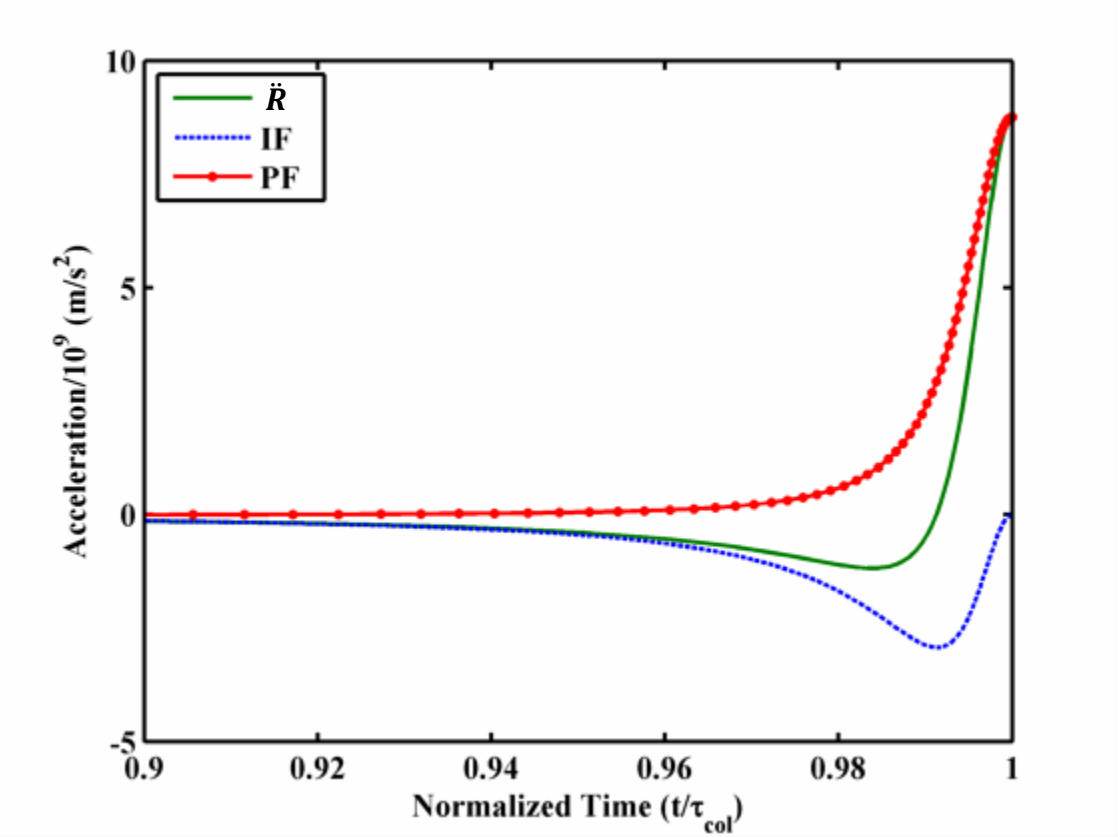

Figure 4: Final stages of collapse for expansion ratio of Figure 3.

Meeting the criterion in Equation (22) is strongly dependent on the ratio of maximum to initial bubble radii. Flynn (1964) has shown Equation (22) will be satisfied for the critical expansion ratio:

$$\frac{R_{MAX}}{R_0} = \left[\frac{7.48\left(P_H + \frac{2\sigma}{R_0} - P_V\right)}{P_H}\right]^{1/3} \approx 2 \qquad (23)$$

It is important to note that neither the Rayleigh cavity, nor the Rayleigh-Plesset equation considers the effects of liquid compressibility. By accounting for compressibility to first order,

Flynn was able to show the inertial and pressure functions are only quantitatively correct when the bubble wall Mach number ($\dot{R}/c$) is less than 0.2 (Neppiras 1980, Flynn 1975). However, the general conclusion remains qualitatively the same: If a bubble's expansion matches the critical expansion ratio the inertial function will dominate the collapse and the bubble will collapse inertially.

1.4.3. The threshold for inertial cavitation

1.4.3.1. The Blake Threshold

For a given acoustic pressure, only a bubble with initial radius larger than some critical size R_C will satisfy Equation (22). Blake (Apfel 1981, Neppiras 1980, Blake 1949) calculated this critical radius by considering the conditions for mechanical stability of the bubble. If the bubble is initially stable, the internal pressure must equal the exterior pressure $P_H + 2\sigma/R_0 - P_V$. When an external sound field of amplitude P_A is applied, the mechanical stability condition becomes

$$P_L = \left(P_H + \frac{2\sigma}{R_0} - P_V\right)\left(\frac{R_0}{R}\right)^{3\gamma} - \frac{2\sigma}{R} + P_V \qquad (24)$$

where $P_L = P_H - P_A$. The critical radius can be calculated by minimizing this relationship [Equation (24)] with respect to R:

$$(R_c)^{3\gamma-1} = \frac{3\gamma R_0^{3\gamma}}{2\sigma}\left(P_H + \frac{2\sigma}{R_0} - P_V\right) \qquad (25)$$

The Blake threshold, P_{Blake}, is defined as the acoustic pressure necessary to make a bubble of size R_0 become mechanically unstable. P_{Blake} can be calculated by substituting Equation (25) into Equation (24). In the isothermal limit, $\gamma = 1$, the Blake threshold can be written

$$P_{Blake} = P_H - P_V + \frac{4\sigma}{3R_0}\sqrt{\frac{2\sigma}{3R_0\left(P_H + \frac{2\sigma}{R_0} - P_V\right)}} \quad (26)$$

1.4.3.2. Analysis of Holland and Apfel

Analytic expressions for the inertial collapse of a pre-existing microbubble, such as the Blake threshold, neglect the growth inhibiting effects of viscosity, surface tension, and the inertia of the liquid. If these effects delay bubble growth over a significant fraction of the tensile portion of the acoustic cycle, the bubble's maximum size will not be large enough for the bubble to undergo an inertial collapse. Apfel (1981, 1986) derived an analytic expression which accounted for the delay times associated with the inertia of the liquid and viscosity. Holland and Apfel (1989) expanded upon Apfel's original work by accounting for the delay time associated with the surface tension in the liquid.

Holland and Apfel's final analytic prediction is a single equation that depends on the parameters of the liquid (surface tension, viscosity, static pressure, etc.) along with the initial bubble size, acoustic driving frequency, and the gas temperature at the minimum radius. This is shown in Equation (27):

$$f = \frac{\frac{1}{3\pi R_0}\sqrt{\frac{P_H\xi}{\rho}}\left(\sqrt{\frac{p-1}{p}} + \sqrt{\frac{p-p_b}{p}}\right)}{\left(\frac{T'}{(\gamma-1)\left(\frac{\xi}{3}+1\right)}\right)^{1/3} - 0.46 + \frac{4\mu}{R_0}\sqrt{\frac{2}{\rho P_0 \xi}} + \frac{2\sigma}{P_H R_0}\left(\frac{1}{p-p_b}\right)^{\frac{3}{2}}\sqrt{\frac{\xi}{3}}} \quad (27)$$

where $T' = T_{MAX}/T_0$ is the ratio of the temperature of the gas inside the bubble at the minimum radius to the ambient gas temperature, $p = P_A/P_H$ is the normalized acoustic pressure, and $p_b = P_B/P_H$ is the normalized Blake threshold [Equation (26)]. ξ is a function of p and p_b:

$$\xi = p_b - 2 + \sqrt{(p-1)(p-p_b)} \qquad (28)$$

Given the physical parameters of the liquid and fundamentals of the sound field (surface tension, acoustic drive frequency, etc), Equation (27) can be solved numerically for the nondimensional transient threshold p. Equation (27) has been shown to be consistent with more exact computational models over a wide range of frequencies and microbubble sizes (Holland and Apfel 1989).

1.4.4. Theoretical Definition of Inertial Cavitation Threshold

From a theoretical perspective, there has been some inconsistency in determining when a collapse becomes inertially dominated. Flynn's analysis of the inertial and pressure functions is certainly the most rigorous. Apfel (1981) has suggested that the collapse should be considered inertial when the Mach number of the bubble wall approaches unity. This would increase the critical expansion ratio from 2 [in Equation (23)] to 2.3. The onset of high temperatures within the gas has also been suggested (Leighton 1994), although Holland and Apfel's model [Equation (27)] is only weakly dependent on the final gas temperature. These definitions are largely a matter of convenience for models when trying to distinguish one type of collapse from another, and in a laboratory setting the threshold would be determined only at the onset of observation (i.e. shock waves, light emission).

1.5. Modes of spherical resonator

Previous experiments for studying cavitation in standing waves typically employ spherical glass boiling flasks or glass cylinders with quality factors on the order of 100 when fluid loaded (Gaitan et al. 1992, Hiller et al. 1995, Galloway 1964, Roy et al. 1985, Strasberg 1959). Because the impedance (Z) of the fluid and the glass shell are similar enough (quartz glass: $Z = 12 \times 10^6$ kg/m^{2}s, water: $Z = 1.5 \times 10^6$ kg/m^{2}s), and the resonator wall is thin enough (~2 mm), the shell can be considered an extension of the fluid and the boundary condition at the outer radius is essentially pressure release. For these experiments, it was necessary to use a different material of increased thickness to withstand the overpressures of the liquid. The fluid/shell boundary was close to an infinitely rigid surface, although a general solution would allow the boundary condition to fall between the two perfect solutions (infinitely rigid and pressure release).

The eigenfrequencies of spherical resonators will be discussed in this section. Results will be derived for a perfect boundary condition (i.e. pressure release or infinitely rigid). An exact solution will be obtained by matching the fluid and shell impedances at the inner surface and allowing for the shell to be compliant.

A diagram of the resonator geometry and relevant nomenclature is shown in Figure 5. For the case of the perfect boundary condition (pressure release or infinitely rigid), the outer radius of the shell (length $\boldsymbol{b}$) will be considered infinite. When $\boldsymbol{b}$ is finite (e.g. when considering the compliance of the shell), the shell will be taken to be in vacuum, and the boundary at $\boldsymbol{b}$ will be a pressure release surface.

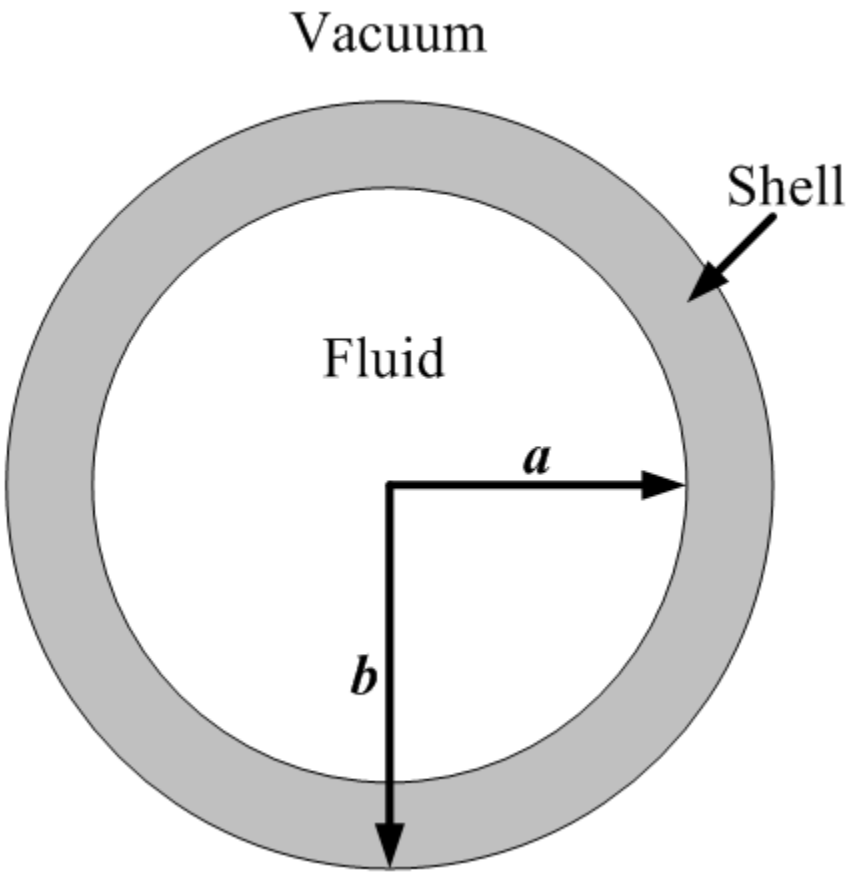

Figure 5: Schematic of shell geometry.

1.5.1. Eigenfrequencies for Ideal Boundary Conditions

The eigenfunctions for the pressure/velocity fields in any geometry are calculated by solving the wave equation. When the time dependence of the eigenfunction is assumed to be harmonic ($\sim e^{i\omega t}$), the wave equation reduces to the Helmholtz equation (Fetter and Walecka 2003)

$$(\nabla + k^2)\Phi = 0 \qquad (29)$$

where Φ is the velocity potential and eigenfunction of the Helmholtz equation, and $k = \omega/c$ is the acoustic wavenumber and eigenvalue of the Helmholtz equation. The velocity and pressure fields can be calculated from the velocity potential:

$$\boldsymbol{v} = -\nabla\Phi \tag{30}$$

$$p = \rho_0 \frac{\partial \Phi}{\partial t} \tag{31}$$

For a spherical geometry, Equation (29) can be expressed as

$$\frac{1}{r^2}\frac{\partial}{\partial r}\left(r^2 \frac{\partial \Phi}{\partial r}\right) + \frac{1}{r^2 \sin\theta}\frac{\partial}{\partial \theta}\left(\sin\theta \frac{\partial \Phi}{\partial \theta}\right) + \frac{1}{r^2 \sin^2\theta}\frac{\partial^2 \Phi}{\partial \phi^2} + k^2\Phi = 0 \tag{32}$$

Equation (32) can be solved by assuming the velocity potential has a separable solution:

$$\Phi = R(r)Y(\theta, \phi) \tag{33}$$

The angular solution, Y (θ, φ), to Equation (32) are the spherical harmonics of order (*n*,*m*) (Jackson 1999). When the angular solution is inserted back into Equation (32), the remaining the radial portion of the Helmholtz equation takes the form

$$\frac{\partial^2 R}{\partial r^2} + \frac{2}{r}\frac{\partial R}{\partial r} + \left[k_n^2 - \frac{n(n+1)}{r^2}\right]R = 0 \tag{34}$$

The radial solutions can be shown to be the spherical Bessel functions of order *n* [corresponding to the spherical harmonic of order (*n*,*m*)] (Boas 1983). Therefore, using Equation (31), the eigenfunctions can be written

$$\Phi(r,\theta,\phi) = p_0\, j_n(k_{ns}r)Y_{nm}(\theta,\phi) \quad (35)$$

where p_0 is a constant. The eigenfrequencies, k_{ns}, can be calculated by implementing the boundary condition at the fluid's surface. There are two limiting cases for the boundary condition will: pressure release and infinitely rigid. The pressure release condition requires $p(r = a) = 0$. Using Equation (31), it is readily seen that $j_n(k_{ns}a) = 0$, and the eigenfrequencies are given by $f_{ns} = \varepsilon_{ns}c/2\pi a$, where ε_{ns} is the *s*th zero of the *n*th spherical Bessel function. If the boundary is infinitely rigid, $\boldsymbol{v}(r = a) = 0$. From Equation (30) $j_n'(k_{ns}a) = 0$ and the eigenfrequencies are given by $f_{ns} = z_{ns}c/2\pi a$, where z_{ns} is the *s*th zero of the derivative of the *n*th spherical Bessel function.

1.5.2. Exact solution: Accounting for shell elasticity

A physical boundary will lie between the infinitely rigid and pressure release conditions. In this generalized situation, the impedances of the fluid and shell must be matched at the boundary to calculate the eigenfrequencies, as developed by Mehl (1985). The fluid eigenfunctions remain the same as those calculated using Equations (30) and (31). The particle displacement $\boldsymbol{s}$ of the shell can be calculated by a modified version of the Helmholtz equation (Fetter and Walecka 2003)

$$-\omega^2\mathbf{s} = c_l^2\nabla\nabla\cdot\mathbf{s} - c_t^2\boldsymbol{\nabla}\times\boldsymbol{\nabla}\times\mathbf{s} \quad (36)$$

where c_l, c_t are the longitudinal and transverse sound speed of the shell, respectively. The solution to Equation (36) can be expressed as a sum of a longitudinal component and two

transverse components, **s** = **L** + **M** + **N**, where **L, M,** and **N** can further be expressed in terms of a scalar field and two vector fields

$$\begin{aligned} k_l \mathbf{L} &= \nabla F(r) \\ \mathbf{M} &= \nabla \times [\boldsymbol{n}_r r G(r)] \\ k_t \mathbf{N} &= \nabla \times \nabla [\boldsymbol{n}_r r H(r)] \end{aligned} \tag{37}$$

F,*G*, and *H* are all solutions to Equation (29) with eigenvalues k_l, k_t, and k_t, respectively. The angular solutions for *F*,*G*, and *H* are the spherical harmonics. Their radial solutions are linear combinations of the spherical Bessel and spherical Neumann functions:

$$\begin{aligned} F_n(r) &= B_1\, j_n(k_l r) + B_2\, y_n(k_l r) \\ H_n(r) &= B_3\, j_n(k_t r) + B_4\, y_n(k_t r) \\ G_n(r) &= B_5\, j_n(k_t r) + B_6\, y_n(k_t r) \end{aligned} \tag{38}$$

Equation (38) can be used in the respective Helmholtz equations for *F*,*G*, and *H* to compute **s**. The stress tensor, τ_{ij}, can be calculated from **s**. The radial components of the stress tensor can be written:

$$\begin{aligned} \tau_{rr} &= \rho_s c_l^2 Q_1(r) Y_{n,m} \\ \tau_{r\theta} &= \rho_s c_t^2 \left(Q_2(r) \frac{\partial Y_{n,m}}{\partial \theta} + \frac{Q_3(r)}{\sin(\theta)} \frac{\partial Y_{n,m}}{\partial \phi} \right) \\ \tau_{r\phi} &= \rho_s c_t^2 \left(-Q_3(r) \frac{\partial Y_{n,m}}{\partial \theta} + Q_2(r) \frac{\partial Y_{n,m}}{\partial \phi} \right) \end{aligned} \tag{39}$$

where ρ_s is the shell density, and

$$Q_1(r) = \left(\frac{2n(n-1)}{(k_l r)^2} - \frac{c_l^2}{c_t^2}\right) k_l^2 F_n + \frac{4}{r} F_{n+1} + \frac{2n(n+1)}{r}\left(\frac{n-1}{k_t r} H_n - H_{n+1}\right)$$

$$Q_2(r) = \frac{2}{r}\left[\frac{n-1}{k_l r} F_n - F_{n+1} + \left(\frac{n^2-1}{k_t r} - \frac{k_t r}{2}\right) H_n + H_{n+1}\right] \quad (40)$$

$$Q_3(r) = \frac{nG_n}{r} - k_t G_{n+1}$$

The undetermined coefficients in Equation (38) can be calculated by matching the radial components of the stress tensor pressures at the boundaries of the shell. At the inner boundary of the shell (r=a), τ_{rr} must be equal in magnitude and opposite in sign to the acoustic pressure amplitude. The other components will vanish when viscosity is neglected:

$$\tau_{rr}(r = a) = -p_0\, j_n(ka) Y_{n,m}(\theta, \phi)$$

$$\tau_{r\theta}(r = a) = 0 \quad (41)$$

$$\tau_{r\phi}(r = a) = 0$$

Once viscosity effects are neglected, the pressure-release condition at the outer radius (r = b) results in all components of the stress tension vanishing:

$$\tau_{rr}(r = b) = 0$$

$$\tau_{r\theta}(r = b) = 0 \quad (42)$$

$$\tau_{r\phi}(r = b) = 0$$

Equations (38)-(42) can be combined into a matrix equation **AB** = **C**, where **B** is a vector of the undetermined coefficients in Equation (38), and **C** is a vector whose first element is $-ap_0\, j_n(ka)/\rho_s c_t^2$ and all other elements are zero. The matrix **A** can be inverted to determine

the coefficients in Equation (38). (Mehl notes that G_n in Q_3 of Equation (40) describes purely torsional modes. The coefficients B_5 and B_6 can be solved from the pair of homogenous equations linear in these coefficients from the boundary conditions, Equations (41) and (42). Hence these coefficients are neglected in the matrix equation and **A** is a 4x4 matrix, and **B** and **C** are 4 x 1 column vectors).

Once the elements of **B** are determined, the boundary condition at the inner radius can be expressed in terms of an effective specific acoustic admittance, β:

$$\beta \equiv \left(\frac{\rho c u_r}{p}\right)_{r=a} = -\left(\frac{i\omega\rho c a}{\rho_s c_l^2}\right) S_n \tag{43}$$

S_n is a dimensionless quantity defined by

$$S_n = \frac{c_l^2}{c_t^2} \sum_{i=1}^{4} \left(\frac{B_i}{C_1}\right) D_i \tag{44}$$

where

$$\begin{aligned} D_1 &= n\frac{j_n(k_l a)}{k_l a} - j_{n+1}(k_l a) \\ D_2 &= n\frac{y_n(k_l a)}{k_l a} - y_{n+1}(k_l a) \\ D_3 &= n(n+1) j_n(k_t a)/(k_t a) \\ D_4 &= n(n+1) y_n(k_t a)/(k_t a) \end{aligned} \tag{45}$$

An analytic form of S_n is available for the n = 0 mode:

$$S_0 = -\frac{q[(1+AB-qB^2)\tan(B-A)-(B-A)-qAB^2]}{[(qA^2-1)(qB^2-1)+AB]\tan(B-A)-(1+qAB)(B-A)} \quad (46)$$

where $A = k_l a$, $B = k_l b$, $q = ½(1-\sigma)/(1-2\sigma)$, and σ is Poisson's ratio.

When Equation (35) is used in Equations (30) and (31), the fluid admittance in Equation (43) can be expressed in terms of the fluid eigenfunctions

$$\frac{j_n'(ka)}{kaj_n(ka)} = -\frac{\rho c^2}{\rho_s c_l^2} S_n \quad (47)$$

Equation (47), along with Equation (44) and Equation (45), can be solved to calculate the non-dimensional eigenfrequencies of the composite fluid/shell system.

2. METHODS

2.1. Description of Fluid Circulation Loop

2.1.1. Loop Overview

A closed loop system, based on the success of Greenspan (1967) and Roy et al. (1985), was used to contain the fluid. A diagram of the loop is seen in Figure 6. The bulk of the loop was composed of stainless steel (types 303, 316, and 17-4), PTFE, and borosilicate glass, except as noted in the text. These materials leach contaminates at very low concentrations, which minimizes so called container effects (Bangham and Hill 1972). Low pressure connectors, fittings, tubing, and valves were Swage components, except where noted in Figure 6. High pressure tubing and valves were HiP components. A screw piston (model 50-6-15, High Pressure Equipment Company, Erie, PA) was used to generate overpressure in the resonator (described in section 2.1.4). The piston shaft was constructed from 17-4PH stainless steel. The shaft was housed in a stainless steel chamber and sealed with a Molythane® PolyPak®. The static pressure was measured with a flush mount pressure transducer (MP-40B, Micron Instruments, Simi Valley, CA), manufactured from highly corrosion resistant titanium (type 6AL4V).

Fluid was circulated through the loop using a variable speed gear pump (Cole Palmer, Vernon Hills, IL). The pump head is composed of a 316 stainless steel body, polyphenylene sulfide gears, and Viton® seals.

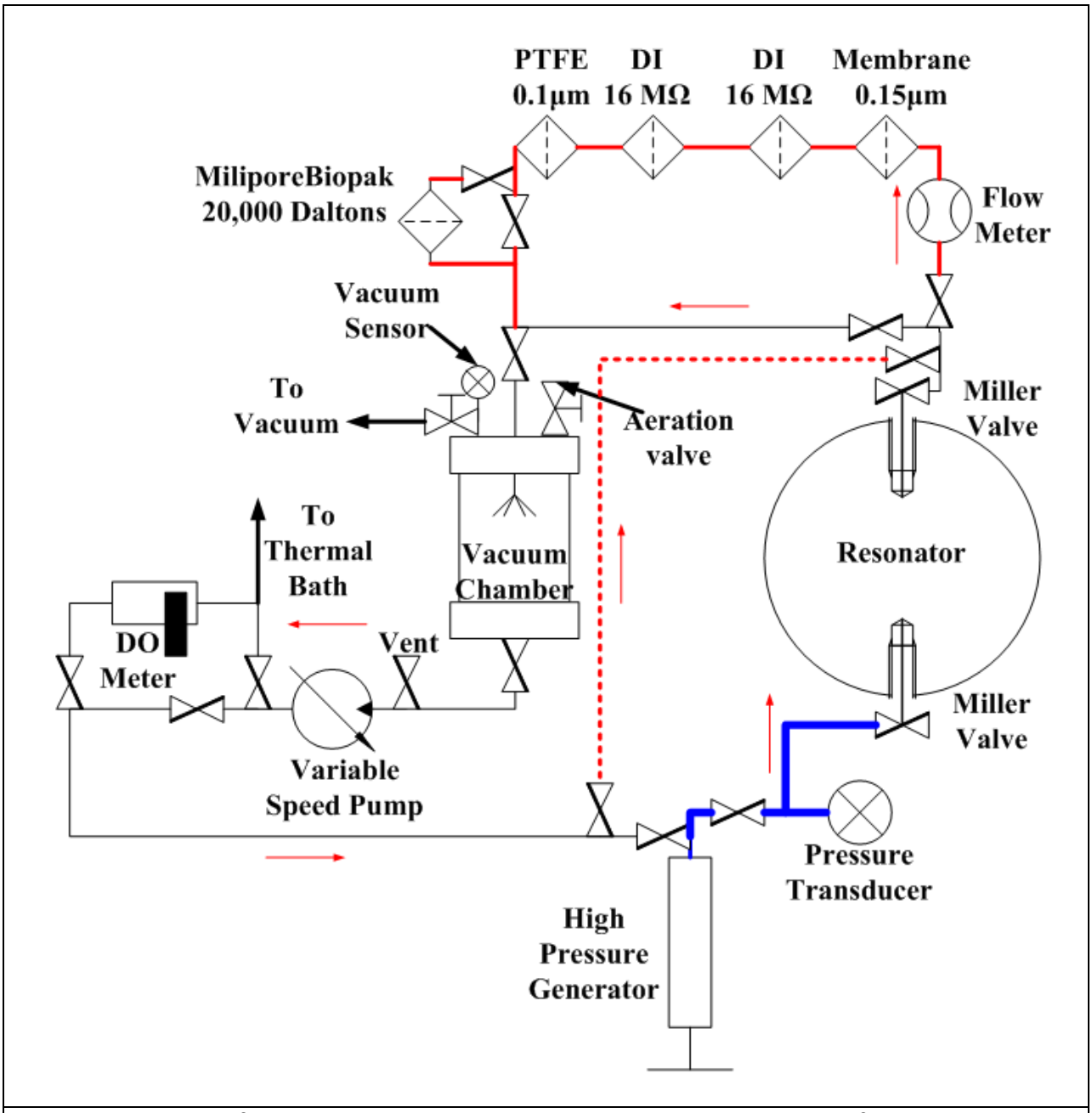

Figure 6: Diagram of loop. The thin, solid lines are 303 stainless steel tubing for low pressure. The thick, blue lines are HiP components (316 SS) for high pressure. The thick red lines are PTFE tubing for the filtering branch. Dashed red lines are PTFE tubing for the high pressure bypass. Arrows indicate flow direction.

2.1.2. Sphere/Loop Preparation

It is well known that fluid contact surfaces can leach particulates into the fluid (Bangham and Hill 1972). To minimize surface contaminates, all of the fluid contact components were cleaned with a procedure consistent with ASTM standard A380-06 (ASTM International 2006) for the cleaning of stainless steels, although the use of more aggressive caustics was avoided due to the epoxy sealant of the Sapphire windows in the sphere. The sphere was cleaned as follows: The sphere was rinsed thoroughly with hot tap water, followed by a rinse with a strong degreaser (Purple Power, Aiken Chemical Company, Inc., Greenville, SC). A layer of Naval Jelly (Henkel Consumer Adhesives, Inc. Avon, OH) was gently rubbed along the inner surface of the sphere via a long handle brush, followed by another hot tap water rinse. The interior of the sphere was treated ultrasonically by driving the sphere at 20 kHz with a 2% Micro-90 solution (Cole Palmer Vernon Hills, IL) for eight hours. This was followed by another hot tap water rinse, a methanol rinse, a hot deionized water rinse, and finally an ultrapure water (18 MΩ-cm resistivity) rinse. The sphere was then baked out at 100 ºC for eight hours in an oven evacuated to 15 Torr.

The remaining fluid contact components (valves, reservoirs, tubing, etc.) underwent an abbreviated version of the procedure outlined for the sphere: rinse with HPLC grade water (Fisher Scientific, Pittsburg, PA), rinse with methanol, rinse with HPLC grade water, and rinse with ultrapure water. The components were then baked out at 100 ºC for 24 hours. Miscellaneous items used in the filtering branch (filter cartridges, housing, PTFE tubing, and the flow meter) were triply rinsed with ultrapure water before installation.

Once loop construction was complete, a leak detector (Varian 938-41, Varian Inc., Lexington, MA) was used to ensure the connectors were completely sealed. The leak detector's mass spectrometer analyzes the helium content of residual gases in the device under test (i.e. the

loop). A helium source is sparingly applied externally to connectors. If a leak is present, the flow rate of helium through the spectrometer will rise significantly from its ambient rate (~10^{-9} cc/s). If a leak is detected, the suspect connector was tightened and rechecked.

After leak checking was completed, the final vacuum recorded in the vacuum chamber was 35 mTorr. Some sections of tubing were replaced after access to the leak detector was no longer possible. The final vacuum pressure after retrofitting the loop was within 10 mTorr of the leak checked final vacuum pressure.

After the loop was finalized, vacuum was pulled on the entire loop (sans filtering branch) for 48 hours. The final vacuum pressure during this evacuation was 45 mTorr. The loop was then back-filled with argon gas to 1 atm and subsequently re-evacuated. The loop was back-filled and evacuated twice more and then evacuated for 72 hours. Finally, just before the loop was filled with the fluid, it was back-filled with argon to 2 Torr.

2.1.3. Fluid Loading Procedure

To minimize the closed loop's exposure to outside contaminants, a rigorous fluid filling procedure was developed, modeled after Herbert et al. (2006). A filling reservoir was constructed by modifying a high purity polypropylene reservoir (Cole-Palmer Vernon Hills, IL). The reservoir is seen in Figure 7 and Figure 8. Preparation of all the fluid contact surfaces on the fill reservoir was as described for the sphere/loop preparation. The fill reservoir was fit with three access ports: a fluid fill port, a gas/vacuum port, and an exit port. The exit port had a barb which extended 3 cm from the bottom of the reservoir. This barb ensured that any heavy particulates which may have been introduced when the fluid was poured into the reservoir would be trapped at the bottom of the reservoir and prevented from flowing into the loop. The fill reservoir's exit port attached to the loop's vent port via PTFE tubing with Swage components.

Figure 7: Fill reservoir used to load ultrapure water into sphere loop. The reservoir was constructed with ultrapure polypropylene, and all other fittings and tubing were stainless steel, PTFE, or ultrapure Tygon®.

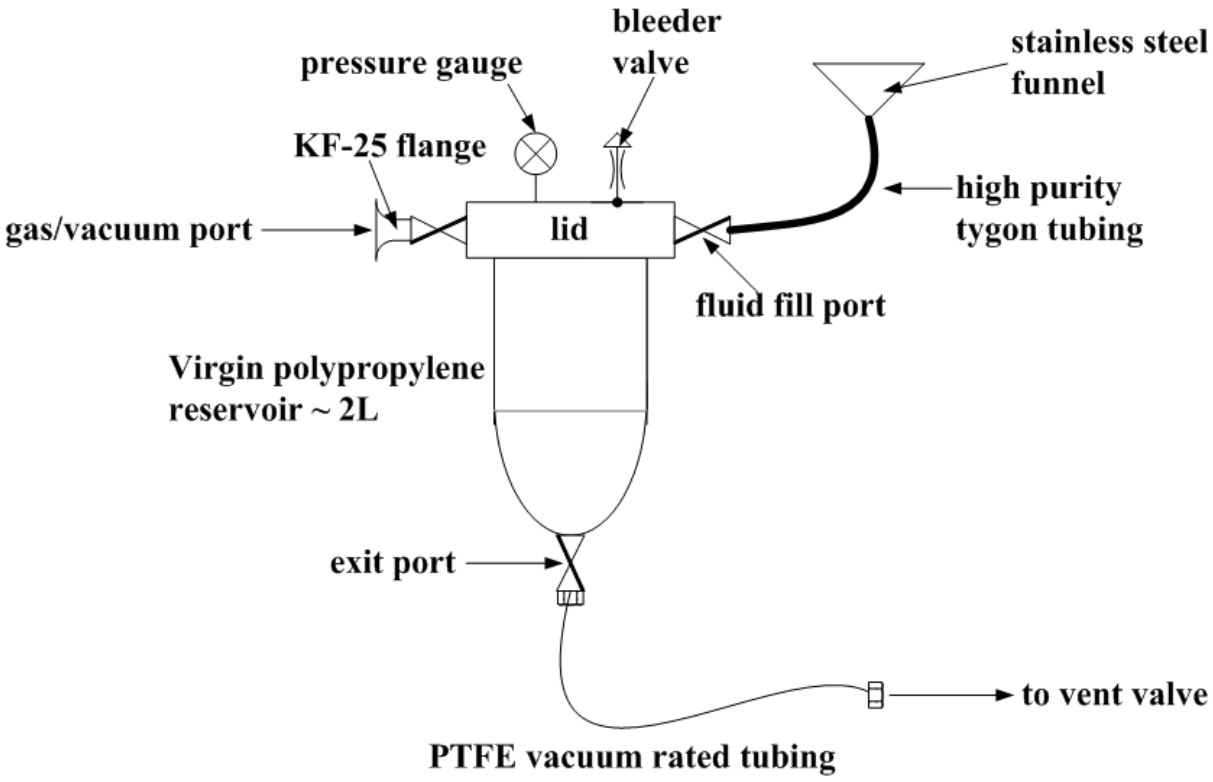

Figure 8: Schematic of fill reservoir.

The fill procedure was as follows: The loop was evacuated to its baseline vacuum (~40 mTorr) and then back-filled with argon to a final pressure of 2 Torr. The fill reservoir was elevated relative to the loop's vent valve, evacuated, and then backfilled with argon to 1 atm. The reservoir was then filled with the baseline fluid, high purity water (Environmental Grade Water, Fisher Scientific, Pittsburgh, PA), via the stainless steel funnel attached to high purity Tygon® tubing. It was necessary to open a bleeder valve in order to get the water to flow into the fill reservoir.

Once the fill reservoir was full, the valves at the reservoir's exit port and the loop's vent valve were opened and the water flowed easily into the loop. A slight amount of argon back

pressure was applied to the fill reservoir to maintain 1 atm total pressure. The loop's gear pump, located in line with the vent valve, was also used to help draw water from the fill reservoir.

Once the fill reservoir was emptied, it was isolated from the loop and the procedure was repeated until the entire loop was filled with water. In total, roughly 12 L of ultrapure water were required to fill the loop. The loop periodically needed to have more fluid added as water vapor was collected in the liquid nitrogen trap during the degassing procedure. The fill procedure was repeated as needed to ensure the loop was adequately filled.

2.1.4. Acoustic Resonator

The acoustic resonator (provided by IDI) was a stainless steel (17-4), spherical shell with 9.5" OD and 8" ID (3/4" thickness). The resonator, shown in Figure 9: was a spherical shell, with a volume of approximately 4.4 L, a 24.13 cm (9.5") outer diameter, and a 1.9 cm (0.75") wall thickness. The eigenmode at which the threshold was measured [(0,6) mode, ~25.5 kHz] had a quality factor on the order of 10^4 when fluid loaded. The (0,6) mode was empirically determined to be the most efficient mode for cavitation (Gaitan et al. 2010). The resonator was initially machined as two separate hemispheres, which were later joined by electron beam welding. There were four ports with access to the resonator's interior. Two of these ports were fitted with custom made needle type valves (1/2" NPT threads) for circulation of fluid through the sphere. One of the remaining ports (1/4" NPT threads) was a custom mount for the hydrophone (603B1, Kistler Instrument Corporation, Amherst, NY) discussed in more detail in section 2.2.1. The remaining port (also ¼" NPT) was sealed with a custom made plug.

The sphere was equipped with four planar, sapphire windows. The windows were initially sealed with epoxy (Epicure 815C, Miller-Stephenson Chemical Company Inc., Danbury, CT).

However, the windows leaked after sustained periods without exposure to high static pressures (> 250 bar). The windows could be re-sealed by leaving the sphere pressurized at 310 bar (~4500 psi) overnight. This was done the night before working at pressures 250 bar and greater.

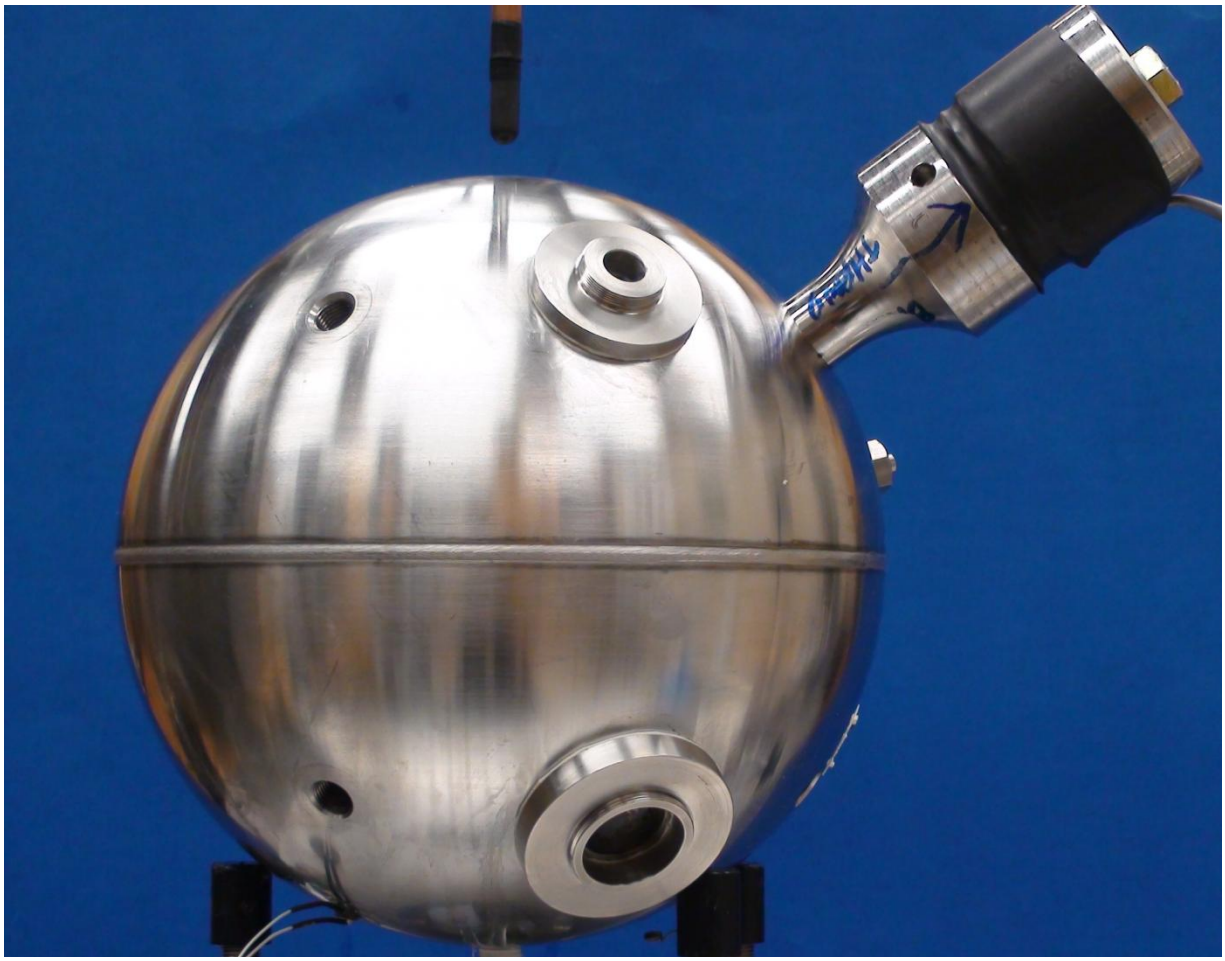

Figure 9: Photograph of spherical resonator used for reported results. The sphere was 9.5” outer diameter, 0.75” thick with a total volume of approximately 4.4 L. The material was type 17-4 stainless steel.

2.1.5. Cavitation Fluid and Filtering Scheme

2.1.5.1. Baseline Fluid

The purity of the fluid is paramount in achieving high cavitation thresholds. The baseline fluid was a high purity water commercially available from Fisher Scientific (environmental grade water, Fisher Scientific, Waltham, MA). The manufacturer specifies that the water quality was at least as pure as ASTM type I water before bottling.

2.1.5.2. Outline of Filtering Scheme

The filtering scheme was modeled after a commercial filtering system (Thermo Scientific Barnstead E-Pure, Thermo Scientific, Asheville, NC), for producing ASTM type I water. It was designed to maintain the water's purity, and therefore further processing such as distillation and reverse osmosis, which are typically used to bring a low purity fluid up to ASTM type I standard, were not used. A schematic of the filtering branch of the loop is reproduced in Figure 10.

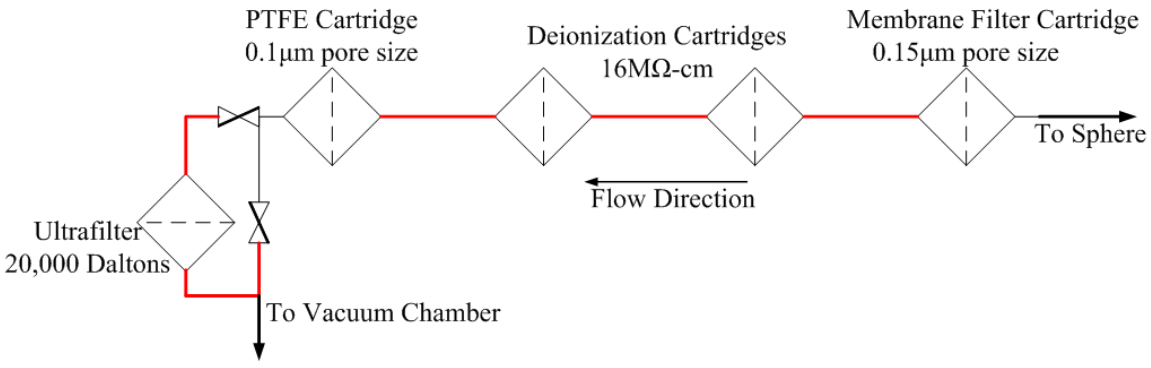

Figure 10: Filtering scheme used to maintain purity of water in loop. The tubing between the cartridges was PTFE (red lines).

The filter cartridge housing was constructed from virgin polypropylene and sealed with a PTFE O-ring, except for the primary membrane filter cartridge which required a specialized housing (lower grade polypropylene, sealed with PTFE o-ring). The ordering of the filters was necessary to either siphon off larger particulates from the final filters, or for removal of particular impurities to protect subsequent filters. These filters are detailed below:

1. The primary filter, a carbon-block membrane cartridge, was chosen for two reasons: First, it was a membrane filter with a pore-size of 0.15 μm. This cartridge had the largest pore size amongst the filters, and it could thus siphon off the largest particles, preventing the filters next in series (with smaller pore sizes) from clogging. Second, the manufacturer specified the filter to remove 99.9999% of bacteria and cysts [the minimum bacteria size is 0.2 μm (Ohmi 1993)]. The resin used in the deionization columns (next in series) can act as a breeding ground for bacteria, especially if the water is allowed to be stagnant for extended periods (G.E. Osmonics 1997). Therefore, the membrane filter was used to remove bacteria before the fluid was allowed to pass through the deionization cartridges.
2. The two deionization cartridges next in series were specified to purge dissolved ions up to 16 MΩ-cm resistivity. The second deionization cartridge was for redundancy. Although the baseline fluid had a high resistivity (18 MΩ-cm), it is well known that the resistivity degrades over time by leaching ions from container wall. The deionization cartridges were implemented to maintain the high resistivity of the fluid. Deionization is the only method available to produce water with high enough resistivity to meet ASTM standards. The cartridges contain a mixed-bed resin of both anions ($R\text{-}SO^-_3\ H^+$) and cations ($R_4N^+\ OH^-$) with surface

layers of H^+ and OH^-, respectively. Dissolved ions in contact with the resin would be attracted to either the cation or anion and would displace an H^+ or OH^-, respectively. The byproducts from the resin (H^+ or OH^-) recombine to form pure water.

3. A PTFE membrane filter of pore size 0.1 µm was next in-line. The filter was specified to remove 99.9% of particles larger than the pore size based on the ASTM F795 test. This cartridge acted as a polishing filter to remove particles that passed through the previous filters to ensure the ultrafilter (next in line) would not clog.
4. The final filter was a commercially available ultrafilter (model name Biopak, Millipore Corporation, Billerica, MA) composed of several polysulfone membrane hollow fibers in an ABS housing. The filter acts as a molecular sieve, with a cutoff weight of 20,000 Daltons. The Biopak is typically placed at the end of water purifying systems to act as a polisher to remove pyrogens (which tend to conglomerate in high purity water), nuclease (e.g. RNA and DNA), and bacteria for cell culture, biochemistry, or molecular biology applications. It was unknown how prevalent these types of contaminants would be in ultrapure water, or if they could eventually contaminate the closed loop system. However, even if such contaminants were not present in the fluid, the ultrafilter acted as a final polishing filter to ensure minimal particulate contamination.

2.1.5.3. Analysis of Fluid Particulate Content/Effectiveness of Filtering Scheme

As previously discussed, nucleation sites are assumed to exist within the bulk of the fluid. Their nature (i.e. hydrophobic, hydrophilic, or amphiphilic), size, and number density are often not known. Messino et al. (1963) used the cavitation threshold to statistically measure the nuclei distribution in his test liquid, although modern advances in light scattering techniques provide more quantitatively accurate results. In order to get an accurate estimate of the size and number density of particulates within the liquid, samples of the test fluid were sent to a laboratory capable of measuring particles sizes down to 0.1 μm (Particle Measuring Systems, Boulder, CO). Three fluid samples with different degrees of "cleanliness" were sent to the lab: A. Manufacturer fresh water (i.e. straight from the bottle), B. Water extracted from the loop after a typical data run, and C. Water extracted from the loop after a typical filtering and degassing cycle. These samples were labeled Group A, Group B, and Group C, respectively. The samples were collected in glass sample jars, with foam backed, PTFE lined caps (p/n 4239T32, McMaster-Carr, Atlanta, GA). The jars were prepared before the samples were collected as follows: The jars and lids were cleaned in an ultrasonic cleaner with a 2% solution of Micro-90 (Cole-Palmer, Vernon Hills, IL) and tap water at 40 ºC for 45 minutes, followed by a rinse with hot tap water. The parts were then triply rinsed with 18 MΩ-cm deionized water, triply rinsed with HPLC grade methanol, and triply rinsed with 18 MΩ-cm deionized water. The containers were then overflowed with 18 MΩ-cm deionized water, capped, and left overnight. The containers were left filled with the 18 MΩ-cm deionized water until minutes before the test fluid was introduced, at which point the jars were agitated by shaking, the 18 MΩ-cm deionized water was then poured out, and the sample fluid was placed in the jar. A fourth control jar, prepared in the same manner, was sent as

a control and tested with a fluid with a known particulate content. A summary of the testing procedure used by Particle Measuring Systems is in Appendix A.

Group A and Group C samples were tested for particles of sizes 0.1 – 0.5 μm, and 0.5 – 20 μm. The Group B samples were tested for particle sizes of 0.2 – 2 μm, and 2 – 125 μm. The number of particles per milliliter for sizes 0.1 – 20 μm is plotted in Figure 11. The cumulative number of particles from a given size up to 20 μm is plotted in Figure 12. The data in Figure 12 were made continuous by averaging the last and first data point of each measured particle size range. For instance, 0.5 μm was the lower and upper measuring range for Groups A and C. There is some difference in this measured value (see Figure 11) due to variations in the measuring instrument used for the two size ranges. A similar discontinuity occurs at 2 μm for Group B data.

The data seems to indicate that a large number of particles are present. Group A has over 10^5 particles/mL over the size range 0.1 – 20 μm. However, the particle count in Group A is on the same order as the control jar, and therefore the particles are likely leached from the sample jar. Group C has 10^6 particles over that size range, almost an order of magnitude more particles than Group A. However, as the particle size increases, the post filtered (Group C) particle count decreases the quickest, and beyond 0.5 μm Groups A and C are within a factor of 2-3. Figure 11 indicates that both Groups B (post data run) and C (post filtration) have roughly the same number of particles up to 0.5 μm. Beyond that, the count in Group C declines rapidly. Hence, the filtration process seems to be most effective for particles larger than 0.5 μm. This is consistent with Flynn's discussion of the strong influence of Brownian motion on particulates of sub-micron size (Flynn 1964).

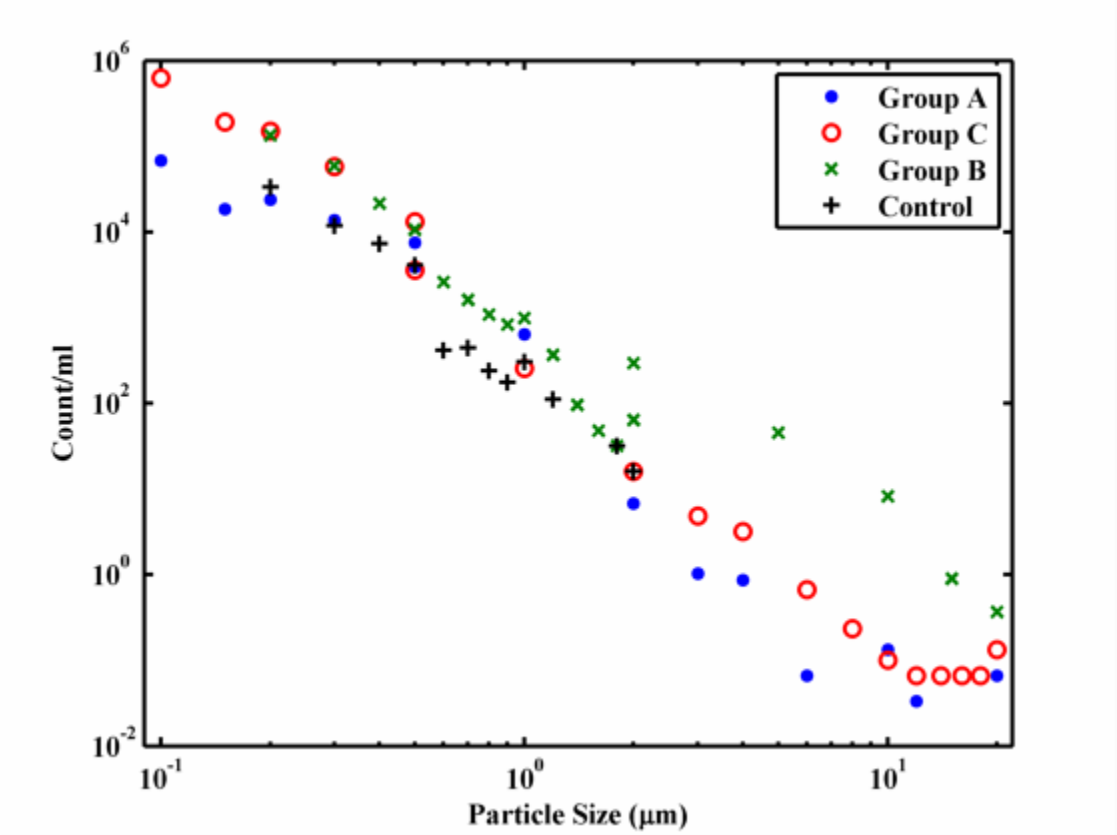

Figure 11: Number of particles per milliliter as a function of particle size.

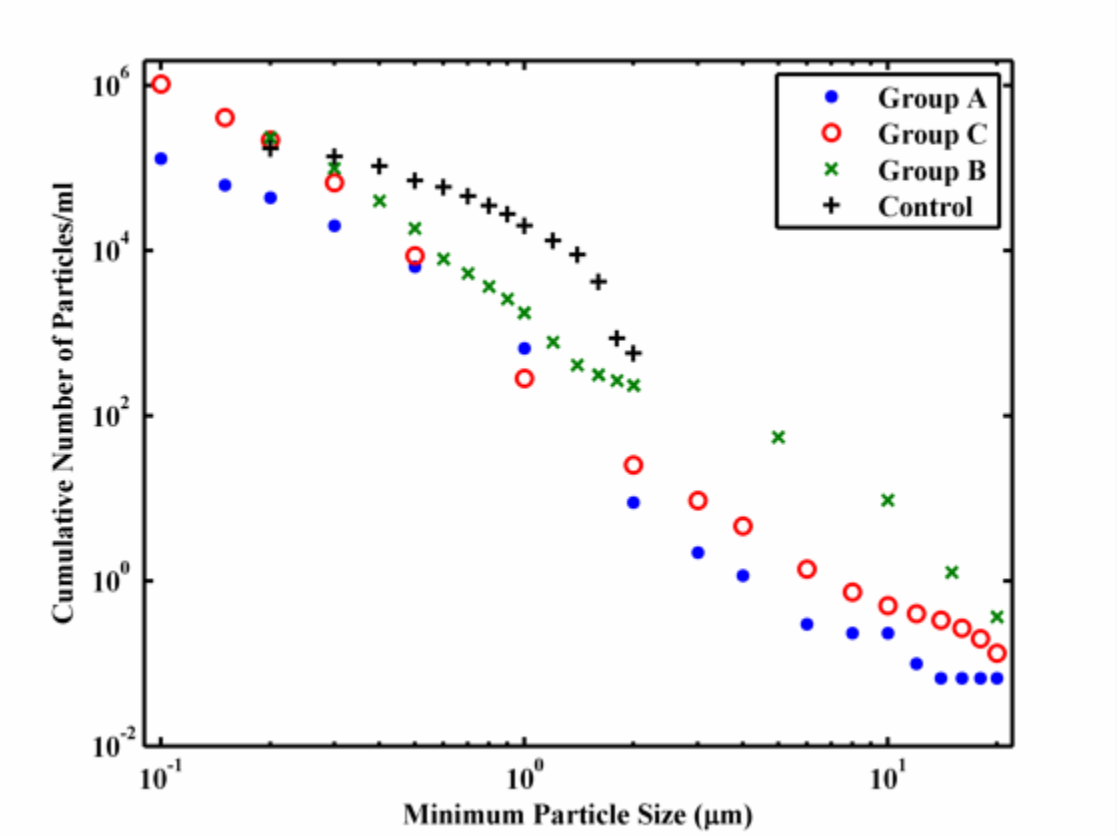

Figure 12: Number of particles per milliliter larger than specified particle size.

The overall volume fraction of these particulates is relatively small considering their abundance. Figure 13 shows the volume fraction as a function of the particle size, and Figure 14 shows the cumulative volume fraction for particles of a minimum size up to 20 µm. Table 3 lists the mean volume fraction over the particle size range of 0.1 – 20 µm for Groups A and C, 0.2 – 20 µm for Group B, and 0.2 – 2 µm for the control sample. Table 4 lists the cumulative volume fraction of particles over the particle size ranges 0.1-20 µm (Groups A and C), 0.2 – 20 µm (Group B), and 0.2 – 2 µm (control). The cumulative volume fraction of the particulates for the pure water (Group A) is approximately 1 in 3 billion. The cumulative volume fraction for the post filtered and degassed water is approximately 1 in 1 billion, and the cumulative volume

fraction for post data collection is approximately 1 in 2.5 x 10^8. To put these numbers into perspective, if the total volume of the fluid were a standard Olympic sized pool holding 2.5 ML of water, the total volume of the particulates would be 0.83 mL, 10 mL, and 2.5 mL for Groups A, B, and C, respectively.

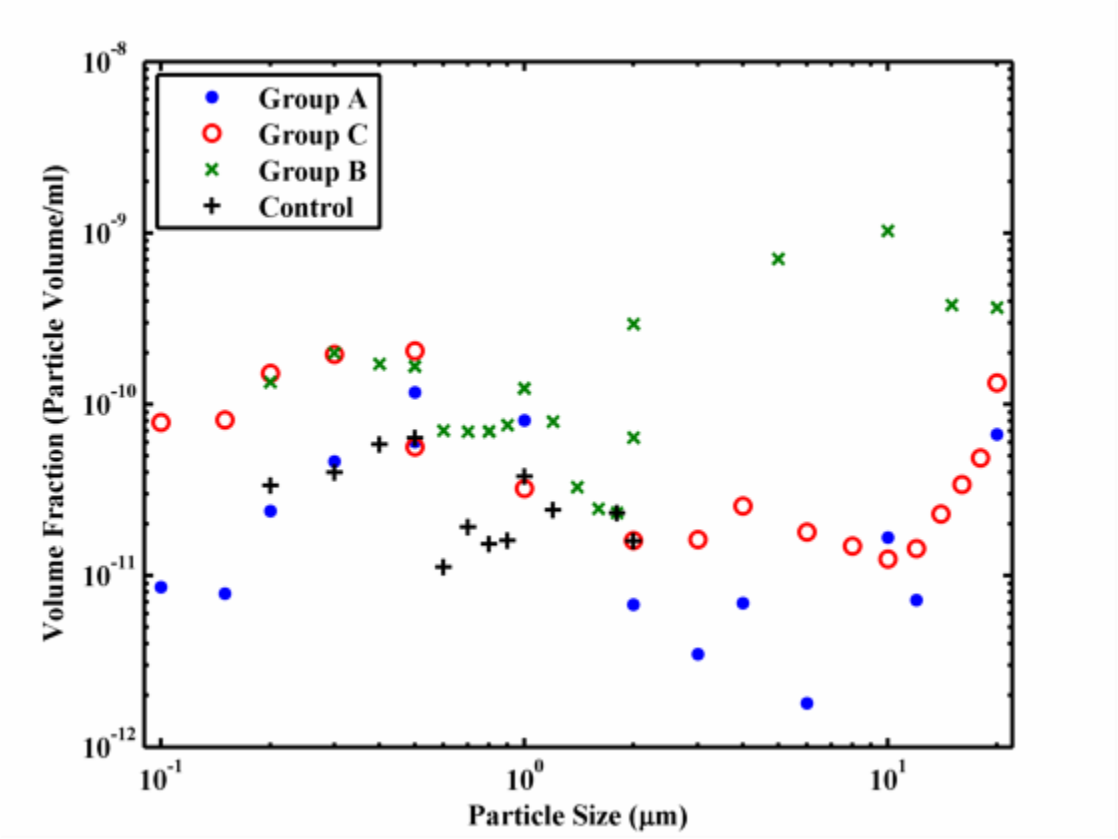

Figure 13: Volume fraction of particles as function of particle size, calculated using the data from Figure 11.

Group	Mean Volume Fraction
A	2.52×10^{-11}
B	1.98×10^{-10}
C	6.43×10^{-11}
Control	2.56×10^{-11}

Table 3: Mean volume fraction of particulates from Figure 13 over the particle size ranges 0.1-20 μm (Groups A and C), 0.2-20 μm (Group B), and 0.2-2 μm (control).

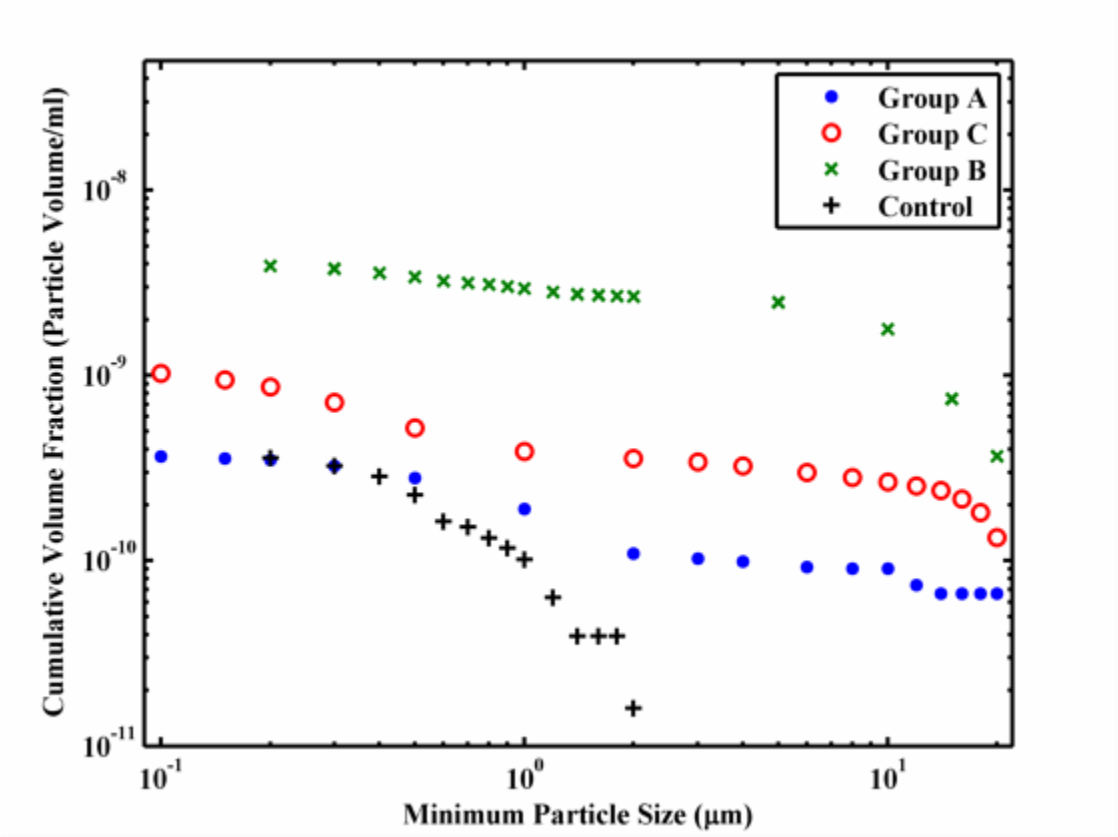

Figure 14: Cumulative volume fraction (volume fraction for particles larger and equal to the minimum particle size up to 20 μm), calculated using the data from Figure 12.

Group	Cumulative Volume Fraction
A	3.66×10^{-10}
B	3.90×10^{-9}
C	1.03×10^{-9}
Control	3.59×10^{-10}

Table 4: Cumulative volume fraction of particulates from Figure 14 over the particle size ranges 0.1-20 μm (Groups A and C), 0.2-20 μm (Group B), and 0.2-2 μm (control).

2.1.6. Vacuum Chamber and the Degassing of the Liquid

Dissolved gases were removed from the liquid in the vacuum chamber (see Figure 6) as the liquid was circulated through the loop. Degassing was done after the liquid was circulated through the filtering loop, since the leak back rate of the filtering branch was unknown. The chamber body (provided by IDI) was constructed from borosilicate glass (Farlow Scientific Grass Valley, CA), and the flanges used an ISO-K 100 type seal (Trinos Vacuum Goettingen, Germany) with a PTFE o-ring. The flanges attached to the glass using an industrial strength epoxy (Epon 815c resin, with Epicure 3140, Miller-Stephenson Chemical Company, Morton Grove, IL). The fluid exited the chamber through 1/4" stainless steel pipe extended 1 cm above the bottom flange. This prevented heavy particulates that collected at the bottom of the chamber from exiting the chamber. If the bottom flange collected several heavy particulates or numerous particles were seen floating in the chamber, the chamber was isolated from the loop and drained via the drain port.

A diagram of the vacuum branch is shown in Figure 15. The vacuum chamber could be pressurized up to 1 atmosphere absolute (the glass limits pressurization above the surrounding atmosphere) or evacuated. The chamber was typically backfilled with argon to 200-400 Torr when the fluid was not being degassed to help the fluid circulating pump move water through the filtering branch. Vacuum was pulled on the chamber with a positive displacement vacuum pump (model 15400, Robinair SPX Corporation, Owatonna, MN). The factor micron rating of the pump was 20 μbar, and the free air displacement of the pump was specified to be 4 ft^3/min.

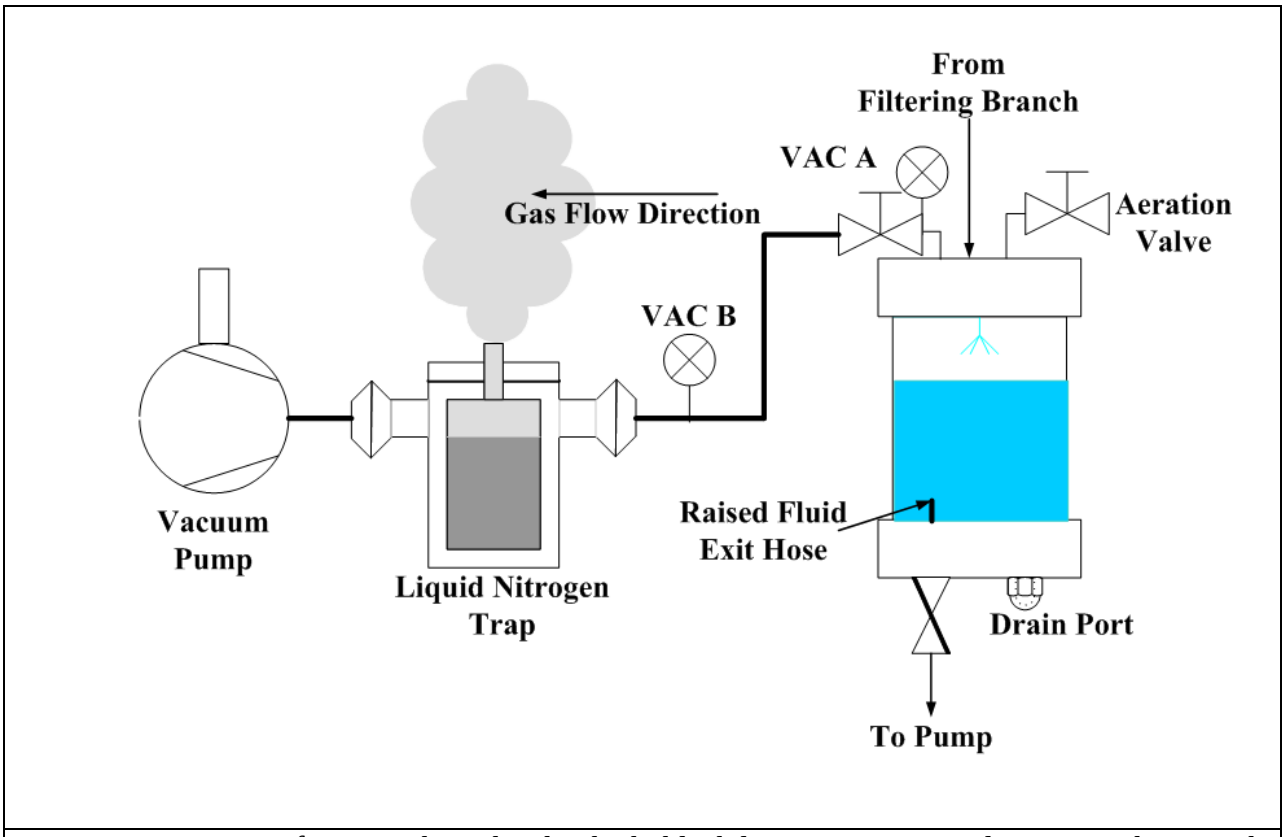

Figure 15: Diagram of vacuum branch. The thick, black lines are corrugated vacuum tubing, with ISO-KF 25 sized flanges. The aeration valve also connects to the argon gas line with an ISO-KF flange. A molecular sieve was used in place of the liquid nitrogen trap during the loop construction.

A liquid nitrogen trap was placed in-line between the vacuum chamber and the vacuum pump. The trap provided protection against oil vapor drifting through the vacuum line into the closed loop and from water vapor entering the pump. Because of the low vapor pressure of oils, retention of oil vapor was not as critical when the chamber was filled with liquid since the final vacuum was limited by the vapor pressure of water (~15 Torr). During leak detection (see section 2.1.2), a molecular sieve (Hyvac Products, Inc. Phoenixville, PA) was used in place of the liquid nitrogen trap.

The pressure in the chamber was measured using a thermocouple vacuum gauge (DST531, Dunniway Stockroom Corp., Mountain View, CA), labeled as VAC-A in Figure 15, which had a large dynamic range (~1 mTorr to 800 Torr). VAC-B was an absolute capacitance manometer with a 1000 Torr pressure range and sensitivity down to 1 mTorr (model 750C13TFE2GA, MKS Instruments, Inc., Wilmington, MA). VAC-B was used to check the vacuum of the vacuum pump. The analog outputs from the vacuum sensors' controllers were recorded with an analog to digital module (USB-120FS, Measurement Computing Corp., Norton, MA) using custom Labview (National Instruments Corporation, Austin, TX) data-logging software.

The gas content of the fluid was monitored *in situ* with a dissolved oxygen meter (CD650, Oakton Instruments, Vernon Hills, IL) with automatic pressure and temperature compensation. The probe body was constructed from Delrin® and had a HDPE membrane (both were fluid contact surfaces). The probe was incorporated into the loop with custom mounts, as shown in Figure 16.

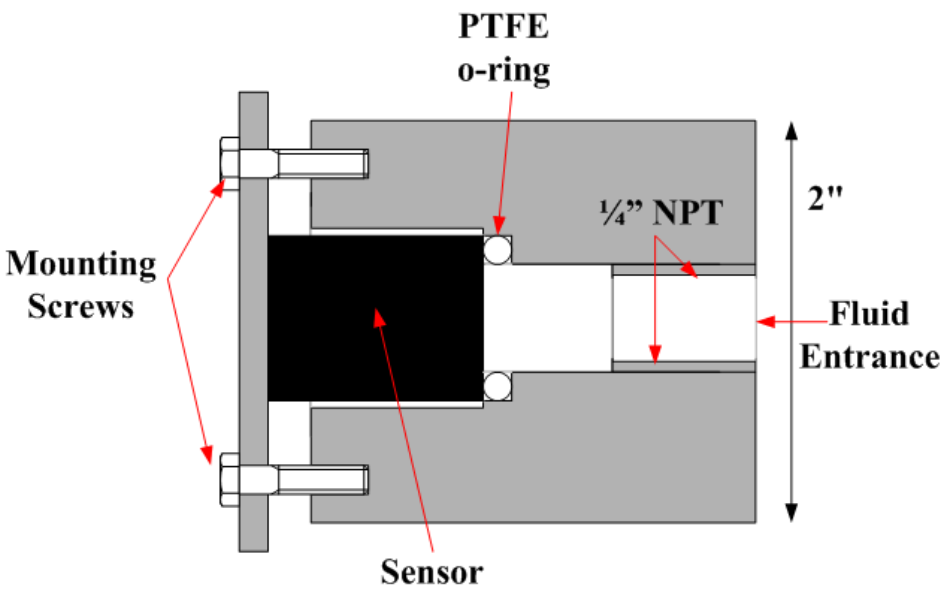

Figure 16: Mount for dissolved oxygen probe. The probe face seals in the mount via a PTFE o-ring. The figure is not to scale.

The amount of dissolved oxygen in saturated, pure water is dependent on the partial pressure of oxygen in the surrounding atmosphere and the temperature. Electro-metric methods of measuring dissolved oxygen are based on this fixed relationship. Oxygen diffuses through the probe's semi-permeable membrane at a rate proportional to the partial pressure in the liquid. The probe is essentially a Galvanic cell with the anode and cathode submerged in an electrolytic solution. Once oxygen is consumed at the cathode, current flows through the anode to the meter proportional to the dissolved oxygen content. Since oxygen is consumed during this process, water continually needs to flow to replenish oxygen.

The probe had automatic temperature and pressure compensation. The temperature affects not only the solubility of gas in the liquid, but also the permeability of the membrane. The probe was calibrated at full fluid saturation (100% saturation) by exposing the probe to the surrounding

air, and at 0% saturation with a zero oxygen solution (Oakton Instruments, Vernon Hills, IL). The fluid contact surfaces were triply rinsed with ASTM type I water before the probe was introduced into the loop.

2.1.7. Fluid Temperature Control

Two methods were used to control the fluid temperature in the loop. Initially, the fluid was heated from room temperature (~16 ºC) via heating rope (HTC-030, Omega Engineering Inc, Stamford, CT) wrapped around the resonator, vacuum chamber, and sections of the high pressure tubing. The rope temperature was controlled with a variable step down transformer (482 ºC at 120 V_{ac}).

Later, changes in the environmental conditions made it necessary to cool the fluid in order to obtain a consistent range of temperatures for each data set. This was accomplished by integrating a temperature regulated bath into the loop. The bath is as shown in Figure 17. A parallel branch was incorporated into the loop, with 9 feet of stainless steel tubing and a cold plate (p/n 35035K46, McMaster-Carr, Atlanta, GA) immersed in a 24 liter cooler filled with a 50% solution of ethylene glycol. The temperature of the ethylene glycol mixture was controlled within 0.1 ºC by a constant temperature circulator (Polystat 12101-10, Cole-Parmer, Vernon Hills, IL). The constant temperature circulator was intended for closed loop systems only, thus a variable speed, gear pump (200 series, Cole-Parmer, Vernon Hills, IL) was used to pump the ethylene glycol mixture from the cooler to the constant temperature circulator. The piping on the remainder of the loop was insulated with universal mat pads (New Pig Corp., Tipton, PA) to minimize heat transfer.

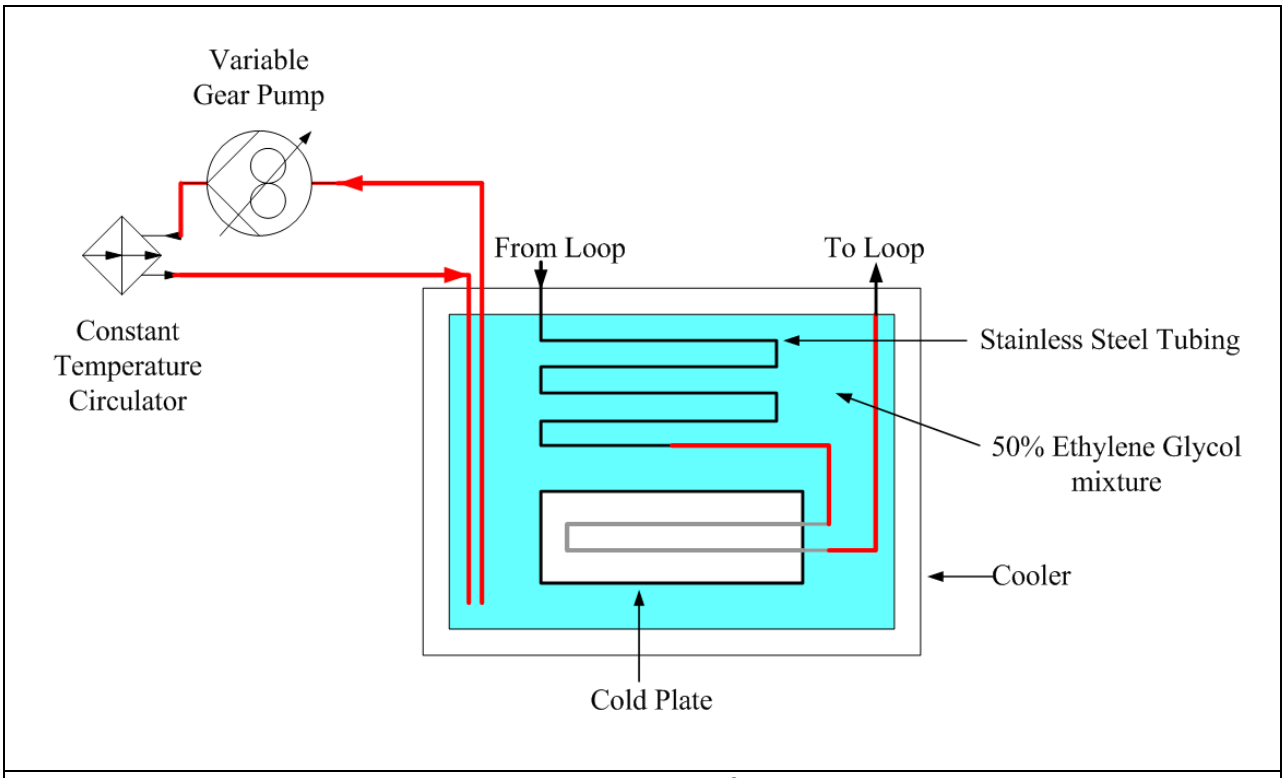

Figure 17: Constant Temperature bath used to regulate fluid temperature in loop. All tubing is stainless steel, except for thick, red lines which are PTFE.

The change in temperature of the fluid in the loop while circulating through the thermal control bath is plotted in Figure 18. The circulator was set at 0 ºC. The temperature of the fluid was measured using the well known relation of the water's sound speed to temperature and pressure (Chen and and Milero 1976). The temperature drop is essentially an exponential decay with a time constant that is proportional to the room temperature. This time constant varied from 270-540 min for ambient temperatures from 20-26 ºC.

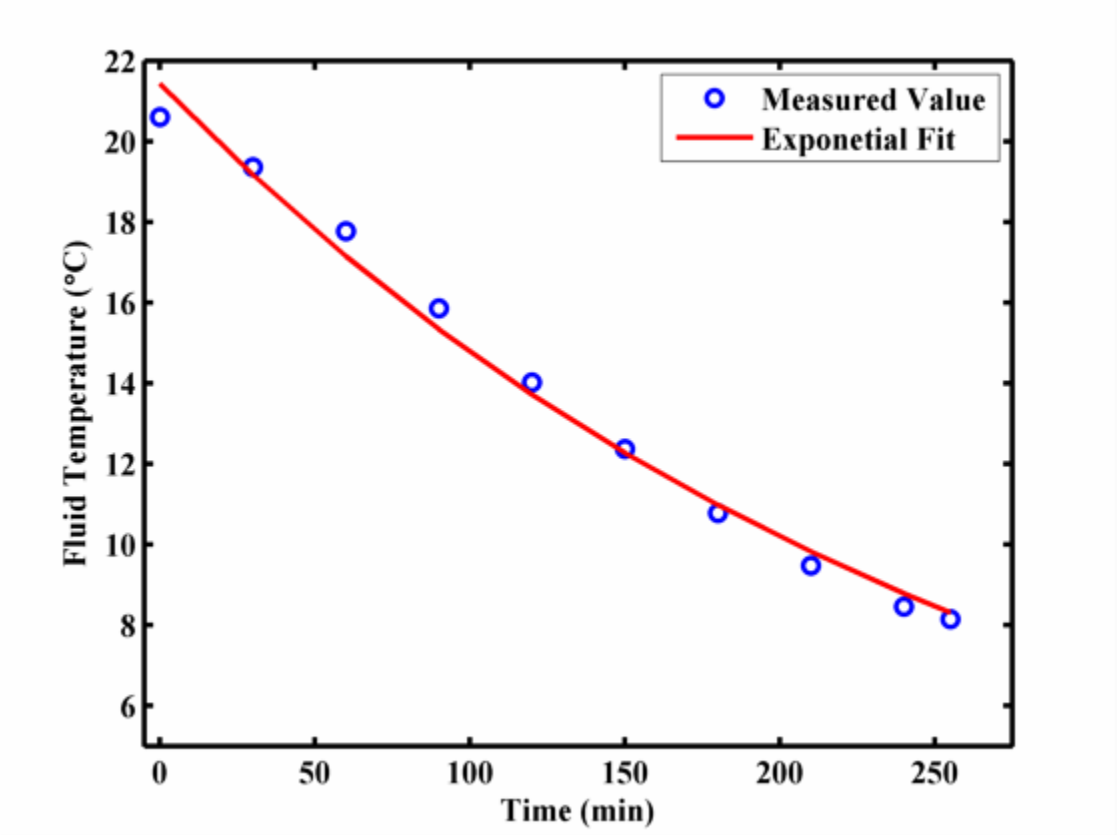

Figure 18: Temperature drop of the fluid in the loop while passing through the constant temperature bath.

The temperature of the fluid within the sphere can increase by several degrees over the course of a data run due to absorption of acoustic energy. To minimize this heating, two equipment cooling fans (p/n 1976k43, McMaster-Car, Atlanta, GA) were used to circulate the air around the resonator.

2.2. System Diagnostics

2.2.1. Wall Mount Hydrophone

The acoustic pressure was measured at the inner wall of the resonator with a calibrated quartz sensor (603B1, Kistler Instruments Corporation, Amherst, NY). A diagram of the sensor is shown in Figure 19. The 603B1 uses a quartz sensing element comprised of a stack of longitudinal quartz plates held together by a preload sleeve, and has an integrated accelerometer whose output nulls out the acceleration effects of the pressure sensitive element. The sensor signal is transmitted through a low noise cable (p/n 1631, Kistler) to a charge-sensitive pre-amp (model 5010, Kistler).

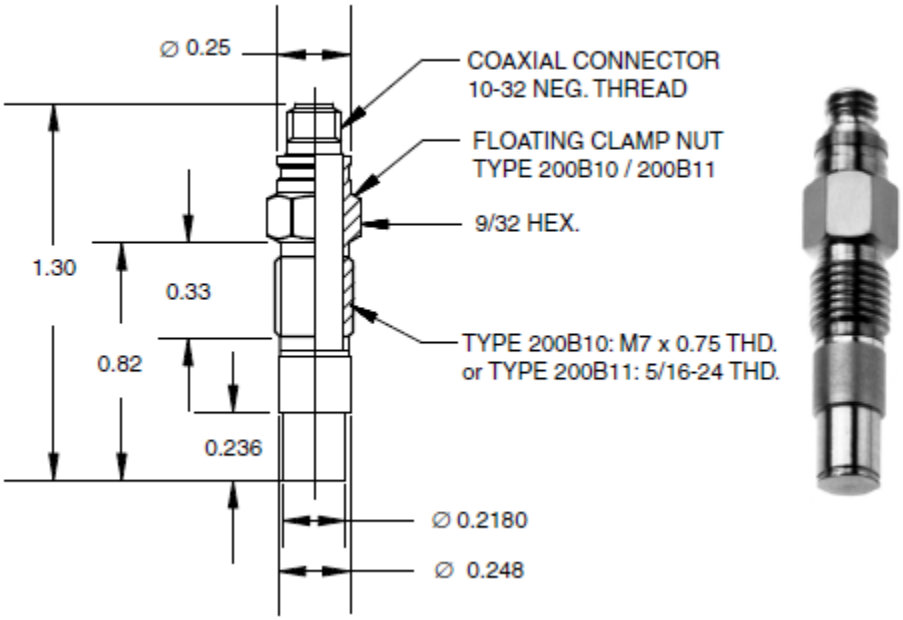

Figure 19: Photo and technical drawing of acoustic pressure sensor, 603B1. After Kistler Instrument Corp. (2003).

The typical frequency response, shown in Figure 20, is treated as a forced vibration of a damped system with a single degree of freedom:

$$Y = \frac{P}{K}\frac{1}{\sqrt{\left[1-\left(\frac{\omega}{\omega_n}\right)^2\right]^2 + 4\zeta^2\left(\frac{\omega}{\omega_n}\right)^2}} \tag{48}$$

where ω_n is the undamped resonance of the sensor, ζ is the damping ratio, and P/K is the so-called magnification factor attributed to the zero frequency static deflection of a spring with stiffness K. The resonant frequency of the 603B1 is typically 500 kHz. As shown in Figure 20, deviations from Equation (48) will occur above $f_n/5 = \omega_n/10\pi$ due to variations in the transducer rigidity, measuring errors, and the presence of sub-resonances. These deviations are reduced to within 2% at $f = f_n/5$, and are within 1% at $f_n/10$ the deviations.

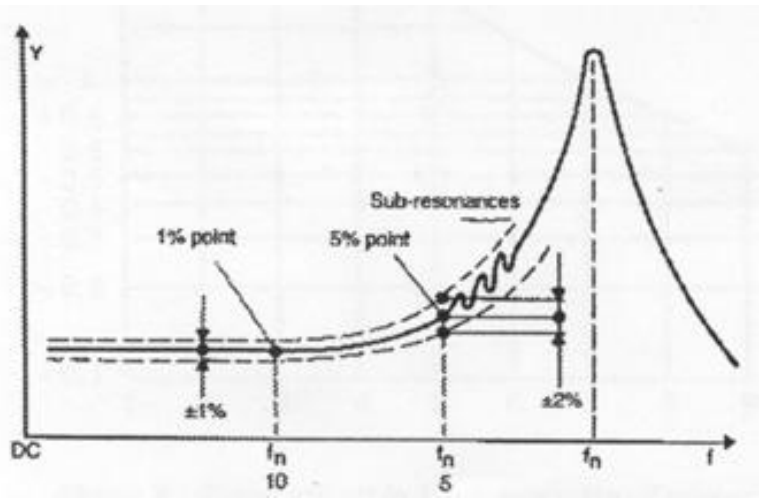

Figure 20: Curve depicting amplitude (arbitrary units) increase and tolerance as a function of frequency. f_n is typically 500 kHz for the 603B1. Taken from Hugli (2011).

A custom fixture was machined for mounting the sensor to the resonator, as shown in Figure 21. The sensor face fits snugly through the bottom through-hole (referenced as Ø.221) on the fixture such that the sensor diaphragm was even with the bottom of the fixture. A floating nut (5/16-18 threads) was used to compress the sensor against a PTFE washer to create a seal near the bottom of the mount. The entire fixture attached to the sphere via ¼" NPT threads. The taper of the threads was adjusted such that the face of the mount (and also the sensor diaphragm) was flush with the inner radius of the sphere.

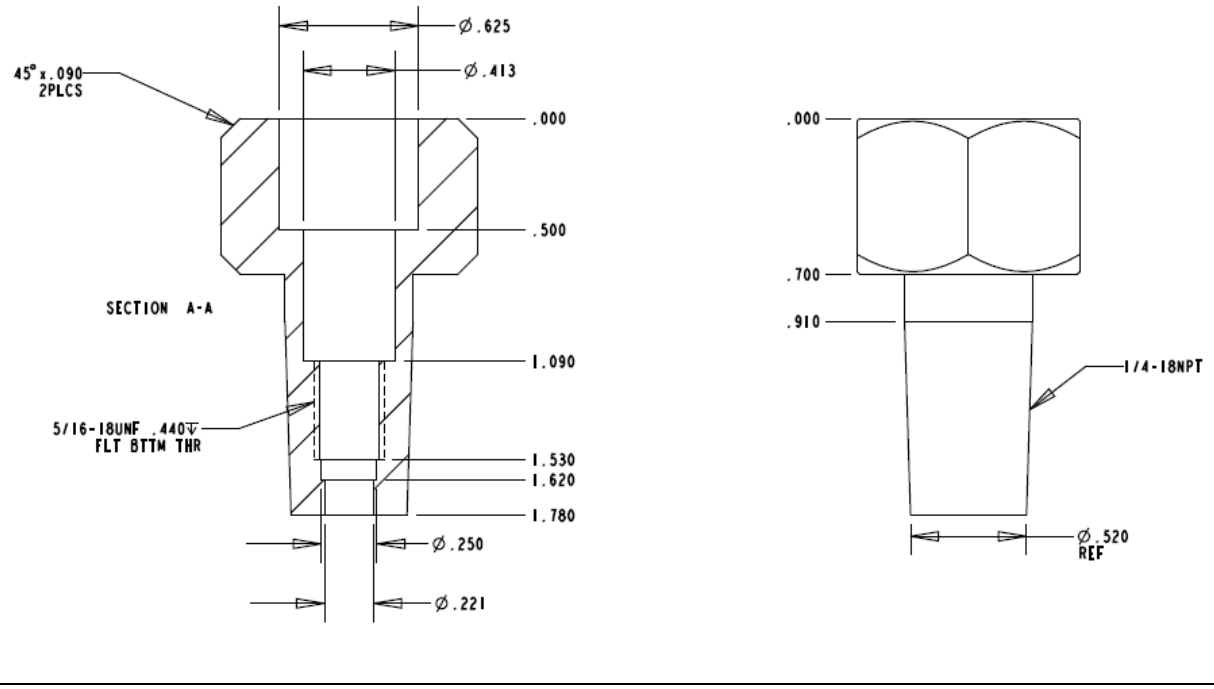

Figure 21: Schematic of mounting fixture for the Kistler 603B1 (courtesy IDI).

Previous experience at large driving amplitudes (~500 bar) consistently resulted in failure of the 603B1. The failure was associated with the singeing of the inner conductor of the microdot coax on the sensor connector, and deformation of the insulating Teflon layer (see Figure 22). Once the co-axial line became singed the signal significantly degraded, rendering the sensor

unusable. The cause of the sensor failure was attributed to localized frictional heating of the sensor connector extension and the floating nut (see Figure 23). No further failures occurred once the connector extension was removed from the sensor (the remaining diaphragm portion of the sensor had M4 threads, which could be used mated with the 1631 cable).

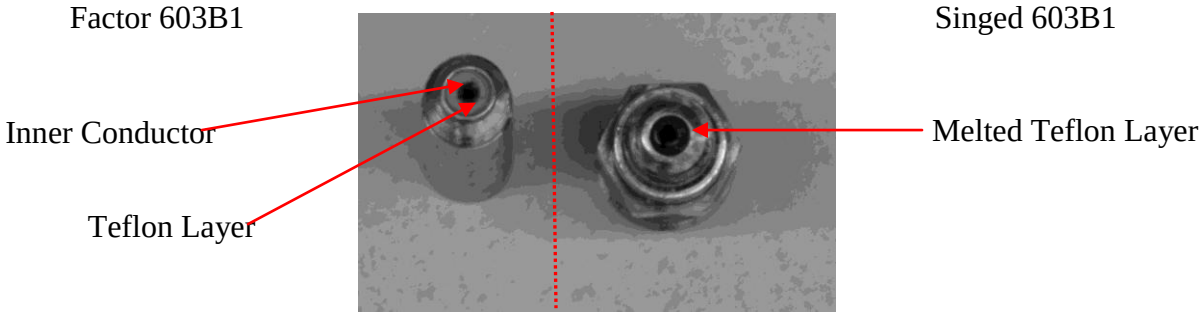

Figure 22: Side by side comparison of singed (and unusable) and factory 603B1. Typical failure of the 603B1 results in the singeing of the insulating Teflon layer and inner conductor, as noted in the picture.

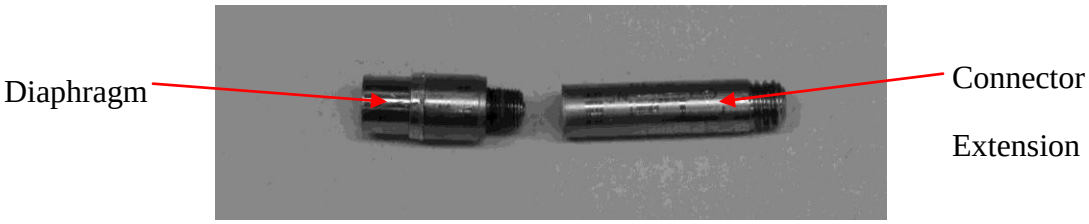

Figure 23: Kistler 603B1 sensor with connector extension removed from diaphragm. The floating nut (not shown) slides over connector extension. Typically, the connector extension is attached to the diaphragm.

2.2.2. Fluid Sound Speed

The fluid's sound speed was measured by the pulse echo time of an ultrasonic signal, which could be measured to a high precision (ppm) and did not require the extra error introduced by variations in the path length. The signal was created by exciting the impulse response of a 10 MHz contact transducer (Panametrics, M1054) with a high voltage spike created by a pulser/receiver unit (PR) (Panametrics model 5800). The RF output of the PR was recorded on a Tektronix TDS 1012 scope. The PR was used in pulse/echo mode so the reflected signals could be detected by the same transducer. The time of flight was measured from the time difference between the envelope of the first and second set of reflections and the sound speed could be computed assuming the path length was the nominal diameter of the fluid-filled resonator (20.32cm, 8"). Variations in the path length due to stretching of the resonator shell were determined to be negligible (Ohno et al. 2001). This procedure was automated using a Matlab script.

2.2.3. Cavitation Diagnostics

2.2.3.1. Shock Wave Detection

Typical cavitation events created in this system were capable of producing high amplitude shock waves and light emission (Gaitan et al. 2010, Tessien et al. 2001). These shock waves were used to indicate the onset of inertial cavitation. Cavitation was detected using a passive cavitation detection scheme, as shown in Figure 24. Shock waves were detected with an ultrasonic delay line element (f_C = 15 MHz, V205, Olympus NDT Inc., Waltham, MA), affixed to the outer wall of the resonator with 5-minute epoxy. The element's signal was high-pass filtered (f_c = 1 MHz) and amplified (+10 dB) using a PR unit (5072PR, Olympus NDT Inc.).

The amplitude of the shocks would typically increase with the static pressure. Due to this variation, the trigger threshold level was empirically determined before each data run. The resulting trigger level was typically set between 150-400 mV.

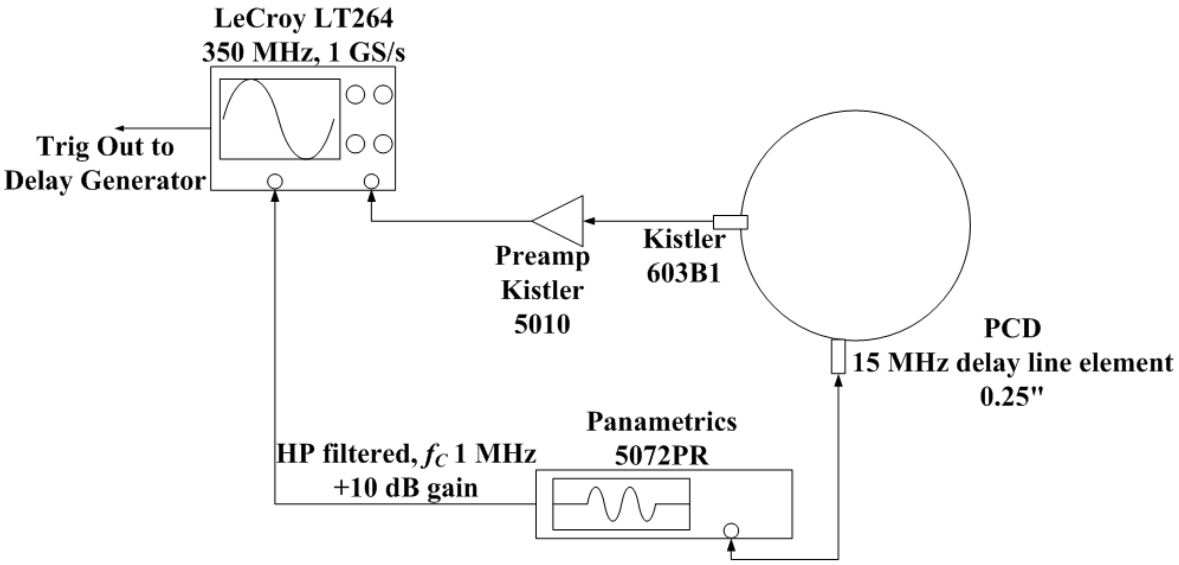

Figure 24: Cavitation detection scheme, along with incorporation of acoustic pressure sensor.

A second delay line element of the same make and model was attached to the sphere to record the collapse "strength" of the shock waves. The signal of this element was recorded on a digital phosphor scope (DPO 7054, Tektronix), and analysis was done offline. The signal was processed by digitally band-pass filtering the signal from 1-25 MHz. This ensured that the acoustic drive signal was eliminated and the resulting signal had enough bandwidth to compliment the element (the upper end of the full width, half max response of the V205 is 23 MHz). The fourth order digital filter was created in Matlab, used Butterworth topology, and had zero phase distortion (i.e. was acausal). A typical post-processing waveform is shown in Figure 25.

The collapse strength of an event was considered using three parameters: the amplitude of the first shock wave, the amplitude of the largest shock wave, and the energy emitted for the entire event. The event energy was calculated in terms of the electrical energy of the signal by integrating the power of the signal (V_{sensor}^2/R) over time. For reference, the sensor was terminated into 1 MΩ. The full angular distribution of the event energy $E_{4\pi}$ was accounted for based on the surface area of the sensor and its distance from the center of the sphere:

$$E_{4\pi} = \frac{\int V_{sensor}^2 dt}{R} \frac{4\pi r_1^2}{\pi r_2^2} \tag{49}$$

where V_{sensor} is the sensor signal, r_1 is the distance of the sensor from the center of the resonator, and r_2 is the radius of the sensor.

The band-pass filtered waveforms were further processed to determine the first and largest shocks. The envelope of the filtered signal was calculated using the Hilbert transform and a peak finding algorithm was used to detect the location and amplitude of the shock waves in the resulting waveform. For the band-passed signal, the amplitude of the first shock was usually within the noise limit of the peak detection algorithm. When the signal was more finely band-passed (2-4 MHz), the noise floor was significantly reduced, and the temporal location of the first shock was clearly visible.

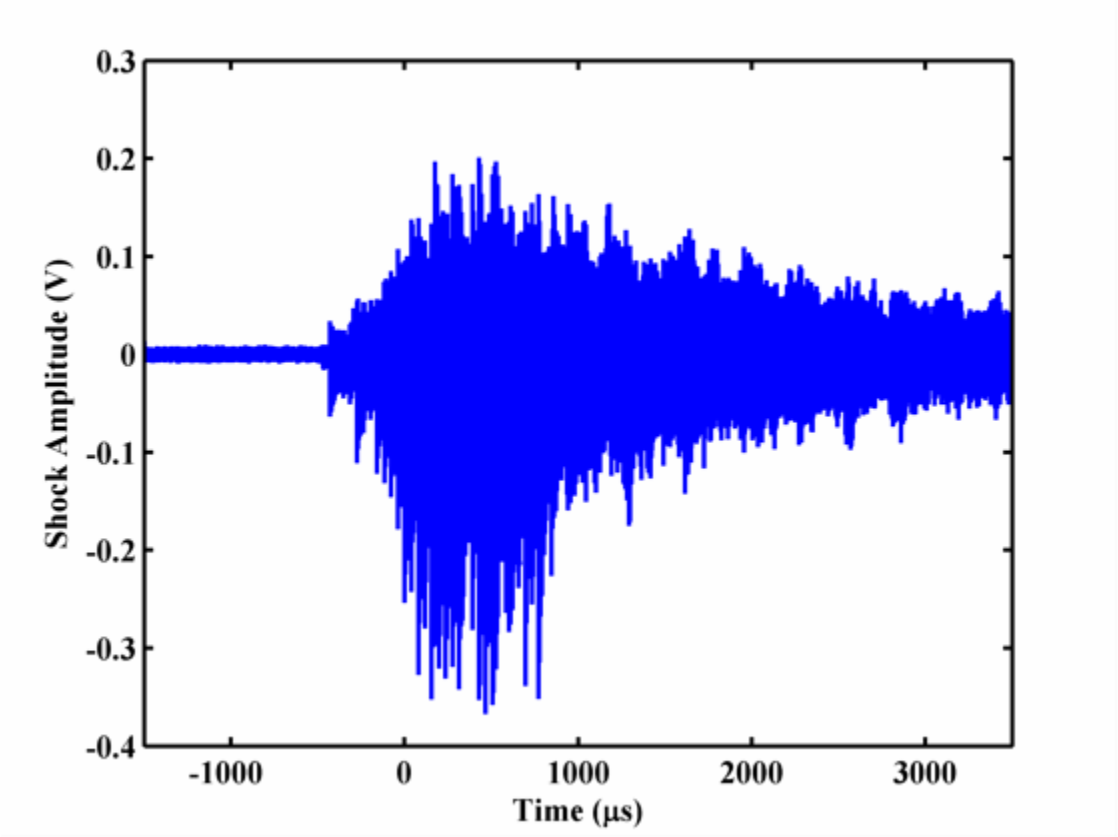

Figure 25: Typical shock waveform for a cavitation event after band pass filtering 1-25 MHz.

2.2.3.2. Light Detection

Light emissions from the cavitation events were detected using photomultiplier tubes (PMT). The R928 (Hamamatsu Corporation, Bridgewater, NJ) tube was chosen due to its high gain, low noise, wide spectral response, and ready availability. The R928 is a side-on type tube with a 192 mm^2 light sensitive area. The tube uses a multialkali photocathode which has a wide spectral response (185-900 nm) and peak quantum efficiency of 25% at 260 nm. The dynodes of the tube need to be biased in order to trigger the electron cascade from the photoelectron. Two of the tubes were incorporated in photomultiplier tube modules (H7732-10 and H957-08, Hamamatsu Corporation, Bridgewater, NJ) which can internally generate the high voltages using a

Cockcroft-Walton circuit. The gain of the tube can be modified by adjusting a reference voltage produced by the module via a 10 kΩ potentiometer. The reference voltage was typically set to 1000 mV and 0 mV for the H7732 and H957, respectively, which correspond to manufacturer tube gains (electrons emitted from the anode per incident photon) of 10^7 and 5.5 x 10^6. The bias voltage on the H957 was limited to -900V, and hence the gain was limited by roughly a factor of 2. The third tube was housed in an Oriel side-on PMT housing (model 7069, Newport Electronics, Stratford, CT), which required a high voltage to bias the tube. This voltage was supplied with a high precision, dual polarity high voltage supply (PS350, Stanford Research Systems, Sunnyvale, CA). The nominal applied voltage was set at -1000 V, which the manufacturer's specifies will set the gain to 10^7.

The tubes were attached to the sphere with custom mounts. Since the spectrum of sonoluminescence is broad-band from 200-800 nm (Hiller et al. 1992), the tubes were filtered for specific portions of the visible spectrum using dielectric edge filters (Thorlabs, Newton, NJ): the H7732 was short pass filtered below 450 nm, the H957 was band pass filtered from 450-650 nm (composed of a 450 nm long pass and 650 nm short pass), and the Oriel was long pass filtered above 650 nm. The signals of each of the PMTs were recorded using a digital phosphor oscilloscope (DPO 7054, Tektronix, Inc., Beaverton, OR), which was triggered by a digital delay generator (the data collection set-up will be discussed in more detail in section 2.4).

An example waveform recorded by the PMT from a cavitation event is shown in Figure 26. The cavitation events emit light for approximately 25 acoustic cycles (~1 ms). Each of the individual flashes was between 1-500 ns duration. A peak finding algorithm and coincidence scheme were used to find the temporal position of each flash.

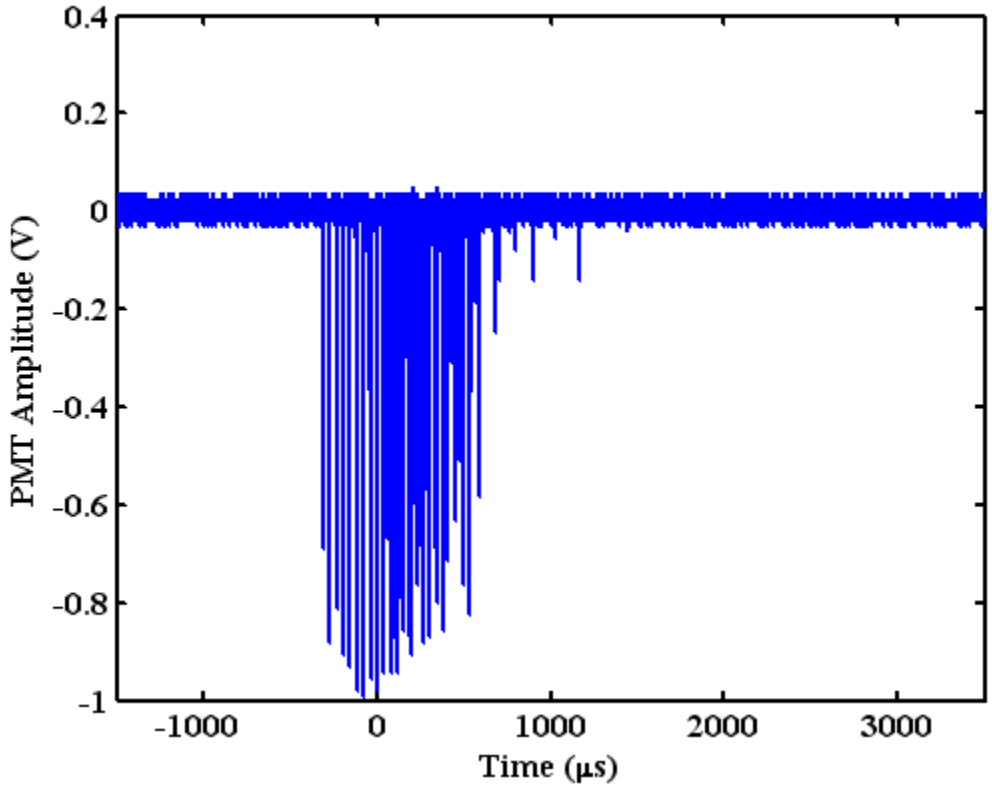

Figure 26: Typical light emission produced by cavitation event as recorded by PMT. The static pressure in the fluid was 100 bar. The tube gain is set at 10^7.

2.2.3.3. Calculation of Incident Number of Photons

PMTs detect light via the photoelectric effect: an incident photon displaces a photoelectron from the photocathode, which starts the electron cascade process. The total number of electrons generated in the cascade depends on the gain of the tube, which is set by the voltages applied to the dynodes. Once the gain is known, the signal from the PMT anode can be used to calculate the number of incident photoelectrons $N_{incident}$:

$$N_{incident} = \frac{\int V_{anode} dt}{(50\Omega)(e)(G)} \quad (50)$$

where 50Ω is the termination impedance of the anode, e = 1.602 x 10^{-19} C is the charge of a single electron, and G is the gain of the tube.

2.2.3.4. PMT Calibration

To check the validity of Equation (50) the PMTs were compared against a PMT with a known single photon peak (signal response to 1 photon). The RCA 8854 tube (Burble Industries, Inc., Lancaster, PA) has a 5" diameter, bialkali photocathode, a 14 stage base, and high gain gallium phosphide dynodes. At typical voltages applied to the base (up to 3 kV) the gain at the first dynode was large enough that the single photon signal could be resolved. The single photon peak was measured by applying enough current to the LED that the tube cascade (i.e. visible signal from the anode) efficiency was roughly 20%, or every fifth excitation of the LED from the pulser produces a visible signal from the PMT. 10^4 waveforms were triggered by the pulser (with both cascade events from the single photon peak and waveforms with no distinguishing features) and digitally stored. The single photon peak could be determined from a histogram of the integrated waveforms (boxcar integration with a 50 ns window).

Once the single photon peak was determined, the RCA tube was exposed to increasing light levels of a blue (468 nm) LED with a digital pulser (DG535 Stanford Research Systems, Sunnyvale, CA). The level of light was adjusted by the voltage amplitude (and therefore current) output on the digital pulser. The PRF of the pulse was 1 kHz, and the pulse width was 11 ns. The number of photons at each voltage level was calculated as the ratio of the time integral of the

RCA tube signal and the single photon peak of the RCA tube. The quantum efficiency (*QE*) of the RCA tube, 16.19% at 468 nm, was also taken into account.

Each of the un-calibrated tubes was then illuminated with the LED at the same settings (sans single photon amplitude), and the signals were digitally recorded (10^4 at each setting). The results are plotted in Figure 27. Two distinct regions appear in Figure 27: a linear region up to nearly 100 photons, and a non-linear region for the remaining two points. It was subsequently determined that the linearity of the RCA tube could not be guaranteed beyond 100 photons, thus the data in the non-linear regime were neglected.

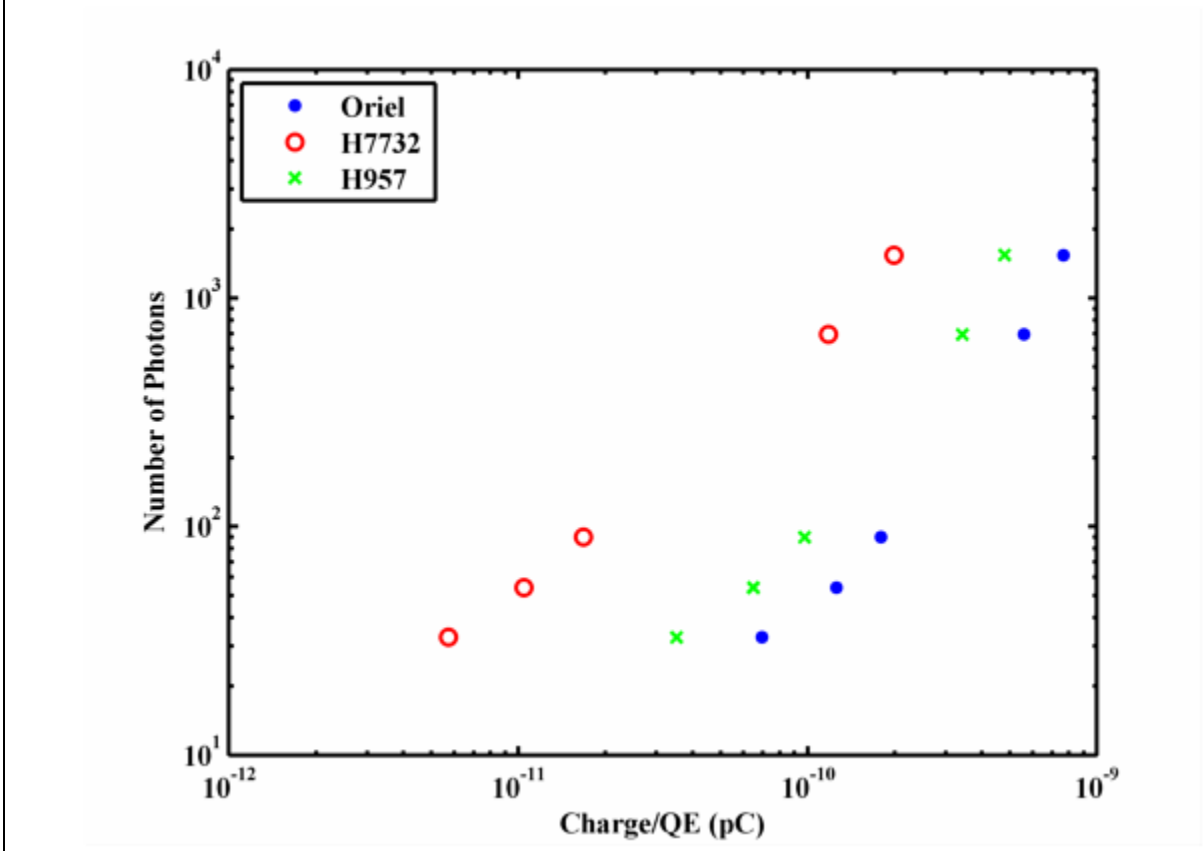

Figure 27: Number of photons as a function of charge from PMT anode (divided by tube *QE*) for the three un-calibrated tubes.

The gain of the un-calibrated tubes was calculated according to

$$G = \frac{\int V_{anode} dt}{(50\Omega)(e)(QE)(N)} \quad (51)$$

where *N* is the number of photons as measured by the RCA tube. The quantum efficiency of the R928 tube is 18.47% at 468 nm. The charge specified in Figure 27 is the ratio of the voltage integral and the anode termination impedance of 50 Ω. The gains calculated from the linear data in Figure 27 are listed in Table 5. The Oriel housing tube and H957 gains calculated using Equation (51) were within the manufacturer's specifications. The H7732 module, however, is roughly an order of magnitude smaller than the manufacturer's specifications.

Tube	**Gain**	**Standard Deviation**	**Manufacturer Specified Gain**	**Calculated Maximum Linearity Count**	**Measured Maximum Linearity Count**
Oriel	1.34×10^7	1.06×10^6	1×10^7	3.10×10^4	3.80×10^3
H7732	1.15×10^6	5.90×10^4	1×10^7	1.78×10^5	2.42×10^4
H957	6.99×10^6	4.29×10^5	4.57×10^6	1.56×10^5	3.24×10^3

Table 5: Gain for un-calibrated tubes, as calculated using Equation (51) and the linear data in Figure 27. The measured max linear count is at 468nm.

Just as for the response of the RCA tube to the two largest light levels in Figure 27, all PMTs will experience a non-linear regime whereby the charge from the anode is no longer linear to the number of photoelectrons. For a voltage divider base, the maximum linear output is limited to a

fraction of the divider current. To mitigate this problem, decoupling capacitors can be connected to the last few stages of the base. If the pulse width of incident light is sufficiently short so that the duty cycle is small, this method makes it possible to derive an output current up to the saturation level. Consequently, a high peak output current more than several thousand times as large as the divider current can be attained (Hamamatsu Corporation 2006). Hence, the linearity is dependent on the amount of charge the decoupling capacitors can hold. The Hamamatsu Corporation guarantees linearity of their tubes up to 1/100 of the maximum charge held by the coupling capacitor, $Q = CV/100$, where Q is the charge, C is the capacitance (10 nF for all three tubes), and V is the voltage drop between the last dynode and the anode (Palmentieri 2011). V was calculated using the gains calculated using Equation (51) and the manufacturer's specifications for gain as a function of voltage applied to the base. Hence, the maximum number of incident photons N in which the tube will respond in a linear fashion for a gain G can be calculated as

$$N_{MAX} = \frac{Q}{(e)(QE)(G)} \tag{52}$$

The QE listed in Table 6 was used to calculate the values for N_{MAX} displayed in Table 5. In practice, the linear range calculated using Equation (52) was larger than the actual saturation limit. The lower bound for tube non-linearity was tested in a similar manner for the data collected in Figure 27: each tube was flashed with a blue LED (468 nm) at increasing current levels (i.e. more light) using the same digital pulser. Next, a neutral density filter (NDF) with optical density 1 (10% transmission) was placed between the PMT and the LED [the specifications of the NDF are described in more detail in the next paragraph], and the measurement was repeated at the same light intensities. The ratio of these two measurements is

shown in Figure 28. At low light levels, the calculated transmission drops to 10% after implementing the NDFs. At larger light levels, the tube becomes non-linear and the number of photons estimated without the NDF is underestimated, shifting the calculated transmission to higher values. Since all three PMTs are subject to the same frequency of light source, the quantum efficiency should be the same and the non-linearity should depend only on the gain of the tube, as indicated by Equation (52). This is reflected in Figure 28 as the high gain tubes, the Oriel housing and H957 module, shift to higher transmission values before the H7732 module. The Oriel housing and H957 also appear to go non-linear at roughly the same intensity, which is consistent with the similar gains for the two tubes calculated for Table 5. Each of the data sets shown in Figure 28 were fit to a square root function, and the tube linearity threshold was defined as when the transmission of the lower bound 95% confidence interval of the fit was greater than 10%. These measured maximum linearity counts are displayed in the last column of Table 5.

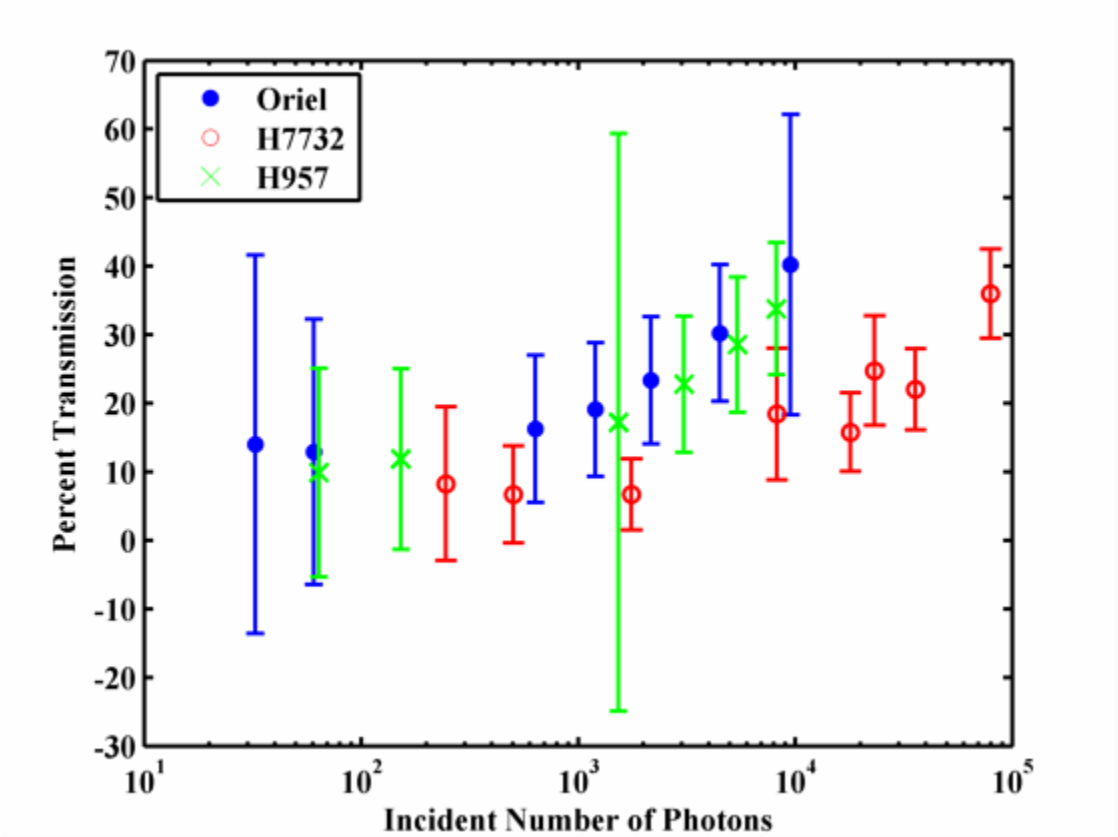

Figure 28: Calculated transmission for PMT after implementation of neutral density filter (optical density 1.0).

In general, as the static pressure increased, the number of photons produced by the events increased. Neutral density filters (NDF) were placed in series with the color filters when the number of incident red photons for the largest flashes reached 30,000. The NDFs (p/n NDUV10B, Thorlabs, Newton, NJ) were an unmounted, reflective Borosilicate Crown glass substrate with an Inconel™ coating, which gives it a flat spectral response from the UV to the mid IR. The optical density was specified to be 1.0 (10% transmission) and the measured transmission (Lambda 18 Spectrometer, Perkin Elmer, Waltham, MA) shown in Figure 29 agrees with the manufacturer's specifications. Although the spectrum in Figure 29 spans the entire

active region of the R928 (185-900nm), the manufacturer only guarantees 10% transmission down to 200 nm.

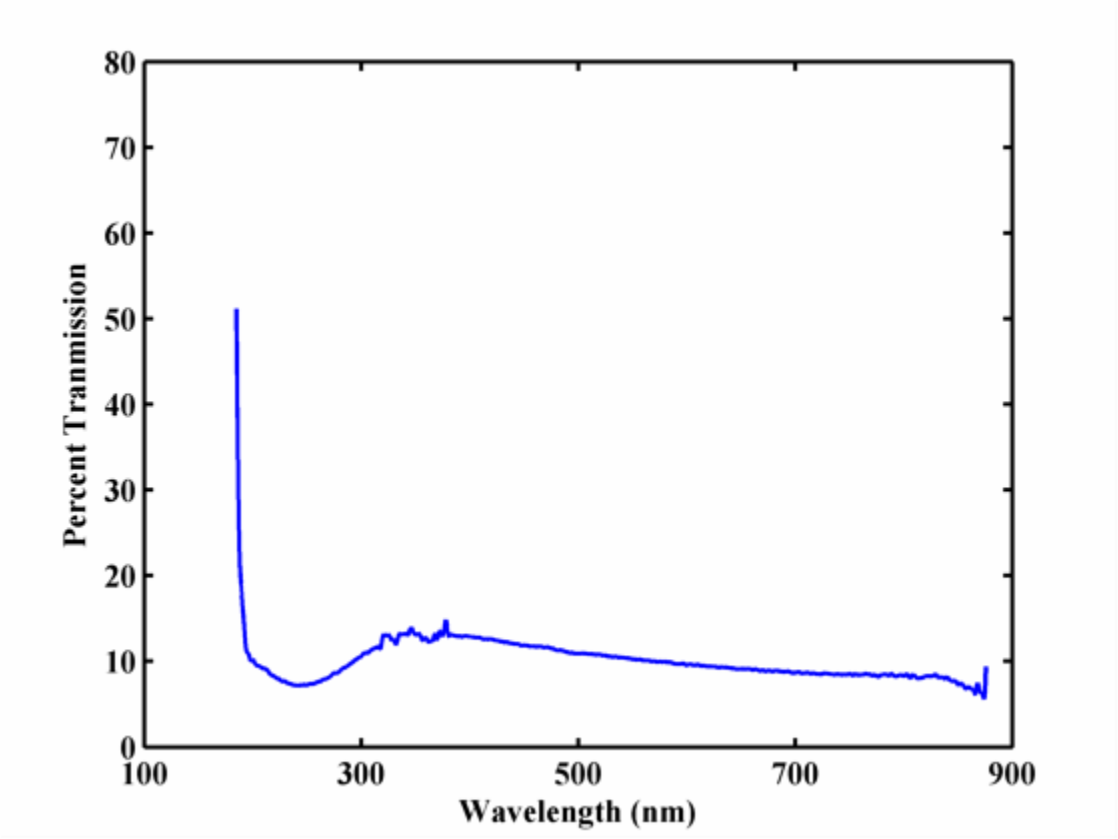

Figure 29: Percent transmission of NDF measured with Lambda 18 Spectrometer (Perkin Elmer, Waltham, MA) .

In order to calculate the number of photons emitted at the source (i.e. at the bubble), the quantum efficiency (*QE*) of the tube, absorption of light across the path length of the water, transmission loss from the NDF, and solid angle of the photocathode need to be accounted for. The light emission is assumed to be spherically symmetric, such that the photocathode of each PMT is uniformly illuminated. Each PMT has a surface area of 192 mm^2 and located 11 cm from

the center of the sphere. The number of photons over the full angular distribution can be calculated as

$$N_{4\pi} = N_{PMT} \frac{4\pi(11cm)^2}{1.92cm^2} \tag{53}$$

where N_{PMT} is the measured number of photons incident on the photocathode.

The quantum efficiency, absorption, and (to a lesser degree) transmission loss through the NDF vary with wavelength. Since the light emissions from the events are broadband (Hiller, Gaitan, et al. 2007), the optimal *QE,* absorption, and transmission over the bandwidth of each PMT were calculated using a weighted average. The wavelength dependent weighting function was chosen to be $F(\lambda)/\alpha(\lambda)$, where $\alpha(\lambda)$ is the absorption of electromagnetic waves in water (Hale and Querry 1973), and $F(\lambda)$ is the transmission spectrum of the color filter. The weighted averaged for these quantities are shown in Table 6. In addition, the measured $F(\lambda)$ (Lambda 18 Spectrometer, Perkin Elmer, Waltham, MA) is plotted for each of the color filters in Figure 30 - Figure 32. For the yellow and red bands (450-650nm and 650-900 nm, respectively), $F(\lambda)$ is well behaved and flat over the desired region. The blue band (185-450nm), however, is limited to long pass at ~350nm. In addition, several resonant peaks, presumably due to the soda lime substrate, are present above 650 nm.

Wavelength (nm)	***QE* (%)**	**Absorption, α (cm^{-1})**	**Transmission (%)**	**Effective Wavelength (nm)**
185-450	20.89	$1.3x10^{-3}$	12.23	391.88
450-650	15.81	$4.6x10^{-4}$	10.85	531.73
650-900	5 84	$1.2x10^{-2}$	8.04	713.34

Table 6: Weighted average for *QE*, absorption of electromagnetic waves through water, and percent transmission through NDF.

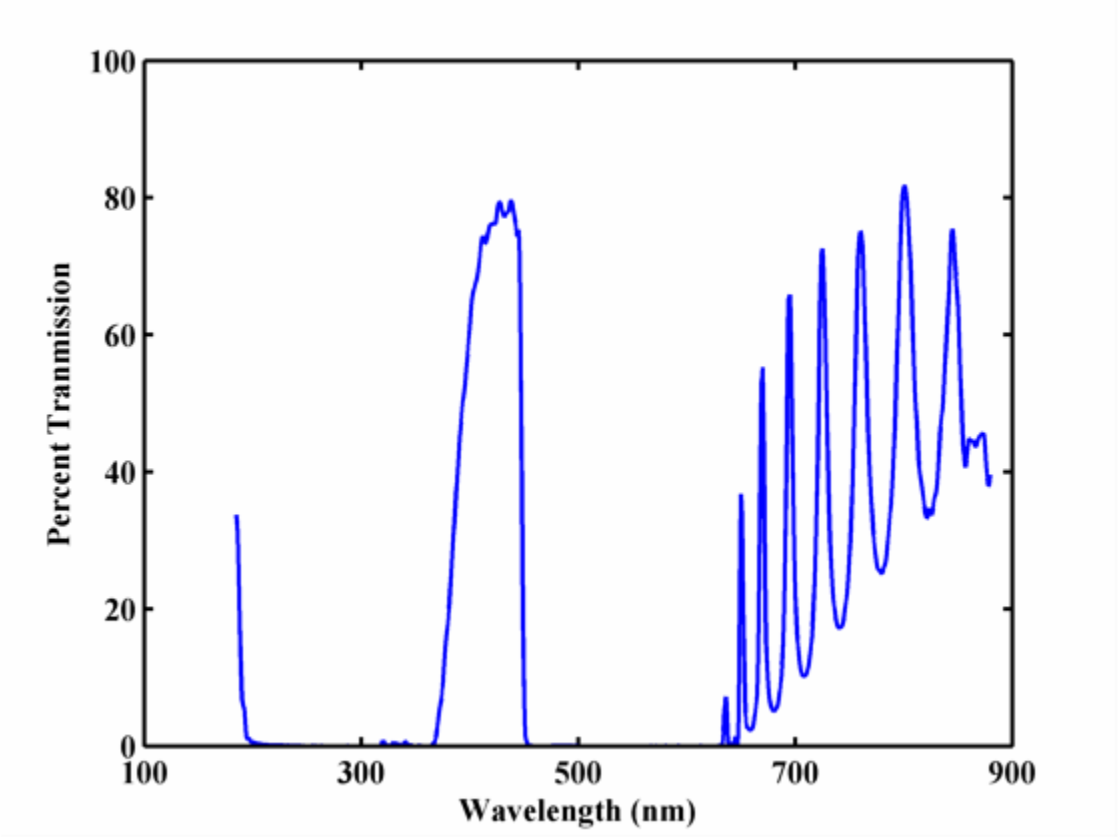

Figure 30: Spectrum of 450 nm short pass filter.

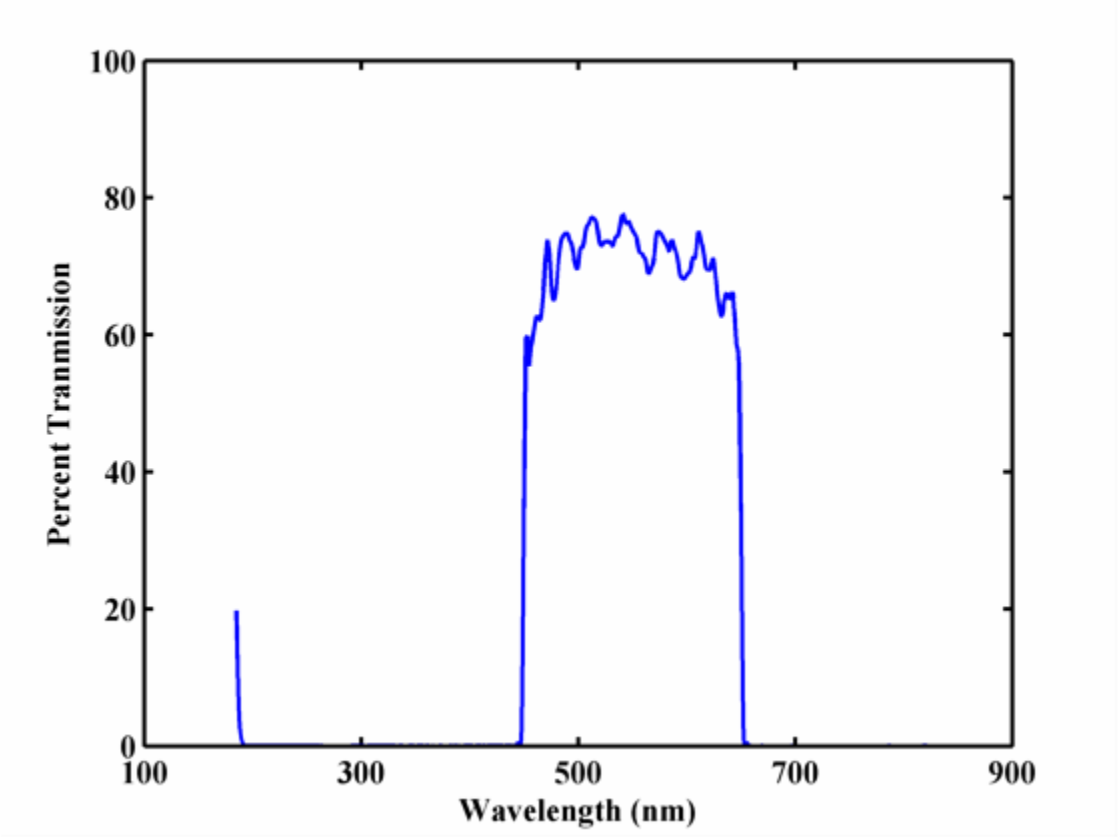

Figure 31: Spectrum of combination 450 nm long pass, 650 nm short pass filters.

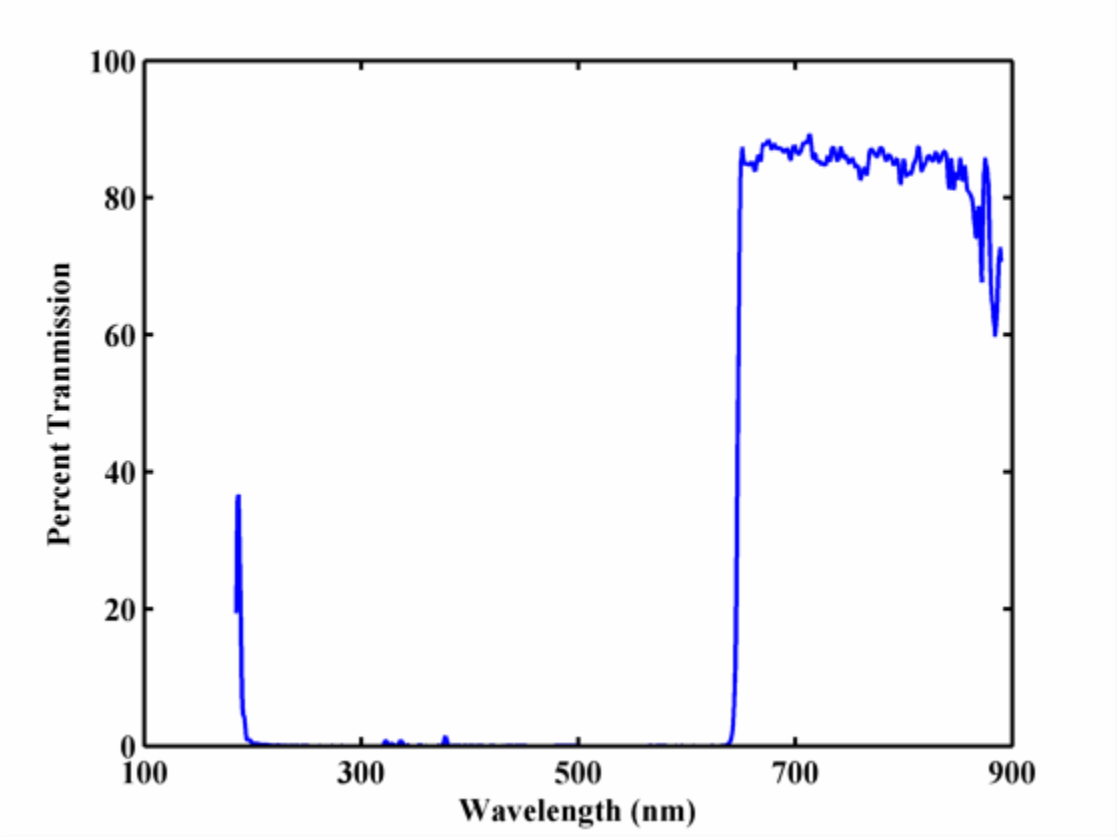

Figure 32: Spectrum of 650 nm long pass filter.

The total number of photons created by the event can be calculated once these correction factors are known:

$$N_{Total} = \frac{N_{4\pi}}{(QE)(NDF)(CF)e^{-\alpha L}} \tag{54}$$

where $N_{4\pi}$ is the number of photons over the full angular distribution as calculated in Equation (53), L is the water path length (10.16cm), NDF is the percent transmission through the color filter, and CF is the percent transmission through the color filter. If the NDF were not used during a particular measurement, Equation (54) would remain unchanged with $NDF = 1$.

2.2.3.5. Coincidence Discrimination of Flashes

A peak-finding algorithm was used to detect the temporal location of flashes in the recorded PMT waveforms. Since the amplitude of the light emissions varies not only with the static pressure, but within individual events, the threshold was set low enough such that every peak was detected. This low threshold would occasionally trigger on noise associated with the "dark current" of the tube associated with thermionic emission, or random thermal emission of electrons from stages within the dynodes of the base (Burble Technologies, Inc. 1980). A coincidence scheme was developed in order to eliminate these dark current flashes. The scheme was as follows: Peak detection was done on the waveforms for each of the three tubes. Next, a gate function was created for each of the three waveforms (i.e. each tube), with value 0 except for a 50 ns width centered on the detected peak, where the gate function was 1. A detected peak was considered to be a true flash if the product of the three gate functions were not zero at the peak location. The gate function and three PMT waveforms are seen in Figure 33.

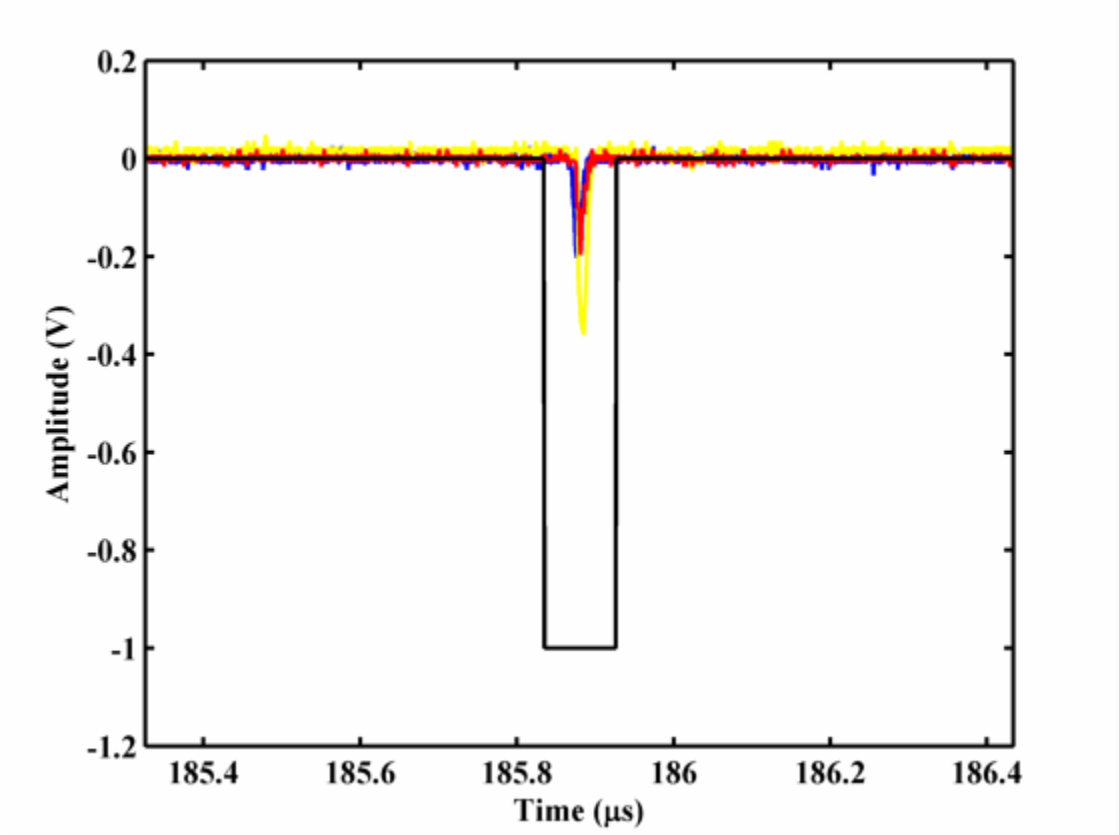

Figure 33: Gate function (solid black line) along with waveform recorded from the three PMTs.

2.2.4. Strength of Collapse

As previously stated, the cavitation events are transient in nature, typically lasting 25 acoustic cycles (~1 ms total duration). Three parameters were used to specify the "strength" of the collapse in terms of light emissions: the total number of photons for the first detected flash, the largest detected flash and total event. These categories were further subdivided by the three portions of the optical spectrum covered by the PMTs (185-450 nm, 450-650 nm, and 650-900 nm), and the relative shift of these three wavelength bins was monitored over the static pressure range.

2.3. Acoustic Driving Electronics

2.3.1. Transducers and Impedance Matching Network

Transducers were used to excite the resonator. In general, a transducer is used to convert one form of energy to another. In these measurements, the driving transducers convert electrical energy into mechanical energy. Any material that accumulates charge in response to mechanical strain can be used as an acoustical transducer. Typical materials include ceramics, crystals, and treated polymers. The transducers used for these experiments were tonpilz type (provided by IDI) composed of two ceramic elements sandwiched between a horn and a rear mass. The driver attached to the resonator via a female screw hole (1/2" machine threads) at the tip of the horn. Complimentary female screw holes are placed symmetrically on the resonator. To ensure the driver was well coupled to the resonator, the driver was tightened onto the sphere using a spanner wrench.

It was empirically determined that four drivers in parallel would satisfy the electrical requirements necessary for cavitation at a static pressure of 300 bar. Additional drivers degraded the *Q* of the acoustic mode. When fewer drivers were used, the impedance mismatch between the amplifier and the reactive load (the drivers appear as capacitors far from their intrinsic resonances) resulted in the majority of the applied power being reflected. Most of the reactivity was solved using a matching network.

The impedance of the unloaded drivers was measured using an impedance analyzer (HP 4192a, Agilent Technologies, Santa Clara, CA). The results are shown in Figure 34. The unclamped capacitance as measured with an LCR meter (875B, BK Precision, Yorba Linda, CA) of each of the drivers is listed in Table 7. Over the frequency range of interest (25-27 kHz), there are no intrinsic resonances (such as near 30 kHz), and the impedance decays with

frequency as a simple capacitor. When the driver is attached to the resonator, the impedance will be modified by the presence of the mechanical modes of the composite system (resonator and driver). The impedance near the (0,6) acoustic mode, as shown in Figure 35, has a distinct resonance/anti-resonance that was not present in the free drivers (Figure 34). The lumped driver/resonator system can be modeled as an equivalent circuit, as shown in Figure 36. The driver is assumed to be far from any intrinsic resonance and is represented by a single capacitor, C_0. The capacitor is in parallel with a series RLC circuit which represents an acoustic mode. To properly model the system, additional parallel branches should be added to account for resonances of both the transducer and the resonator. These contributions can be neglected at frequencies far from these parallel branches' equivalent RLC resonance.

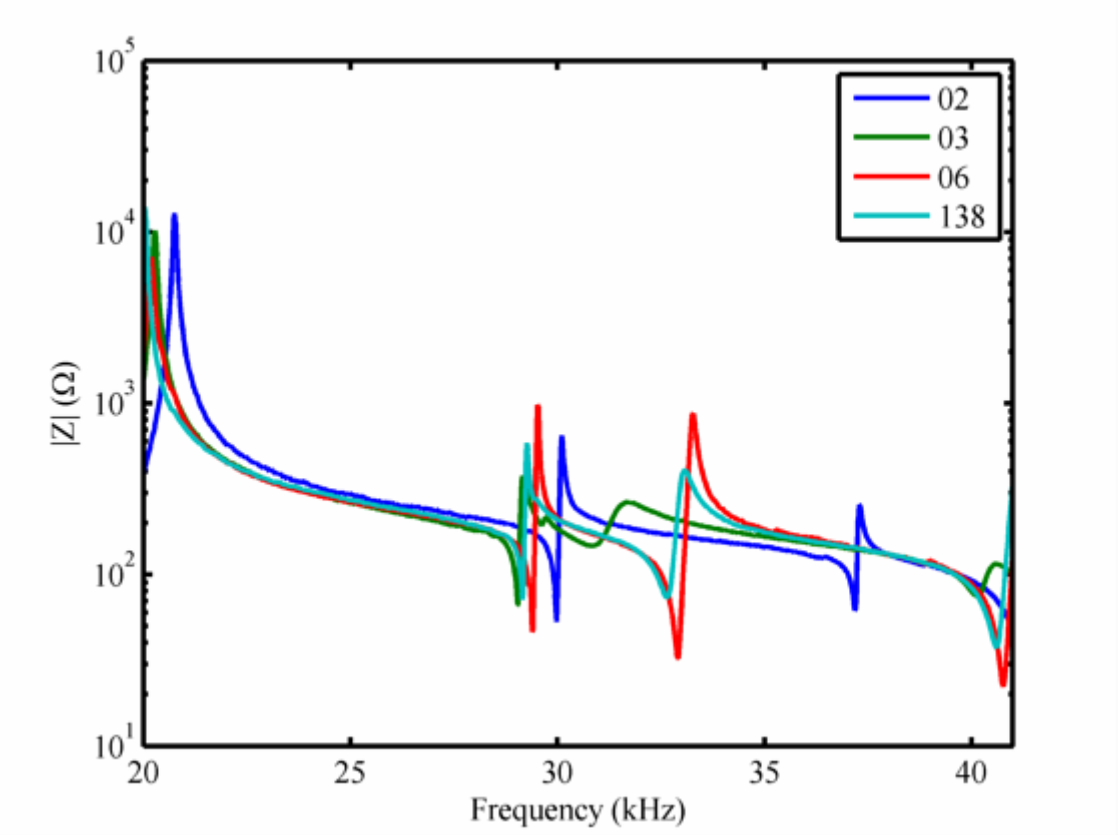

Figure 34: Unloaded impedance of drivers used to excite the resonator. Note the log scale on the ordinate. The legend denotes the labeling scheme used to specify the drivers.

Driver Reference Number	Capacitance
02	7.30
03	7.23
06	7.23
138	7.20

Table 7: Driver identification and capacitance.

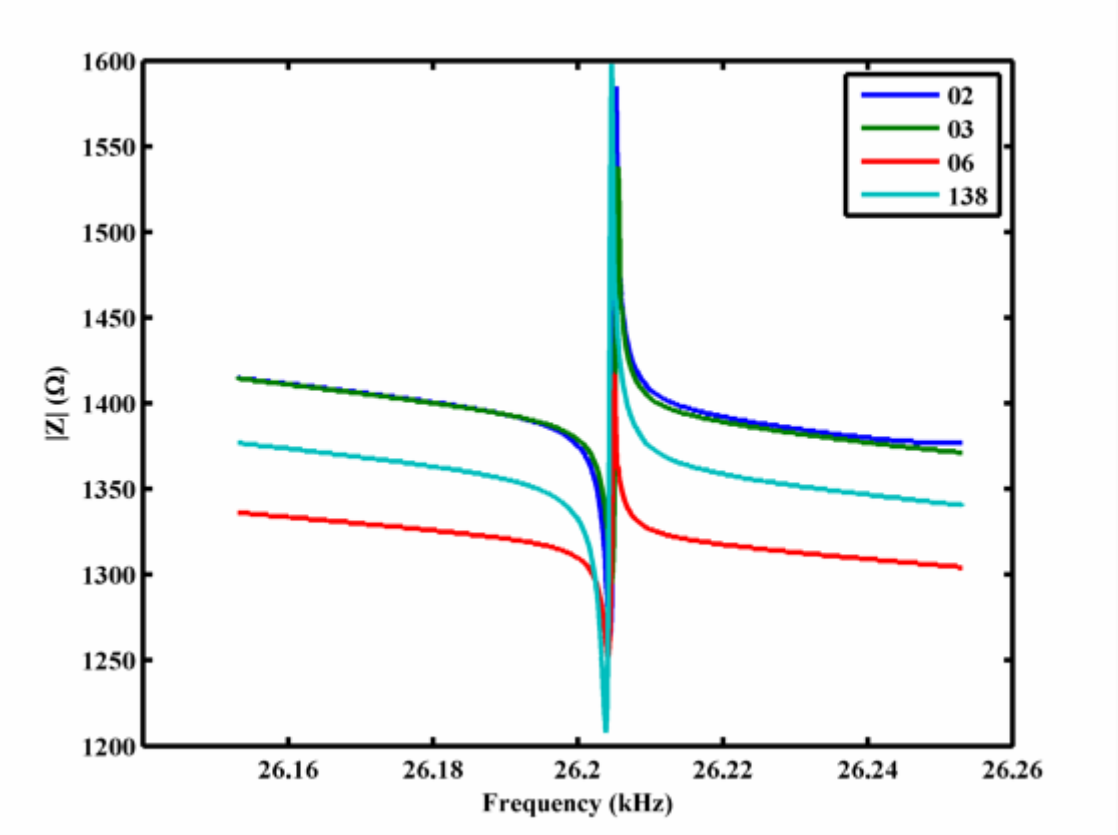

Figure 35: Impedance of drivers near (0,6) acoustic mode. The fluid is at room temperature, and the static pressure of the fluid in the resonator is 250 bar. The presence of the acoustic mode modifies the impedance as the structure seen above is absent in the free driver impedance (Figure 34).

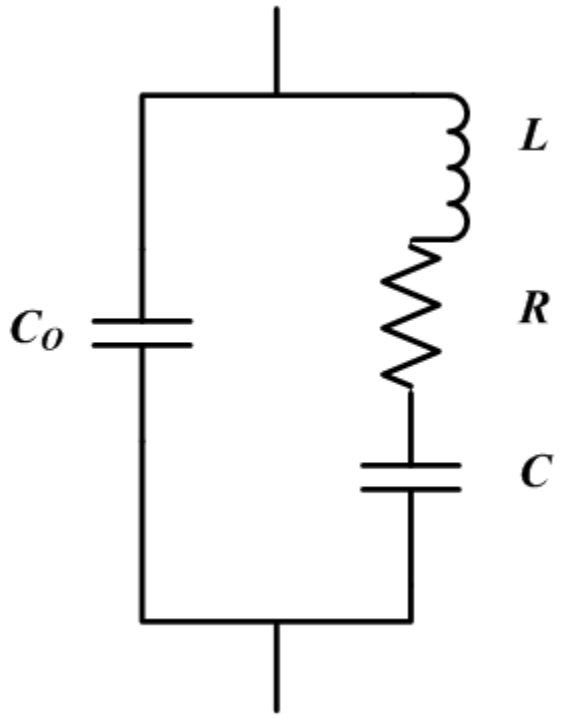

Figure 36: Electrical model of driver on resonator. The driver is assumed to be far from any intrinsic resonance and is modeled as a capacitor (C_0). The series RLC branch represents the acoustic mode, and neglects the presents of additional acoustic modes.

The equivalent impedance of the circuit shown in Figure 36 can be written

$$Z_{equiv} = \frac{R + j\left[\left(1 - \omega^2 LC_0 + \frac{C_0}{C}\right)\left(\omega L - \frac{1}{\omega C}\right) - \omega C_0 R^2\right]}{\left(1 - \omega^2 LC_0 + \frac{C_0}{C}\right)^2 + (\omega C_0 R)^2} \quad (55)$$

The data from Figure 35 were fit to Equation (55) using an unconstrained nonlinear optimization routine to solve for the RLC variables. C_0 was taken from the data in Table 7 (the measured clamped capacitance of the drivers did not change significantly from the unclamped values). Representative values for the RLC data are shown in Table 8.

R	3500 kΩ
L	940 H
C	0.04 pF

Table 8: Representative values for RLC values of the equivalent circuit shown in Figure 36. The values are calculated by fitting Equation (55) to the data shown in Figure 35, assuming the clamped capacitance of the driver is given by the values in Table 7. The resonant frequency is 26.205 kHz, and the static pressure in the fluid is 250 bar.

At the acoustic mode, the impedance is dominated by the reactive capacitance of the driver. This reactive impedance became problematic when attempting to drive at high amplitudes, either due to reaching the rail voltage of the amplifier or reaching the power amplifier's tolerance of reflected power (the ENI 1140LA will handle up to 400 W reflected power before overloading). To compensate for the load mismatch, voltage step up transformers (turn ratio 1/9.64, CMI-4627 0938, Corona Magnetics, Inc, Corona, CA) were used as a form of impedance matching. A schematic of the transformers used is shown in Figure 37. Transformers alter voltage/current relations in a circuit based on the relative number of windings on the primary and secondary coils:

$$\frac{Z_p}{Z_s} = \left(\frac{N_p}{N_s}\right)^2 \tag{56}$$

where *N* is the number of windings, *Z* is the impedance, the subscript *p* refers to the primary coil, and *s* refers to the secondary coil. Since the mechanical Q of the resonator is so large, the

inherently broadband nature of transformers is an advantage over narrow band techniques, such as resonant circuits.

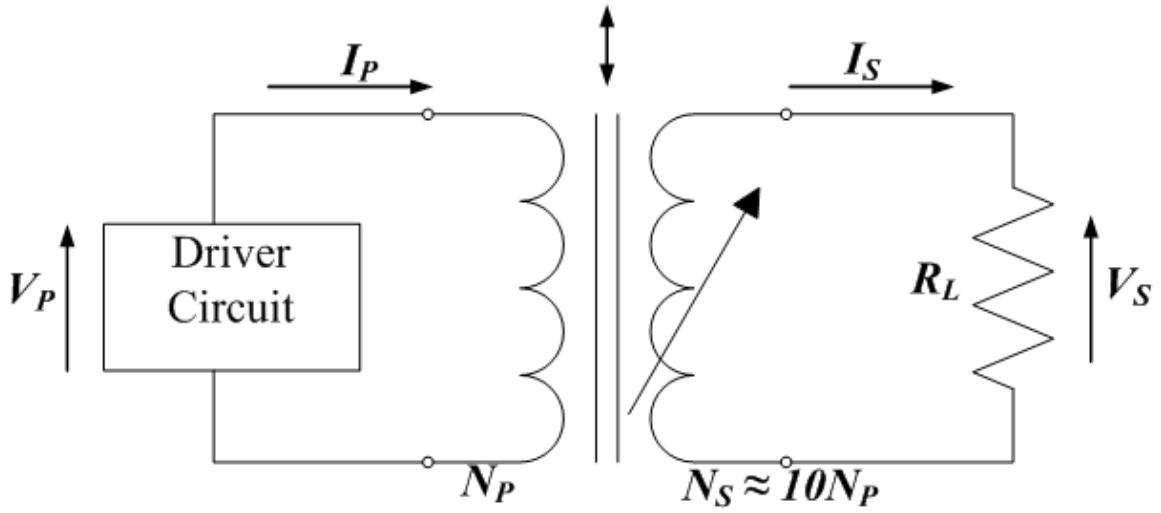

Figure 37: Schematic of transformers used. Each transformer was equipped with an adjustable ferrite core. The number of windings on the secondary coil was also adjustable.

The transformers were equipped with an adjustable ferrite core to tune the driver/transformer resonance to the acoustic resonance. The driver/transformer impedances near the (0,6) mode are seen in Figure 38.

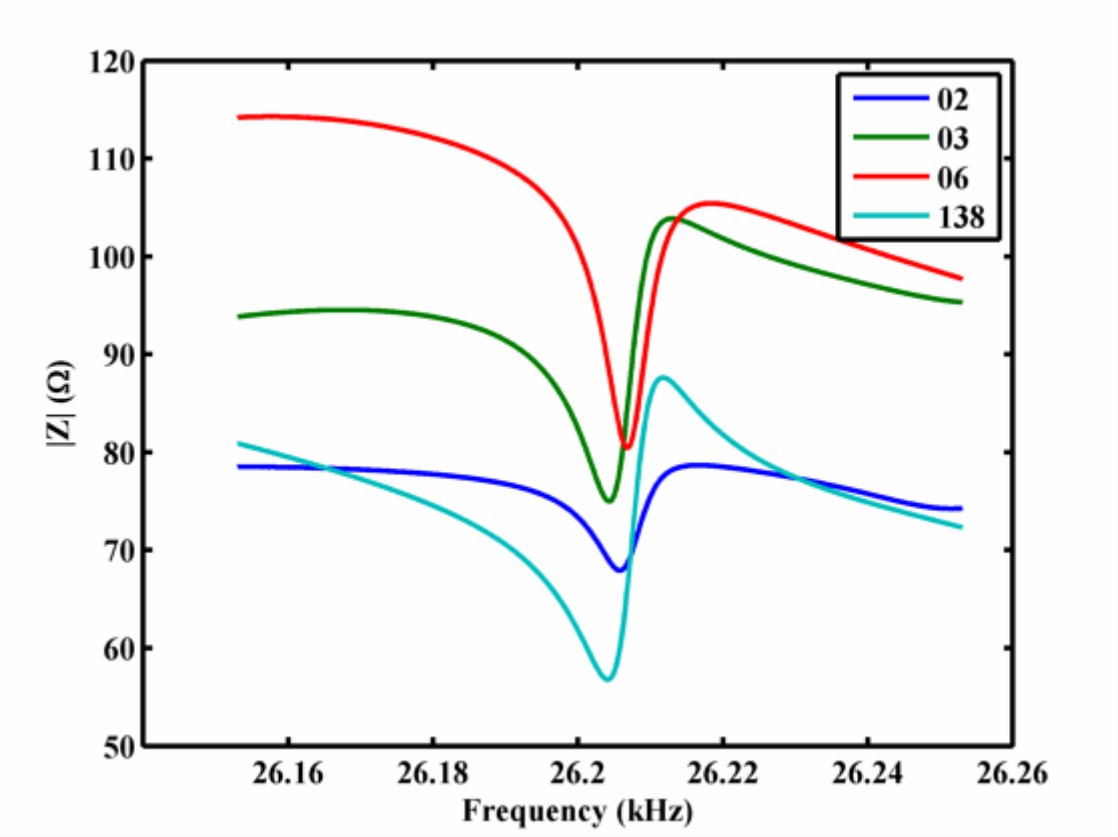

Figure 38: Impedance of drivers in series with transformers near (0,6) acoustic mode. The fluid is at room temperature, and the static pressure of the fluid in the resonator is 250 bar. The presence of the acoustic mode modifies the impedance as the structure seen above is absent in the free driver impedance (Figure 34).

The impedance near resonance approaches 50 Ω with the transformers, which is roughly a factor of 20 lower than without the transformers. In practice, the power to the transducers was maximized when the secondary coil was adjusted so the turn ratio was approximately 1:8. For comparison, in the case of a perfect transformer with a turn ratio of 1:8, Equation (56) shows that the impedance on the secondary coil should be a factor of 64 larger than on the primary coil. Loss mechanisms in transformers are usually the results of heating, either due to the resistive

losses from the windings or heating of the ferrite core via hysteresis, eddy losses within the core, or magnetostriction.

2.3.2. Resonance Frequency Tracking

The fluid temperature would typically drift over the course of a measurement, resulting in shifts of the sound speed and therefore resonant frequency of the system. A 1 ºC change in temperature would shift the resonant frequency by approximately 50 Hz. Since the Q of the system was so large, it was critical that the system be continuously driven at the resonance. This was accomplished by the use of a phase locked loop (PLL), provided by IDI.

The PLL operates by generating a DC voltage proportional to the phase shift between a reference signal and a diagnostic signal of the system. The DC voltage modulates the system via a feedback loop to keep the phase difference between the two signals constant.

The PLL, shown in Figure 39, was composed of four elements: a phase shifter, a phase detector, an integrator, and a voltage controlled oscillator (VCO). The phase detector (AD630 Analog Devices, Norwood, MA) measures the phase shift between a reference signal and a diagnostic sensor. Only the hydrophone had a one-to-one correspondence with the phase of the reference signal near resonance, and was therefore chosen to be the aforementioned diagnostic sensor. The signal from the hydrophone was passed through a narrow bandwidth filter (25-27 kHz) before being input to the phase detector. The reference signal was generated internally by the phase shifter. When the system was at resonance, the phase shifter was manually adjusted so the reference input signal (the sync out from function generator, 33250A, Agilent Technologies, Inc., Santa Clara, CA) was in phase with the sensor. When the PLL was activated, it thus acted to keep the reference and sensor signals in phase.

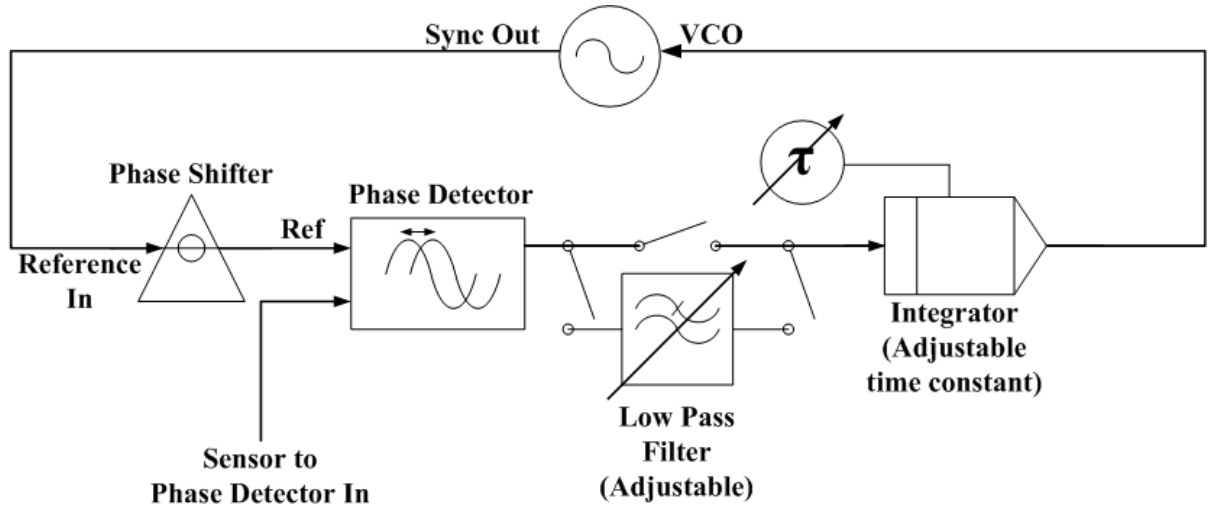

Figure 39: Schematic of the phase locked loop.

Analog phase detectors, such as the AD630, continuously generate an output wave. This causes minute ripples in minimizing the phase between the reference and sensor signal (Horowitz and Hill 1989). These ripples were smoothed out by passing the output of the phase detector through an adjustable low pass filter (f_c = 0.1-10 Hz). The low pass filter could also be bypassed. The signal from the phase detector was integrated with a single-pole, low-pass filter with adjustable time constant (0.01-100 seconds in decade steps). The filtering time was typically set at 1 s or less, so that the PLL responded quicker than the shift in resonance (Horowitz and Hill 1989).

The DC voltage output of the integrator was proportional to the shift in frequency necessary to keep the system on resonance. The PLL was designed for a function generator whose modulation input required a negative voltage to indicate a shift up in frequency (e.g. +1 V would indicate a -1 Hz shift in frequency and -1 V would indicate a +1 Hz shift in frequency). Since the 33250A required a positive voltage to shift up in frequency, it was necessary to put the output of

the integrator through a voltage inverter. The output from the voltage inverter was passed onto the VCO (33250A) to complete the feedback loop. The gain of the integrator could be controlled manually by the VCO. However, because the frequency changes were very slow, the integrator gain was not critical. The gain was typically set at 200 Hz/V. Since the maximum input voltage to the VCO was 5 V, the maximum possible frequency shift was 1 kHz.

2.3.3. Amplitude Modulation

A waveform generator that could be simultaneously frequency and amplitude modulated was not readily available. It was therefore necessary to build a custom amplitude modulation circuit. A diagram of the circuit is seen in Figure 40 and Figure 41. As shown in Figure 42, the waveform generator's output went to the amplitude modulation circuit, and the amplitude modulation's signal output went to the power amplifier.

The circuit was composed of three sub-circuits: a ramp generator, an analog multiplier, and a low-pass filter. The ramp generator produced a linear DC ramp from 0-12 V (the rail voltage of the op amp). The ramp signal was fed into one input of the analog multiplier. The other input to the multiplier was the acoustic signal from the waveform generator. The output from the analog multiplier was then low-pass filtered (f_c = 45 kHz) and sent through a buffer. The output from the buffer was the signal out from the amplitude modulation circuit. Each of the subsections of the circuit is discussed in more detail below.

2.3.3.1. Ramp Generator

The ramp generator was a first-order, low-pass filter acting as an integrator: A voltage reference IC (MAX6250 Maxim Integrated Products, Inc. Sunnyvale, CA) charged a 10 µF capacitor. The RC time constant of the integrator was chosen to be large to ensure that the ramp

was linear for the desired time (~100 seconds). The ramp rate would be the ratio of the reference voltage (from the voltage reference IC) and the RC time constant. The ramp rate was controlled by a voltage divider equipped with a variable resistor at the output of the voltage reference. By varying the variable resister, the voltage charging the capacitor could be adjusted to the desired ramp rate. The ramp voltage was fed through an op amp (LF411) which was configured as a follower with a gain of 20. A MOSFET switch (2N7000 Fairchild Semiconductor South Portland, ME) in parallel with the charging capacitor was used to discharge the capacitor and disable the ramp.

2.3.3.2. Analog Multiplier

An analog multiplier chip was used to combine the voltage ramp and the driving signal from the function generator. The chip (AD633 Analog Devices Inc, Norwood, MA) had a multiplier core with two differential inputs and a summing node. In general, the overall transfer function of the chip was

$$W = \frac{(X1 - X2)(Y1 - Y2)}{10V} + Z \tag{57}$$

where *X* and *Y* are the differential inputs and *Z* is the summing input. When the summing input was connected to one of the differential inputs, as shown in Figure 40, the transfer function could be used as an amplitude modulator:

$$W = X1\left(1 + \frac{Y1}{10V}\right) \tag{58}$$

where *X*1 was the acoustic signal from the waveform generator and *Y*1 was the signal from the voltage ramp.

2.3.3.3. Low Pass Filter

To remove any non-linearities or transients that may occur in the circuit, the signal from the analog multiplier was put through a 6th order, unity gain, low pass filter with f_c = 45 kHz. This critical frequency was chosen to be low enough that the second harmonic of the (0,6) mode was eliminated, but large enough that higher order modes, such as the (0,7) at 33 kHz and (0,8) at 40 kHz, could still be tested. Each of the op amps used in Figure 40 and Figure 41 are LF411. To accommodate arbitrary impedances the circuit might connect to, a buffer was implemented at the final stage of the circuit's output.

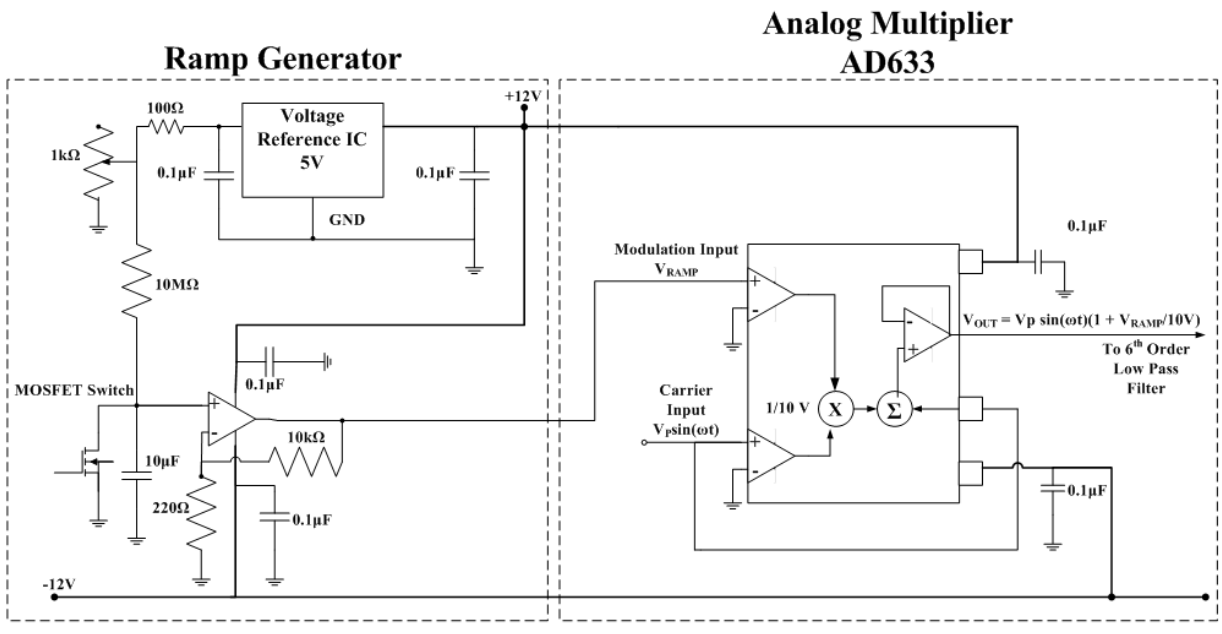

Figure 40: Schematic of ramp generator and analog multiplier in amplitude modulation circuit.

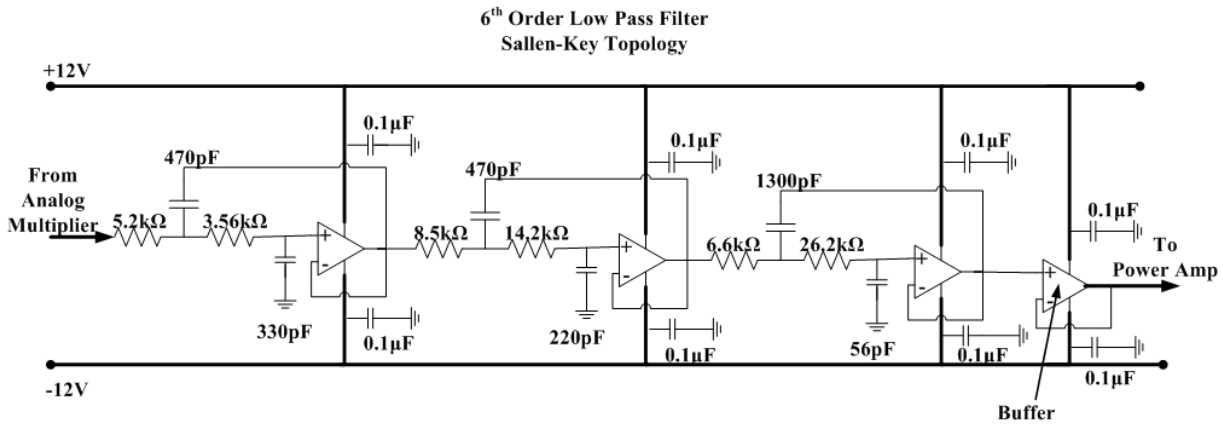

Figure 41: Schematic of low pass, unity gain, 6th order filter used in amplitude modulation circuit. The critical frequency is 45 kHz. A buffer follows the output of the filter. All op amps used were LF411.

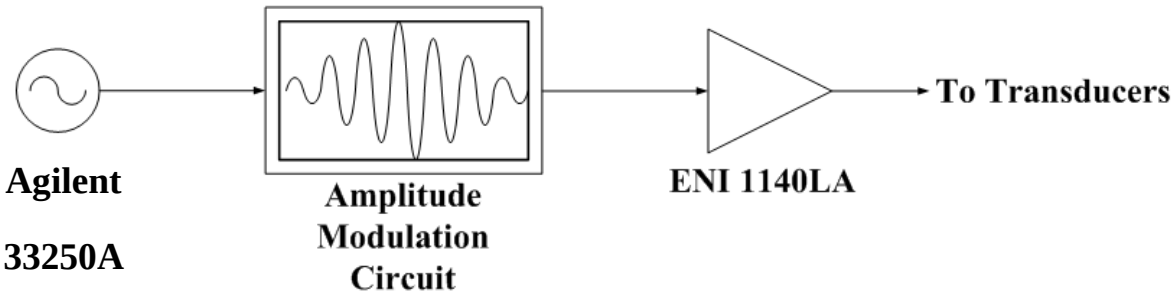

Figure 42: Position of amplitude modulation circuit within the driving electronics.

2.4. Data Collection Procedure

The elements of the experimental set-up outlined previously are combined together to finalize the data collection procedure. The procedure is similar to that used by Roy et al. (1985), whereby the system is driven continuously at resonance while increasing the acoustic pressure

until inertial cavitation occurs, and the system resets to a quiescent state. The driving electronics are outlined in Figure 43 and the cavitation detection scheme is shown in Figure 24. The procedure was as follows:

1. Liquid preparation: The fluid was circulated through the filtering branch for one circuit (approximate circulation time 45 min). The liquid was then degassed for 40 minutes by pulling vacuum on the vacuum chamber while continuously circulating the fluid. At the end of the degassing cycle, the measured dissolved oxygen was <0.2 mg/l (approximately 2% of saturation). If necessary, the liquid was cycled through the loop until the desired fluid temperature was reached.
2. Driver preparation: The high pressure section of the loop was isolated and the sphere was pressurized to the desired level. The static pressure was monitored with a pressure transducer (MP40B, Micron Instruments, Simi Valley, CA). Resonance was found by measuring the sound speed of the fluid and employing the previously mentioned fit of sound speed to resonant frequency. The cores of the matching transformers were then adjusted such that the power factor (cosine of the phase difference between the driving voltage and current) was unity at resonance.
3. Mode locking: The waveform generator was then switched to VCO mode, and the PLL was used to keep the driving frequency locked at resonance. Typically the hydrophone, whose signal was passed through a narrow band filter (~2 kHz), was used as the input signal to the phase detector on the PLL.
4. Quiescent state/ramp rate: The acoustic pressure was then adjusted to the quiescent amplitude, such that $P_{CAV}/P_{QUIESCENT} \sim 1.7$. For example, at 100 bar static pressure, the approximate cavitation threshold was 300 bar, and hence the quiescent amplitude was

175 bar. This amplitude was chosen to accommodate the limited range of the voltage ramp on the AM circuit. After the quiescent amplitude was set, the ramp rate was adjusted so that the acoustic pressure increased by 1 bar/s. This was accomplished by setting a delay generator (DG645, Stanford Research Systems, Inc., Sunny Vale, CA) to send a one second TTL pulse to the AM circuit at a rate of 0.5 Hz. The TTL would close the MOSFET switch, thereby continuously discharging the capacitor on the single pole integrator.

5. Data collection: The data collection was automated using a Matlab script (The Mathworks, Natick, MA). The automation was carried out by a Dell Precision T3400 computer and using GPIB (IEEE-4888) protocol communications. The control signal arrangement is shown in Figure 44. The automated data collection process began by disengaging the TTL pulse from the delay generator, thereby allowing the acoustic pressure to increase until the onset of inertial cavitation as detected via PCD. Once the PCD signal reached the predetermined threshold, the LeCroy LT264 scope (LeCroy Corporation, Chestnut Ridge, NY) recording the hydrophone signal was triggered. The scope was set to 100 μs/div with a sample rate of 1 MS/s and set in the single trigger mode. The ramp was then disengaged by a TTL signal from the delay generator, and the system returned to its quiescent state for 20 seconds (the approximate recovery time of the system was one second). The triggered acoustic pressure, voltage, and current waveforms were downloaded from the oscilloscope, and the process began again. Typically, during each data run 100 cavitation events were recorded (i.e. the acoustic pressure was allowed to ramp up 100 times). If the strength of the cavitation collapse were also measured during a data run, the PMT and shock sensor data were recorded on a

separate, deep memory scope (Tektronix DPO 7054), set at 500 μs/div and 1 GS/s sampling rate. The scope was triggered in external mode from a TTL pulse from the delay generator.

6. Post measurement: When the measurement was finished, the sound speed, c_1, in the fluid was measured in order to estimate the pressure drift over the course of the measurement. Since the temperature may also vary over the course of the measurement, the sphere was set to a known pressure and the sound speed, c_2, was re-measured. Since the static pressure was known for c_2 the temperature of the fluid could be calculated using the well known relationship between water's sound speed, pressure, and temperature (Chen and and Milero 1976). The temperature calculated from c_2 was then used in c_1 to calculate the pressure drift, assuming that the fluid temperature did not drift while varying the static pressure (~ 5minutes).

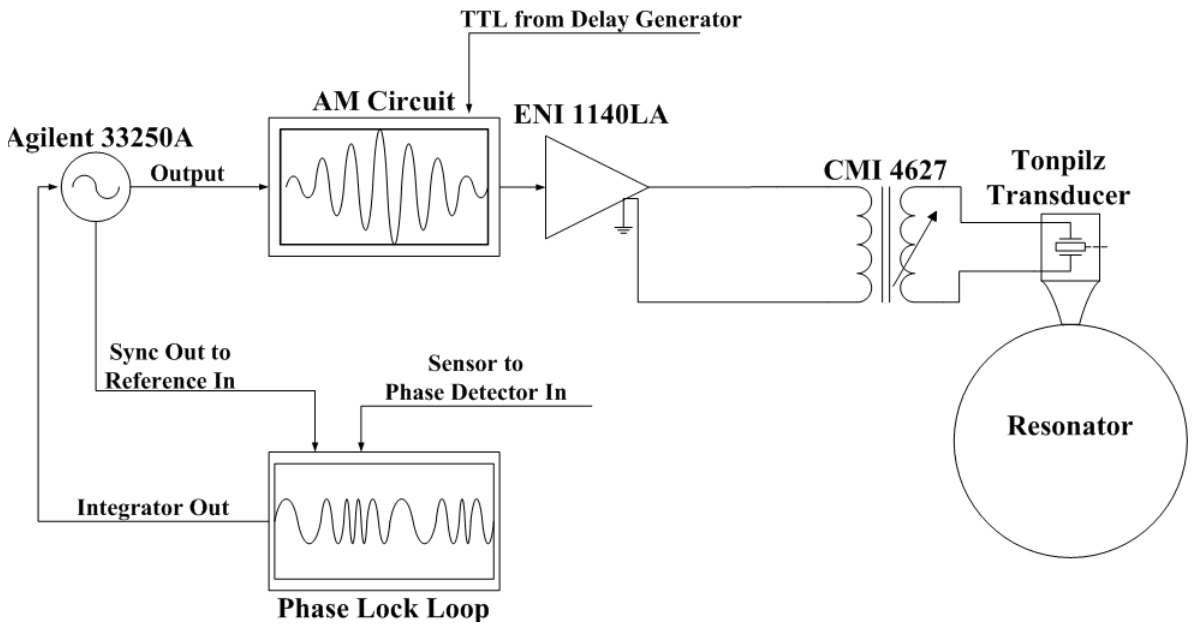

Figure 43: Diagram of driving electronics

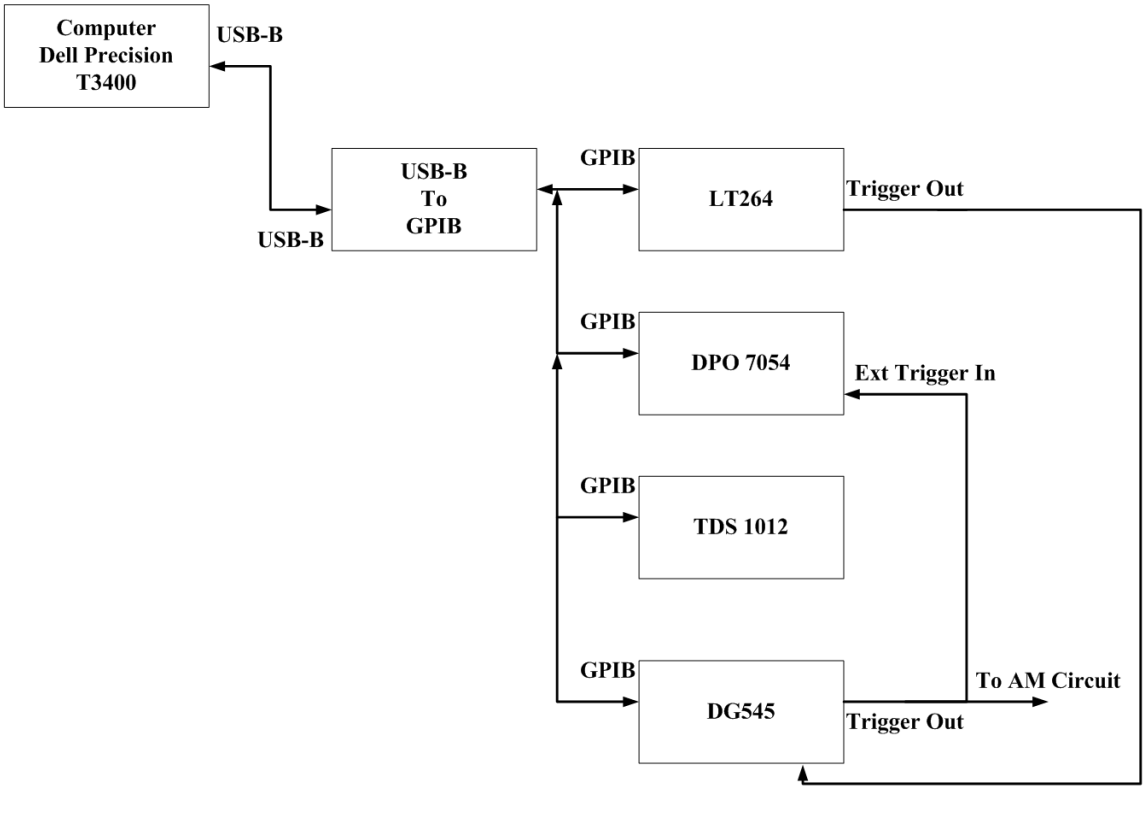

Figure 44: Block diagram of computer control

2.5. Data Analysis

The voltage, current, and acoustic pressure waveforms were downloaded from the LeCroy oscilloscope. The oscilloscope's time base was set to capture 1 ms worth of data at a sample rate of 1 MS/s. The sample rate was chosen such that by zero padding the waveforms to 10^6 total points, the frequency of the waveform could be calculated within 1 Hz using an FFT. The scope was set to act as a pre-trigger, thereby capturing data before the trigger from the PCD. An example waveform is shown in Figure 45.

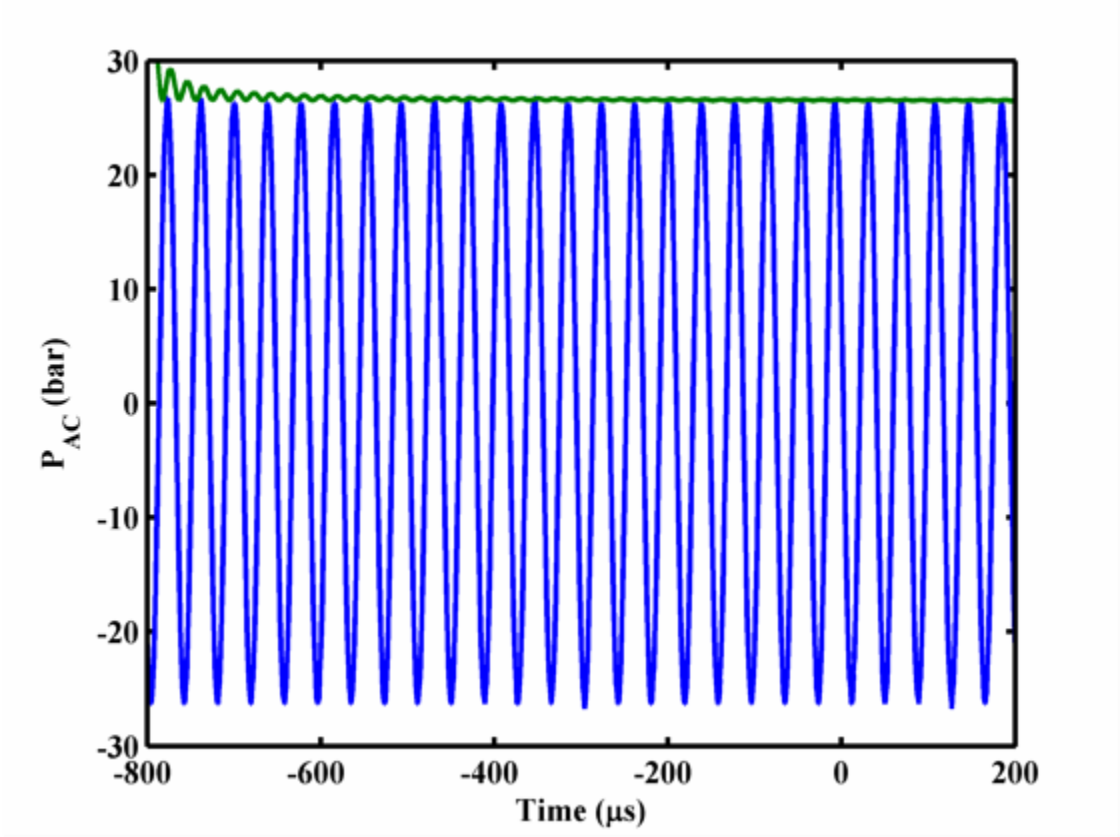

Figure 45: Waveform of acoustic pressure measured by Kistler sensor at the inner wall of the sphere. The scope is triggered by the PCD at time 0. The calculated amplitude (green curve) is shown above the sinusoidal pressure waveform.

The amplitude of the waveform was determined by the product of the root mean square of the waveform and $\sqrt{2}$. To eliminate any transients in the signal, the threshold amplitude was taken to be the average of the calculated amplitude over 10 cycles previous to the trigger (Time = 0). The radial pressure profile of the fluid in a spherical cavity can be described by the spherical Bessel functions j_n:

$$P(r) = P_0\, j_n(k_{ns} r) \qquad (59)$$

where the eigenfrequencies k_{ns} can be calculated as described in section 1.5. When Equation (59) is evaluated for the zero order modes, the pressure at the center of the resonator can be calculated as a function of the pressure measured at the wall:

$$P_{center} = P_{WALL}\, ka/\sin(ka) \qquad (60)$$

where a is the inner radius of the spherical resonator.

3. RESULTS

3.1. Properties of the Acoustic Resonator

3.1.1. Eigenmodes of the Resonator

The modes predicted by Mehl (1985) in section 1.5 can be compared to those of the spherical resonator used for these experiments shown in Figure 9. Although the vessel is spherical, it should be noted that there will be imperfections in the geometry, due in part to the manufacturing (i.e. connecting of the hemispheres) and necessary instrumentation (i.e. NPT ports, flat windows). The resonator was driven at zero-order modes to create cavitation. These radially symmetric modes are non-degenerate, and are insensitive to geometrical imperfections to first order (Moldover et al. 1986). Furthermore, the damping of the zero-order modes is only due to the properties of the fluid (Moldover et al. 1986). This minimizes losses at resonance, resulting in large quality factors.

The resonant frequencies of the (0,6), (0,7), and (0,8) modes were measured as a function of the sound speed of the fluid over the range 1492 – 1534 m/s by varying the static pressure of the fluid. The experimental set-up is seen in Figure 46. The frequency response of the resonator was measured using a dynamic signal analyzer (Hewlett Packard, model number 35655A). The Kistler hydrophone was used to measure the response of the system. The sound speed of the fluid was measured using the previously mentioned automated procedure.

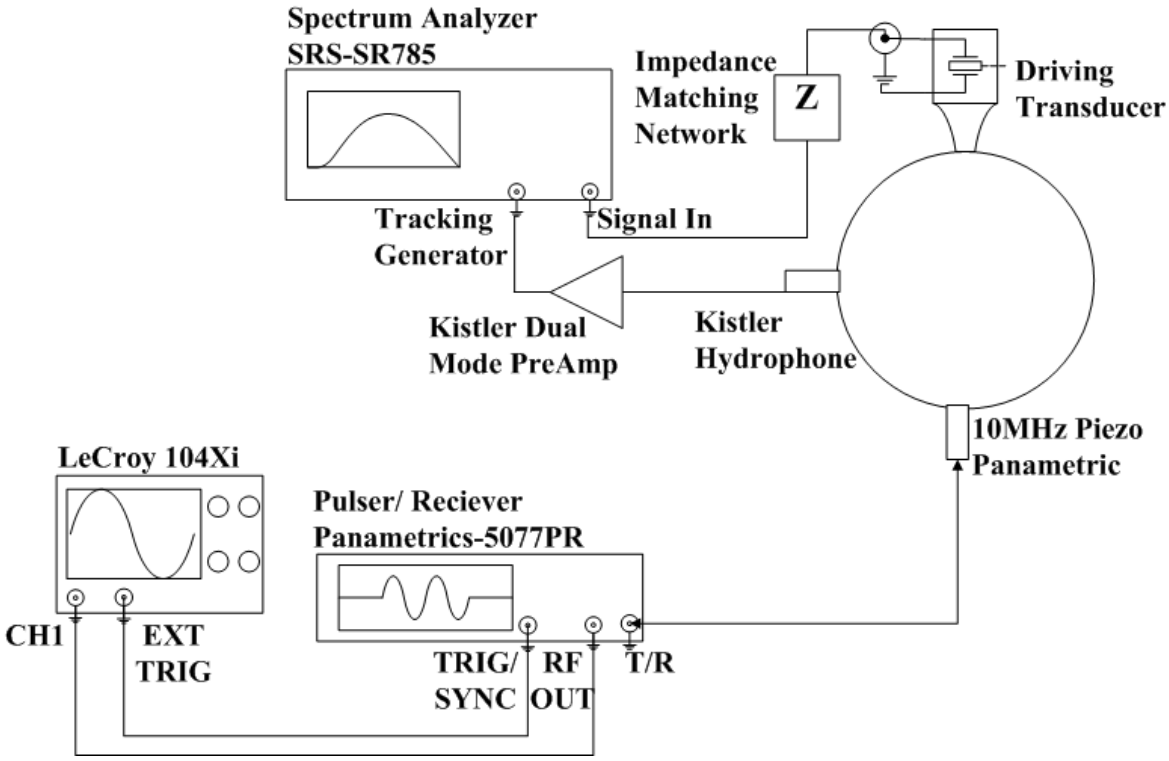

Figure 46: Experimental set-up for measuring sound speed and resonant frequency.

The measured modes and the exact solution calculated using Equation (47) are shown in Figure 47-Figure 49. The infinitely rigid and pressure release solutions are also shown. The measured and predicted resonance frequencies depend linearly on the sound speed. The linear fitting parameters for each predicted mode and measurement are shown in Table 9-Table 11.

The exact solutions are within a fraction of a percent to the infinitely rigid boundary condition. The measured solutions were always slightly larger than the exact and infinitely rigid solutions, and the pressure release boundary conditions were always significantly lower than the mean of the remaining models/measurements by 30-55 standard deviations. The infinitely rigid solution and the measured frequencies are within 1%. The measured solutions and the exact solutions are also within 1%, and are a factor of 1.5-2 closer than the infinitely rigid solution.

The measured resonances do not occur between the infinitely rigid and pressure release solutions as expected. However, considering the proximity of the measured solution to the rigid solution, the boundary appears to act essentially rigid and some mechanism, such as imperfections in the geometry or attachments to the external surface of the resonator, has the effect of shifting the resonance slightly higher.

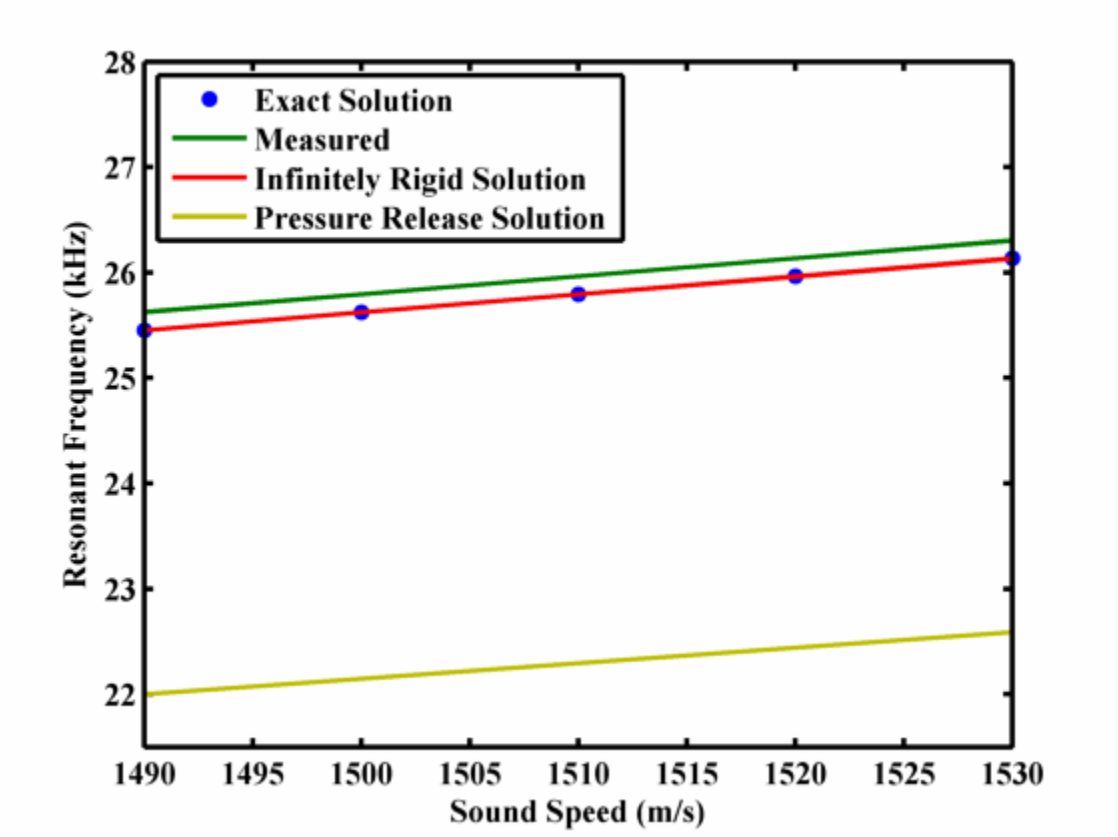

Figure 47: Resonant frequency as a function of sound speed for the (0,6) mode.

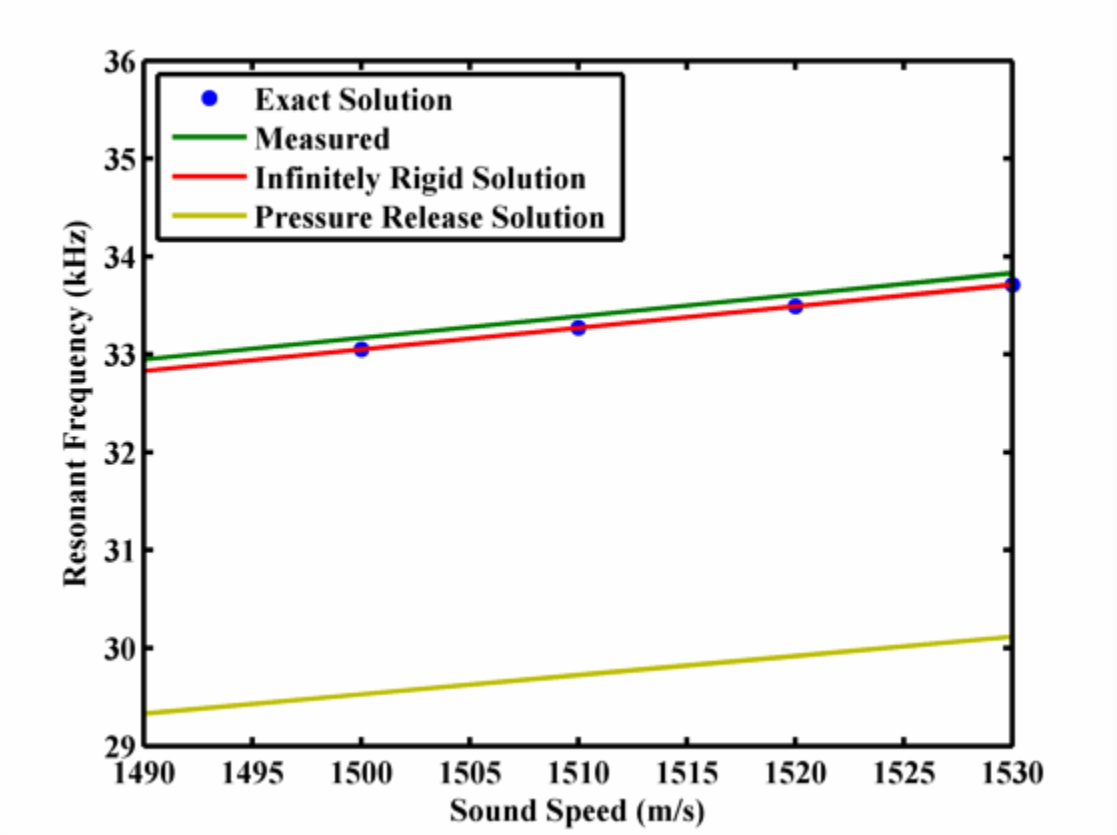

Figure 48: Resonant frequency as a function of sound speed for the (0,7) mode.

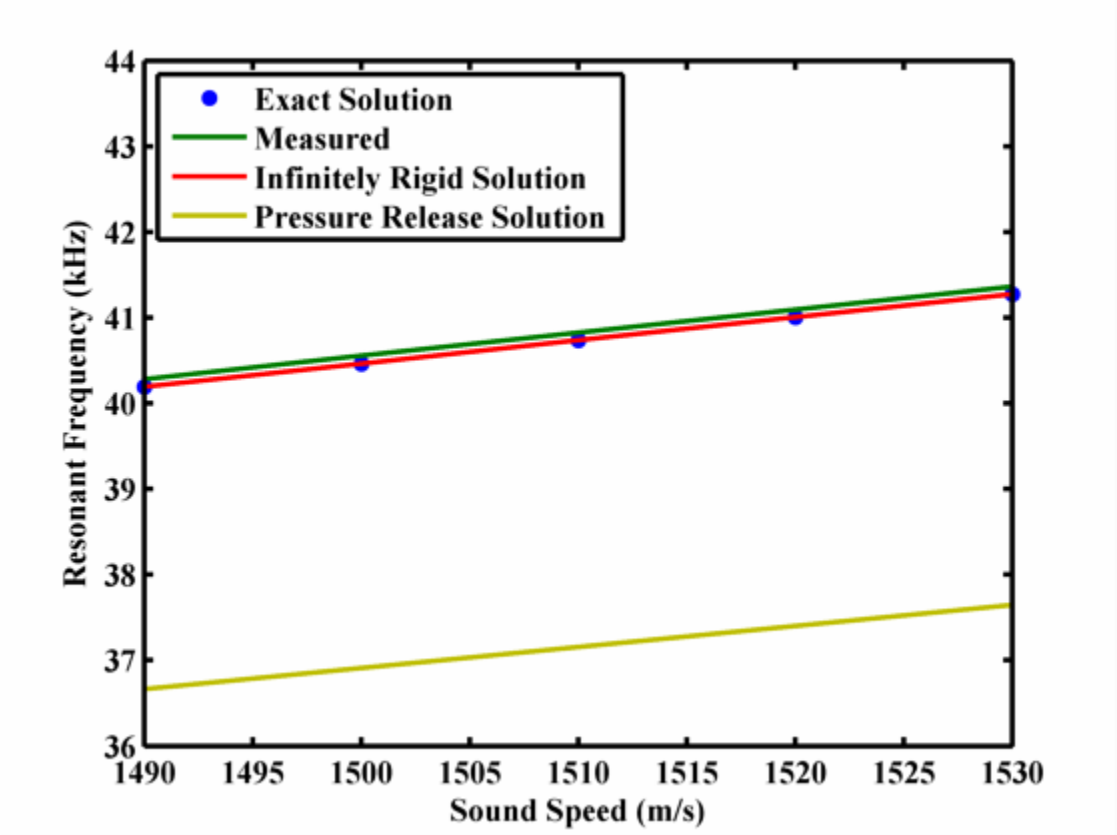

Figure 49: Resonant frequency as a function of sound speed for the (0,8) mode.

Model/Data	Slope (Hz/m/s)	y-Intercept (Hz)
Measured	17.01	283.22
Full Solution	17.08	0.00
Infinitely Rigid Solution	17.08	0.00
Pressure Release Solution	14.76	0.00

Table 9: Parameter for linear fits of resonant frequency dependence on sound speed for (0,6) mode

Model/Data	Slope (Hz/m/s)	y-Intercept (Hz)
Measured	22.06	84.64
Full Solution	22.04	-0.50
Infinitely Rigid Solution	22.03	0.00
Pressure Release Solution	19.68	0.00

Table 10: Parameter for linear fits of resonant frequency dependence on sound speed for (0,7) mode

Model/Data	Slope (Hz/m/s)	y-Intercept (Hz)
Measured	27.00	43.58
Full Solution	25.80	1723.10
Infinitely Rigid Solution	26.98	0.00
Pressure Release Solution	24.61	0.00

Table 11: Parameter for linear fits of resonant frequency dependence on sound speed for (0,8) mode

3.1.2. The Quality Factor of the Resonator: Evidence for Mode Overlapping and the Case for Using Sound Speed to Determine the Resonant Frequency

The quality factor (Q) of the (0,6) mode was also measured using the full width at half max (FWHM) method:

$$Q = \frac{f_0}{\Delta f} \tag{61}$$

where f_0 is the resonant frequency, and Δf is the spread in frequency over the full width at half max (FWHM), as demonstrated in Figure 50. The set-up for the experiment was the same as depicted in Figure 46. The spectrum analyzer recorded the frequency response of the system from the hydrophone over a 50 Hz span, centered on the resonant frequency.

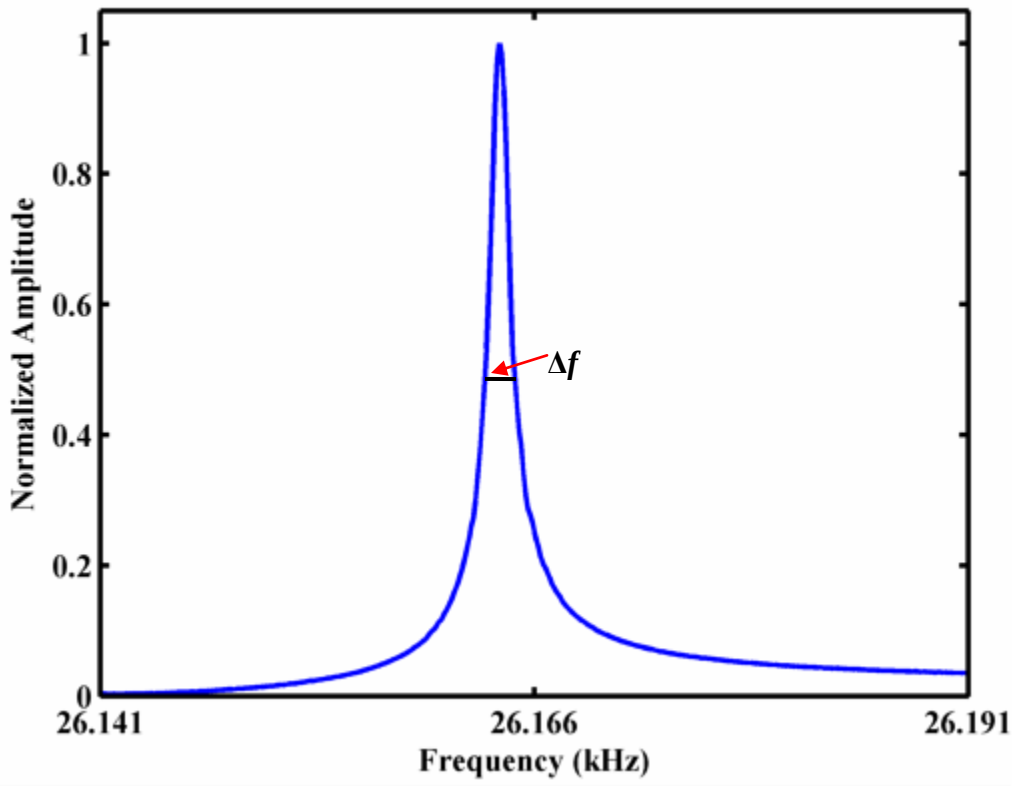

Figure 50: Frequency response of resonator near (0,6) mode. The sound speed of the fluid is 1520.5 m/s and the fluid is pressurized to 300 bar.

Q is shown over the sound speed range in Figure 51. *Q* increases approximately linearly over the range of static pressures, although classical damping mechanisms vary slowly with frequency over this range (Gaitan et al. 2010). It is likely that the resonant driver configuration was

influencing the measurement as previous measurements with non-resonant driver configurations vary little over the sound speed range.

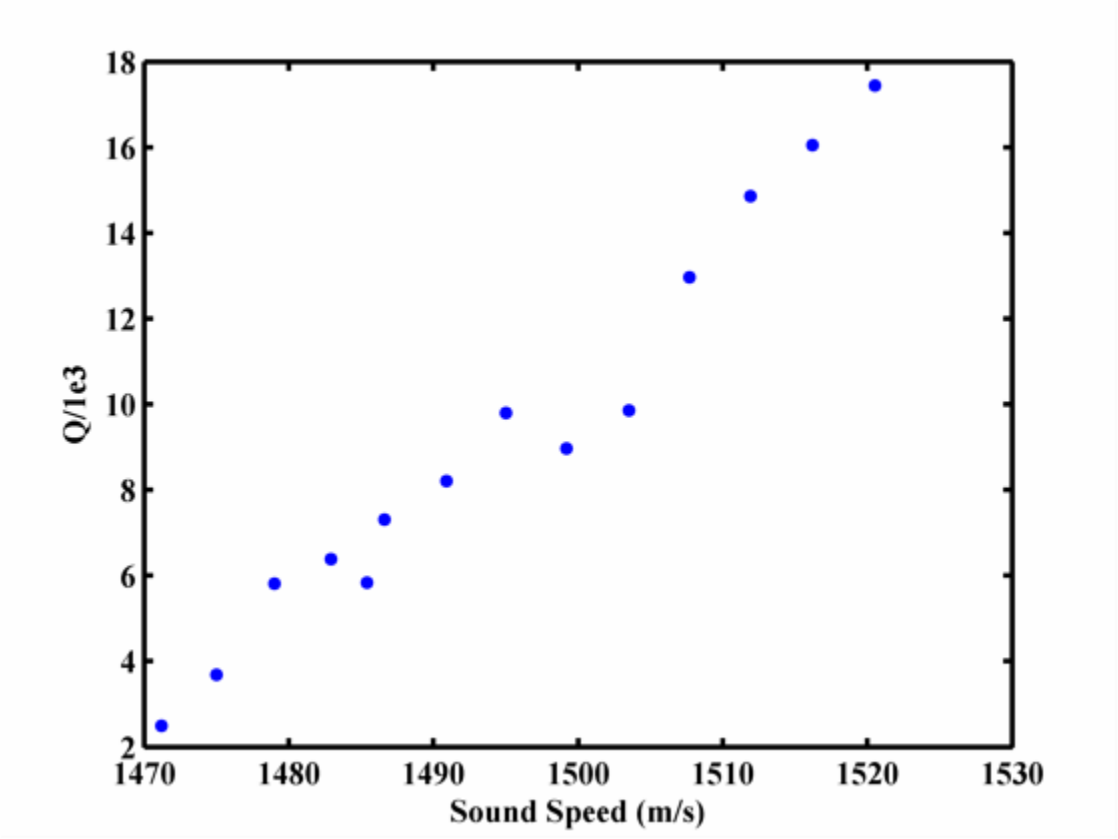

Figure 51: Quality factor as a function of sound speed. The *Q* was calculated using the full width, half max method, illustrated in Figure 50 and Equation (61).

Although the data in Figure 51 were taken over the working range of static pressures (0-300 bar) (i.e. the range of static pressure in which cavitation was created), variations in environmental factors such as room temperature can influence the sound speed, and therefore resonant frequency, of the system. The *Q* data from Figure 51 is re-plotted in Figure 52 as a function of static pressure in the fluid. The fluid temperature was 16.5 ºC. Also depicted in Figure 52 are *Q* data taken when the fluid temperature was 21.6 ºC.

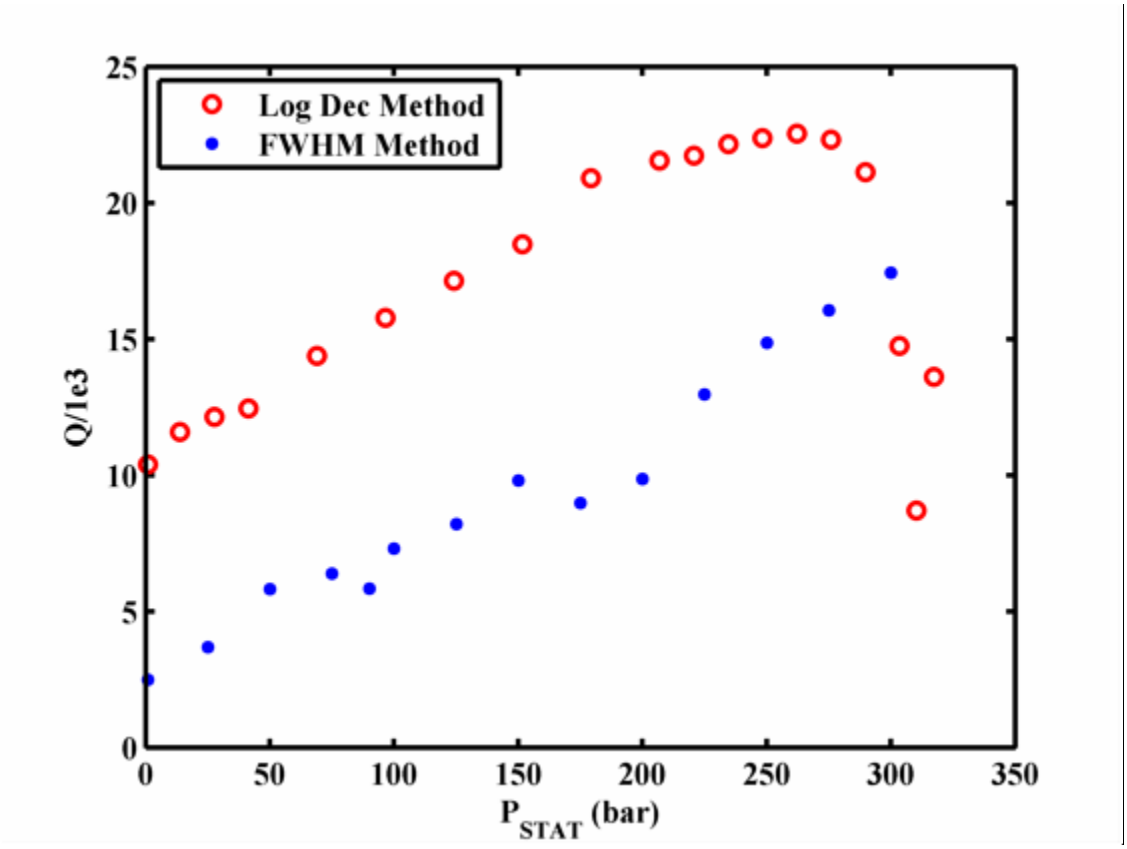

Figure 52: Quality factor of (0,6) mode as function of static pressure. The water temperature for the log decrement method (red circle data) was approximately 21.6 ºC. The water temperature for the full width, half max method was approximately 16.5 ºC.

It should be noted there are inconsistencies in experimental conditions between the two data sets. At 21.6 ºC, there was no impedance matching network used, the response of the system was measured with a piezoelectric sensor at the center of the sphere (i.e. at the acoustic pressure maximum) instead of at the wall, and the port configuration was slightly different (there were two ¼" NPT ports and one HiP type port). In addition, the *Q* was measured using the log decrement method, which defines *Q* as the number of cycles it takes for the system's response to drop by a factor of $e^{-\pi}$:

$$Q = \frac{\omega_0 \tau_{decay}}{2} \quad (62)$$

where $\tau_{decay}/2$ is the time required for the system response to drop $e^{-\pi}$, and $\omega_0 = 2\pi f_0$ is the angular resonant frequency. Previous measurements verified that the log decrement method is qualitatively consistent with the full width half max method.

The data sets have qualitative differences despite the inconsistency in experimental methods. Most notably, the *Q* at 21.6 ºC has a very prominent drop [the so-called Raymond trench (Internal communication)] in the quality factor above 275 bar. The mechanism causing the Raymond trench has been attributed to overlapping of the (0,6) mode and with another eigenmode, which has been shown in the past to diminish the response of resonant systems (Lonzaga et al. 2011, Pitre et al. 2006). Further data are needed to confirm this hypothesis.

The lack of the Raymond's trench in the FWHM data can be explained by plotting the *Q* as a function of sound speed in the fluid, as shown in Figure 53. From this data it is evident that the sound speed of the data at 16.5 ºC is not large enough to moving into the Raymond trench (~1540 m/s), and hence *Q* remains in a linear regime.

Despite the differences in experimental conditions and methods, the percent difference in the two data sets over the sound speed range 1485-1520 m/s is approximately 30.7%, and the log decrement method is approximately a factor of 1.5-2 greater than the FWHM method over the sound speed range 1485-1520 m/s. These values are consistent with previous comparisons of the two methods for identical experimental and environmental conditions. In contrast, if only the static pressure were considered, the difference would be approximately 76% over this sound speed range.

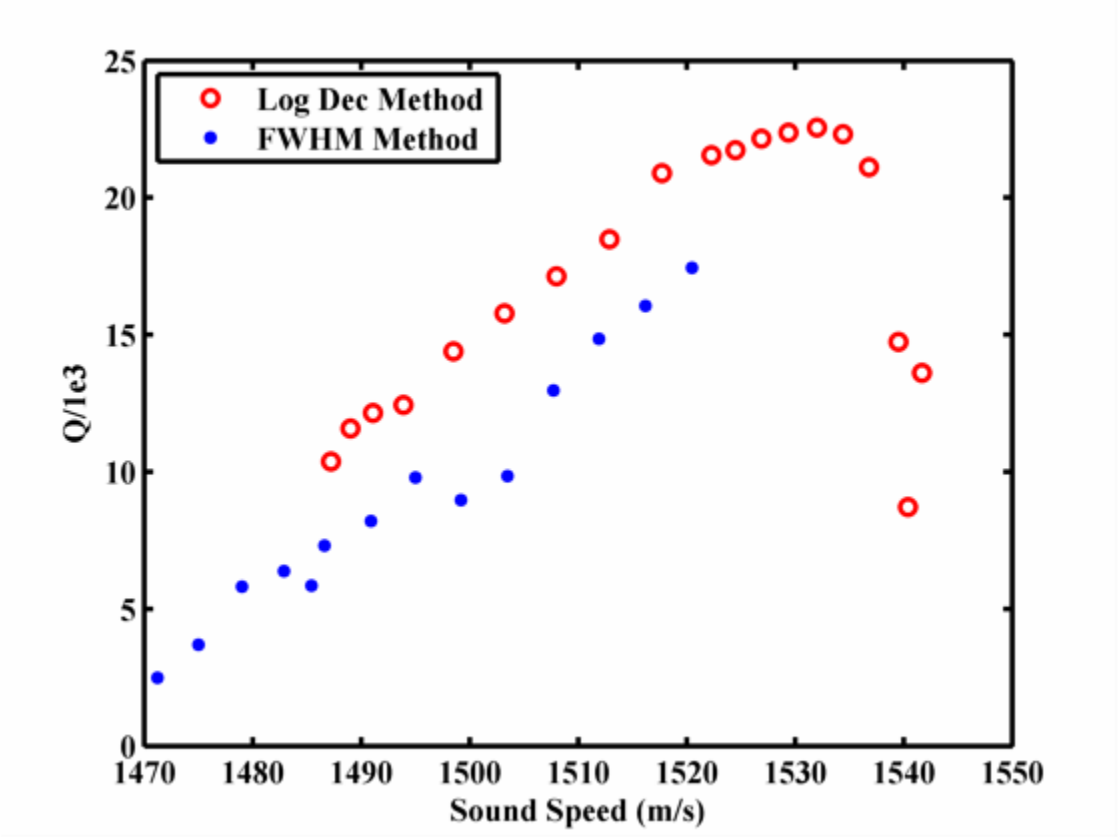

Figure 53: Quality factor of (0,6) mode as function of sound speed. The water temperature for the log decrement method (red circle data) was approximately 21.6 ºC. The water temperature for the full width, half max method was approximately 16.5 ºC.

The data in Figure 53 illustrates the important of using sound speed, and not fluid temperature or pressure alone, to locate the resonance frequency. Hence, the empirical fit of the resonant frequency to the sound speed (shown in Table 9-Table 11) was used as day-to-day measures for determining the resonant frequency.

3.1.3. Extrapolation of Acoustic Pressure to the Center of the Resonator at Large Driving Amplitudes

From Equation (31), the radial pressure profile of the fluid in a spherical cavity can be described by the spherical Bessel functions j_n:

$$P(r) = P_0\, j_n(k_{ns} r) \tag{63}$$

where the eigenfrequencies k_{ns} can be calculated as described in section 1.5. The zero-order modes were typically used to generate cavitation due to their intrinsically high quality factors (Moldover et al. 1986). In addition, it was empirically determined that modes near the intrinsic resonance of the driver (~20 kHz) were most efficient at generating cavitation (Gaitan et al. 2010). For this reason, the (0,6) mode (~25.5 kHz, see Table 9) was chosen for the threshold measurements.

An example of the radial pressure profile calculated from Equation (59) is shown in Figure 54. The acoustic pressure maximum's location prevents a direct assessment of its amplitude without invasively disrupting the acoustic field (e.g. with a probe hydrophone). Therefore, the acoustic pressure was measured at the inner radius of the sphere (~10.1 cm radius). The pressure at the center of the resonator can then be extrapolated by substituting in the $n = 0$ spherical Bessel functions in Equation (59):

$$P_{center} = P_{WALL}\, k_{0,s} r / \sin\,(k_{0,s} r) \tag{64}$$

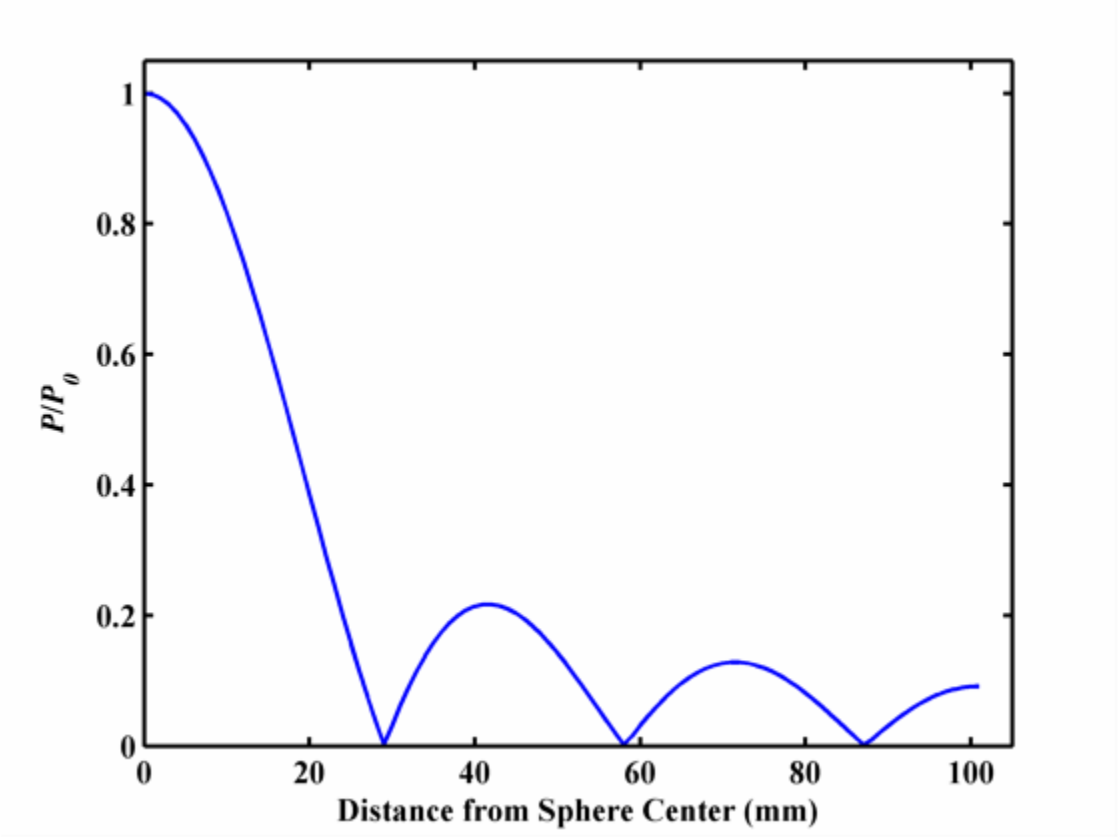

Figure 54: Theoretical radial pressure profile of (0,6) mode. For reference, the inner radius (fluid radius) is approximately 10.1 cm (4").

Equation (59) and Equation (60) have previously been found to be accurate for low driving amplitudes. Typical measured radial profiles are shown in Figure 55. Deviations from the predicted radial pressure profile in these figures are due to perturbations of the probe hydrophone and variations in the boundary condition (the top port of the resonator was a pressure release point since it was open to the atmosphere to accommodate the probe). However, the accuracy of Equation (60) is not known beyond the low-amplitude limit, such as the acoustic pressure required to cavitate at high static pressures.

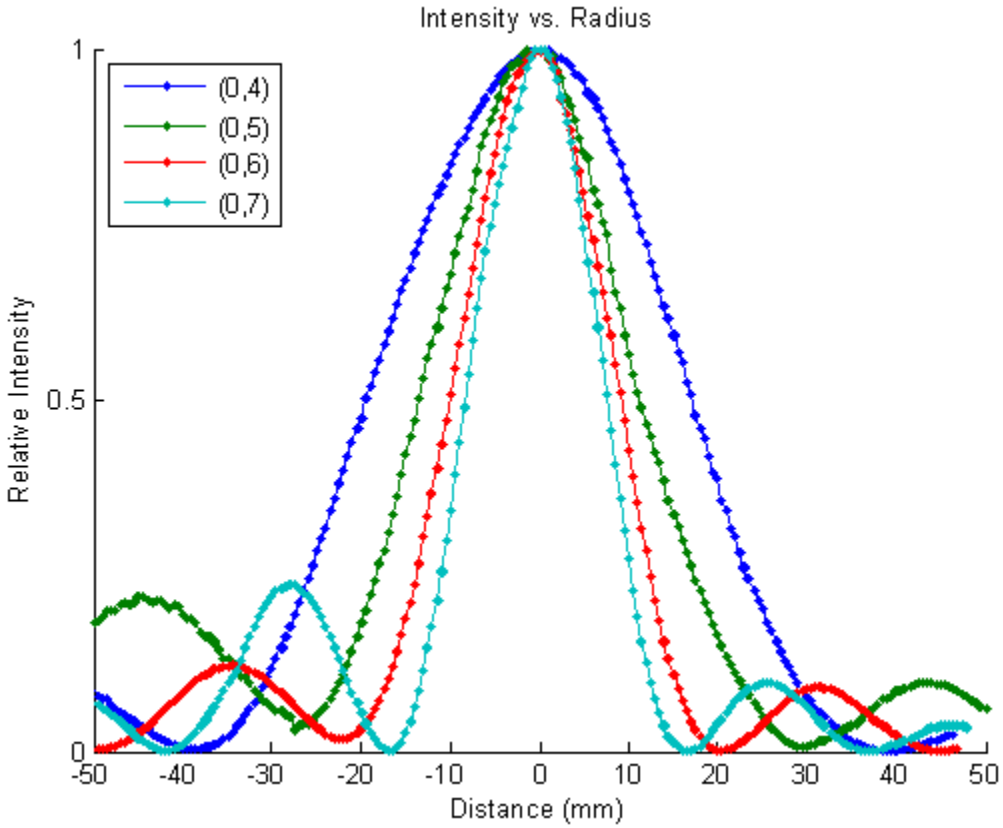

Figure 55: Normalized radial intensity profile of $n = 0$ modes, for a 9.5" OD, 0.5" thick spherical resonator.

Since the pressure at the center of the sphere is of paramount importance for determining the cavitation threshold, the relative amplitude of the Kislter wall-mount hydrophone was compared to pressure at the center of the resonator at high (up to ~100 bar predicted at the center) driving amplitudes. The pressure at the center of the resonator was measured using an in-house designed probe hydrophone. The pressure sensitive element of the probe was a small PZT cylinder of 0.125" outer diameter (Boston Piezo-Optics, Inc.). The lead wire was attached to the PZT element using a low-temperature solder. A schematic of the probe is shown in Figure 56 and a photograph of the finished probe is shown in Figure 57.

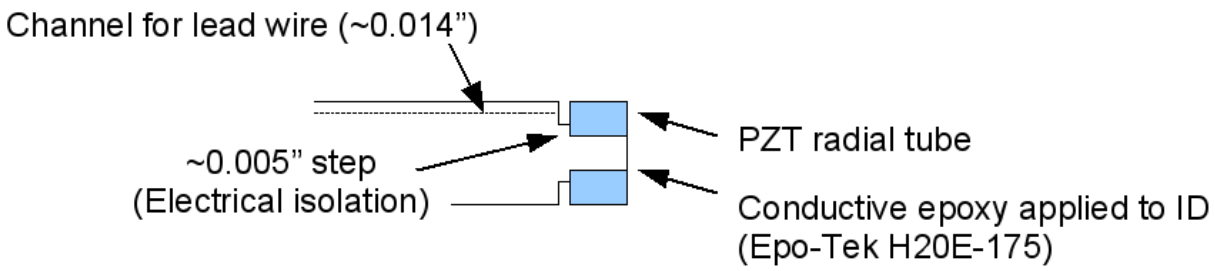

Figure 56: Design/assembly specifics for prototype cylindrical probe hydrophone.

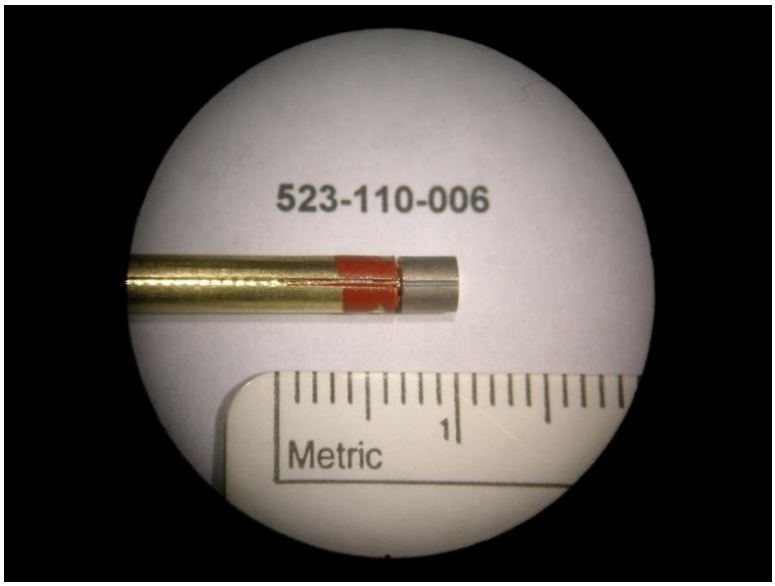

Figure 57: Photograph of the hydrophone mount after assembly of the PZT element. (S/N 523-110-006)

It was necessary to do the measurement at elevated static pressure (100 bar) so that the acoustic pressure could be raised to appreciable levels without cavitation occurring. To accommodate the elevated static pressures, the probe hydrophone was mounted to the resonator with a Swage ultra Torr fitting. The seal on the fitting is made by an o-ring, which allowed the

probe position to be set at the desired depth. This depth was determined by the depth of the probe at its maximum response while driving the system at the (0,6) mode at atmospheric pressure. The o-ring would degrade when the system was driven at high amplitudes due to frictional heating from the probe, and it was necessary to periodically replace the o-ring. The probe was also fit with a custom clamp which prevented it from projecting from the resonator if the o-ring failed.

With the static pressure at 100 bar, the (0,6) mode was excited and the probe voltage (acoustic pressure at the center of the resonator) was measured as a function of the acoustic pressure measured at the wall with the Kistler wall mount hydrophone. For reference, the acoustic pressure at the center, using Equation (60), is approximately a factor of 10 larger than the acoustic pressure at the wall. Larger amplitudes resulted in degradation of the o-ring seal, and, in some cases, sensor failure. The probe voltage was linear over the measured driving range, with an $r^2 = 0.997$.

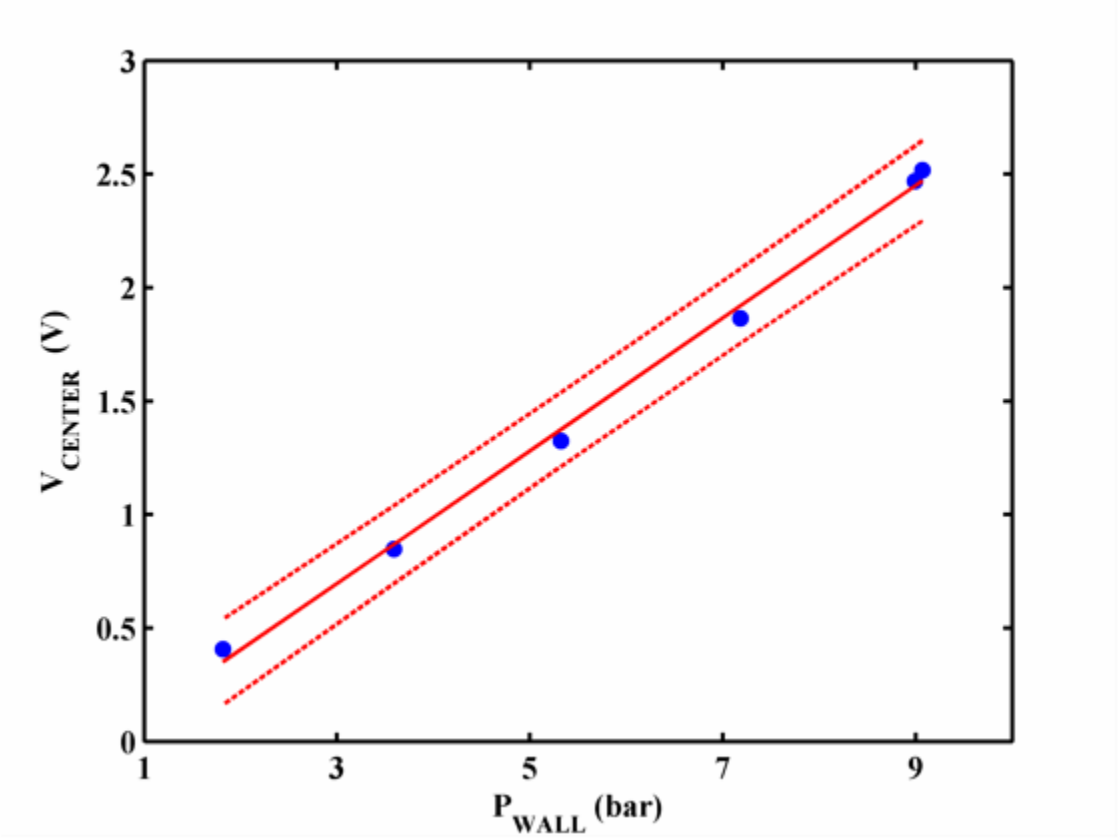

Figure 58: Amplitude of the probe hydrophone's signal as a function of the acoustic pressure measured at the wall of the resonator. The static pressure of the fluid was 100 bar and the resonator was driven at the (0,6) mode. The solid red line is a linear fit to the data, and the dashed red lines are the 95% confidence intervals of the fit to the data.

The probe voltage normalized to the acoustic pressure measured at the wall is plotted in Figure 59. If the system were to remain linear, the normalized probe voltage would remain constant over the entire range of driving amplitudes. The deviation from the constant normalized probe voltages could be due to unanticipated responses of the probe at large driving amplitudes, such as the acceleration of the element (the Kistler wall mount hydrophone is acceleration compensated) or excitation of the normal modes of the rod (such as bending and flexing) in the

fluid. Another possibility is the onset of non-linear steepening of the acoustic field due to spherical convergence.

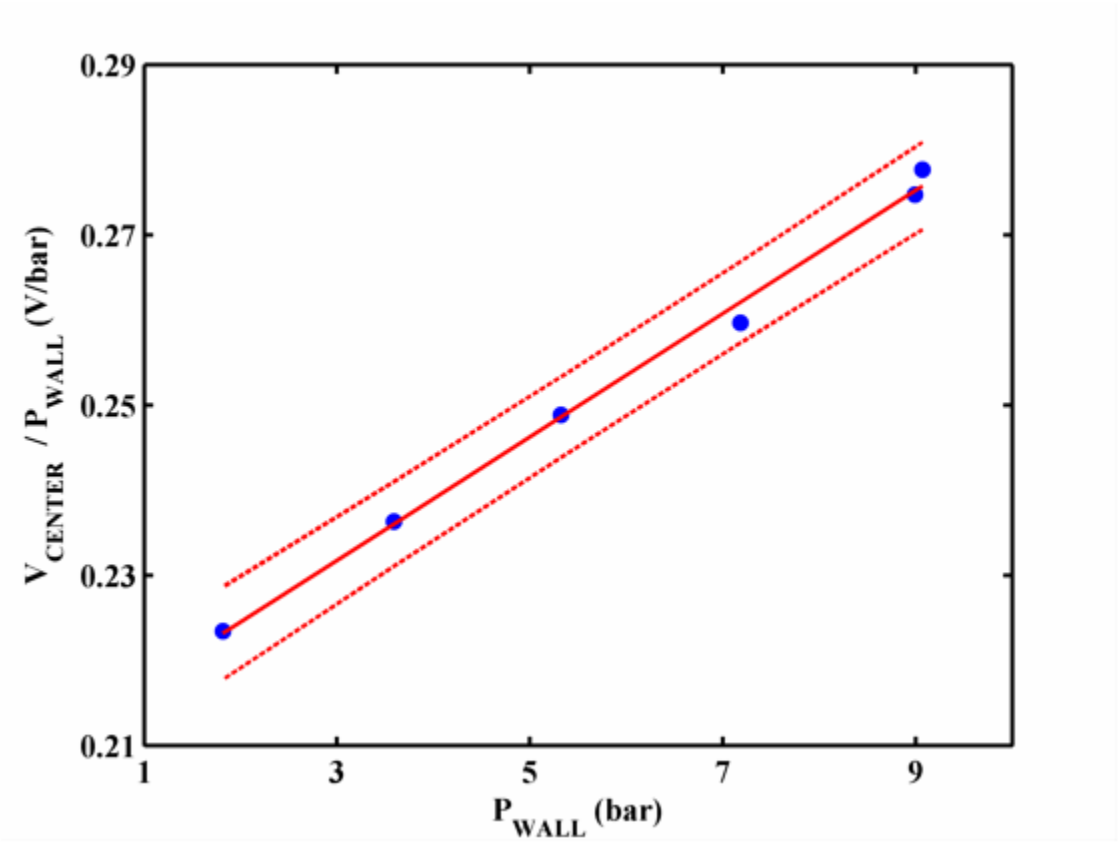

Figure 59: Probe voltage normalized to the acoustic pressure measured at the wall as a function of the driving amplitude (acoustic pressure measured at the wall). The solid red line is a linear fit to the data, and the dashed red lines are the 95% confidence intervals of the fit to the data.

The frequency spectrum of the probe hydrophone is plotted in Figure 60 for the lowest and highest driving amplitudes. The spectrum at largest amplitudes appears to have excited higher frequency content, as noted by the larger abundance of peaks. These could be due to excitations of the resonances of the cylindrical piezo element due to non-linear oscillations of the probe itself. In Figure 61, the probe voltage has been high-pass filtered using a digital, fourth-order

Butterworth filter with a critical frequency of 100 kHz. It is apparent that the extraneous noise at the largest driving amplitude is on the order of the lowest driving amplitude, and the increase in bandwidth at the largest amplitude is likely due to the sensor itself and not non-linear steepening of the acoustic pressure.

While non-linear resonant systems do exhibit complex behavior (Lasič and Torzo 2001, Breazeale and Ostrovsky 2008), a detailed investigation of such behavior is beyond the scope of these studies. The linearity of the probe voltage in Figure 58 and the relatively narrowband frequency spectra in Figure 60 and Figure 61 at both driving amplitudes suggest that the acoustic pressure at the center can be accurately estimated via Equation (60).

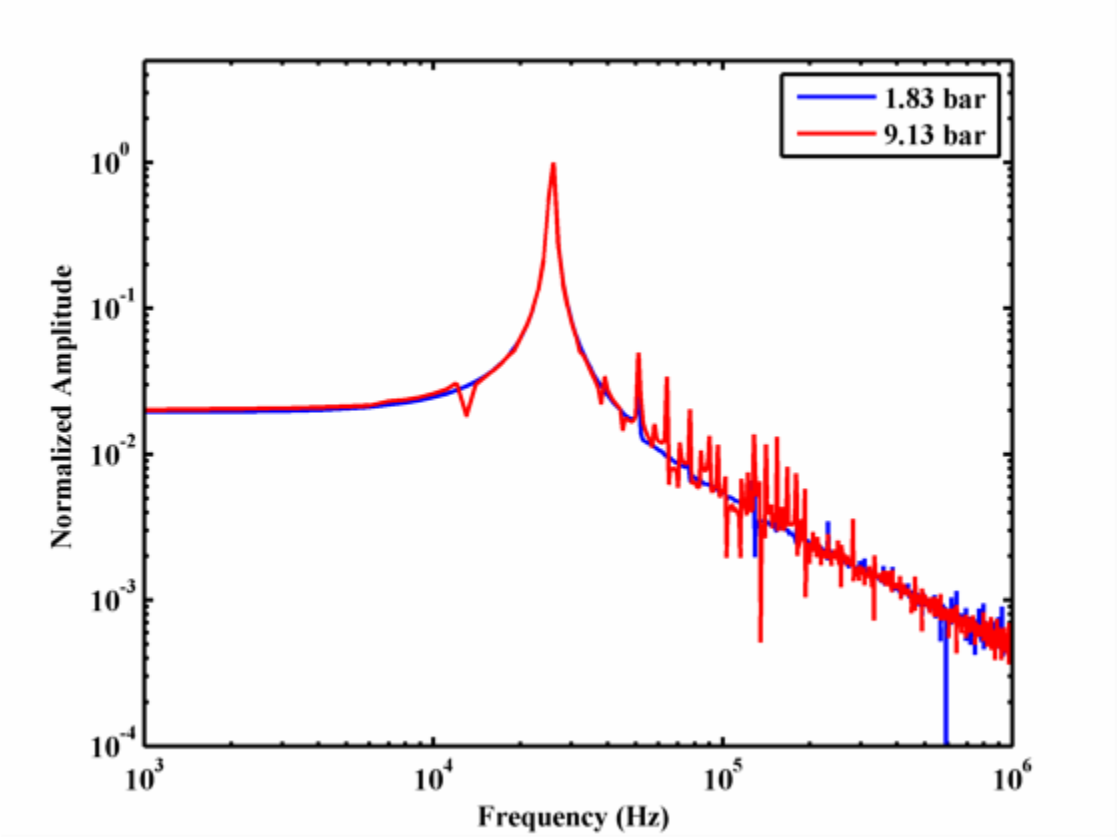

Figure 60: Normalized frequency spectrum of probe voltage at the smallest and largest driving amplitudes. The legend indicates the acoustic pressure measured at the wall. The sample rate was 1 GS/s.

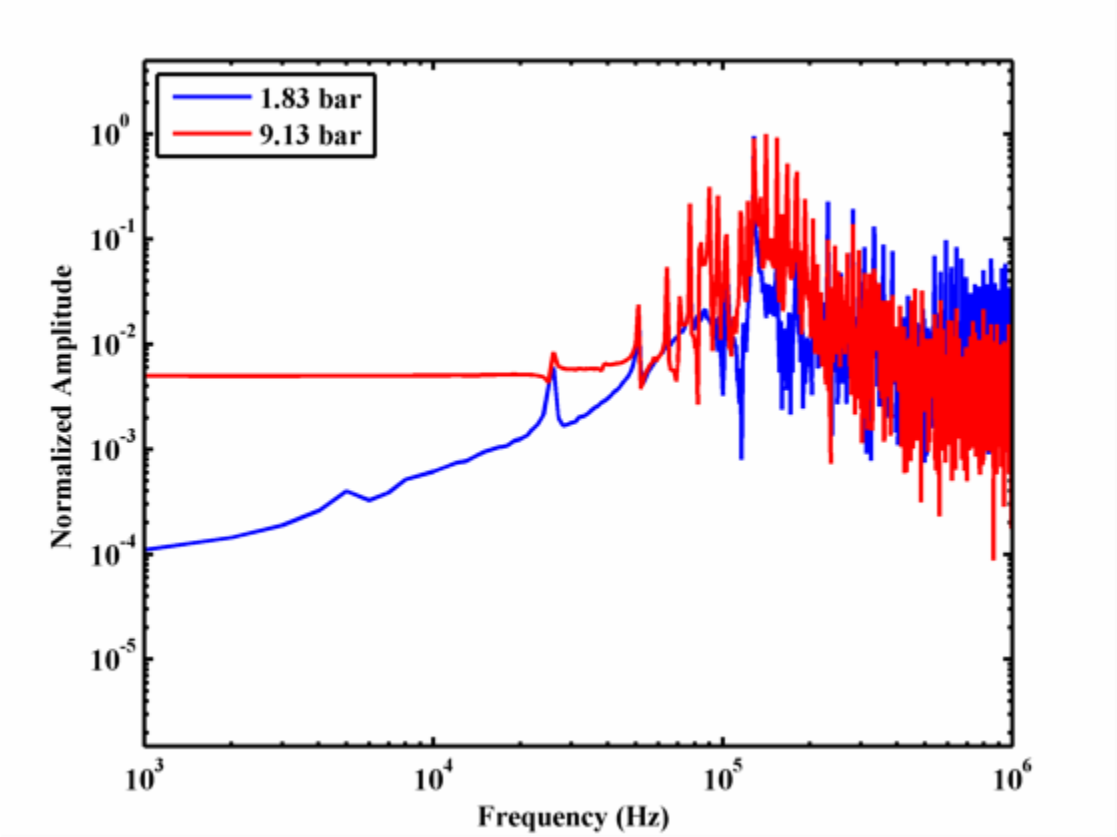

Figure 61: Normalized frequency spectrum of probe voltage (high pass filtered 100 kHz) at the smallest and largest driving amplitudes. The legend indicates the acoustic pressure measured at the wall. The sample rate was 1 GS/s.

3.2. The Cavitation Threshold

3.2.1. The Repeatability of Measurements and Effectiveness of Filtration

The effectiveness of the filtration system is of interest for the repeatability of the measurements, particularly if major modifications to the loop are required. Serendipitously, this query was able to be tested due to a break in the epoxy seal on the vacuum chamber. The break occurred during a routine refilling of the chamber. The chamber was not totally evacuated (total pressure 400 Torr), thus as the water was filling the chamber, the pressure within the chamber

became slightly positive and the epoxy seal ruptured. The chamber was immediately isolated from the rest of the loop, drained via the emergency drain nut, and the fractured glass body was removed from the loop. The intact top and bottom flanges, o-rings, and spacers were rinsed with methanol and triply rinsed with 18 MΩ-cm water. The replacement vacuum chamber was cleaned as previously described (see section 2.1). The replacement vacuum chamber had the same flange size as the previous chamber (ISO-K-100), although it was longer and therefore contained a larger volume of fluid (~2 L. The original chamber could hold up to 1 L). One length of piping in the fluid loop had to be replaced to accommodate the new height of the chamber. This length of piping was cleaned as previously described in section 2.1.2.

Once the chamber was replaced, it was alternatively backfilled with argon gas and evacuated to 1 Torr. It was not possible to attain the final vacuum that the initial chamber would achieve, approximately 30 mTorr, due to residual water vapor on the flanges. The chamber was then reintegrated into the remainder of the loop and filled as previously described (see section 2.1.3).

The replacement of the vacuum chamber was an obvious potential source of introducing new contaminates into the loop. To investigate this possibility, the threshold was re-measured at room temperature for each of the previously measured static pressures. The results are shown in Figure 62. At each static pressure, the temperature dependence of threshold for the measurements before replacing the vacuum chamber was fit to a double exponential of the form

$$P_{CAV} = Ae^{BT} + Ce^{DT} \quad (65)$$

where P_{CAV} is the cavitation threshold in bar extrapolated to the center of the resonator from the pressure measured at the wall using Equation (64), T is the water temperature in Celsius, and A, B, C, and D are fitting parameters. P_{CAV} is defined as the acoustic pressure amplitude at the

center of the resonator extrapolated using the measured acoustic pressure at the wall of the resonator and Equation (64) (see section 2.5 for further details). Equation (65) was used to predict the previously measured threshold before the chamber was replaced at the same temperature as the threshold measured after the vacuum chamber was replaced.

The data shown in Figure 62 indicate that measurements made before and after the replacement of the vacuum chamber are consistent within the error bars of the data [the error bars for the data taken before the vacuum chamber replacement are calculated from the 95% confidence intervals of Equation (65)]. The mean difference of the two data sets is 1.3% (+/- 0.95%). The consistency of the two data sets indicates that the filtration system is robust enough to maintain the purity of the fluid, even for such major modifications to the loop as described above. Furthermore, the data collection procedure is robust enough to produce consistent results.

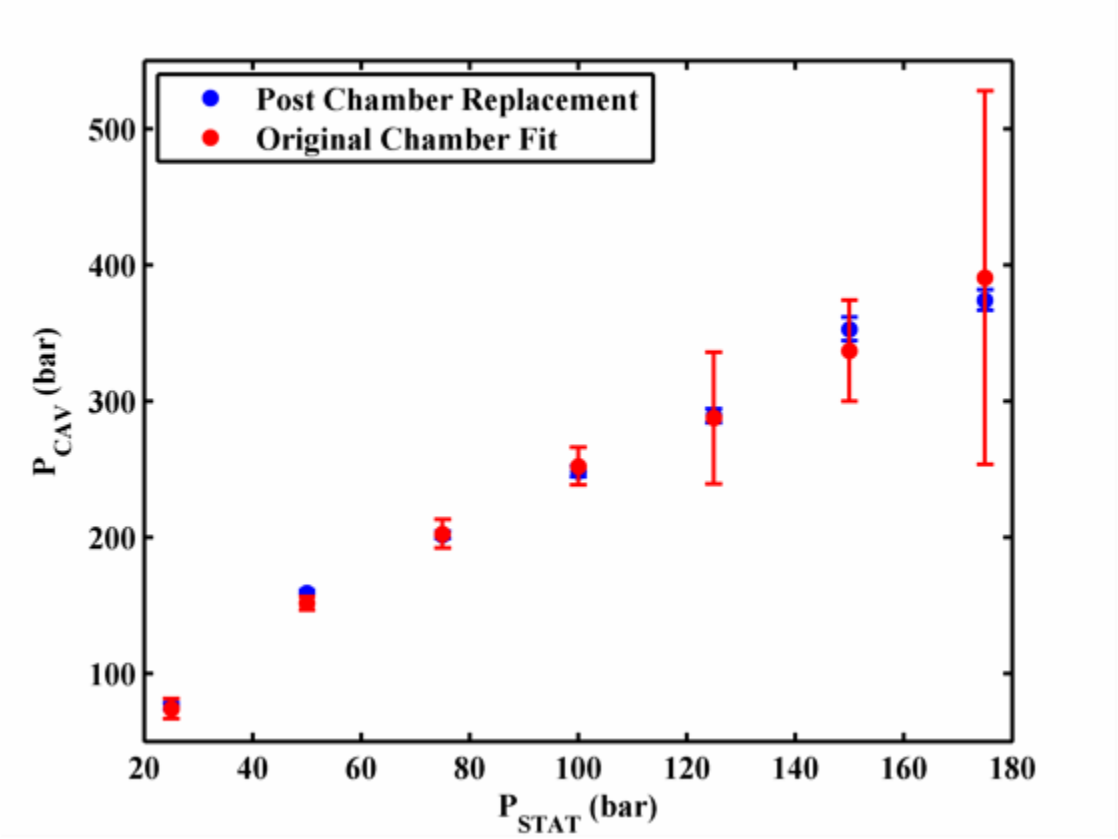

Figure 62: Comparison of threshold measured before and after the replacement of the vacuum chamber. The data collected before the chamber replacement was calculated from the temperature dependence of the threshold, as calculated via Equation (65). The error bars for the data collected before the chamber replacement were calculated from the 95% confidence intervals of Equation (65).

3.2.2. Threshold Sensitivity to Ramp Rate, Quiescent Amplitude

There was no statistically significant variation of the threshold with the ramp rate (~0.5-27 bar/s) or quiescent amplitude ($P_{CAV}/P_{QUIESCNT}$ ~ 1.25-1.75). However, the scatter in the data, and therefore the standard deviation, was proportional to the quiescent amplitude, as shown in Figure 63. This observation is in agreement with Roy et al. (1985).

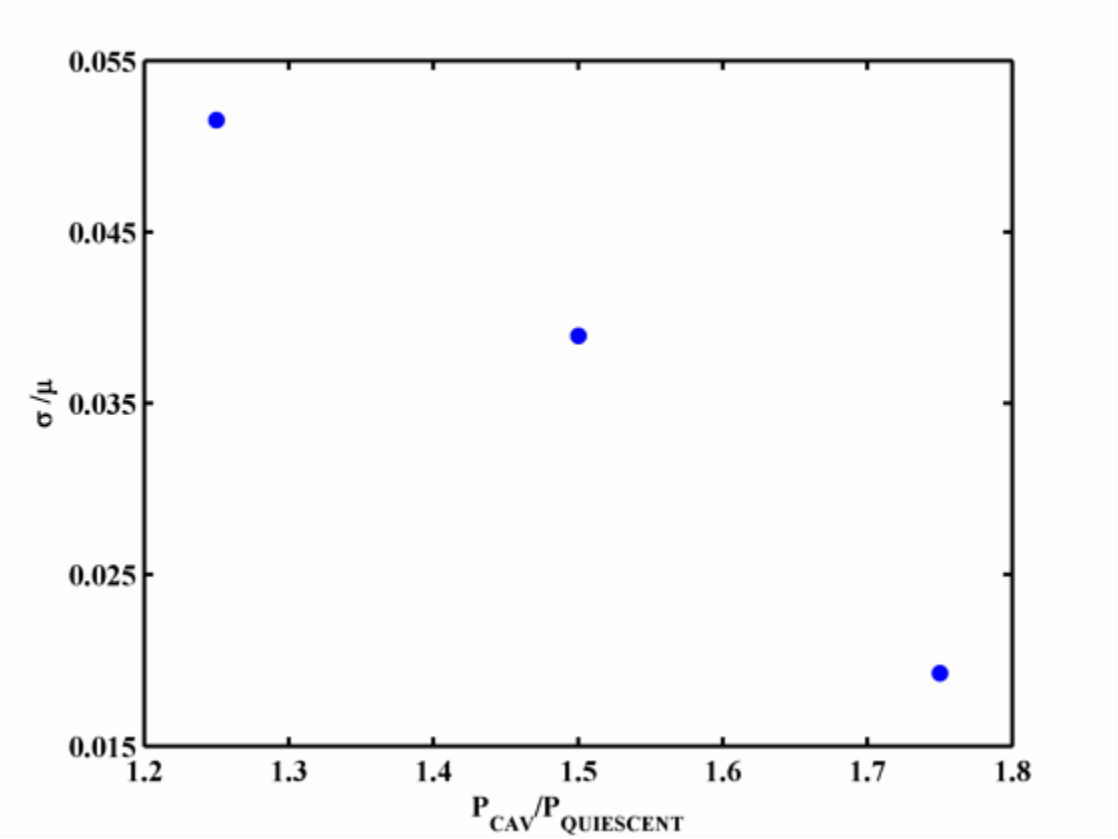

Figure 63: The standard deviation of the threshold, σ, normalized to the mean threshold, μ, as a function of quiescent amplitude. For the data shown, the static pressure was 100 bar, the fluid temperature was 20.6º C, and the ramp rate was 1 bar/s.

3.2.3. The Temperature Dependence of the Threshold

The cavitation threshold measured using the procedure outlined in section 2.4 is plotted as a function of the fluid temperature at each static pressure in Figure 64-Figure 66. Each data point is the mean of the measured threshold over the data set (typically 100 events at static pressures below 250 bar, between 50 and 100 events at 250 and 275 bar, and 20 events at 300 bar). The vertical error bars are the standard deviation in the threshold for the data set, and the horizontal error bars are the drift in temperature over the data set.

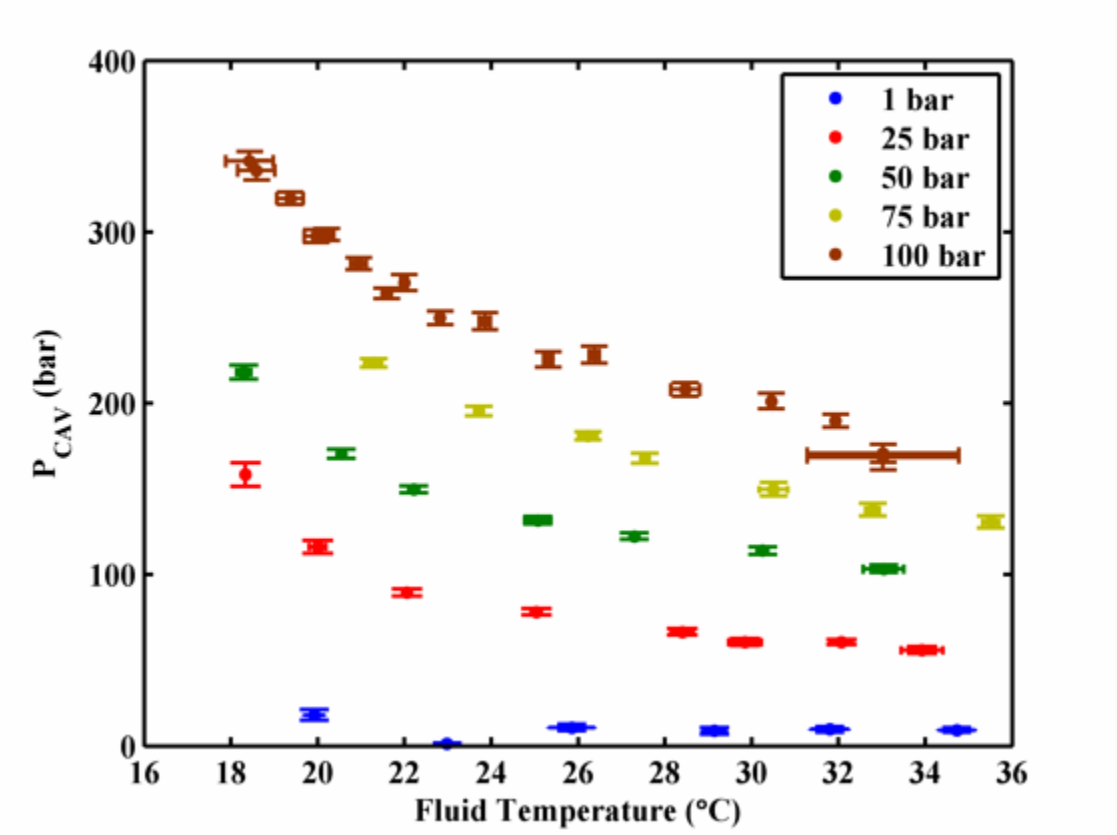

Figure 64: The temperature dependence of the cavitation threshold over the range 1-100 bar static pressure.

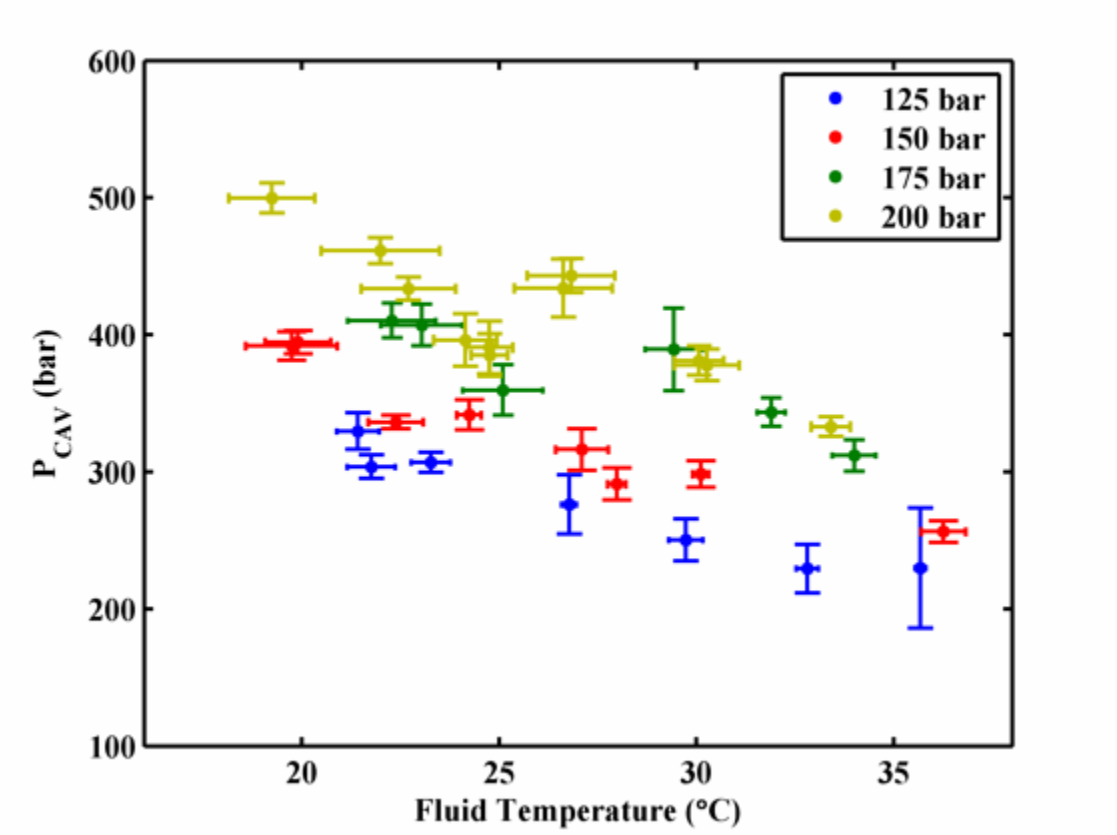

Figure 65: The temperature dependence of the cavitation threshold over the range 125-200 bar static pressure.

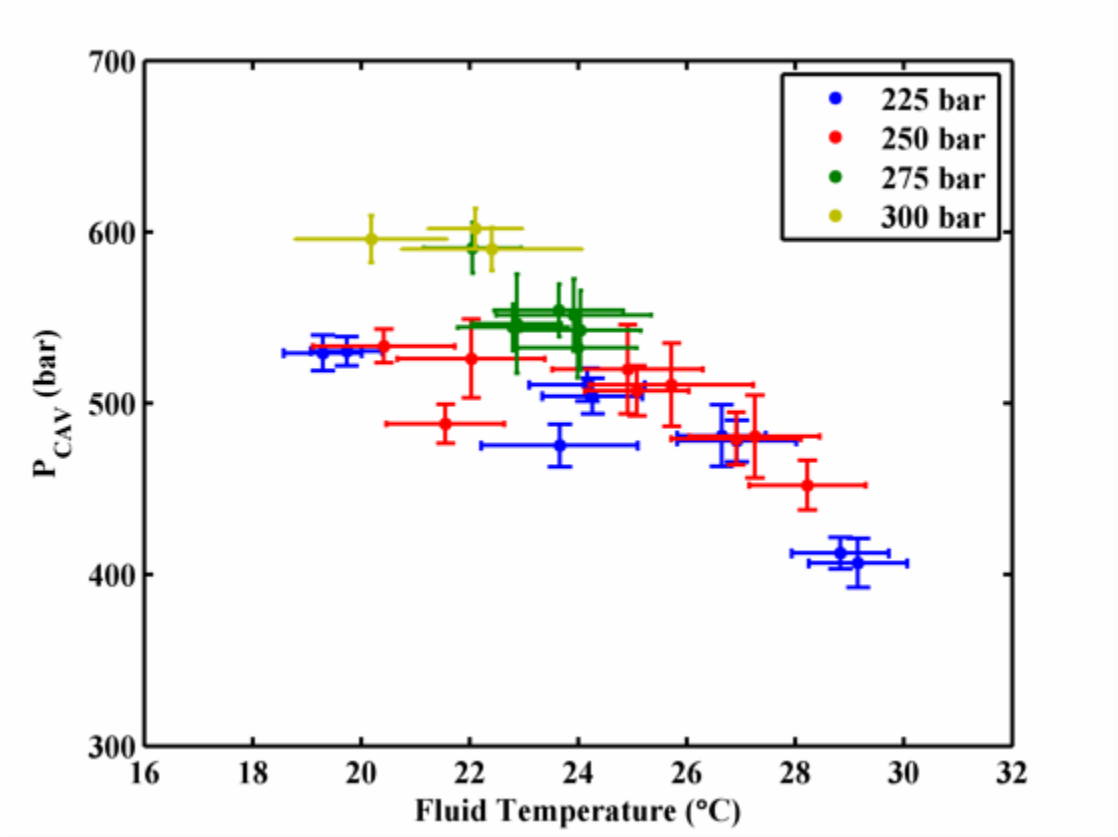

Figure 66: The temperature dependence of the cavitation threshold over the range 225-300 bar static pressure.

3.2.4. The Static Pressure Dependence of the Threshold

In Figure 67 the cavitation threshold is plotted as function of static pressure over the temperature range 18 ºC – 34 ºC. In Figure 68 the mean threshold at each static pressure over the range of measured temperatures is plotted as a function of the static pressure.

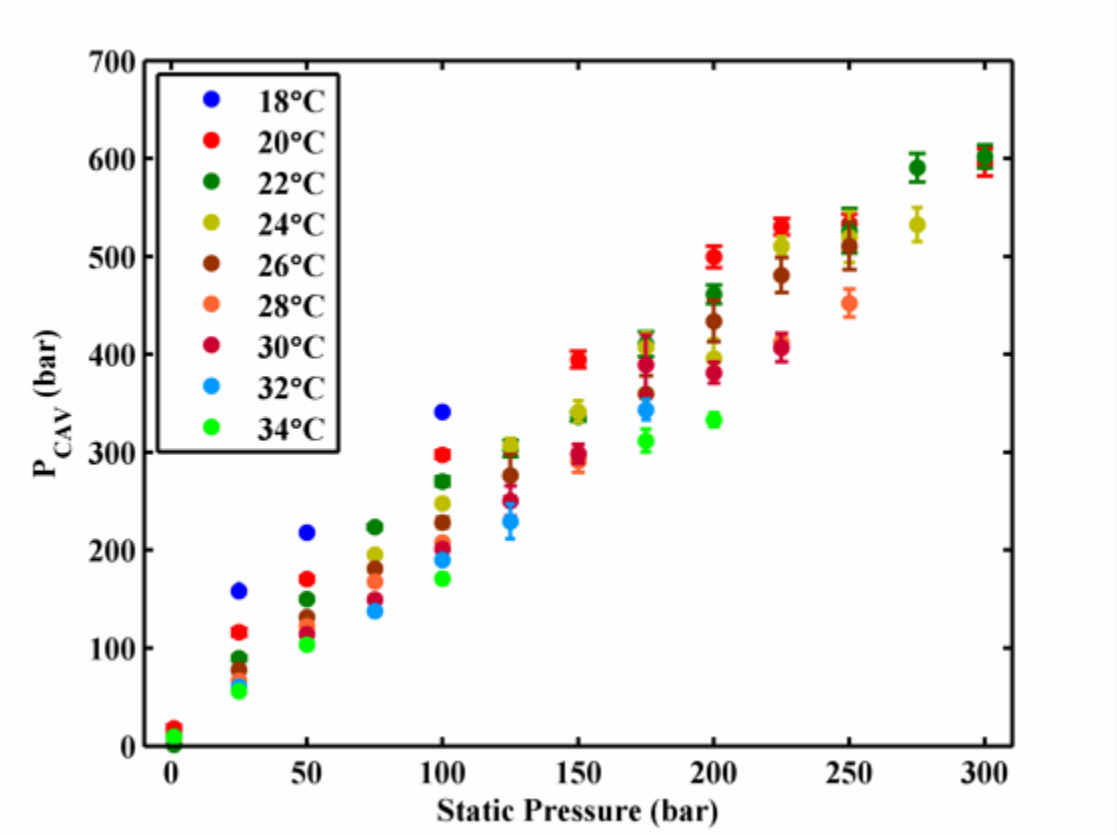

Figure 67: The static pressure dependence of the cavitation threshold plotted as a function of fluid temperature (+/-1 ºC) over the range 18 ºC – 34 ºC. The vertical error bars are the standard deviation of the threshold for the data set, and are not large enough to be seen below 100 bar.

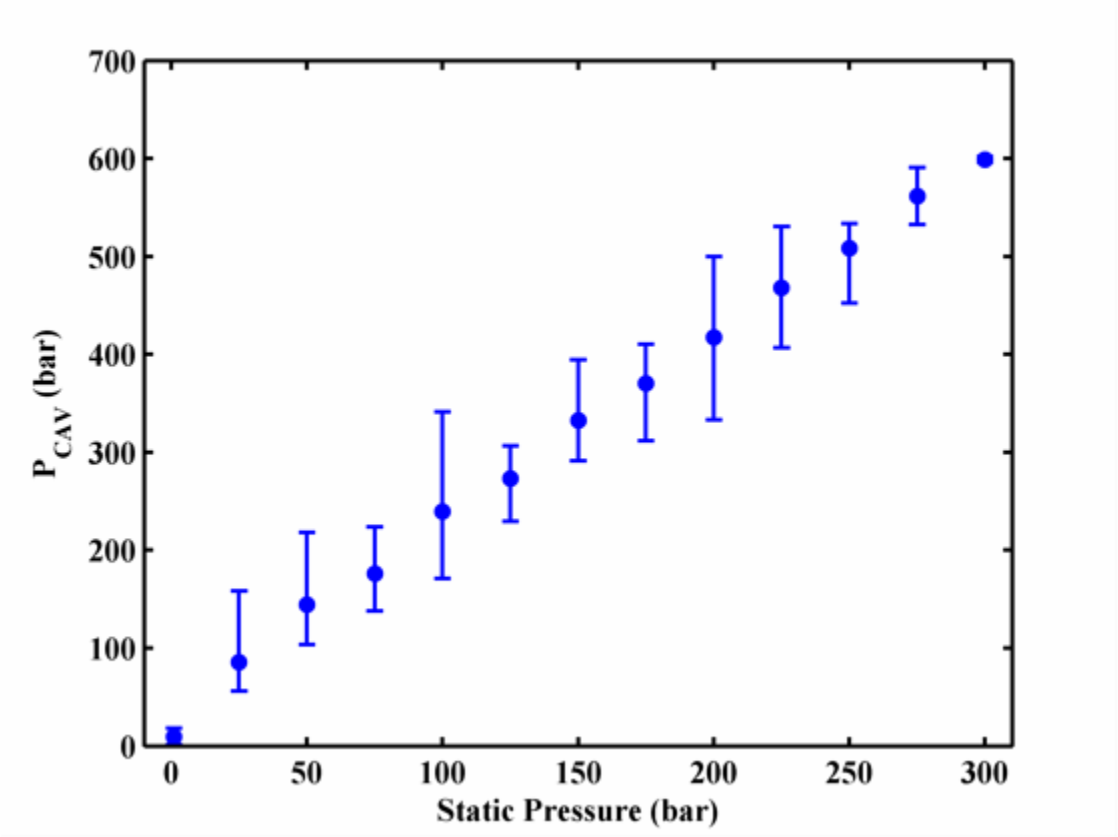

Figure 68: The static pressure dependence of the cavitation threshold. Each data point represents the mean threshold of each of the temperatures plotted in Figure 67. The vertical bars are the spread in P_{CAV} over the temperature range shown in Figure 67.

The temperature dependent thresholds shown in Figure 67 and Figure 68 are approximately linear with the static pressure. Each isotherm threshold shown in Figure 67 was fit to a linear curve using a non-linear least squares routine. The bet fit linear parameters are shown in Table 12.

Fluid Temperature (ºC)	Slope (bar/bar)	Ordinate-Intercept (bar)	r^2	$\sigma_{\bar{X}}$ (bar)
18	2.44	96.82	0.999	0.981
2	1.94	70.89	0.968	39.837
22	1.96	48.75	0.985	24.976
24	1.75	77.84	0.965	24.246
26	1.99	24.82	0.996	10.696
28	1.68	35.73	0.998	6.519
30	1.87	15.54	0.985	20.158
32	1.87	5.95	0.995	9.451
34	1.64	13.23	0.996	9.280

Table 12: Best fit parameters for linear fit of P_{CAV} (bar) as a function of P_{STAT} (bar) for data in Figure 67. The goodness-of-fit parameters coefficient of determination (r^2) and the standard error ($\sigma_{\bar{X}}$) are in the last two columns.

The linearity of the temperature independent threshold data in Figure 68 suggest that it can be used as a rule of thumb for calculating the static pressure dependence of the cavitation threshold:

$$P_{CAV} = 1.92P_{STAT} + 34.64 \quad (66)$$

where P_{CAV} and P_{STAT} are both in units of bar. The goodness-of-fit parameters for Equation (66) are r^2 = 0.997 and $\sigma_{\bar{X}}$ = 11.121.

3.3. Strength of Collapse

The collapse strength for the events was also investigated as a function of the static pressure. A single, defining characteristic of the collapse strength was thought to be too simplistic due to the evolution of the transient events: Briefly, as described by Gaitan et al. (2010), the events are thought to originate from a single bubble that undergoes a strong, inertially driven collapse. A diverging shock wave will form from the converging liquid impinging on the halted bubble wall. The diverging shock nucleates the surrounding medium such that a bubble cloud or cluster is formed. Alternatively, the original bubble may break up after the collapse into micronuclei, resulting in a bubble cluster. The cluster continues to grow by a similar mechanism and oscillates with the acoustic pressure. In addition, a second cloud may be formed by the converging reflection off the resonator wall from the shock wave initiated by an off center event. The cloud(s) will continue to oscillate until sufficient energy has been extract to detune the resonant system, at which point the vapor bubbles will dissolve back into solution. The largest light emissions and shocks are known to occur later in the lifetime of the event, after the onset of cloud dynamics which may be complicated not only by the emissions of many bubbles, but many clouds as well. To accommodate the varying dynamics of the cavitation events, the collapse strength was quantified by three parameters: the first shock/flash, the largest shock/flash, and the total emission for the event. These parameters span the major points of interest of the event.

3.3.1. Strength of Shock Waves

The band-pass (1-25 MHz) shock strength parameters were as mentioned above and in section 2.2.3.1: the amplitude of the first shock wave, the amplitude of the largest shock wave, and the shock energy for the entire event. These results are shown in Figure 69-Figure 71. Each

data point represents the mean of the data recorded for all three data sets (300 events for each static pressure up to 200 bar, 270 events for 225 bar, 120 events for 250 bar, 100 events for 275 bar, and 60 events for 300 bar). The vertical bars are the standard deviation of the data for all three data sets. The three data sets spanned the temperature range 18 ºC – 25 ºC. There was no observable change in the shock strength parameters over this temperature range.

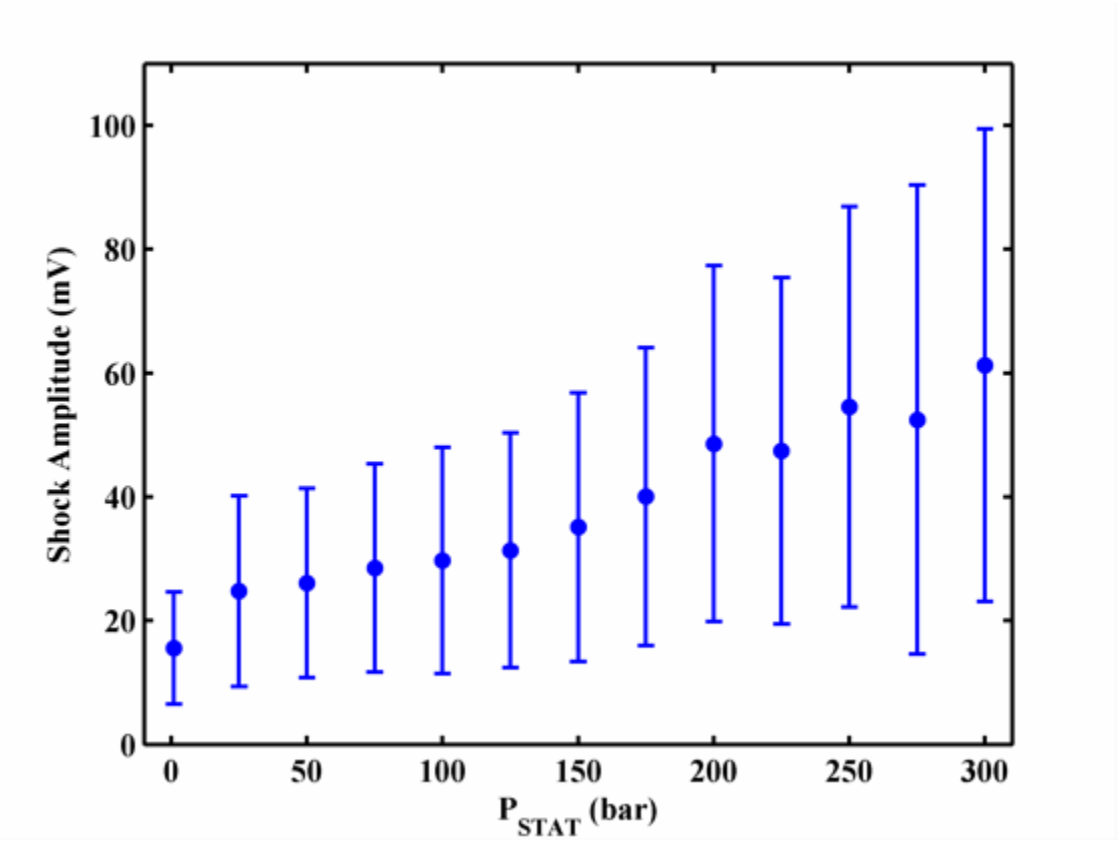

Figure 69: Amplitude of the first shock wave of the cavitation event as a function of the static pressure.

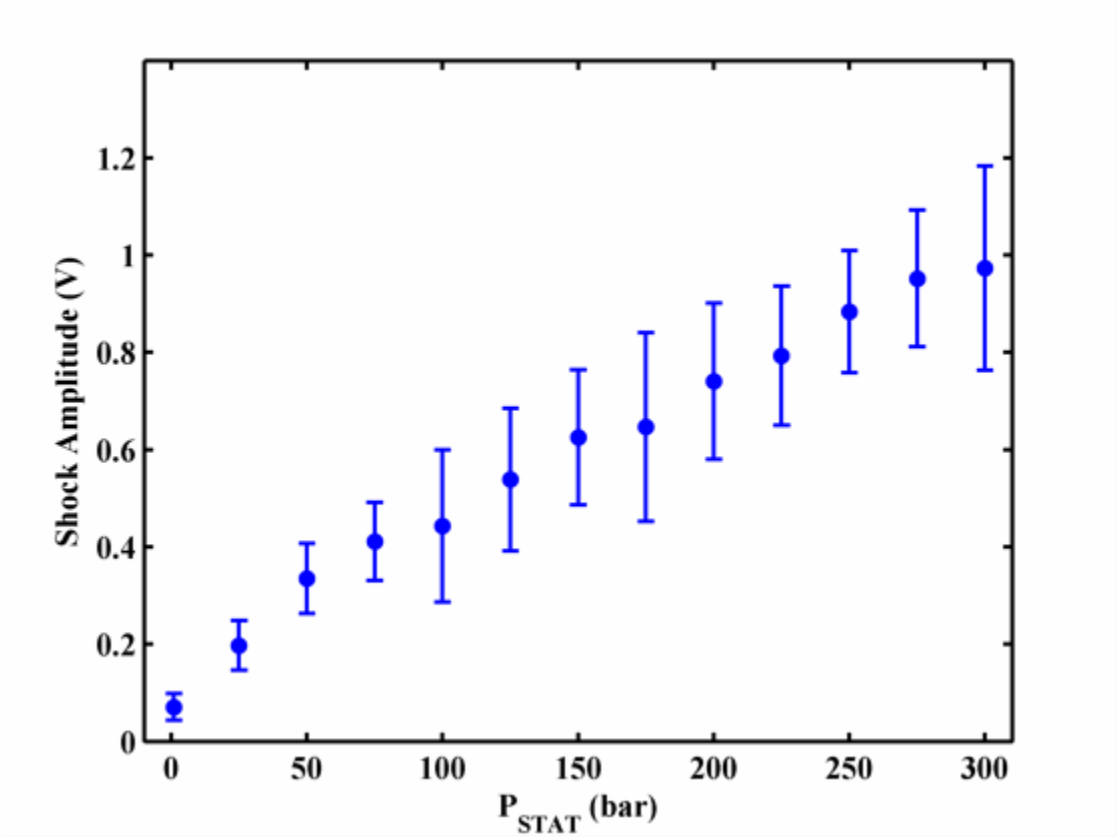

Figure 70: Amplitude of the largest shock wave of the cavitation event as a function of the static pressure.

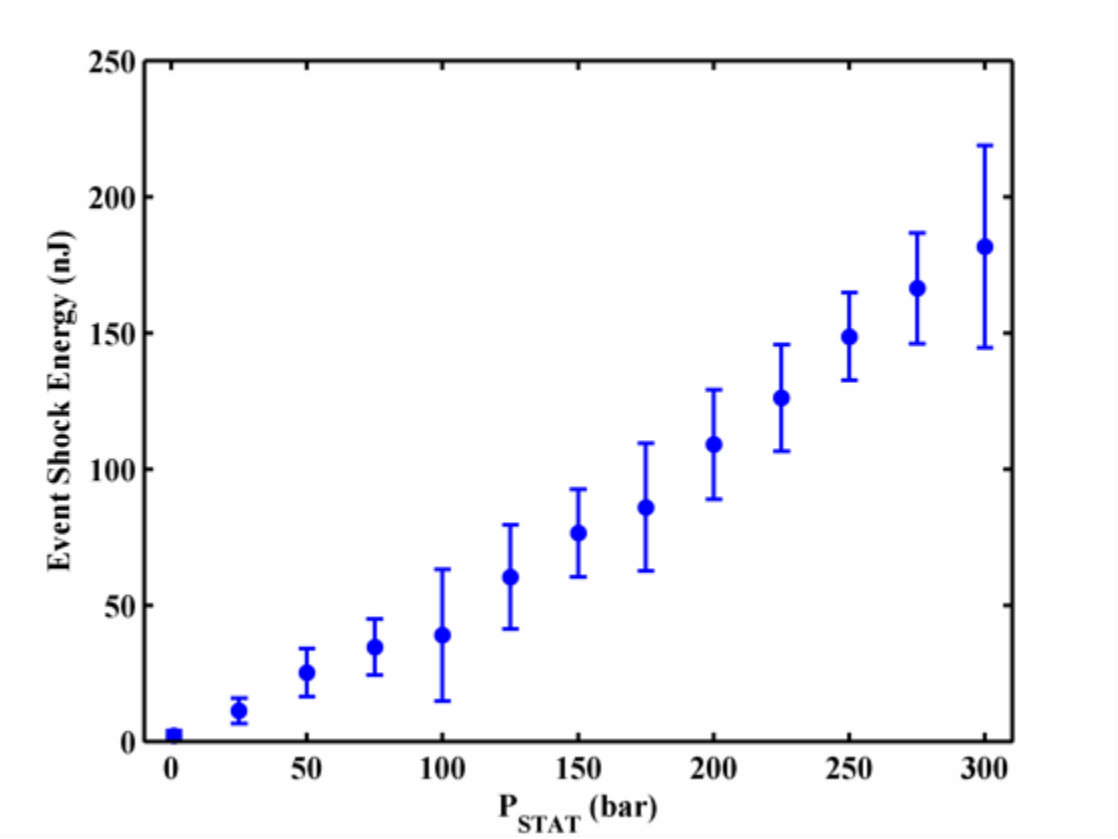

Figure 71: Shock wave energy for entire cavitation event as a function of the static pressure.

Each of these shock strength-of-collapse parameters scales with the static pressure. The first and largest shocks increase linearly, and the event energy increase quadratically. The coefficients for these fits are shown in Table 13.

Shock Type	A	B	C	r^2	$\sigma_{\bar{X}}$
First	0	1.39×10^{-4}	1.73×10^{-2}	0.963	2.70×10^{-3}
Largest	0	2.91×10^{-3}	0.15	0.984	3.79×10^{-2}
Event	8.63×10^{-4}	3.54×10^{-1}	2.01	0.997	3.58

Table 13: Coefficient for linear and quadratic fits of data shown in Figure 69-Figure 71. Here, $X_{OUT} = A\ P_{STAT}^2 + B\ P_{STAT} + C$, where X_{OUT} is the shock amplitude [V] for the first and second rows, and the event energy [nJ] for the third row. r^2 is the coefficient of determination of the fit, and $\sigma_{\bar{X}}$ is the standard error of the fit.

3.3.2. Strength of Light Emissions

As with the shock wave emissions, the strength of collapse for light emissions was characterized using three parameters: the number of photons of the first collapse, of the largest collapse, and of the entire cavitation event. These results are shown in Figure 72 - Figure 74. Each data point represents the mean of the data recorded for three data sets (300 events for static pressures up to 200 bar, 270 events for 225 bar, 120 events for 250 bar, 100 events for 275 bar, and 60 events for 300 bar), and the error bars are the standard deviation of the data for all three data sets. The Oriel housing measured the 650-900 nm range, the H957-08 measured the 450-650 nm range, and the H7732-10 measured the 185-450 nm range. The three data sets spanned the temperature range 18 ºC – 25 ºC. There was no observable change in the strength parameters over this temperature range.

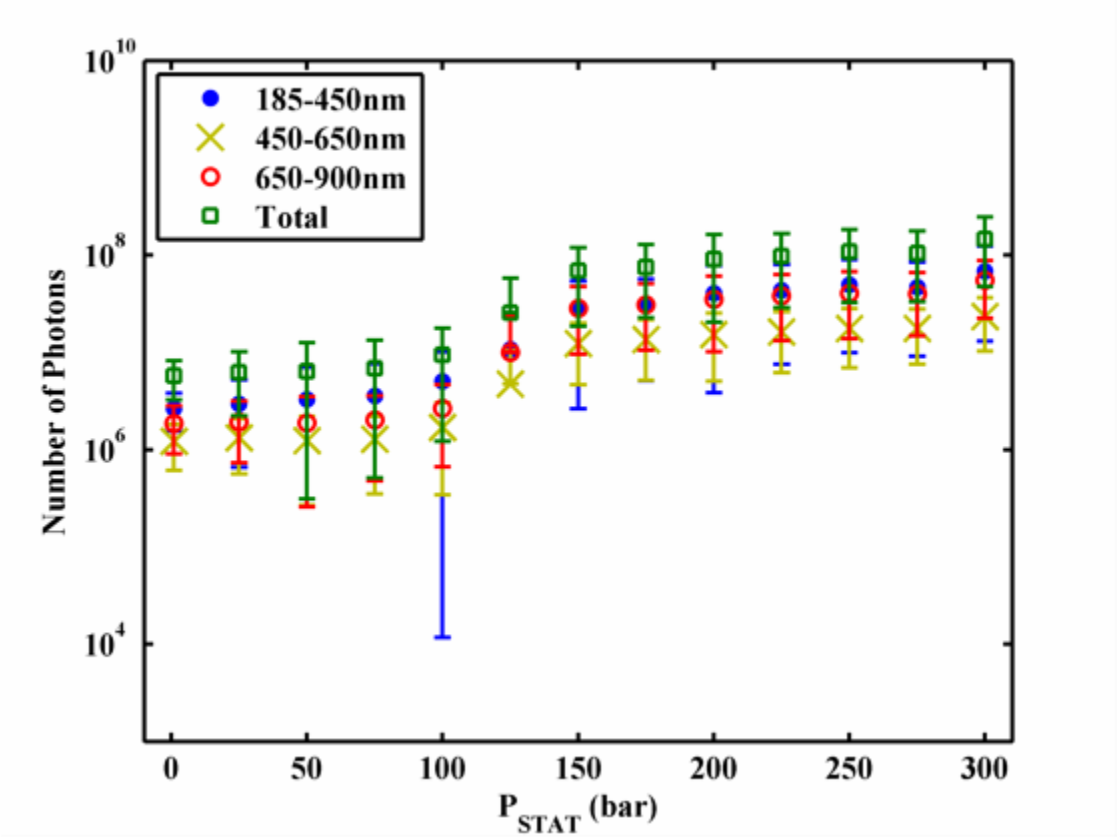

Figure 72: Number of photons from the first flash of the cavitation event as a function of static pressure. The lower error bars for data at 125 bar were less than 0, and therefore were not able to be shown on the log scale.

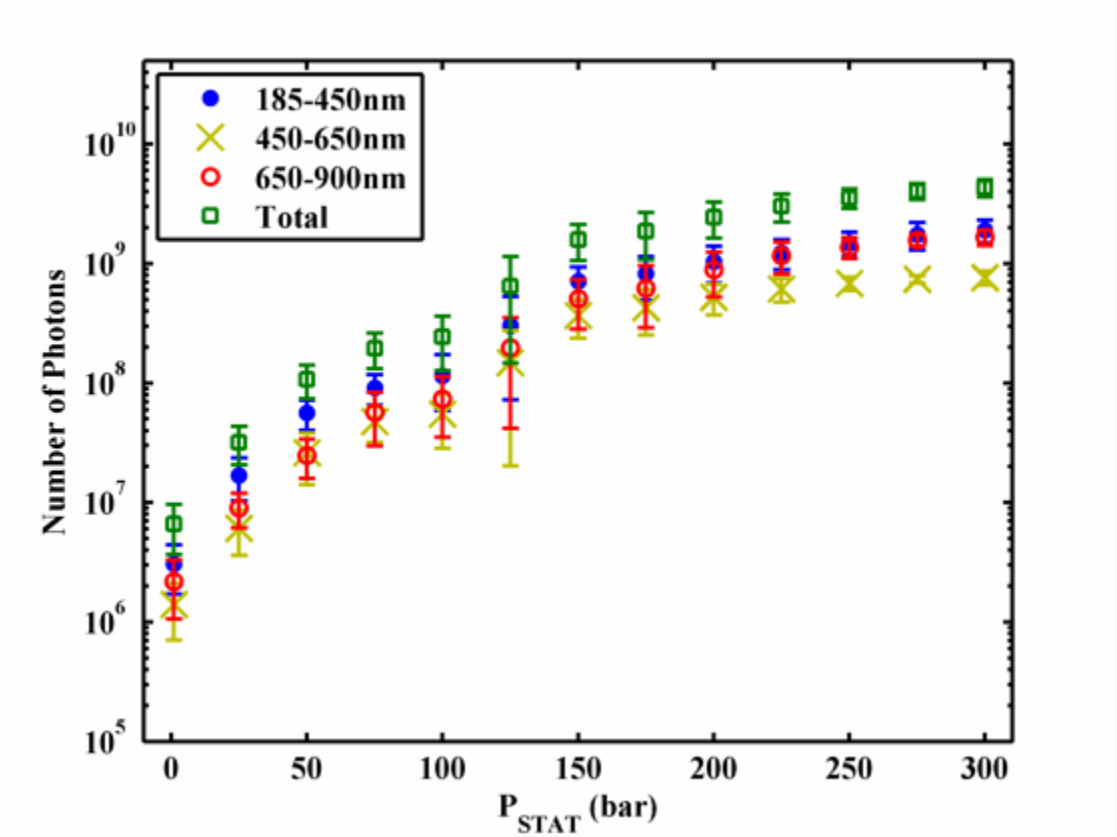

Figure 73: Number of photons from the largest flash of the cavitation event as a function of static pressure.

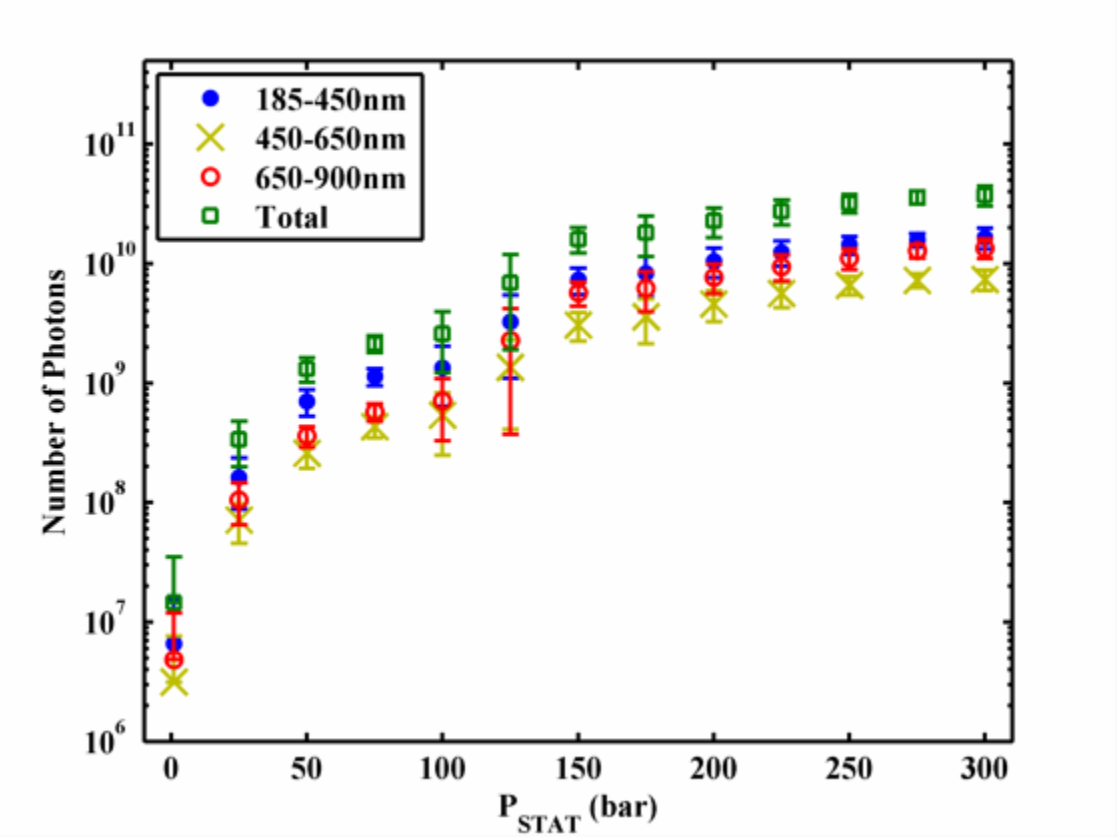

Figure 74: Number of photons from the total cavitation event as a function of static pressure. The lower error bars for data at 1 bar were less than 0, and therefore were not able to be shown on the log scale.

Alternatively, the collapse strength could be viewed in terms of the photon energy:

$$E(\lambda) = \frac{hc}{\lambda} \tag{67}$$

where h = 6.626 x 10^{-34} [J-s] is Plank's constant, c is the speed of light in vacuum, and λ is the wavelength of light, taken from Table 6. These results are plotted in Figure 75-Figure 77.

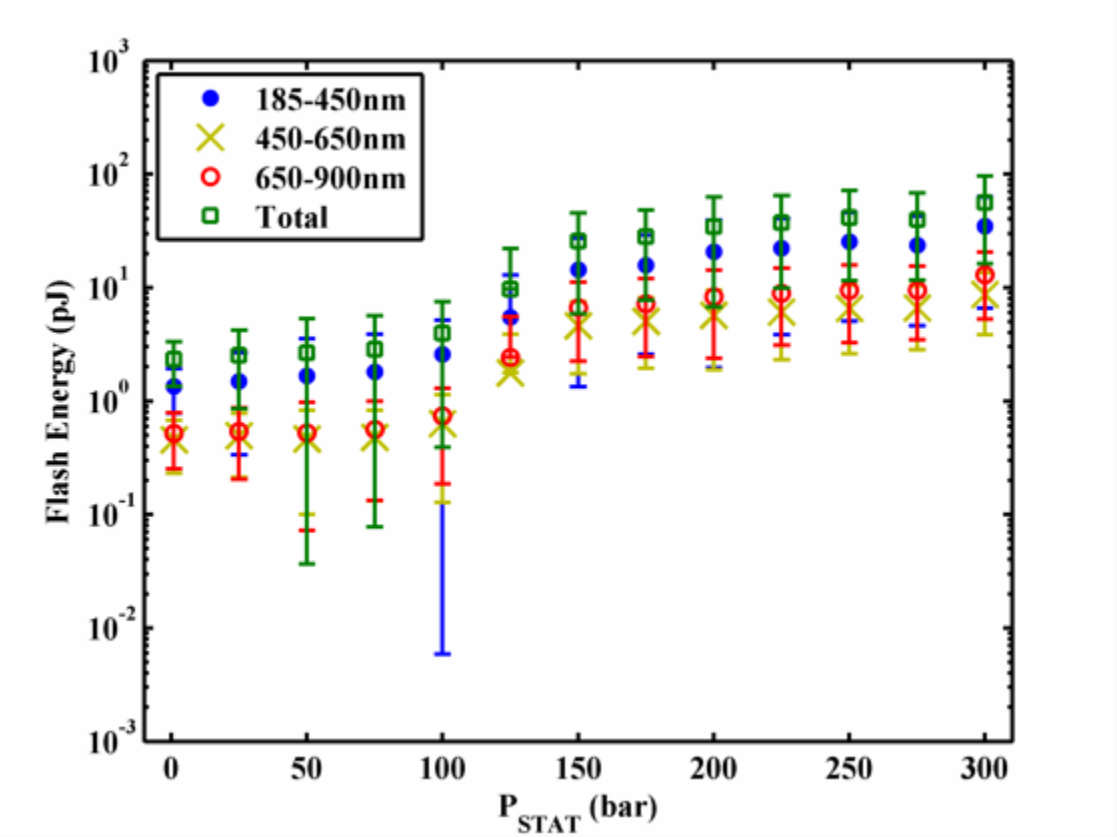

Figure 75: Energy from the first flash of the cavitation event as a function of static pressure. The lower error bars for data at 125 bar were less than 0, and therefore were not able to be shown on the log scale.

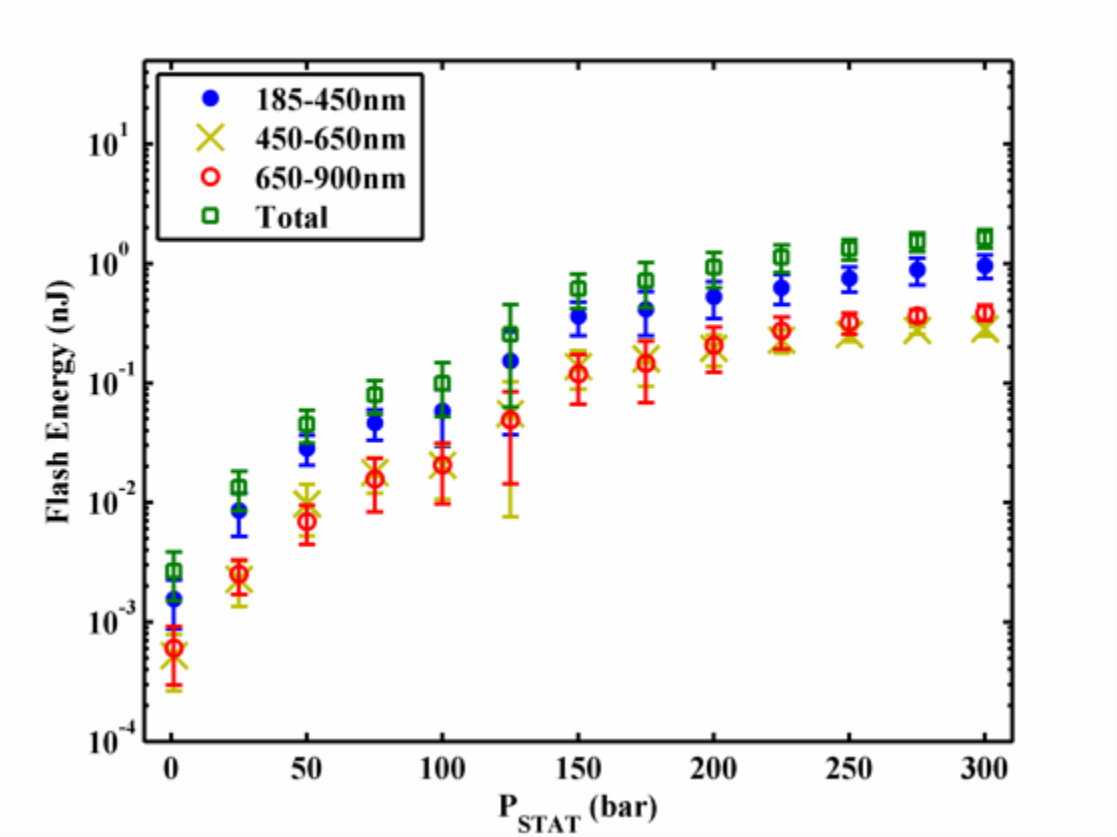

Figure 76: Energy from the largest flash of the cavitation event as a function of static pressure.

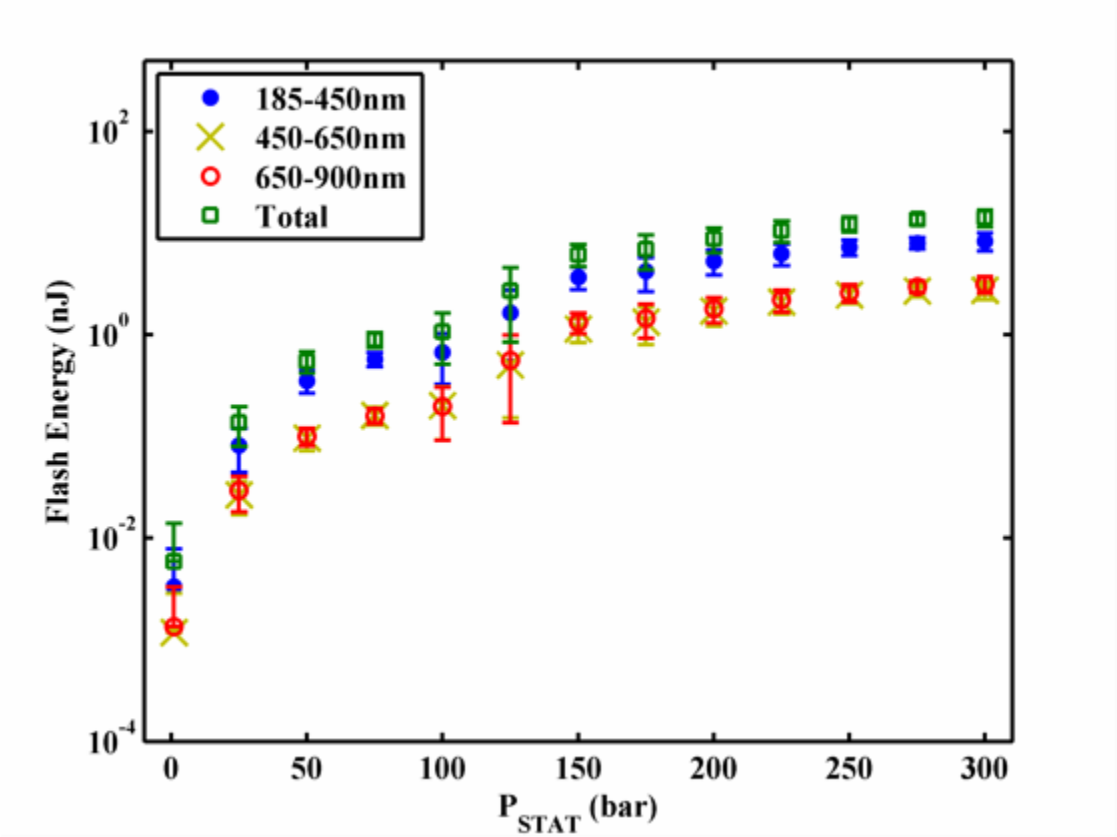

Figure 77: Energy from the total cavitation event as a function of static pressure. The lower error bars for data at 1 bar were less than 0, and therefore were not able to be shown on the log scale.

The flash energy (and number of photons) increases quadratically for all the strength parameters with the static pressure. The coefficients of these fits for the blue band (185-450 nm) and the total flash are listed in Table 14 and Table 15, respectively.

Flash Type	A	B	C	r^2	$\sigma_{\bar{X}}$
First	2.36×10^{-4}	4.23×10^{-2}	-0.54	0.946	2.91
Largest	8.73×10^{-6}	9.02×10^{-4}	-0.04	0.981	4.86×10^{-2}
Event	5.18×10^{-5}	1.67×10^{-2}	-0.54	0.966	5.97×10^{-1}

Table 14: Coefficient for quadratic fits of the blue flash data shown in Figure 75-Figure 77. Here, $X_{OUT} = A\ P_{STAT}^2 + B\ P_{STAT} + C$, where X_{OUT} is the flash energy in [pJ] for the first row, and [nJ] for the second and third rows. r^2 is the coefficient of determination of the fit, and $\sigma_{\bar{X}}$ is the standard error of the fit.

Flash Type	A	B	C	r^2	$\sigma_{\bar{X}}$
First	3.25×10^{-4}	8.91×10^{-2}	-1.44	0.927	5.11
Largest	1.44 x 10-5	1.80×10^{-3}	-0.07	0.977	9.32×10^{-2}
Event	9.66×10^{-5}	2.60×10^{-2}	-0.88	0.973	9.91×10^{-1}

Table 15: Coefficient for quadratic fits of the total flash data shown in Figure 75-Figure 77. Here, $X_{OUT} = A\ P_{STAT}^2 + B\ P_{STAT} + C$, where X_{OUT} is the flash energy in [pJ] for the first row, and [nJ] for the second and third rows. r^2 is the coefficient of determination of the fit, and $\sigma_{\bar{X}}$ is the standard error of the fit.

4. DISCUSSION

4.1. Cavitation Threshold

4.1.1. Range of Fluid Temperature

When possible, the threshold was measured from room temperature (17-22 ºC) up to 35 ºC at each static pressure. In practice, once the sound speed was greater than 1540 m/s it became difficult to produce repeatable data sets due to the (0,6) mode overlapping with a shell dominated mode (see section 3.1.2). This sound speed (~1540 m/s) occurred at lower temperatures as the static pressure was increased, thus limiting the range of temperatures investigated for increasing static pressure.

4.1.2. Temperature Resolution

There was a noticeable influence of temperature on the cavitation threshold for static pressures over an appreciable temperature range. The influence of temperature on the sensors is negligible over this temperature range: the Kistler wall mount hydrophone and Micron static pressure transducer vary in sensitivity by less than 0.1%. As noted in the introduction (see section 1.2), temperature usually only has a strong influence on the threshold for water with appreciable nucleation sites or moderate amounts of dissolved gases. Apfel (1970) notes in the case of a high purity fluid, such as the measurements of Greenspan (1967), the threshold is largely independent of variation in the experimental conditions (in particular, the gas content) because the nucleation sites present are much smaller than the critical size.

However, even in the case of high purity fluids the temperature dependence of water's vapor pressure and surface tension are strong. These temperature-dependent parameters, in turn, strongly influence the threshold predictions of the crevice model.

The temperature dependence of the cavitation thresholds for static pressures 50, 100, and 150 bar are re-plotted in Figure 78 along with a temperature dependent fit (via the temperature dependence of vapor pressure and surface tension) of Equation (11) to the data using a non-linear least squares method. The applicability of this model to the data is discussed in section 4.1.4 below. The data fall within the 95% confidence intervals of the fit, which is suggestive that the model is consistent with the temperature dependence of the data. The values for the fitting parameters are shown in Table 16. Since the contact angle will vary with temperature, the overall volume, and therefore the internal pressure, will also be affected by temperature. Hence, the gas pressure, P_G, was also used as a fitting parameter in Equation (11).

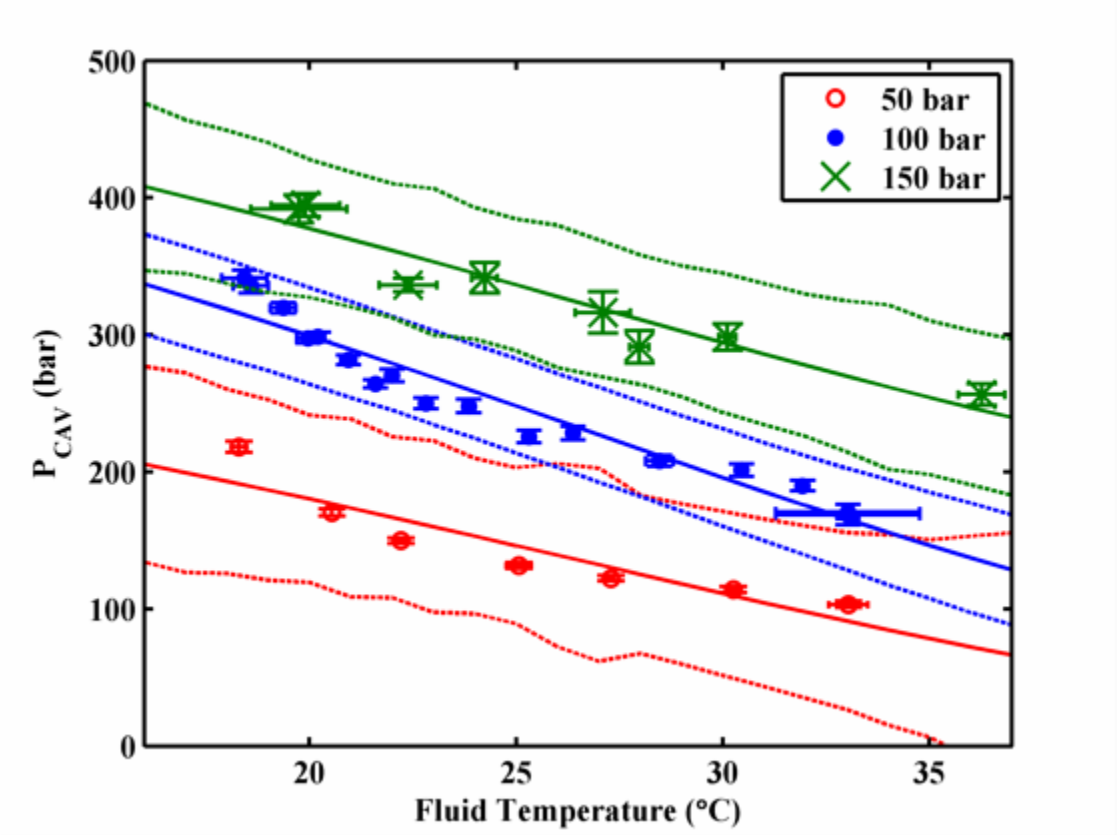

Figure 78: P_{CAV} as a function of fluid temperature at static pressures 50, 100, and 150 bar. The solid lines are fits to Crum's model for nucleation from a crevice [Equation (11)], and the dashed lines are the 95% confidence intervals of the fit to the data.

P_{STAT} (bar)	γ	δ	φ	P_G
50	1 (fixed)	1.24×10^{-2} (-88.45, 88.47)	3.43 (-85.16, 92.03)	1078 -3.57×10^{10}, 3.57×10^{10})
100	1 (fixed)	1.65×10^{-2} (-10.37, 10.4)	3.43 (-10.85, 17.71)	1560 (-8.64×10^{9}, 8.64×10^{9})
150	1 (fixed)	3.07×10^{-2} (-26.4, 33.23)	3.42 (-26.4, 33. 3)	1069 (-1.46×10^{10}, 1.46×10^{10})

Table 16: Best fit parameters of crevice model to temperature dependent threshold. The 95% confidence intervals are shown in brackets. The value of γ was fixed at its physical bounds by the fitting algorithm.

Besides the crevice model, the temperature dependence of the data was modeled by an exponential decay of the form $P_{CAV} = A \exp[-\alpha T]$ up to 250 bar. The best-fit decay constant (using a non-linear least square method) α is plotted as a function of the static pressure in Figure 79. The decay constant itself decays exponentially with the static pressure, as evidenced by the exponential fit (solid red line in Figure 79) of α to P_{STAT}. The solid red curve in Figure 79 has the form:

$$\alpha = 0.0536 \exp\left[-0.004178 P_{STAT}\right] \quad (68)$$

The threshold at 1 bar deviates from the linear predictions of the threshold dependence of static pressure (see section 4.1.3). If the data point at 1 bar in Figure 79 are neglected, the amplitude and decay constants in Equation (68) become

$$\alpha = 0.0799\exp\left[-0.007245P_{STAT}\right] \quad (69)$$

The coefficient of determination is $r^2 = 0.484$ and the standard error is $\sigma_{\bar{x}} = 1.32 \times 10^{-2}$ for Equation (68). For Equation (69), the coefficient of determination is $r^2 = 0.914$ and the standard error is $\sigma_{\bar{x}} = 5.60 \times 10^{-3}$.

The correspondence of α to the exponential fits of Equation (68) and Equation (69) suggest that the influence of temperature on the threshold has a diminishing effect as the static pressure of the fluid is increased. If the upper range of strong temperature dependence is taken to be the decay constants of Equation (68) and Equation (69), the cavitation threshold should be largely independent of the fluid temperature in the range of 138-240 bar. Hence, beyond this range of static pressures, the temperature dependence of vapor pressure and surface tension no longer have as strong an influence on the crevice model, and nucleation may depend solely on overcoming the large overpressure.

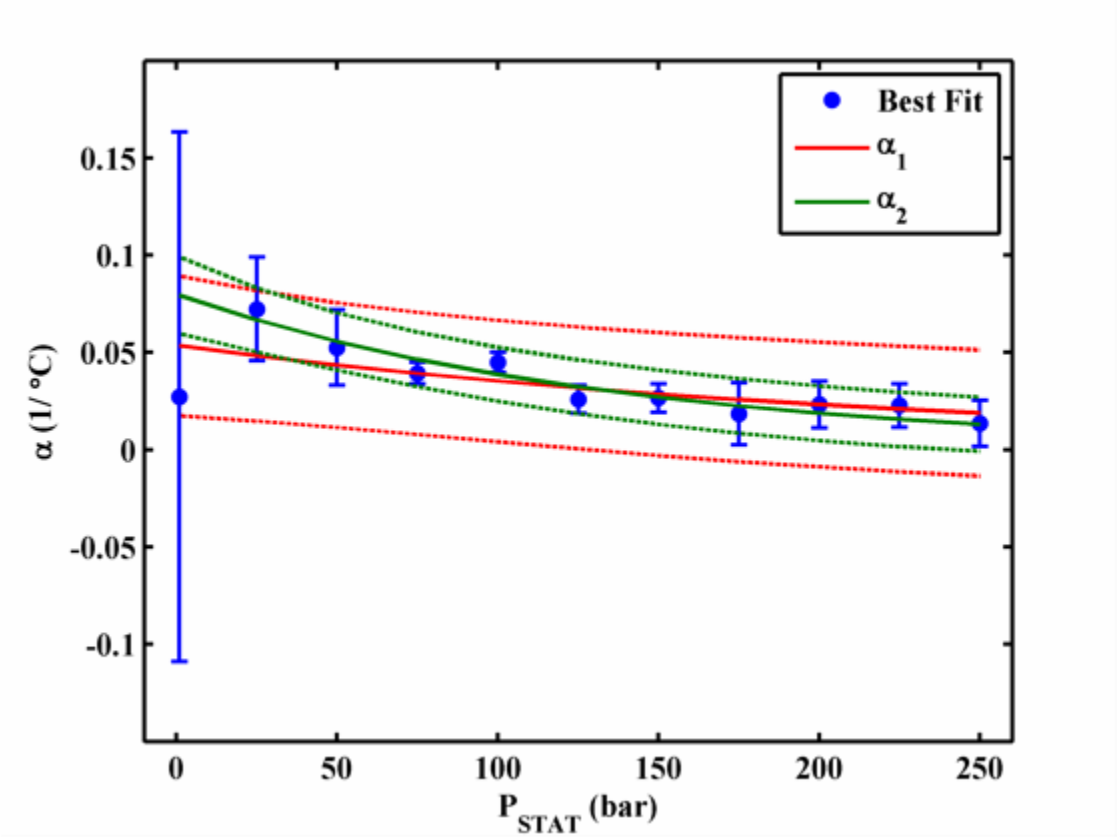

Figure 79: Exponential coefficient α as a function of static pressure. The vertical error bars come from the 95% confidence intervals of the fit to the data. The solid red line the exponential fit of α to the entire static pressure range [Equation (68)], and the dashed lines are the 95% confidence intervals of the fit. . The solid green line the exponential fit of α to 25-250 bar [Equation (69)], and the dashed lines are the 95% confidence intervals of the fit.

4.1.3. Static Pressure Resolution

The cavitation threshold increases linearly with the static pressure as evident in Figure 67 and Figure 68, especially above 1 bar. The deviation from linearity at 1 bar was also observed by Herbert et al. (2006), who concluded it was due to either the presence of impurities in the form of air bubbles or that the properties of the focused transducer were pressure dependent.

The threshold was fit linearly to the static pressure for each of the temperatures shown in Figure 67. These fitting parameters are plotted in Figure 80 and Figure 81 as a function of fluid temperature. Both of these parameters decrease slightly over the measured temperature range. However, no fitting functions were found to adequately describe the data. Regardless, the decreasing trend with temperature for both parameters suggests lower temperatures result in higher cavitation thresholds.

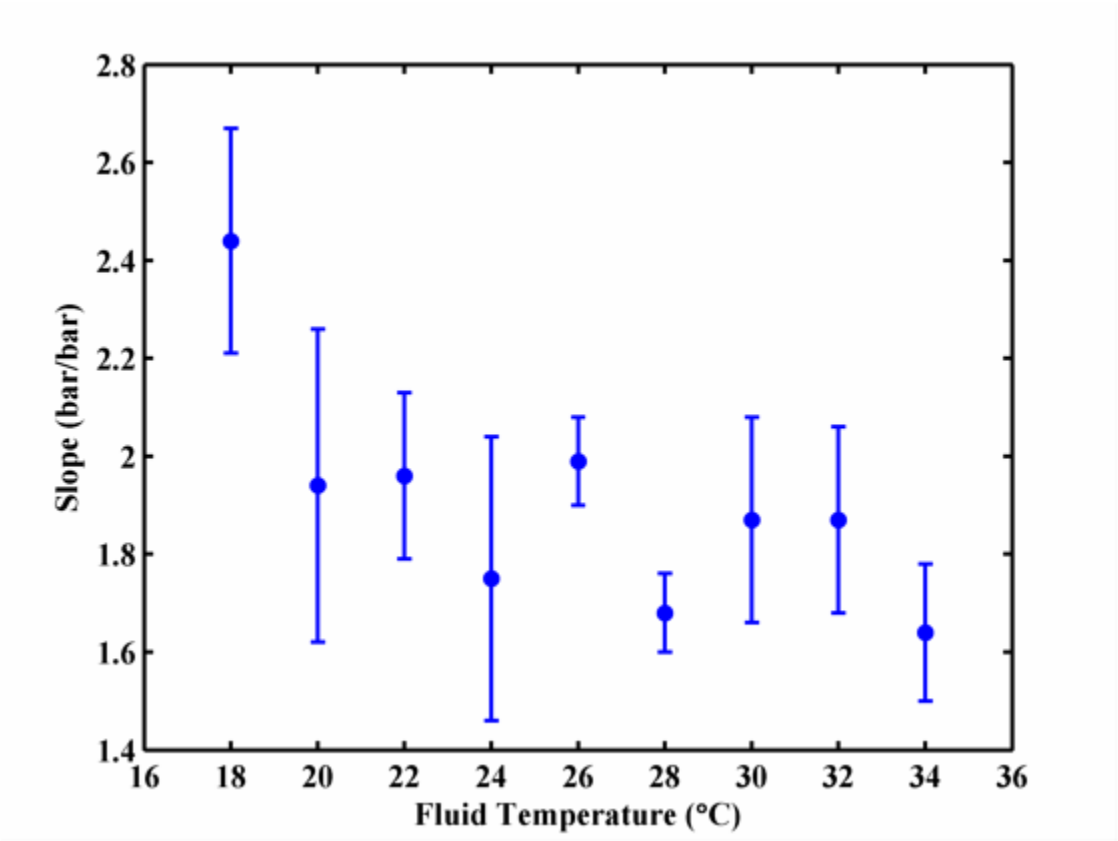

Figure 80: Slope of linear fit of P_{CAV} to P_{STAT} as a function of fluid temperature (+/- 1 ºC) recorded in Table 12. The magnitude of the error bars are calculated by the 95% confidence intervals of the fitting parameters.

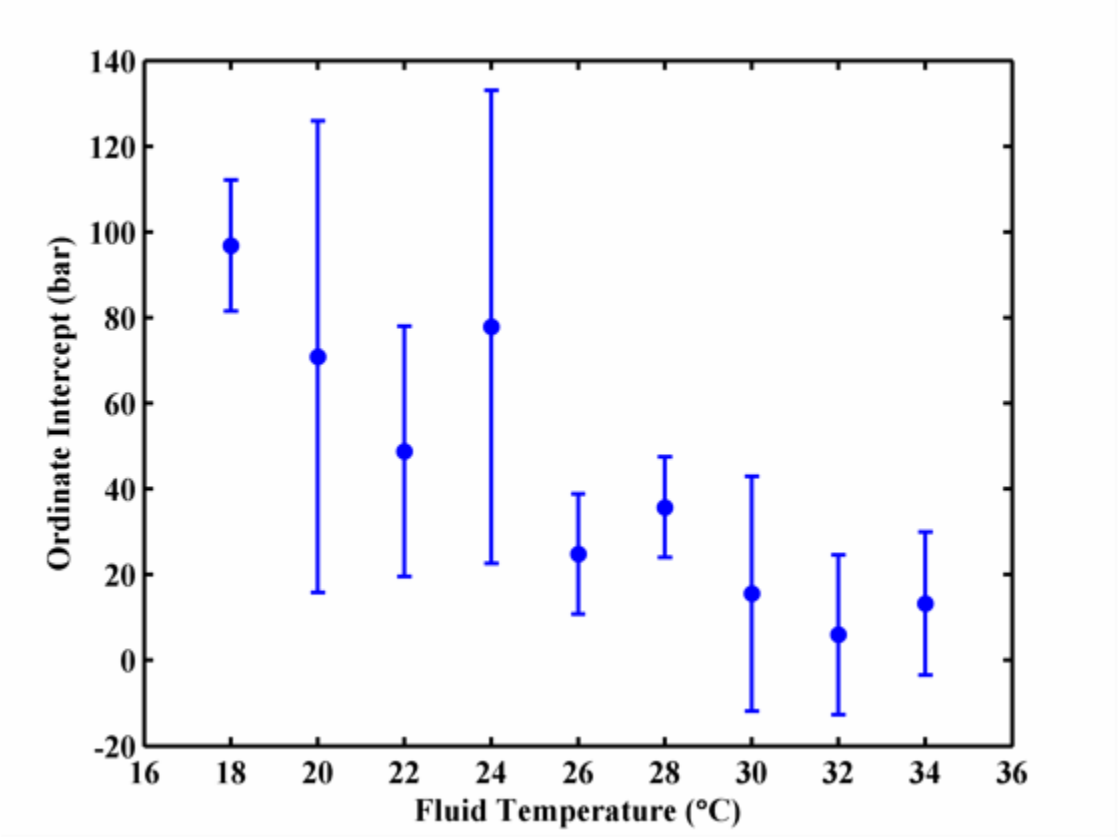

Figure 81: Ordinate intercept of linear fit of P_{CAV} to P_{STAT} as a function of fluid temperature recorded in Table 12. The magnitude of the error bars are calculated by the 95% confidence intervals of the fitting parameters

The static pressure dependence of the "temperature averaged" cavitation threshold was found to be:

$$P_{CAV} = 1.92P_{STAT} + 34.64 \quad (70)$$

where P_{CAV} and P_{STAT} are both in units of bar. The absolute tension required to produce cavitation, $|P_{CAV} - P_{STAT}|$, is readily calculated from Equation (66):

$$|P_{CAV} - P_{STAT}| = 0.92P_{STAT} + 34.64 \quad (71)$$

The linear relation between the static pressure and the tension required to reach the cavitation threshold is in contradiction with the findings of Herbert et al. (2006) who found the absolute tension required for cavitation essentially constant, although temperature dependent, up to 80 bar (160-250 bar tension required for cavitation over the temperature range 2-82 ºC). Equation (71) indicates the static pressure must be approximately 230 bar for the data used to fit Equation (66) before Herbert's largest tensions (~250 bar at 2 ºC) are reached. The tension required for inertial cavitation at 266 bar static pressure is 280 bar. This is the same tensional strength of water measured as by Briggs (1950), which is generally accepted as the largest tension required for cavitation (Mørch 2007, Finch 1964, Leighton 1994, Apfel 1984), excluding the mineral inclusion method (Caupin and Herbert 2006). At 300 bar static pressure, the tension required for inertial cavitation is 310 bar, some 30 bar larger than Briggs' measurement.

4.1.4. Nucleation Mechanisms

The linear dependence of the tension on the static pressure suggests that the nucleation sites within the fluid are becoming more difficult to nucleate at the elevated static pressures. The nature of these nucleation sites can be investigated by comparing the static pressure temperature averaged threshold to the models for bubble nucleation/onset of inertial collapse discussed previously in section 1.3: homogenous nucleation (section 1.3.1), the crevice model for nucleation [Equation (11)], and Holland's model for the onset of inertial cavitation for a pre-existing bubble [Equation (27)]. The homogenous threshold is defined when the product of *n* in Equation (9), the volume over which cavitation can occur, and the time over which cavitation

can occur, is greater than 1. The cavitating volume was defined as the volume over which the acoustic pressure amplitude is greater than 95% of its maximum value (this corresponded to a sphere of radius 5 mm). The time was defined as 1 second (the ramp rate was 1 bar/s).

The input parameters for the inertial threshold of pre-existing bubbles in Equation (27) were chosen to be representative of the data sets taken. The driving frequency was taken directly from the data sets. The pre-existing initial bubble radii at atmospheric pressure were set to 50 nm based on the smallest pore size of the filter (100 nm). The initial bubble radii at elevated static pressure were computed assuming isothermal compression

$$P_{H2} = \left(P_{H1} + \frac{2\sigma}{R_{01}} - P_V\right)\left(\frac{R_{01}}{R_{02}}\right)^{3\gamma} + P_V - \frac{2\sigma}{R_{02}} \tag{72}$$

where the subscript 1 denotes values at 1 bar static pressure, and the subscript 2 denotes values at some elevated static pressure. The fluid density was calculated from the static pressure using the Tait equation of state. Holland's model only has a weak dependence on *T*. *T* was set to ~ 40, which corresponds to a final gas temperature of 1eV (~10000 K) and initial temperature of 298 K (20 ºC). The fitting parameters in the crevice model in Equation (11) were adjusted (within the range of physical values for the parameters) to best-fits of the temperature-averaged data.

The temperature-averaged threshold, along with the predictions of each model, are shown in Figure 82. The crevice model appears most consistent with the data, although this is the only model with fitting parameters. Nevertheless, the crevice model is likely giving the closest view of the nucleation mechanisms at work: homogenous nucleation has never been achieved, except in the controversial mineral exclusion methods (Mørch 2007) and other circumstances requiring acoustically levitated liquid drops near the vaporization temperature (Apfel 1970a). The survival

of any existing free bubbles (i.e. not trapped in any crevice or supported by an amphiphilic shell) seems unlikely. Even in the case of gassy fluids, bubbles at 1 atm have been shown to dissolve into solution (due to surface tension) within seconds of inception (Leighton 1994). Furthermore, the analysis of the particulate content of the liquid indicates that were some 10^6 particles/mL present for particle sizes 0.1-20 μm (see Figure 12). Based on the data in Figure 11, the particulates are likely leached from the wall of the resonator due to the impingement of the high amplitude shockwaves associated with the collapse of the cavitation events, which is consistent with the findings of Greenspan (1967). These particulates are likely in the form of stainless steel burrs that, owing to the nature in which they were leached from the resonator wall, will have similarly rugged topology to those documented by Crum (1979). Such topology would place the particulates as prime candidates for the crevice model.

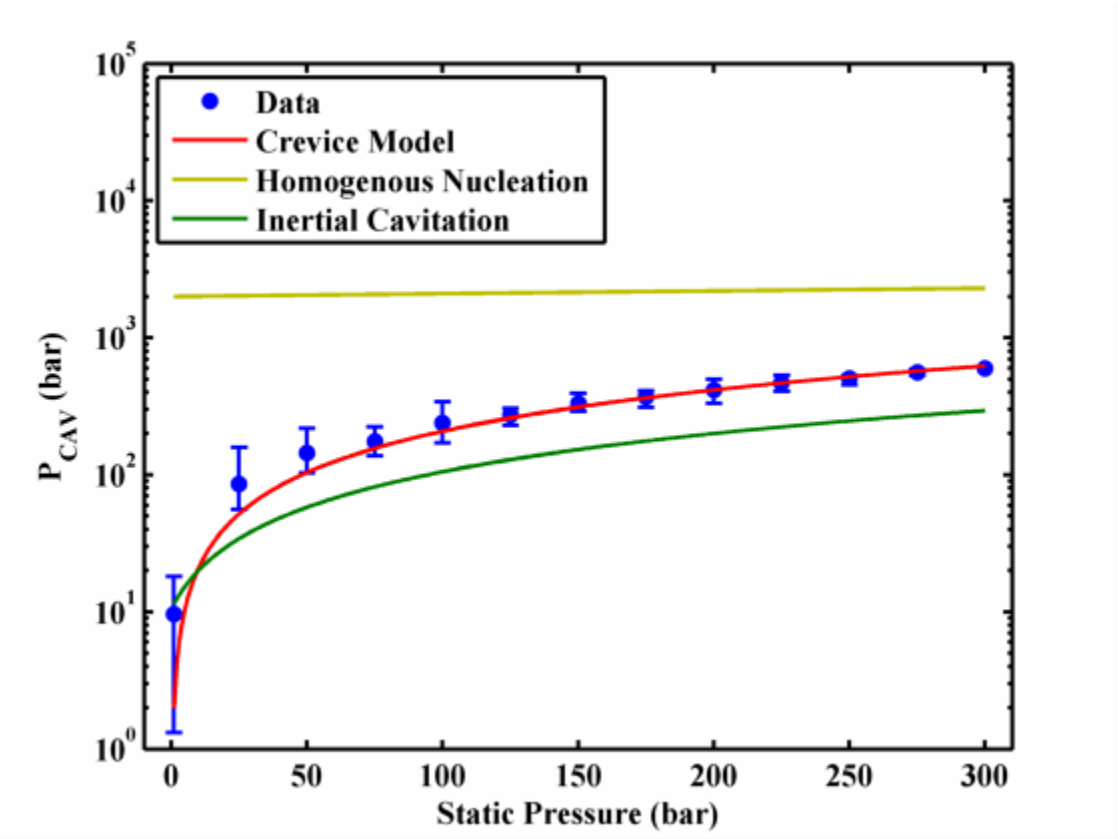

Figure 82: Static pressure dependence of temperature averaged cavitation threshold compared to the predictions of the crevice model for nucleation, homogenous nucleation theory, and the threshold for the onset of inertial cavitation of pre-existing bubbles. The vertical error bars on the data represent the spread in measured threshold with temperature.

The homogenous nucleation threshold is approximately linear, although it has a (relatively) weak dependence on the static pressure, with a slope of ~1 [bar/bar]. The crevice model (also linear), in contrast, has a slope of nearly 2 [bar/bar]. If these linear fits remain applicable at higher static pressures, the two thresholds should intersect at ~ 1.85 kbar static pressure. Therefore, beyond the 1.85 kbar mark the threshold is no longer dictated by the particulate

content (i.e. nucleation sites) but by homogenous nucleation and the creation of vapor bubbles. The measured threshold, Equation (66), intersects the homogenous threshold at 2.14 kbar.

However, the crevice model will dominate the limit of the cavitation threshold over the measured static pressure range. The linear dependence of tension with the static pressure suggests that the nucleation sites within the fluid are becoming more difficult to nucleate at elevated static pressures. To explore this possibility, the crevice model can be used to calculate the size of the crevice mouth, *a*, as a function of the static pressure. The fitting parameter δ in Crum's model [Equation (11)] can be written in terms of the advancing contact angle, α_A, and the half angle of the conical crevice, β:

$$\delta = |\cos(\alpha_A - \beta)| \tag{73}$$

Equation (73) can be used along with Equation (2) from Apel (1970) to calculate the radius of the crevice at the liquid/gas interface *a:*

$$a = \frac{2\sigma\delta}{P_H - P_V - P_G} \tag{74}$$

These calculated crevice sizes were sub-nanometer and there was a weak decrease in the crevice size with the static pressure. However, the 95 % confidence intervals of δ were large enough that the predicted crevice size had over an order of magnitude error bar and no definite trends could be established. The results are summarized in Appendix B.

4.2. Strength of Collapse

4.2.1. Shock Waves

4.2.1.1. Relative Increase with Static Pressure

As discussed in section 1.1, the motivation for looking at cavitation in high static pressures is to create conditions capable of producing thermonuclear reactions within the collapsing bubble. Since the shock sensor was not calibrated in terms of pressure, it was instructive to consider relative change in the shock strength parameters to resolve their static pressure dependence. These plots, along with the appropriate polynomial fits are shown in Figure 83-Figure 85. The forms of the polynomial fitting functions are shown in Table 17.

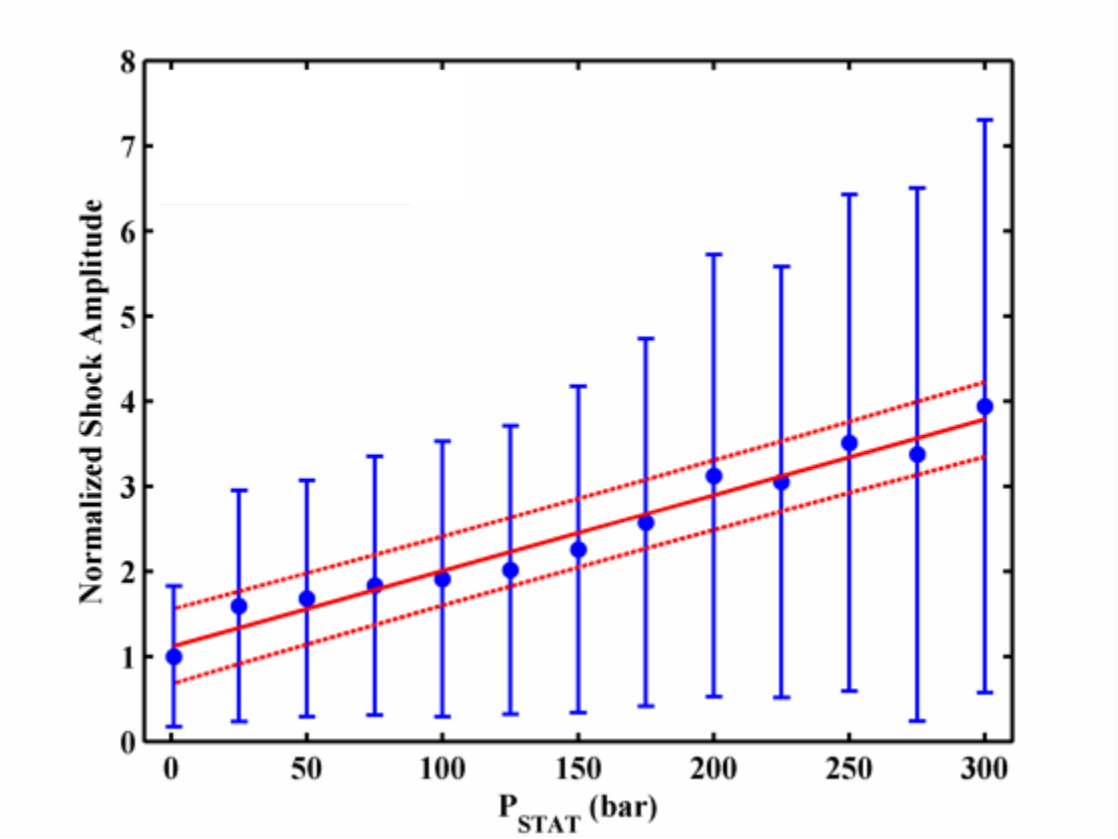

Figure 83: Amplitude of the first shock wave of cavitation event, normalized to the amplitude at 1 bar as a function of the static pressure. The solid red line is a linear fit to the data, while the dashed red lines are the 95% confidence intervals of the fit to the data.

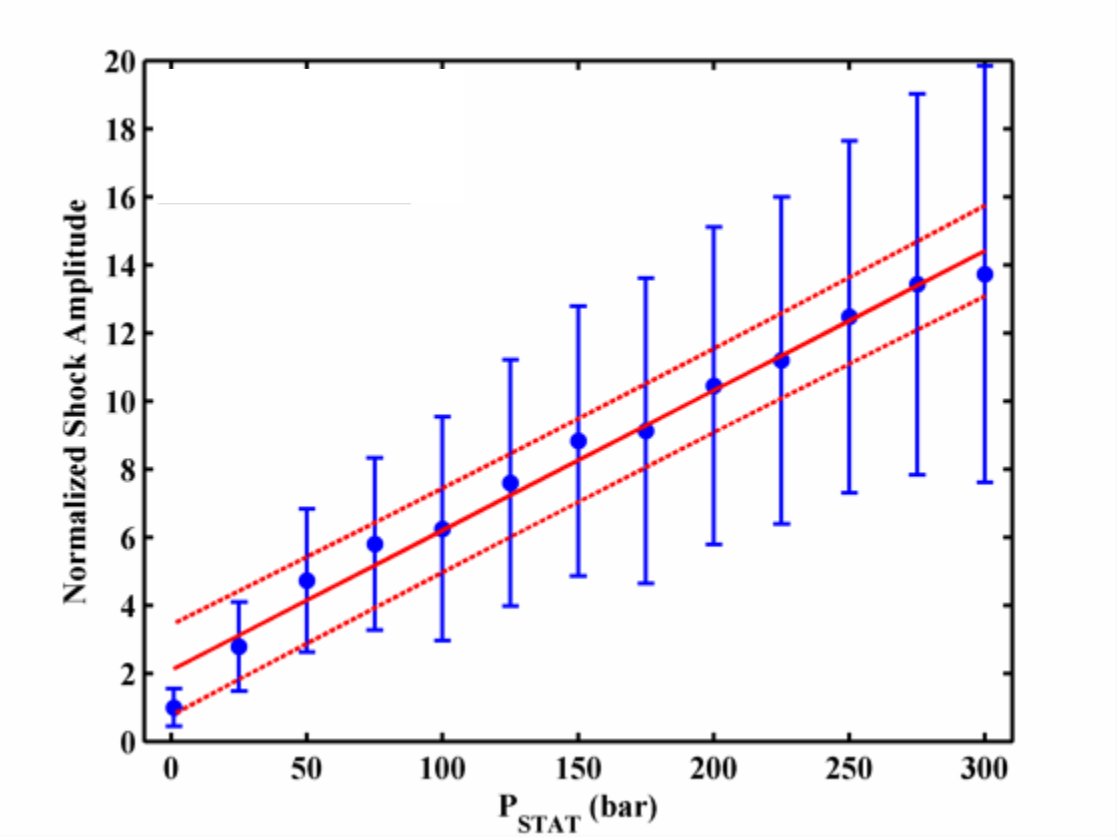

Figure 84: Amplitude of the largest shock wave of cavitation event, normalized to the amplitude at 1 bar, as a function of the static pressure. The solid red line is a linear fit to the data, while the dashed red lines are the 95% confidence intervals of the fit to the data.

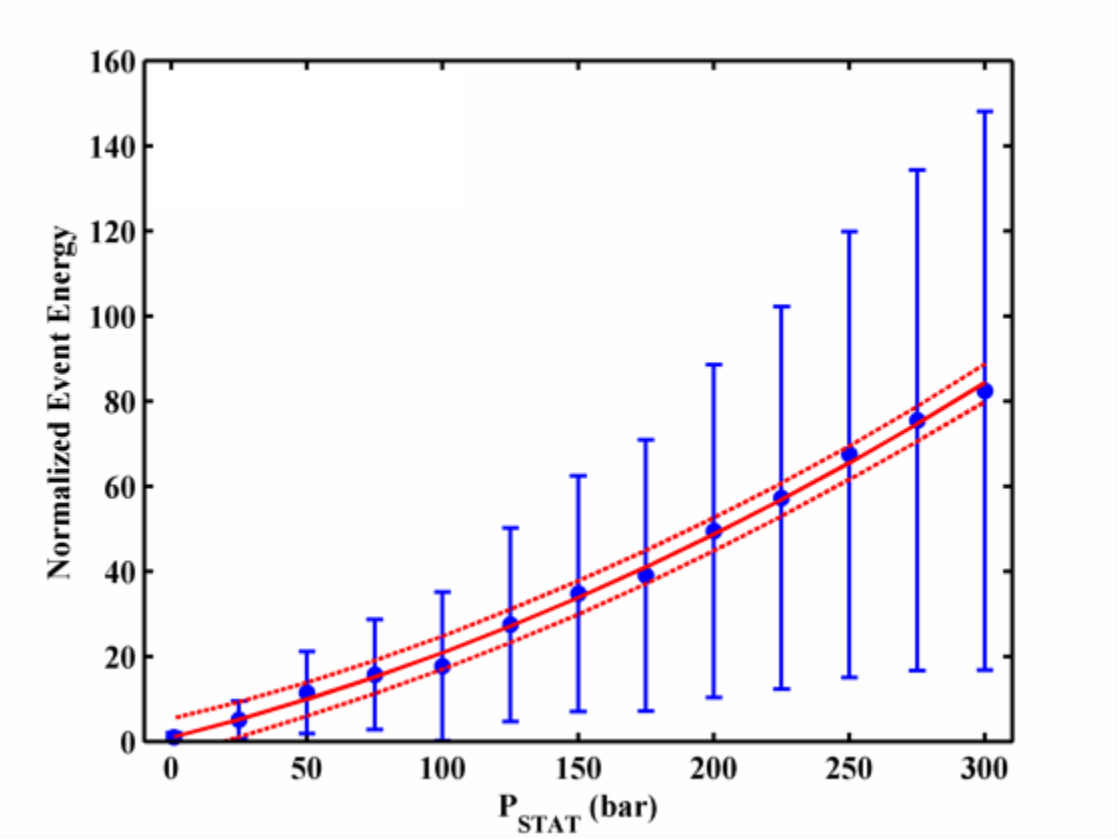

Figure 85: Shock wave energy of cavitation event, normalized to event energy at 1 bar, as a function of the static pressure. The solid red line is a quadratic fit to the data, while the dashed red lines are the 95% confidence intervals of the fit to the data.

Shock Type	A	B	C	r^2	$\sigma_{\bar{X}}$
First	0	8.91×10^{-3}	1.11	0.963	1.77×10^{-1}
Largest	0	4.11×10^{-2}	2.10	0.984	5.44×10^{-1}
Event	3.92×10^{-4}	1.61×10^{-1}	9.13×10^{-1}	0.996	1.63

Table 17: Coefficient for linear and quadratic fits of data shown in Figure 69-Figure 71. Here, $X_{OUT} = A\ P_{STAT}^2 + B\ P_{STAT} + C$, where X_{OUT} is the shock amplitude normalized to the amplitude at 1 bar for the first and second rows, and the event energy normalized to the energy at 1 bar for the third row. r^2 is the coefficient of determination of the fit, and $\sigma_{\bar{X}}$ is the standard error of the fit.

4.2.1.2. Prospects for Thermonuclear Fusion

Over the 0-300 bar static pressure range, the first shock increases by a factor of 4, the largest shock increases by a factor of 14, and the event shock energy increases by a factor of 84. These scale factors with the static pressure are consistent with a stronger inertial collapse at elevated static pressures. However, as discussed in section 4.1, the tension (and therefore acoustic energy) required to reach the nucleation threshold also increases with the static pressure. The ratio of the event energy and acoustic energy ($\sim P^2_{CAV}$) is plotted in Figure 88, and is approximately constant over the static pressure range. The normalized shock amplitudes (first in Figure 83 and largest in Figure 84) are also approximately constant over the static pressure range. The lack of static pressure dependence for these ratios suggests that the increase in the event shock energy (or amplitude) is not due to the larger overpressures driving the collapse, but to the larger amount of acoustic energy available to the system. Hence, increased static pressure does not increase the collapse strength in the intended way. Instead of imparting an additional inertia to the liquid,

forcing the bubbles to collapse stronger, the high static pressures increase the cavitation threshold, thereby increasing the amount of acoustic energy that can be stored in the system. As with any mechanical system, the stored acoustic energy is converted to other forms such as the creation of the cavitation event and the subsequent cavitation activities (e.g. oscillation, the emission of shock waves, light production, etc.). Hence, the more energy in the system, the larger the shock energy will be in proportion.

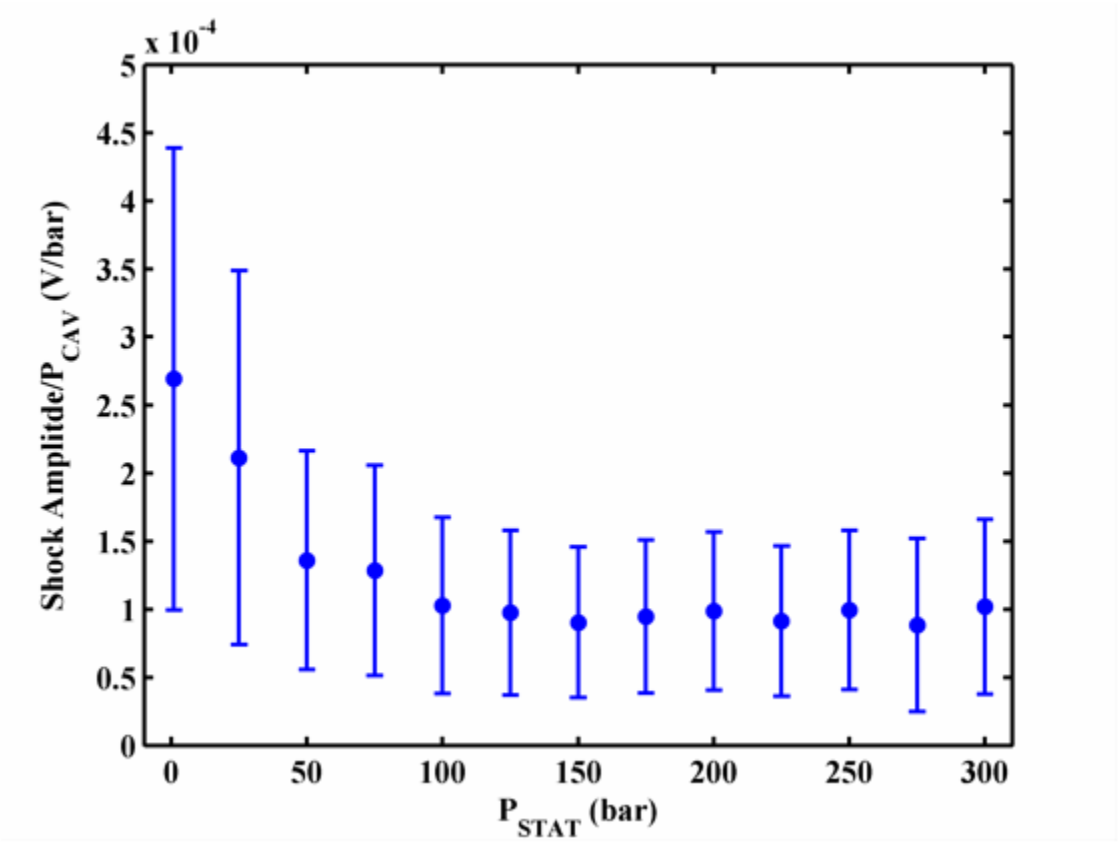

Figure 86: Amplitude of the first shock of cavitation event normalized to P_{CAV} as a function of the static pressure in the fluid.

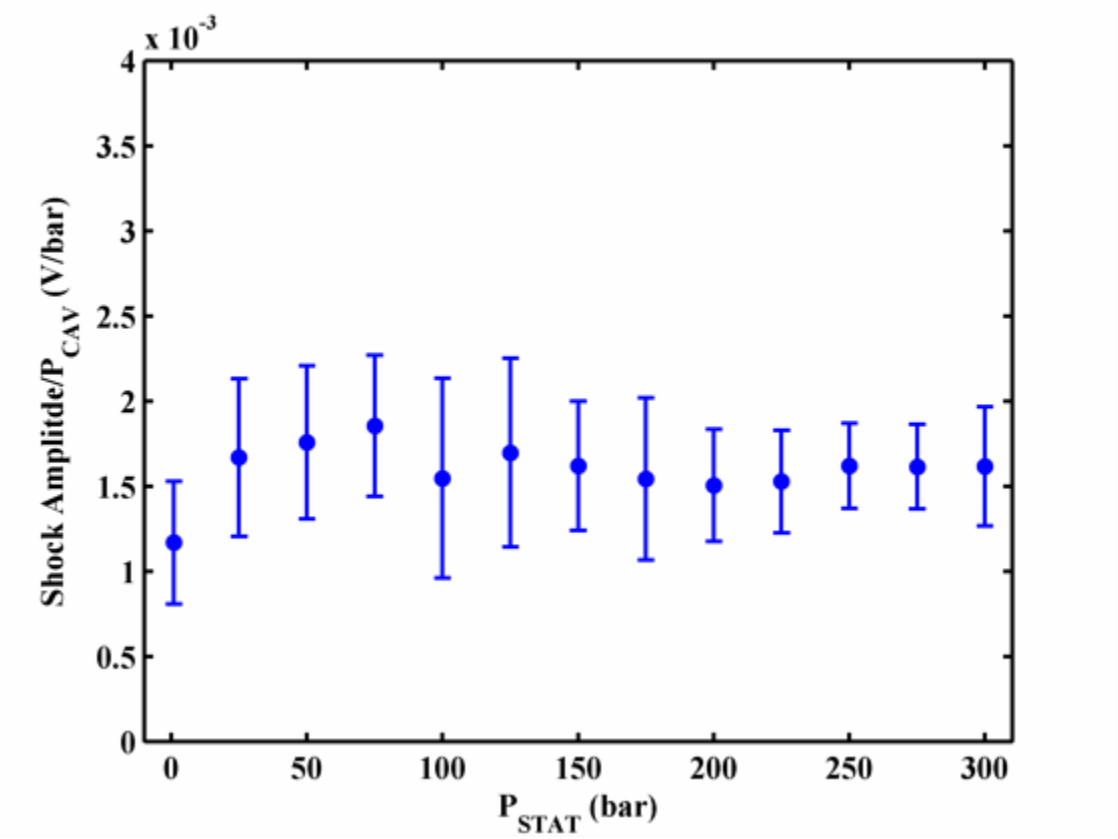

Figure 87: Amplitude of the largest shock of cavitation event normalized to P_{CAV} as a function of the static pressure in the fluid.

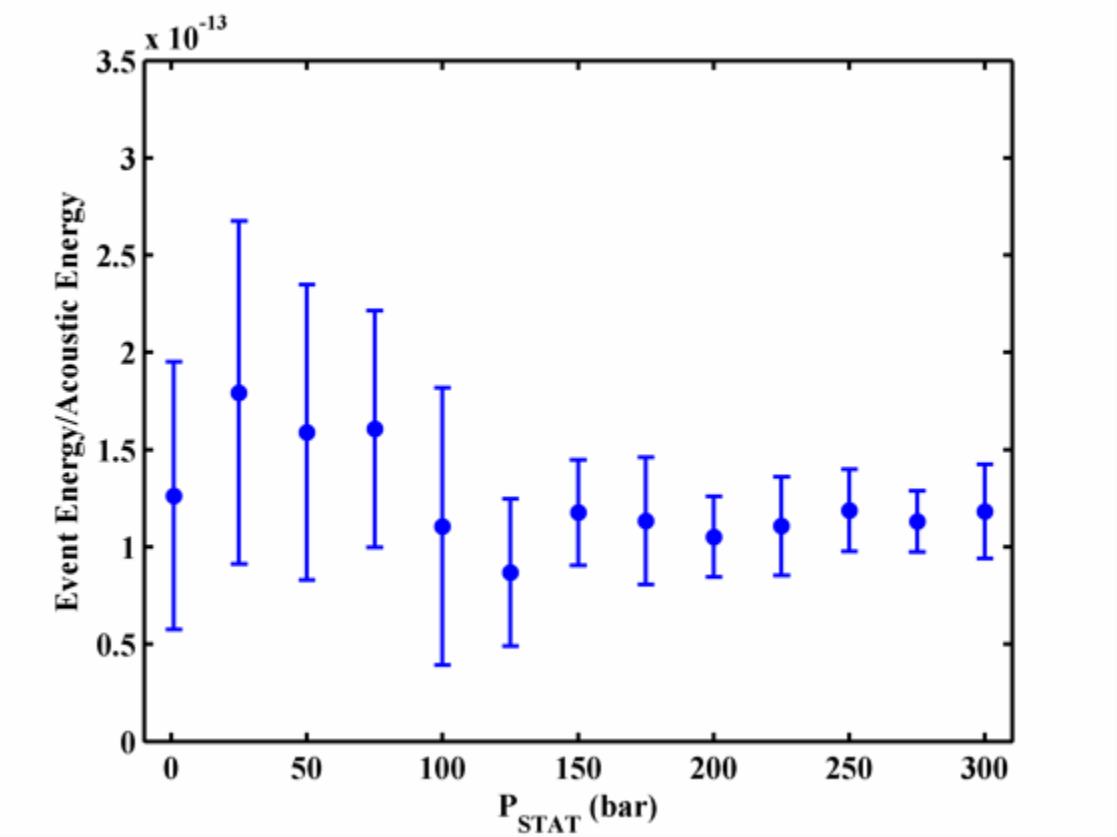

Figure 88: Shock wave energy of the cavitation event normalized to acoustic energy (P_{CAV}) as a function of the static pressure in the fluid.

4.2.2. Light Emissions

4.2.2.1. PMT Saturation

The light emissions in section 3.3.2 had an apparent discontinuity after the neutral density filters were implemented at 125 bar. This was likely caused by non-linearity saturation of the PMTs, since the transmission spectrum of the NDF are within the manufacturer's specifications as shown in Figure 29. The maximum linear count from Table 5 was measured at 468 nm. The maximum linear count at wavelength λ can be calculated as

$$N_{MAX}(\lambda) = N_{MAX}(\lambda')\frac{QE(\lambda')}{QE(\lambda)} \quad (75)$$

where $N_{MAX}(\lambda)$ is the maximum linear count at wavelength λ, $QE(\lambda)$ is the quantum efficiency of the tube at wavelength λ, and the prime indicates a known quantity. At 468 nm, the R928 has a *QE* of 18.47%. The adjusted maximum linear count for each of the three tubes at the effective wavelength of the tube (from Table 6) is shown in Table 18. Also shown are the total number of photons for the flash, accounting for the quantum efficiency of the tube, full angular distribution, and absorption of light through the water path.

Tube	**Effective Wavelength (nm)**	**Maximum Linear Count**	**Total Number of Photons**
Oriel	713.34	1.20×10^4	5.78×10^7
H957	531.73	3.79×10^3	1.56×10^7
H7732	391.88	2.14×10^4	9.95×10^7

Table 18: Maximum linear count for each PMT using Equation (75) and data from Table 5. The total number of photons account for the quantum efficiency of the tube, full angular distribution, and absorption of light through the water path.

The useful range of data in Figure 72-Figure 74 can be determined from the wavelength adjusted maximum linearity count, the last column in Table 18. All the tubes are within the linear regime for the first flash. For the largest flash, the Oriel (650-900 nm) saturates beyond 200 bar, the H957 (450-650 nm) saturates beyond 50 bar, and the H7732 (185-450 nm) saturates beyond 225 bar. The data shown in figures Figure 72-Figure 74 represent a lower limit to the light

emissions at the saturation limit for each band. Despite these apparent saturations, the total light emissions are the same order of magnitude as reported by others (Gaitan et al. 2010, Hiller et al. 2007).

Even with tube saturation, there is still an unaccounted for discontinuity after implementing the NDFs in the first flash in Figure 75, where all tubes are still in the linear regime. The possible contribution of the NDFs to the discontinuity could not be determined. The following possible contributions of the NDFs to the discontinuity were investigated:

- Tube saturation was an issue for the largest flashes. However, it was not an issue for the first flashes (as previously stated).
- The transmission spectra of the NDFs were found to be as specified.
- The manufacturer's specification for damage threshold, in the limit of continuous use, for the NDFs is 750 mW/cm^2. For the most intense flashes at 300 bars, the (lower limit due to saturation) energy emitted is approximately 20 nJ over the full angular distribution (the NDFs are approximately 22cm from the center of the sphere), the flash width is approximately 100 ns, and the area of the NDFs are 5 cm^2. The intensity of most energetic flashes incident on the NDFs are 0.13 mW/cm^2, well below the damage threshold of the NDF.
- The NDFs are designed to be reflective (90% of incident light is reflected). If the reflected light were normally incidence on a surface with index of refraction *n*, the effective amount of light transmitted through the NDF can be calculated as

$$T = 0.1\left[\sum_{i=0}^{\infty}\left(0.9\frac{n-1}{n+1}\right)^{i}\right] \tag{76}$$

Any likely planar-like reflections would most likely occur between the sapphire windows and the NDF. Sapphire's index of refraction is nominally 1.8, and $T \sim 0.13$. For $T = 0.2$, the index of refraction for the reflecting surface would have to be 3.55.

Regardless, there is some apparent discontinuity before and after the NDFs were implemented.

4.2.2.2. Relative Increase with Static Pressure

The light emissions from the blue band (185-400 nm, H7732 PMT module), where tube saturation was minimal, will be used in the following analysis of the light emission dependence on the static pressure. Each of the flash strength-of-collapse parameters (first flash, largest flash, and light emissions from the entire event) in Figure 75-Figure 77 increase quadratically with the static pressure. The coefficients for these quadratic fits were listed in Table 14. As discussed with the shock wave data, the strength parameters normalized to their 1 bar values resolve their relative static pressure dependence. The normalized flash data are plotted in Figure 89-Figure 91. The normalized quadratic fit coefficients are listed in Table 19.

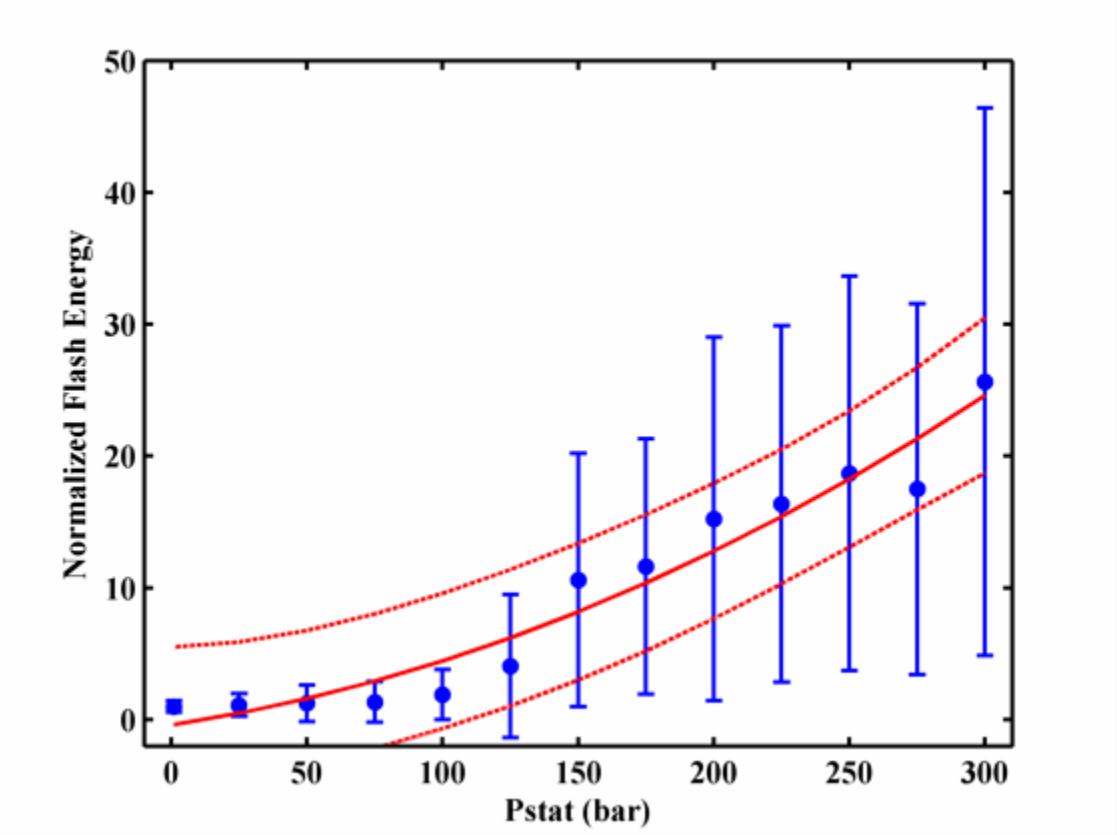

Figure 89: Energy of the first flash of the blue band (185-400 nm) of the cavitation event, normalized to the amplitude at 1 bar as a function of the static pressure. The solid red line is a linear fit to the data, while the dashed red lines are the 95% confidence intervals of the fit to the data.

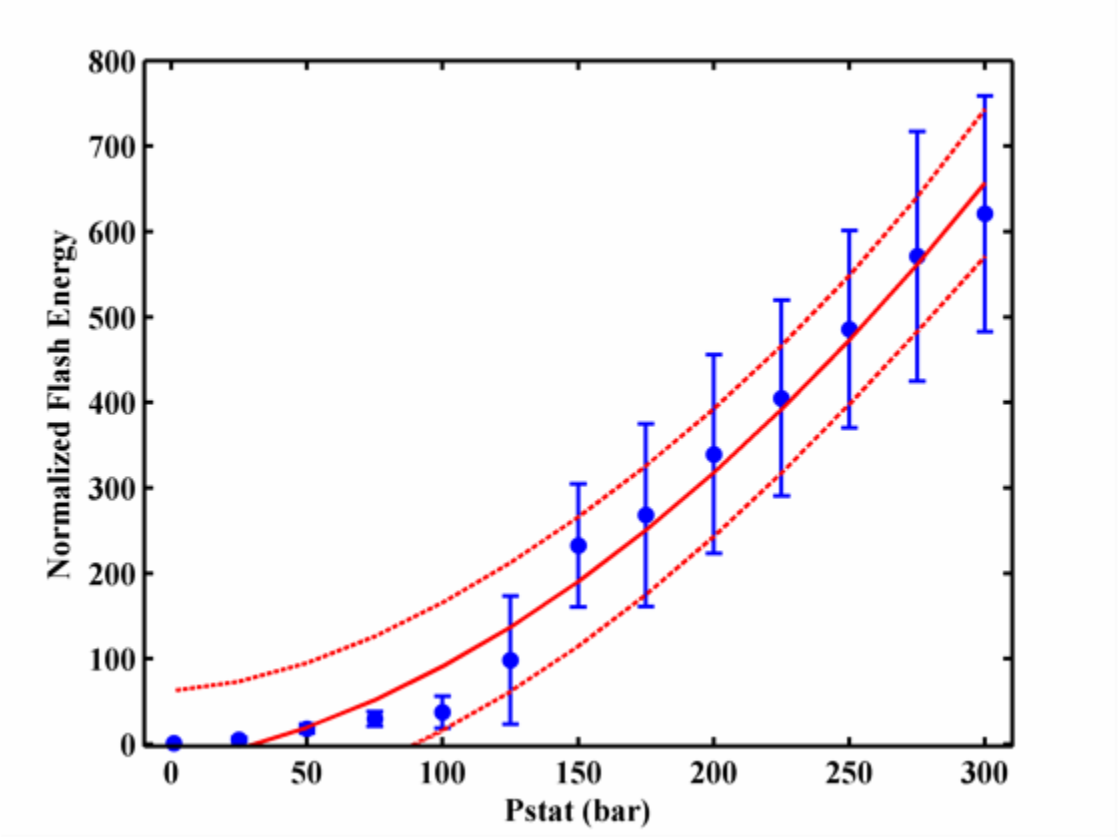

Figure 90: Energy of the largest flash of the blue band (185-400 nm) of cavitation event, normalized to the amplitude at 1 bar, as a function of the static pressure. The solid red line is a linear fit to the data, while the dashed red lines are the 95% confidence intervals of the fit to the data.

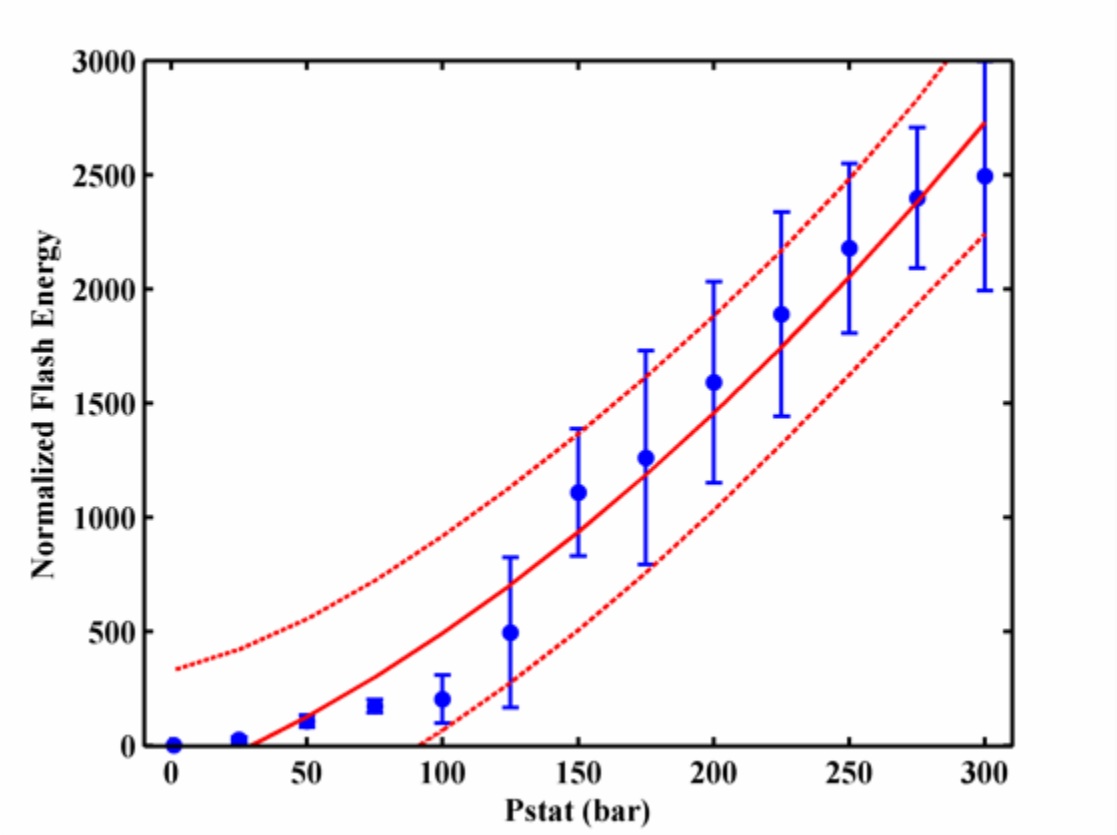

Figure 91: Energy of total light emitted in the blue band (185-450 nm) of the cavitation event, normalized to event energy at 1 bar, as a function of the static pressure. The solid red line is a quadratic fit to the data, while the dashed red lines are the 95% confidence intervals of the fit to the data.

Flash Type	A	B	C	r^2	$\sigma_{\bar{X}}$
First	1.74×10^{-4}	3.12×10^{-2}	4.00×10^{-1}	0.946	2. 5
Largest	5.62×10^{-3}	5.81×10^{-1}	-23.4	0.984	31.30
Event	1.55×10^{-2}	4.99	-162.2	0.971	178.08

Table 19: Coefficients for quadratic fits for data shown in Figure 89-Figure 91.

The quadratic fits do not agree as well with the data below 1250. bar where the NDFs were implemented. If saturation is the issue, as no other alternative seems viable as per previous discussion, these normalized values should still hold as light emissions at 1 bar were still well below the saturation limits of the tube. Over the entire 300 bar range, the energy of the blue light emissions increase by a factor of roughly 25 for the first flash, a factor of 620 for the largest flash, and a factor of 2500 for the entire event.

4.2.2.3. The Prospects for Thermonuclear Fusion

As with the shock wave data, the light emissions increase in energy with the static pressure. However, there is also an increase in the amount of acoustic energy in the system due to the increased cavitation threshold. The ratios of these two energies are plotted in Figure 92-Figure 94. For all three parameters (first flash, largest flash, and event flash) there appears to be a discontinuity after implementing the NDFs similar to that discussed with previous PMT data. Nevertheless, as with the shock wave data, the ratio of the two energies is approximately constant with the static pressure. As discussed with the shock wave data, the onset of any fusion reaction would likely shift this ratio to higher values.

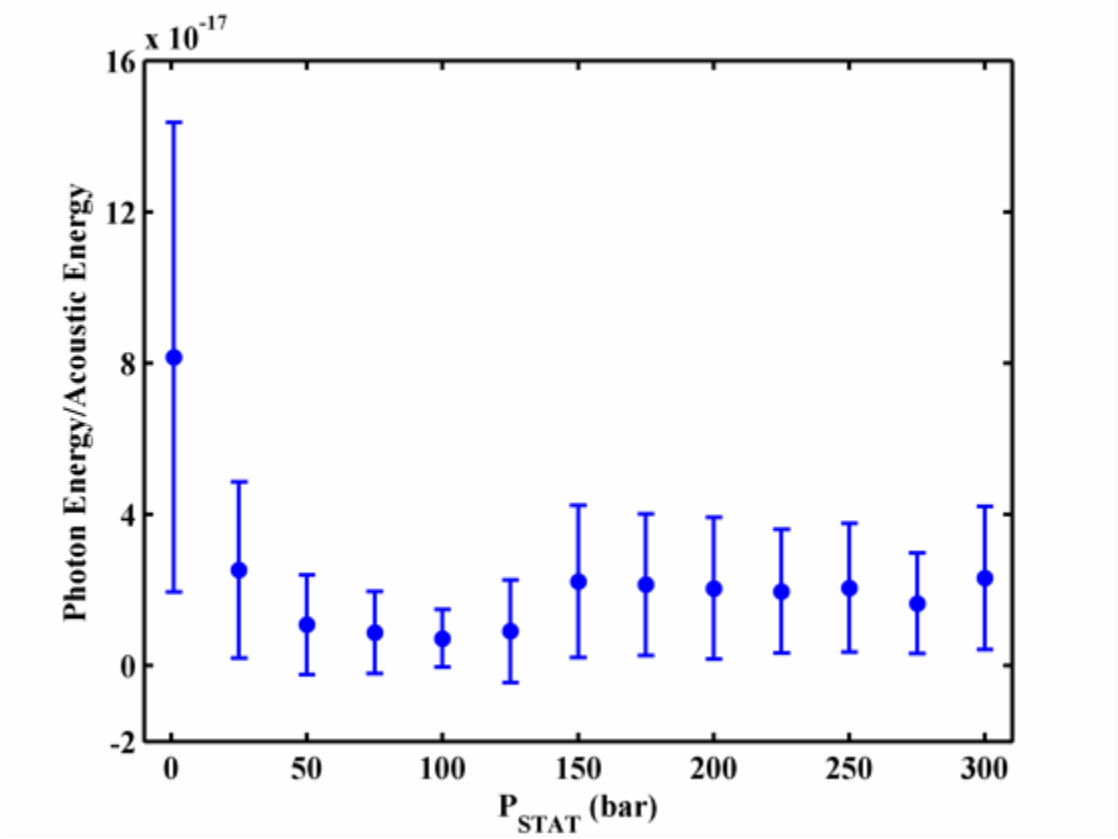

Figure 92: Ratio of blue light energy emitted by the event's first flash to acoustic energy.

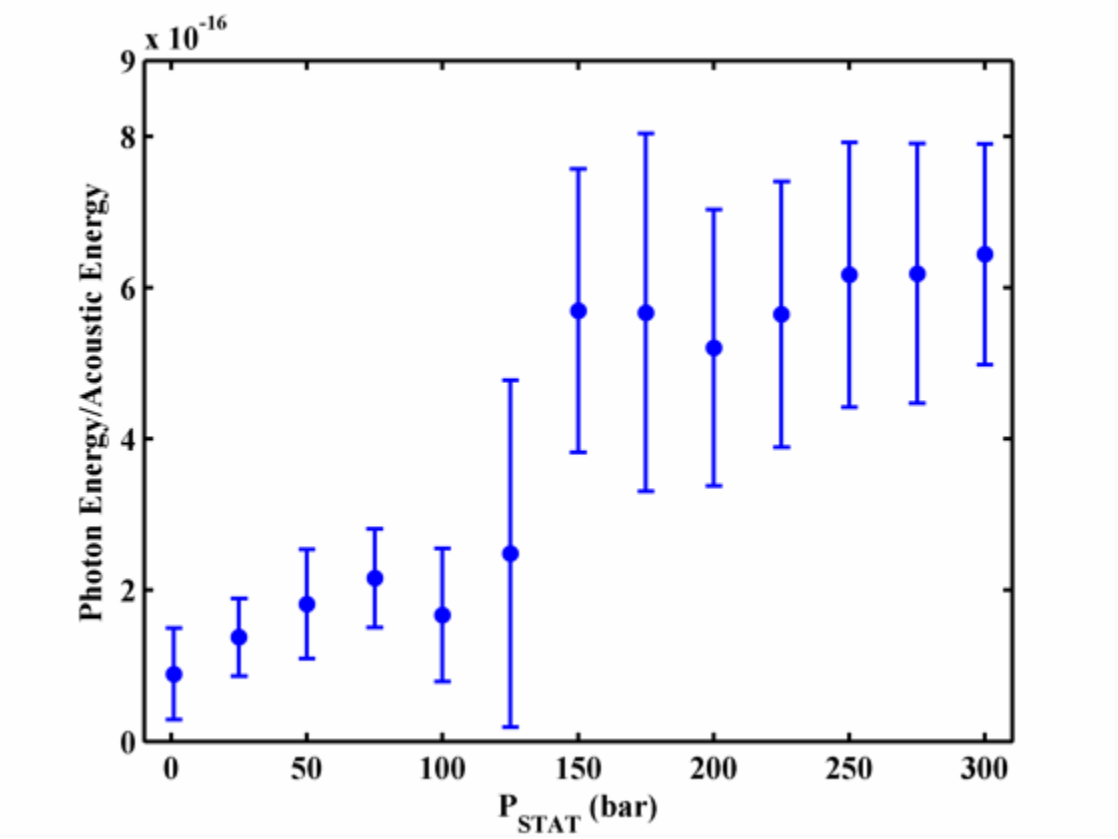

Figure 93: Ratio of blue light energy emitted by the event's largest flash to acoustic energy.

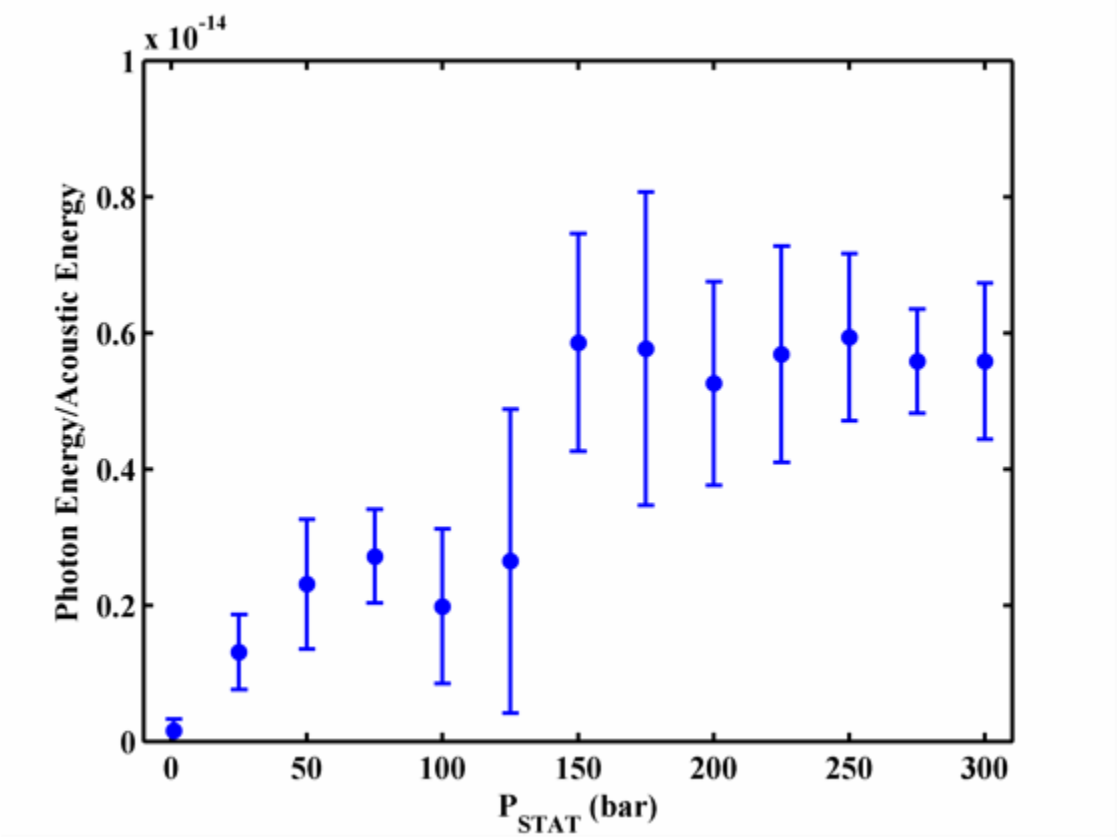

Figure 94: Ratio of blue light energy emitted by the event to acoustic energy.

4.2.2.4. Color Spectrum and Black Body Fit

The onset on any fusion reaction will require high temperatures of the contents of the bubble. For instance, the fusion reaction rate varies nearly 5 orders of magnitude (10^{-26} – 10^{-21}) over the temperature range 1-72 keV (1 eV ~ 1x10^4 K). The temperatures of other light emitting cavitation are typically characterized by their black body spectrum (Hiller et al. 1992). The radiance from black body emission is described by Planck's law (Zel'dovich and Raizer 1967):

$$I(\lambda, T) = \frac{4\pi\hbar c^2}{\lambda^5} \frac{1}{\exp\left[\frac{hc}{\lambda k_B T}\right] - 1} \quad (77)$$

where $I(\lambda, T)$ is the intensity of light (energy per unit time per surface area of emitter) emitted by the black body at temperature T, per solid angle, per wavelength, emitted at wavelength λ. The black body temperatures for the strength parameters were calculated by fitting energy spectrum from Figure 75-Figure 77 to a modified form of Equation (77). However, the results are questionable due to the saturation of the tubes at the higher static pressures. In addition, the error on the black body fits was over an order of magnitude due to the limited sample of the spectrum and no distinct trends were observed. A summary of the analysis is in Appendix C.

5. CONCLUSIONS

5.1. Summary

The properties of transient, inertial cavitation were investigated at elevated static pressures (up to 300 bar) with the long-range goal of creating a fusion reaction within the bubbles during the final stages of collapse (Gaitan et al. 2010). The subset of data shown reported on the measured cavitation threshold as a function of static pressure in ultrapure water (18 MΩ-cm). The cavitation events were nucleated by exciting standing waves in a high quality factor ($Q \sim 10^4$), spherical resonator. The isothermal threshold was found to increase linearly with the static pressure. The thresholds decreased with increasing temperature, although the decrease was mitigated at static pressures above ~ 250 bar. The measured thresholds were consistent with the crevice model for nucleation (Crum 1979), and an independent measurement of the particulate content of the fluid confirmed an adequate supply of nucleation sites within the fluid. In addition, the cavitation collapse strength was measured as a function of static pressure via light emissions and shock waves using three parameters (of the transient event): the first shock/flash, the largest shock/flash, and the total energy emission of the event (both shock and light). All three parameters were found to increase with the static pressure.

5.2. Improvements to the Measurement

There were three major areas in which the experiment could have been improved: loop design or construction, light detection, and cavitation detection. In terms of the loop design, Swagelok components with wider, tempered tubing should have been used to construct the high pressure sections. The narrow, low flow HiP components limited the circulation time of the fluid through the loop to ~ 15min. A wider tubing in concert with Swagelok components would have reduced the circulation time and the low flow sections would have been restricted to the HiP type ports on the inlet and outlet valves of the resonator. This change was not implemented for three reasons: First, these sections of tubing had already been leak checked and the leak detector had already been returned; Second, the high pressure section had been *a priori* minimized (~20" of HiP components, sans inlet/outlet valves on the resonators); Third, the flow rate was high enough that experiments could be performed in a timely manner, and any opening of the loop could introduce further impurities into the fluid. As a final note on loop design, further improvements could be done with the NPT ports on the resonators. NPT ports rely on tapered threads, which are not guaranteed to seal at the intended distance (i.e. the male portion can be recessed or protruding from the female opening in the resonator). This can result in perturbations of the spherical symmetry of the inner surface of the resonator. While NPT threads are a logical choice for a first generation resonator (they are easy to machine and will seal up to 300 bar), improved plug/port combinations could be designed to maintain the spherical symmetry inside the resonator.

In terms of use of the PMTs (light detection), there were three major issues that could have been improved. First, the calibration of the tube gain referenced in the section 2.2.3.2 was done after all the data had been gathered. Prior to that, the number of photoelectrons and saturation

limit of the tube were estimated using the manufacturer's specifications. Only after analyzing the pressure resolution was it apparent that these specifications were incorrect. Secondly, the tube gain should have been reduced to ensure that that each of the tubes remained in the linear regime over the entire static pressure range. PMTs are typically used for low level light sources. It is therefore not surprising the tubes saturated at the relatively high gain set since the brightest flashes have a 700-fold increase in the number of photons over the static pressure range. Third, the neutral density filters should have been implemented for all the data sets for consistency. Alternatively, the gain should have been set such that the PMTs would remain in the linear regime over the entire static pressure range and the NDF should have been disregarded. Also, avalanche photodiodes, which have a larger dynamic range than PMTs, would have been a sensible alternative for light detection.

Finally, improvements could have been made with the cavitation detection scheme. A coincidence scheme with a network of several shock sensors would be straightforward to implement. If this were done in hardware, the signal from each of the sensors could be high pass filtered and full wave rectified (absolute value circuit). The resulting signal could have been sent to a comparator, whose other input would have been a pre-determined trigger threshold. The threshold for the comparators could be set using a voltage reference chip. The TTL signal from the comparator could then be sent to a timing chip (such as the LMC555) which would send out a longer 5 μs TTL to account for any delay in the arrival time of the shock to the various sensors. The TTL from each of the timing chips could then be sent to an AND gate, which, if the signals from both timing chips overlapped, would output a TTL signal when cavitation occurred. Such a coincidence circuit would have two advantages: First, this hardware approach would negate the need for a second pulser/receiver in the experimental set-up, and second, since it is unlikely that

undesired signals from both sensors would simultaneously reach the comparator's threshold, the trigger threshold (on the comparators) could be as low as desired (above the noise floor of the circuit). Hence, the coincidence circuit would doubly confirm the onset of shock waves, and could be used to trigger off the smallest of shockwaves without having to worry about triggering off of transient noise.

5.3. Predictions and Final Thoughts

The collapse strength and acoustic energy required for cavitation were shown to scale with the static pressure at the same rate in section 4.2. As discussed, this implies no fusion reactions are occurring and the system is behaving as a mechanical system: some amount of energy imparted to the system is converted to shock waves and light emissions from the cavitation events. It should be noted that the abundance of heavy water molecules (D_2O) in the ultrapure water used as the cavitating medium was not known, although was likely quite small (heavy water molecules comprise some 150 ppm to regular water molecules in the ocean) which would make any fusion reaction difficult to achieve.

At low static pressures, the threshold (and therefore the amount of energy that can be stored in the system) is dominated by the particulate content of the liquid. Beyond 2.14 kbar, however, the threshold would be dominated by homogenous nucleation, assuming Equation (66) is valid to such static pressures. Because the homogenous nucleation threshold (HNT) is a relatively weak function of the static pressure (i.e. nearly constant with the static pressure), there should be two noticeable effects if the HNT were reached: First, the threshold should deviate from the linear predictions of Equation (66) to that of the linear predictions of HNT ($P_{CAV} = P_{STAT} + 2\text{x}10^3$, with P_{STAT} and P_{CAV} in units of bar), resulting in a shallower slope of the threshold with static

pressure. Second, the altered thresholds would, in turn, alter the predicted forms of the collapse strength such that the aforementioned ratio of photon energy to acoustic energy would remain constant. Hence, the effect of the static pressure on the collapse strength would be mitigated beyond the HNT. For instance, from Figure 93, the ratio of (blue) emission energy to acoustic energy is ~ 5 x 10^{-16}. Using this ratio and the predicted threshold of Equation (66), the (blue) flash energy increases by a factor of ~8000 from 1-2136 bar and increases by a factor of ~3 from 2136-4272 bar. These calculations are consistent with the quadratic predictions in Table 14. In contrast, the energy increases by a factor of ~2.6 over the range 1-2136 bar and increases by a factor of ~1.8 from 2136-4272 bar for the HNT.

The diminishing effect of static pressure past the HNT will retard the progress of reaching the parameter space necessary to reach the break-even point of fusion (if it hasn't already been reached). Instead of progressing to arbitrarily higher and higher static pressures past the HNT, accurate information of the static pressure resolved black body temperature [or other models that may be more appropriate for the type of emitter equated with cavitation (Brenner et al. 2002)] would allow for concrete predictions of the break-even point. Knowledge of this goal parameter space would be invaluable for engineering the system to sustain both the high static pressures and electronics necessary for generating sufficiently high driving amplitudes. The goal parameter space would also be a connecting point between theory and experiment, which could preclude or facilitate the possibility of ever achieving the break even temperature.

It should be noted that the preceding analysis assumes that the fluid temperature remains constant at 20 ºC. However, heating of the fluid due to absorption will increase proportional to the acoustic intensity (Nyborg 1975) as the threshold increases. This will increase the vapor pressure and lower the surface tension, resulting in lower thresholds for both crevice model and

homogenous nucleation. Therefore, the HNT may be reached at lower than anticipated static pressures.

Finally, to maximize the amount of energy available to the collapse, it is necessary to maximize the amount of energy that can be stored in the system (i.e. maximize the cavitation threshold). In order to do that, the fluid must be quenched of as many nucleation sites as possible. For water systems, the current set-up could be improved by reducing the fluid volume by using a smaller resonator and introducing custom, in-line filters to the loop (which requires smaller volumes of fluid). This would reduce the number of valves, which are known to grind on surfaces and create new particulates (Thompson 2010). The entire system could be kept in a clean room which would minimize contamination when introducing fluid into the loop. Another method to raise the threshold would be to explore alternative liquids with low vapor pressures, high surface tensions, and/or which would fully wet any foreign particulates. In the past, some authors have mixed glycerin or ethylene glycol to create more intense sonoluminescence (Gaitan et al. 1992). Certain mineral acids with low vapor pressures, such as sulfuric acid, have also been shown to produce very bright bubbles (Suslick 2008). These liquids would inactivate any hydrophobic nucleation sites that were present in the water.

Bibliography

Akulichev, V. A. *Soviet Physical Acoustics* 12 (1966): 144-149.

Apfel, R.E. "A novel technique for measuring the strength of liquids." *The Journal of the Acoustical Society of America* 49, no. 1 (1970a): 145-155.

Apfel, R.E. *Acoustic Cavitation.* Vol. 19, chap. 7 in *Methods of Experimental Physics: Ultrasonics*, by P.D. Edmonds, 356-411. New York: Academic Press, Inc., 1981.

Apfel, R.E. "Acoustic cavitation inception." *Ultrasonics* 22, no. 4 (1984): 167-173.

Apfel, R.E. "Possibility of micro-cavitation from diagnostic ultrasound." *IEEE Transations on Ultrasonics, ferroelectric, and frequency control* 33, no. 2 (1986): 139-142.

Apfel, R.E. "The role of impurities in cavitation-threshold determination." *The Journal of the Acoustical Society of America* 48, no. 5 (1970): 1179-1186.

ASTM International. "ASTM A380-06 Standard practice for cleaning, descaling, and passivation of stainless steel parts, equipment, and systems." *Annual book of ASTM standards.* West Conshohockem: ASTM, 2006. A380-06.

Atchley, A.A., and A. Prosperetti. "The crevice model of nucleation." *The Journal of the Acoustical Society of America* 86, no. 3 (1989): 1065-1084.

Atchley, A.A., L.A. Crum, J.R. Reidy, and R.A. Roy. "The influence of the dissolved ion concentration on the acoustic cavitation threshold of water." *The Journal of the Acoustical Society of America* 75, no. S1 (1984): S35.

Bangham, A.D., and M.W. Hill. "Distillation and storage of water." *Nature* 237 (1972): 408.

Barger, J.E. *Thresholds of acoustic cavitation in water.* Technical Memorandum NO. 57, Engineering and Applied Physics, Harvard University, Office of Naval Research, 1964.

Blake, F.G. JR. *The tensile strength of liquids.* Technical Memorandum NO.12 , Engineering Sciences and Applied Physics, Harvard University, Office of Naval Research, 1949.

Boas, M.L. *Mathematical methods in the physical sciences.* New York: John Wiley & Sons, Inc., 1983.

Borkent, B.M., S. Gekle, A. Prosperetti, and D. Lohse. "Nucleation threshold and deactivation mechanisms of nanoscopic cavitation nuclei." *The Physics of Fluids* 21, no. 10 (2009): 102003.

Breazeale, M.A., and L.A. Ostrovsky. "On the development of acoustical parametric oscillators." *18th International symposium on nonlinear acoustics.* Stockholm: AIP, 2008. 139-142.

Brenner, M.P., S. Hilgenfeldt, and D. Lohse. "Single-bubble sonoluminescence." *Review of Modern Physics* 74 (2002): 425-484.

Briggs, L. "Limiting negative pressure of water." *Journal of Applied Physics* 21 (1950): 721-722.

Brujan, E.A., D.S. Hecht, F. Lee, and A. G. Williams. "Properties of luminescence from laser-created bubbles in pressurized water." *Physical Review E* 72 (2005): 066310.

Burble Technologies, Inc. "Photomultiplier Handbook." 1980.

Caupin, F., and E. Herbert. "Cavitation in water: A review." *Comptes Rendus Physique* 7 (2006): 1000-1010.

Chappell, M.A., and S.J. Payne. "The effect of cavity geometry on the nucleation of bubbles from cavities." *The Journal of the Acoustical Society of America* 121, no. 2 (2007): 853-862.

Chen, C., and F.J. and Milero. "Reevaluation of Wilson's sound-speed measurements for pure water." *The Journal of the Acoustical Society of America* 60, no. 6 (1976): 1270-1273.

Church. "Stable cavitation description and characterization." *The Journal of the Acoustical Society of America* 122, no. 5 (2007): 3051.

Church, C.C. "Spontaneous homogeneous nucleation, inertial cavitation and the safety of diagnostic ultrasound." *Ultrasound in Medicine and Biology* 28, no. 10 (2002): 1349-1364.

Crum, L.A. "Acoustic cavitation threshold in water." Edited by W. Lauterborn. *Cavitation and inhomogeneities in underwater acoustics.* Gottingen: Springer, Inc., 1979. 84-89.

Crum, L.A. "Nucleation and stabilization of microbubbles in liquids." *Applied Scientific Research* 38 (1982): 101-115.

Crum, L.A. "Tensile strength of water." *Nature* 278 (1979): 148-149.

Davitt, K., A. Arvengas, and F. Caupin. "Water at the cavitation limit: Density of the metastable liquid and size of the critical bubble." *European Physics Letters* 90 (2010): 16002.

Evans, A. "The influence of modest overpressure on the persistence of air bubbles in water." Edited by W. Lauterborn. *Cavitation and inhomogeneities in underwater acoustics.* Gottingen: Springer, Inc., 1979. 90-94.

Fetter, W.A., and J.D. Walecka. *Theoretical mechanics of particles and continua.* New York: Dover Publications, Inc., 2003.

Finch, R.D. "Influence of radiation on the cavitation threshold of degassed water." *The Journal of the Acoustical Society of America* 36, no. 12 (1964): 2287-2292.

Fisher, J.C. "Nucleation." *Journal of Applied Physics* 19 (1948a): 775-784.

Fisher, J.C. "The fracture of liquids." *The Journal of Applied Physics* 19 (1948): 1062-1067.

Flannigan, D. J., and K. S. Suslick. "Inertially confined plasma in an imploding bubble." *Nature Physics* 6 (2010): 598-601.

Flynn, H.G. United States of America Patent 4,333,796. 1982.

Flynn, H.G. "Cavitation Dynamics II." *The Journal of the Acoustical Society of America* 58, no. 6 (1975): 1160-1170.

Flynn, H.G. *Physics of acoustic cavitation in liquids.* Vols. I-B, chap. 9 in *Physical Acoustics*, by W.P. Mason, 58-172. New York: Academic Press, Inc., 1964.

Fowlkes, J.B., Crum L.A. "Cavitation threshold measurements for microsecond length pulses of ultrasound." *The Journal of the Acoustical Society of America* 86, no. 3 (1988): 2190-2201.

Fox, F.E., and K.F. Herzfeld. "Gas bubbles with organic skin as nuclei." *The Journal of the Acoustical Society of America* 26, no. 6 (1954): 984-989.

Frenzel, H., and H. Schultes. "Luminescenz im ultraschallbeschickten wasser." *Z. Phys. Chem. B* 27 (1934): 421-424.

G.E. Oscmonics. "Pure Water Handbook." *G.E. Oscmonics Labstore.* 1997. http://osmolabstore.com/documents/pwh-s.pdf (accessed April 2011, 2011).

Gaitan, D.F., et al. "Transient Cavitation in high-quality-factor resonators at high static pressures." *The Journal of the Acoustical Society of America* 127, no. 6 (2010): 3456-3465.

Gaitan, D.F., L. A. Crum, C. C. Church, and R. A. Roy. "Sonoluminescence and bubble dynamics for a single, stable, cavitation bubble." *The Journal of the Acoustical Society of America* 91, no. 6 (1992): 3166-3183.

Galloway, W.J. "An experimental study of acoustically induced cavitation in liquids." *The Journal of the Acoustical Society of America* 26, no. 5 (1964): 849-857.

Gernez, M. "On the disengagement of gases from their saturated solutions." *Philosophical Magazine* 33 (1867): 479-481.

Gompf, B., R. Günther, G. Nick, R. Pecha, and W. Eisenmenger. "Resolving sonoluminescence pulse width with time-correlated single photon counting." *Physical Review Letters* 79, no. 7 (1997): 1045-1048.

Greenspan, M., and C.E. Tscheigg. "Radition-induced acoustic cavitation." *Journal of Research of the Nation Bureau of Standards-C* 71C, no. 4 (1967): 299-312.

Hale, G.M., and M.R. Querry. "Optical constants of water in the 200 nm to 200 μm wavelength region." *Applied Optics* 12 (1973): 555-563.

Hamamatsu Corporation. "Photomultiplier Tubes." *Hamamatsu Corportation Web site.* 2006. http://sales.hamamatsu.com/assets/applications/ETD/pmt_handbook_complete.pdf (accessed April 12, 2011).

Harvey, N. E., D.K. Barnes, W.D. McElroy, A.H. Whiteley, D.C. Pease, and K.W. Cooper. "Bubble formation in animals." *Journal of Celluar Physiology* 24, no. 1 (1944): 1-22.

Harvey, N.E. "Sonoluninescence and sonic chemiluminescence." *Journal of the American Chemical Society* 61 (1939): 2392-2398.

Herbert, E., S. Balibar, and F. Caupin. "Cavitation pressure in water." *Physical Review E.* 74, no. 4 (2006): 041603.

Herbertz, J. "Spontaneous cavitation in liquids free of nuclei." *Fortschritte der Akustik DAGA.* Bad Honnef: DPG-G,bH, 1988. 439-442.

Hiller, R.A. "The spectrum of single-bubble sonoluminescence." *Ph.D. Dissertation.* University of California, Los Angeles, 1995.

Hiller, R.A., D.F. Gaitan, R. Tessien, and J. Alstadter. "Optical spectroscopy of transient cavitation at high pressure." *The Journal of the Acoustical Society of America* 122, no. 5 (2007): 2991.

Hiller, R.A., S.J. Putterman, and B.P. Barber. "Spectrum of snchronous picosecond sonoluminescence." *Physical Review Letters* 69, no. 8 (1992): 1182-1184.

Hiller, R.A., S.J. Putterman, and K.R. Weninger. "Time-resolved spectra of sonoluminescence." *Physical Review Letters* 80, no. 5 (1998): 1090-1093.

Hodnett, M., and B. Zeqiri. "Toward a reference ultrasonic cavitation vessel." *IEEE Transactions on Ultrasonics, Ferroelectrics, and Frequency Control* 55, no. 8 (2008): 1809-1822.

Holland, C. K., and R. E. Apfel. "An improved theory for prediction of micro cavitation thresholds." *IEEE Transations on Ultrasonics,Ferroelectric, and Frequency Control* 36, no. 2 (1989): 204-208.

Holland, C.K., and R.E. Apfel. "Thresholds for transient cavitation produced by pulsed ultrasound in a controlled nuclei enviroment." *The Journal of the Acoustical Society* 88, no. 5 (1990): 2059-2069.

Horowitz, P, and W. Hill. *The art of electronics.* 2. New York: Cambridge University Press, 1989.

Hugli, H.W. "Frequency response of piezoelectric transducers." Vers. Ed. 10.01. *KistlerInstrument Corporation Web site.* http://www.kistler.com/mediaaccess/en-us/K20.260e-10.01.pdf (accessed April 12, 2011).

Jackson, J.D. *Classical Electrodynamics.* Hoboken: John Wiley & Sons, Inc., 1999.

Johnson, B.D., and R.C. Cooke. "Generation of stabilized microbubbles in seawater." *Science* 213 (1981): 209-211.

Kistler Instrument Corp. "603B1 data sheet." *Kistler Instrument web site.* 2003. http://www.kistler.com/mediaaccess/000-427a-04.03.pdf (accessed April 11, 2011).

Lasič, S., and G. Torzo. "Torson pendulum." *GIREP Sem.* Udine, 2001.

Leighton, T.G. *The Acoustic Bubble.* San Diego: Academic Press, Inc., 1994.

Lieberman, D. "Radiation-induced cavitation." *The Physics of Fluids* 2, no. 4 (1959): 466-468.

Lonzaga, J.B., J.L. Raymond, J. Mobley, and D.F. Gaitan. "Supression of an acoustic mode by an elastic mode of a liquid-filled spherical shell resonator." *The Journal of the Acoustical Society of America* 129, no. 2 (2011): 597-603.

Mehl, J.B. "Spherical acoustic resonator." *The Journal of the Acoustical Society of America* 78, no. 2 (1985): 762-768.

Messino, C.D., D. Sette, and F. Wanderlingh. "Effects of solid impurities on cavitation nuclei in water." *The Journal of the Acoustical Society of America* 41, no. 3 (1967): 573-583.

Messino, D., D. Sette, and F. Wanderlingh. "Statistical approach to ultrasonic cavitation." *The Journal of the Acoustical Society of America* 35, no. 10 (1963): 1575-1583.

Moldover, M.R., J.B. Mehl, and M. Greenspan. "Gas-filled spherical resonators." *The Journal of the Acoustical Sociey of America* 79, no. 2 (1986): 253-272.

Mørch, K.A. "Reflections on cavitation nuclei in water." *The Physics of Fluids* 19, no. 7 (2007): 072104.

Neppiras, E.A. "Acoustic Cavitation." *Physics Reports* 3 (1980): 159-251.

Nyborg, W.L. *Intermediate biophysical mechanics.* Menlo Park: Cummings Publishing Company, 1975.

Ohmi, T. *Ultraclean Technology Handbook.* Vol. 1. New York: Marcel Dekker, Inc., 1993.

Ohno, I., M. Kimura, Y. Hanayama, H. Oda, and I. Suzuki. "Pressure dependence of the elasticity of a steel sphere measured by the cavity resonance method." *The Journal of the Acoustical Society of America* 110, no. 2 (2001): 830-836.

Palmentieri, P., interview by K. Bader. *Private communication with Hamamatsu Corportion application engineer* (March 4, 2011).

Pettersen, M.S., and S., Maris H.J. Balibar. "Experimental investigation of cavitation in superfluid 4He." *Physical Review B* 49, no. 17 (1994): 49-57.

Pitre, L., M.R. Moldover, and W.L. Tew. "Acoustic thermometry." *Metrologia* 43 (2006): 142-162.

Prosperetti, A., and A. Lezzi. "Bubble dynamics in a compressible liquid." *The Journal of Fluid Mechanics* 168 (1986): 457-478.

Roy, R.A., A.A. Atchley, L.A. Crum, J.B. Fowlkes, and J.J. Reidy. "A precise technique for the measurement of acoustic cavitation thresholds and some preliminary results." *The Journal of the Acoustical Society of America* 78, no. 5 (1985): 1799-1805.

Roy, R.A., S.I. Madanshetty, and R.E. Apfel. "An acoustic backscatterin technique for the detection of transient cavitation produced by microsecond pulses of ultrasound." *The Journal of the Acoustical Society of America* 87, no. 6 (1990): 2451-2458.

Sette, D., and F. Wanderlingh. "Nucleation by cosmic rays in ultrasonic cavitation." *Physical Review* (125) 2 (1962): 409-417.

Shapira, D., and M. Saltmarsh. "Nuclear fusion in collapsing bubbles-Is it there? An attempt to repeat the observations of nuclear emissions from sonoluminescence." *Physical Review Letters* 89 (2002): 104302.

Sirotuk, M.G. *Soviet Physical Acoustics* 16 (1970): 237-240.

Strasberg, M. "Onset of ultrasonic cavitation in tap water." *The Journal of the Acoustical Society of America* 31, no. 2 (1959): 163-176.

Suslick, K.S., Flannigan, D.J. "Inside a collapsing bubble." *Annual Review of Physical Chemistry* 59 (2008): 659-683.

Tajima, E., M Adachi, T Doke, S Kubota, and M. Tsukuda. *Journal of the Physical Society of Japan* 22 (1967): 355-360.

Taleyarkhen, R. P., C. D. West, J. S. Cho, R. T. Lahey JR., R. I. Nigmatulin, and R. C. Block. "Evidence for nuclear emissions during acoustic cavitation." *Science* 295 (2002): 1868.

Tessien, R.A., H. Tardif, R.A. Hiller, J. Schaefer, and D.F. Gaitan. "Morphology of transient cavitation in 300 bar resonator (A)." *The Journal of the Acoustical Society of America* 122 (2001): 2992.

Thermo Scientific. "Thermo Scientific Waterbook." *Thermo Fisher Scientific, Inc.* 2009. https://fscimage.fishersci.com/images/D17384~.pdf (accessed April 11, 2011).

Thompson, R., interview by K. Bader. *Private communication with Particle Measuring Systems application engineer* (August 2010).

Tolman, R.C. *The principles of statistical mechanics.* New York: Dover Publications, Inc., 1979.

Tomlinson, C. "On the so-called "inactive" conditions of solids." *Philosophical Magazine* 34 (1867): 136-143, 229-230.

Trevena, D.H. *Cavitation and tension in liquids.* Philadelphia: IOP Publishing Ltd., 1987.

Walton, A. J., and G. T. Reynolds. "Sonoluninescence." *Advances in Physics* 33, no. 6 (1984): 595-660.

Willard, G.W. "Ultrasonically induced cavitation in water." *The Journal of the Acoustical Society of America* 25, no. 4 (1953): 669-686.

Wolfrum, B., T. Kurz, O. Lindau, and W. Lauterborn. "Luminescence of transient bubbles at elevated ambient pressure." *Physical Review E* 64 (2001): 046306.

Yount, D.E. "On the elastic properties of the interfaces that stabilize gas cavitation nuclei." *Journal of Colloid and Interface Science* 193 (1997): 50-59.

Yount, D.E. "Skins of varying permeability." *The Journal of the Acoustical Society of America* 65, no. 6 (1979): 1429-1439.

Yount, D.E., E.W. Gillary, and D.C. Hoffman. "A microscopic investigation of bubble formation nuclei." *The Journal of the Acoustical Society of America* 76, no. 5 (1984): 1511-1521.

Zel'dovich, Ya.B., and Yu.P Raizer. *Physics of shock waves and high-temperature hydrodynamic phenomena.* Translated by W.D. Hayes and R.F. Probstein. New York: Academic Press, 1967.

List of Appendices

Appendix A. Summary of Test Procedure Used by Particle Measuring Systems

The following procedures, in chronological order were used by the technicians at PMS to prepare the measuring instruments and samples before performing the measurements.

1. Instrumentation is verified to have a current calibration (less than one year old).
2. The system hardware is prepared for testing by verifying proper cleaning and operation of all components.
3. The system software is prepared by entering the test recipes and particle size thresholds as defined above in the Setup section.
4. Filtered de-ionized (DI) water is run through the particle counter to flush the tubing and syringe of the system and verify that the DC Light level (a status indicator of the cleanliness of the capillary of the particle counter) is within acceptable range.

Each sample is tested in the following manner:

1. The sample container is "swirled" manually prior to testing so that any particles in the solution that may have settled are mixed into the solution.
2. The sampler container is placed on the test stand of the syringe sampler such that the fill tube to the particle counter is in the liquid sample.
3. With the test recipe having been already configured, the "Go" button is pressed in the software and the sample ID is entered by the operator. When the sample ID is entered and acknowledged, the software initiates the sampling system to begin taking its first aliquot of fluid from the beaker.
4. The sampling system automatically and consecutively draws the aliquots from the beaker, as defined in the test recipe (discharging each aliquot before the next aliquot is taken). Note that the data from the first of the four aliquots is electronically discarded

from the software data storage. Also, the first mL of each aliquot is electronically discarded as a tare volume, and the remaining sample volume is drawn and the data electronically recorded.

5. The measurement data from each aliquot is recorded and stored in the software and is later downloaded as a comma separated variable (CSV) file in Microsoft Excel.

In the event that a sample contained a particle concentration exceeding the saturation limit of the instrument the sample is diluted in the following manner:

6. An ultrasonically cleaned beaker (431.3 mL) is allowed to overflow with particle free water at a flow of >500 mL/min. while stirring with an overhead lab stir bar.
7. Background counts are monitored with the particle counter of interest until counts are <10 particles/mL cumulative greater than the smallest channel.
8. The flow of particle free water is diverted from the beaker.
9. The sample container is “swirled” manually prior to testing so that any particles in the solution that may have settled are mixed into the solution.
10. Using an automatic pipette, 1 mL of particle free water is removed from the beaker.
11. Using an automatic pipette, 1 mL of sample is added to the beaker.
12. The diluted sample is tested according to *Sample Testing* steps 3-5.

Appendix B. Calculation of Crevice Size

The temperature dependent data in Figure 64 - Figure 66 was fit to Crum's model (see Figure 78 for representative fits) up to 250 bar. From these fits, δ [and therefore *a* via Equation (74)] could be determined as a function of the static pressure. The results are plotted in Figure 95. P_V and P_G are assumed to be 2 kPa, and σ was assumed to be 72 dyn/cm. It should be noted that the 95% confidence intervals of the fit make δ larger than 1 (and therefore unphysical). Hence, the vertical error bars show the spread in range of physical values of δ (0-1).

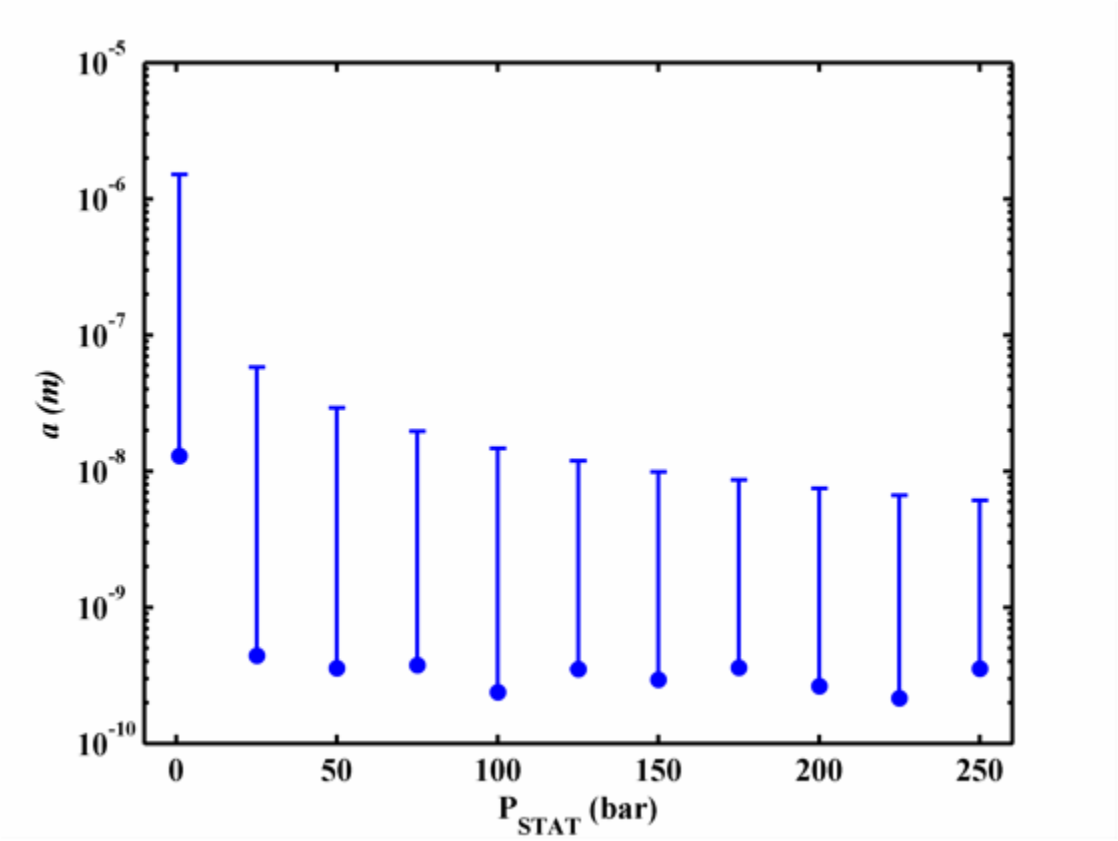

Figure 95: *a* as calculated using Equation (74) and fitting parameter δ from Equation (11) as a function of static pressure in the fluid. The vertical error bars are chosen such that δ = 1. The lower bound error bars are negative, and therefore unable to be shown on the log scale.

The crevice size is relatively large at 1 bar (12 nm), but then quickly drops to sub nanometer size. The crevice size weakly decreases linearly over the static pressure range 25-250 bar:

$$a = -4.95x10^{-13}P_{STAT} + 3.92x10^{-10} \quad (78)$$

where P_{STAT} is in units of bar and a is in units of meter. Apfel suggests that a is approximately 1/5 of the effective crevice radius. If this were the case, the mote size at 1 bar would be roughly 65 nm, while at 25-250 bar the mean mote size would be 2 nm. It is hard to compare these mote sizes with the known size distribution of particulates in the fluid (see section 2.1.5.3). From Figure 11 it is apparent that the number of particles of a certain size is inversely proportional to the particulates size on a log-log scale, and it could also be assumed that particulates much smaller than the smallest measured size (100 nm) would be in abundance in the fluid. Hence, it is reasonable to conclude that particulates with adequate size (say a factor of five larger than the effective mote size) would be present within the fluid. If the mote is assumed to be harbored in a particulate an order of magnitude larger than the effective mote size, then the nucleating particulates would be roughly 650 nm at 1 bar and 20 nm for the particulates at 25-250 bar. For reference, Figure 11 indicates that there are nearly 1 million particulates 100 nm in size, and therefore there is an abundance of adequately sized particulates at the effective particulate size.

Appendix C. Calculation of the Black Body Temperature

Most of the parameters required to calculate *I* were readily available: the energy spectra shown in Figure 75-Figure 77 account for the full angular distribution, the wavelength intervals were determined from the spectra of the color filters in Figure 30-Figure 32, and the effective wavelengths were listed in Table 18. The pulse widths, shown in Figure 96-Figure 98, were measured from the PMT waveforms. Each data point (error bar) represents the averaged (standard deviation) for one data set at each static pressure. Averaging all three data sets had negligible effect. The event pulse width was calculated from the summed individual pulse widths of each flash in the event.

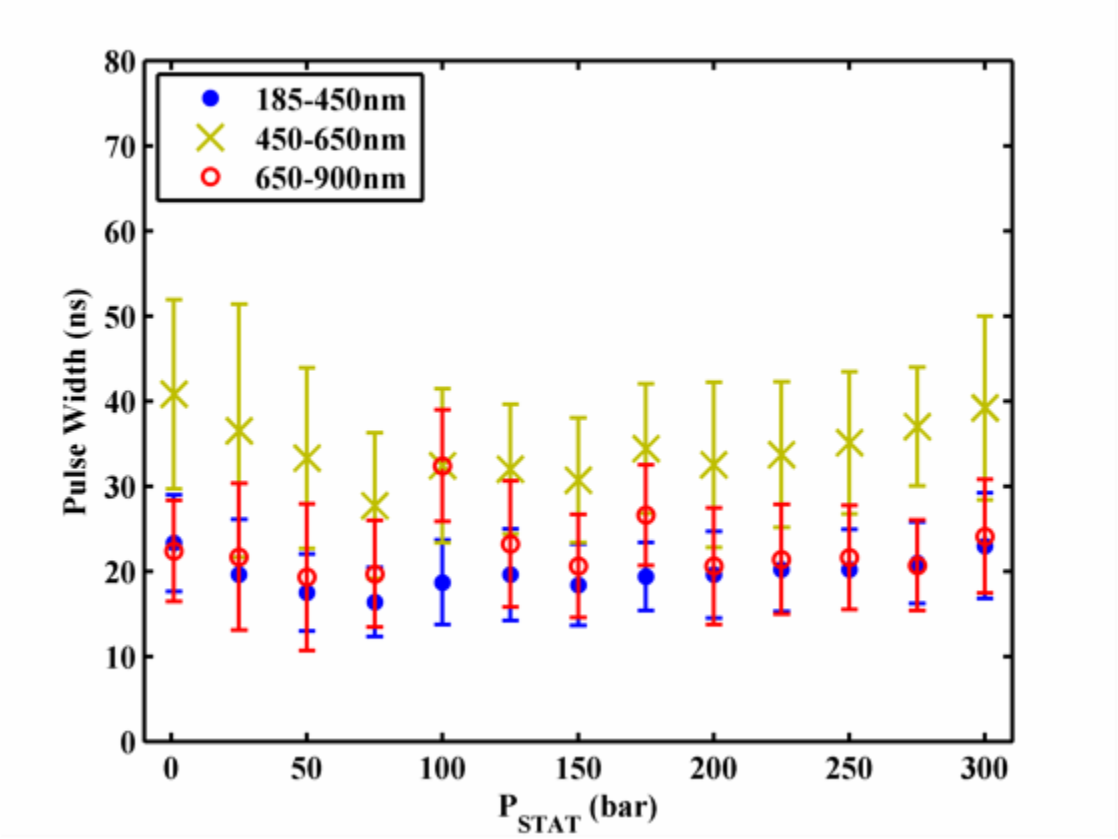

Figure 96: Width of the first flash of cavitation event as a function of static pressure.

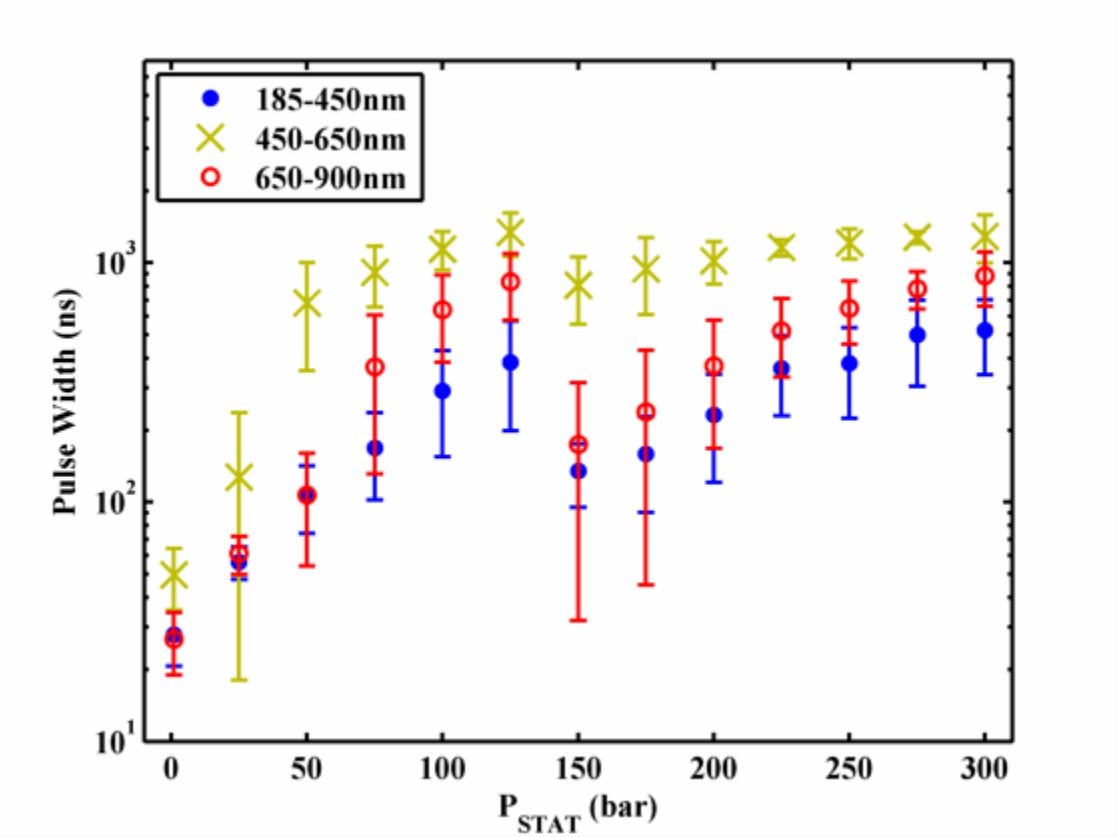

Figure 97: Width of the largest flash of cavitation event as a function of static pressure.

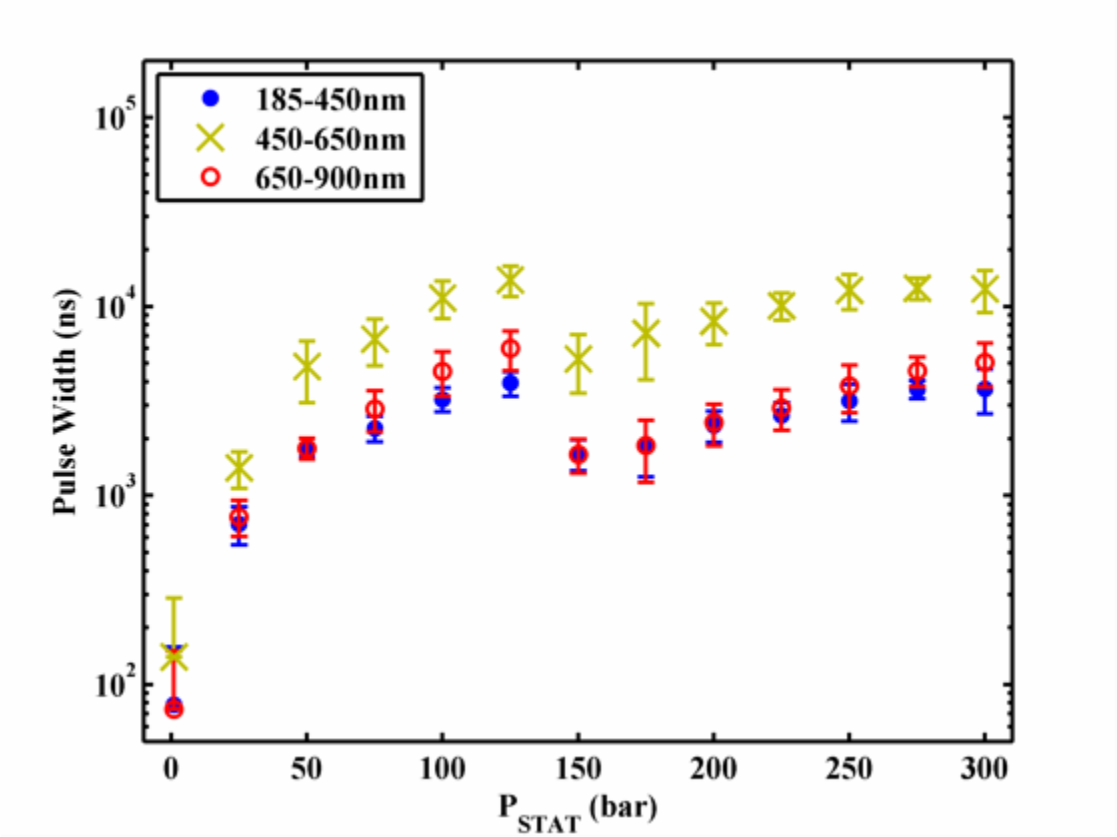

Figure 98: Width of the event light emission of cavitation event as a function of static pressure.

Two features are of interest from the pulse widths. First, the recorded pulse width of the first flash appears to be constant over the entire range of static pressures. It is possible that pulse width was too short for the PMT to resolve. For pulse widths shorter than the resolution of the measuring instrument, techniques like time-correlated single photon counting (Hiller et al. 1998, Gompf et al. 1997) are required to obtain an accurate measure of the pulse width. However, the rise time of the PMTs (2.2 ns) are short enough that the measured widths (~20 ns) are within the measuring capabilities of the instrument. The second feature is the noticeable discontinuity in Figure 97 and Figure 98 after implementing the NDFs at 150 bar (the particular data set used to calculate the pulse width at 125 bar did not have the NDFs in place).

The surface area of the emitter was the only experimental parameter absent for calculating the radiance. Thus, an additional fitting parameter was used to obtain a best-fit surface area in Equation (77). The final fitting function had the form:

$$I'(\lambda, T, A) = \frac{4\pi\hbar c^2}{\lambda^5} \frac{A}{\exp\left[\frac{hc}{\lambda k_B T}\right] - 1} \tag{79}$$

where *A* is the surface area of the emitter, and the prime indicates that the radiance has been multiplied by the emitter's surface area (and, for the first flash, the pulse width). An example fit of Equation (79) to the measured *I'* is shown in Figure 99.

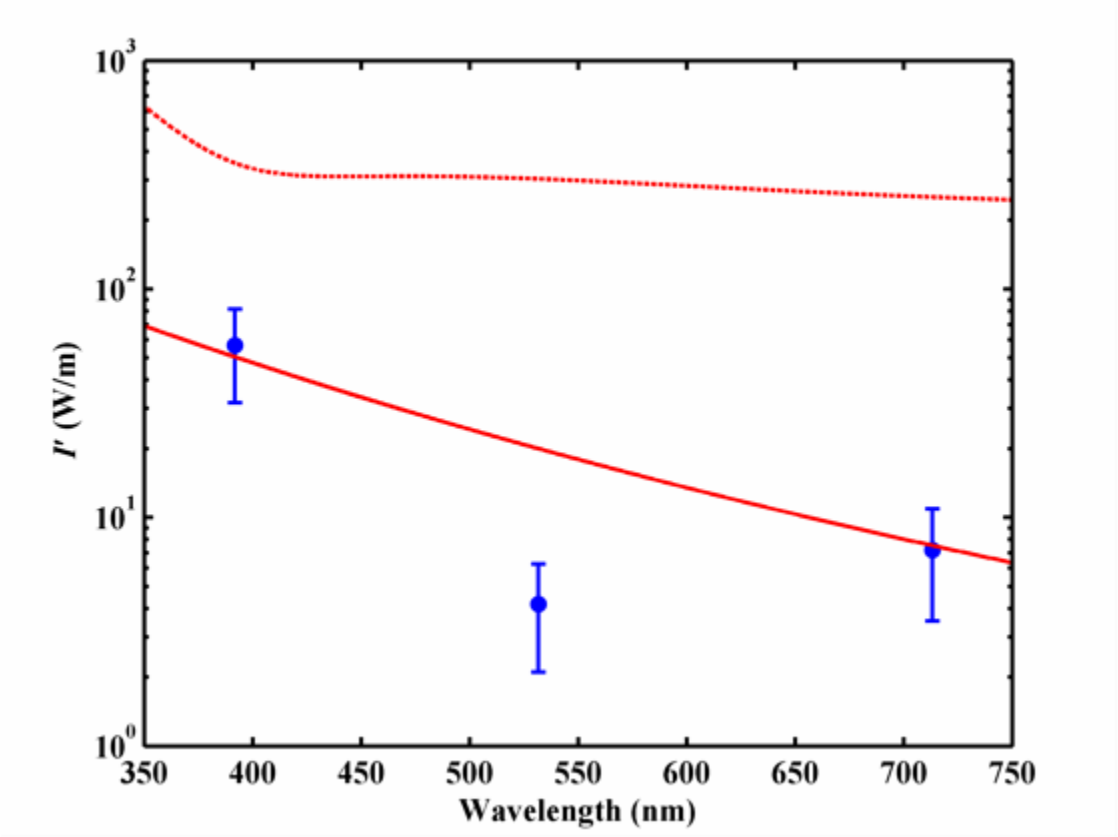

Figure 99: The measured, surface independent, radiance (*I'*) for each of the three sampled wavelengths. The data is from 1 bar static pressure of the largest flash from the cavitation event. The solid red line is the fit of Equation (79) to the measured radiance (dots). The dashed red line is the upper 95% confidence interval. The lower 95% confidence interval was negative and therefore unable to show up on the log scale. The best fit black body temperature is 2.04 eV (+/- 49.91 eV). The best fit radius, calculated from *A* in Equation (79), was 39.67 nm (+/- 269.22 nm).

The calculated black body temperatures for the strength parameters (first flash, largest flash, and total emission from the event) are shown in Figure 100-Figure 102. The vertical error bars on the data are the 95% confidence intervals of the best fit temperature. The sizeable error bars

(note the log scale) obscure any static pressure dependent trends that the black body temperature may have. The sizes of the error bars are warranted considering the limited wavelengths sampled, number of fitting parameters, and the saturation of the yellow and red tubes. A more accurate measure of the black body temperature would require sampling several more wavelengths (i.e. more sensors) but would be well worth the effort. The static pressure dependence of the black body (or other model) temperature would give a predictive measure of the parameter space required (static pressure, acoustic pressure, electronic requirements, resonant frequency, etc) for the cavitation event to produce a sizeable yield of fusion reactions. This, in turn, would guide theoretical studies (i.e. hydrocodes such as HYADES, Cascade Applied Sciences, Inc, Boulder, CO) to the parameter spaces that need to be explored.

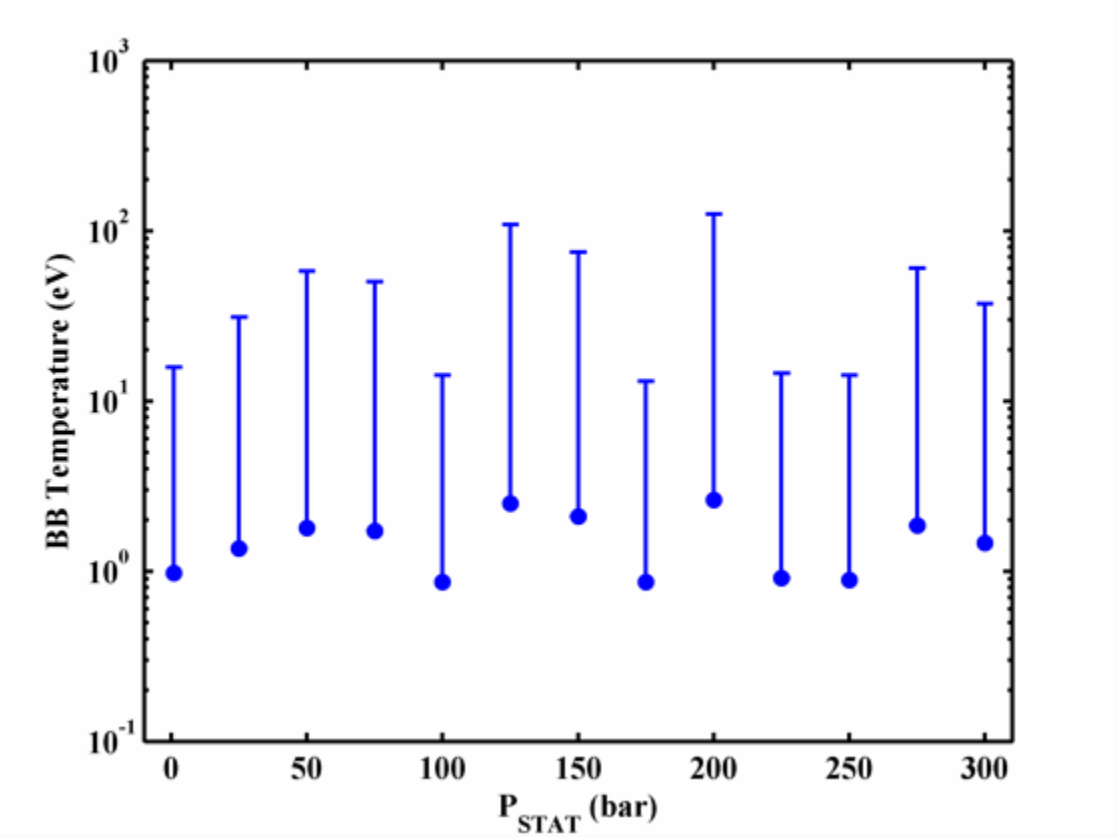

Figure 100: Calculated black body temperature of the largest flash as a function of static pressure. The lower bound error bars were less than zero and therefore could not be displayed on the log scale.

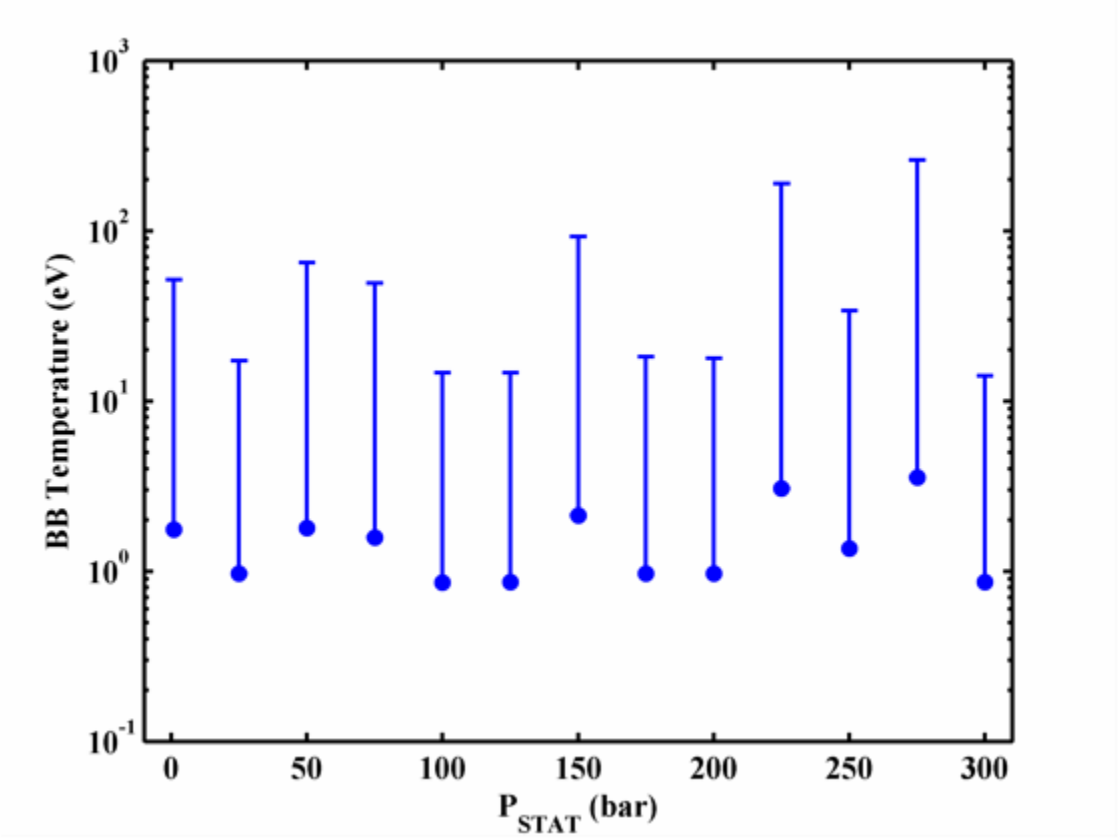

Figure 101: Calculated black body temperature of the largest flash as a function of static pressure. The lower bound error bars were less than zero and therefore could not be displayed on the log scale.

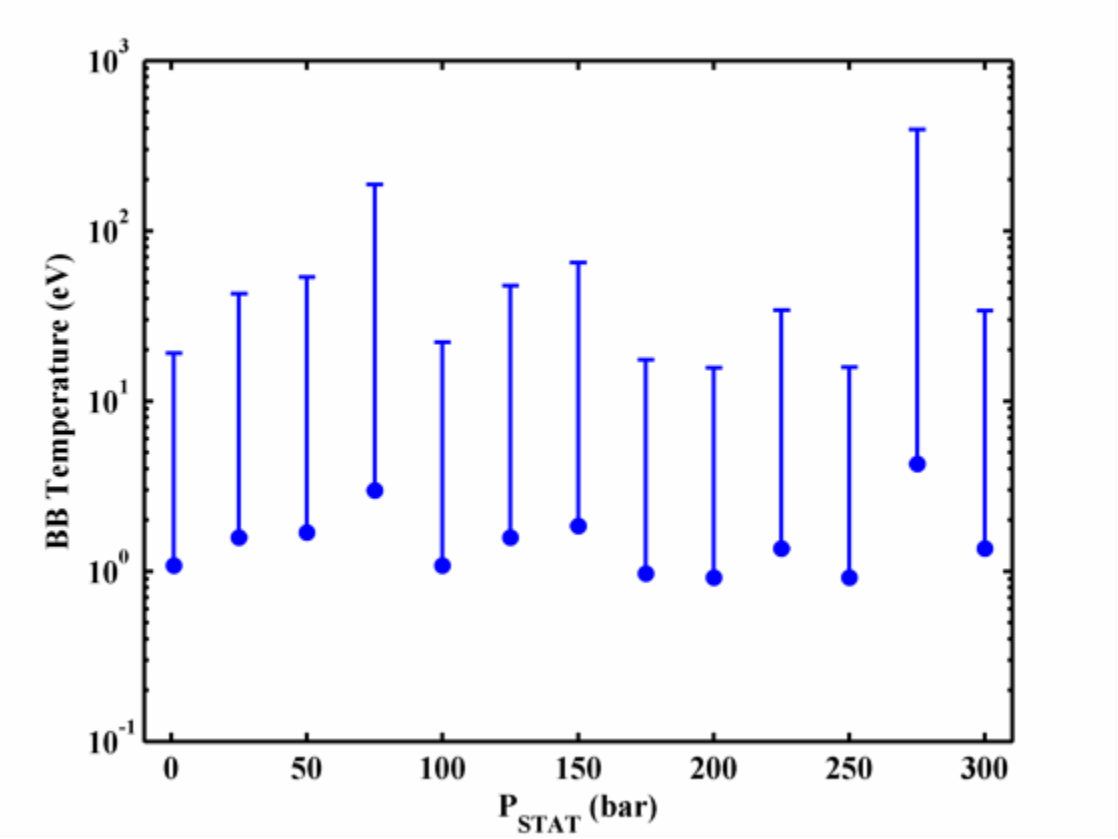

Figure 102: Calculated black body temperature of the total event emission as a function of static pressure. The lower bound error bars were less than zero and therefore could not be displayed on the log scale.

VITA

Kenneth Bader was born on May 2, 1982 in Evansville, IN and graduated from Mt. Vernon High School (Mt. Vernon, IN) in 2000. He attended Grand Valley State University (Allendale, MI) and where he received at Bachelors of Science in physics in 2005. He then attended the University of Mississippi for graduate school, where he received a Master of Arts in physics in 2007.